Published by Empress Catherine II
Saint Petersburg Mining University

SINCE 1907

ISSN 2411-3336
E-ISSN 2541-9404

JOURNAL OF MINING INSTITUTE

ZAPISKI GORNOGO INSTITUTA

SCIENTIFIC JOURNAL

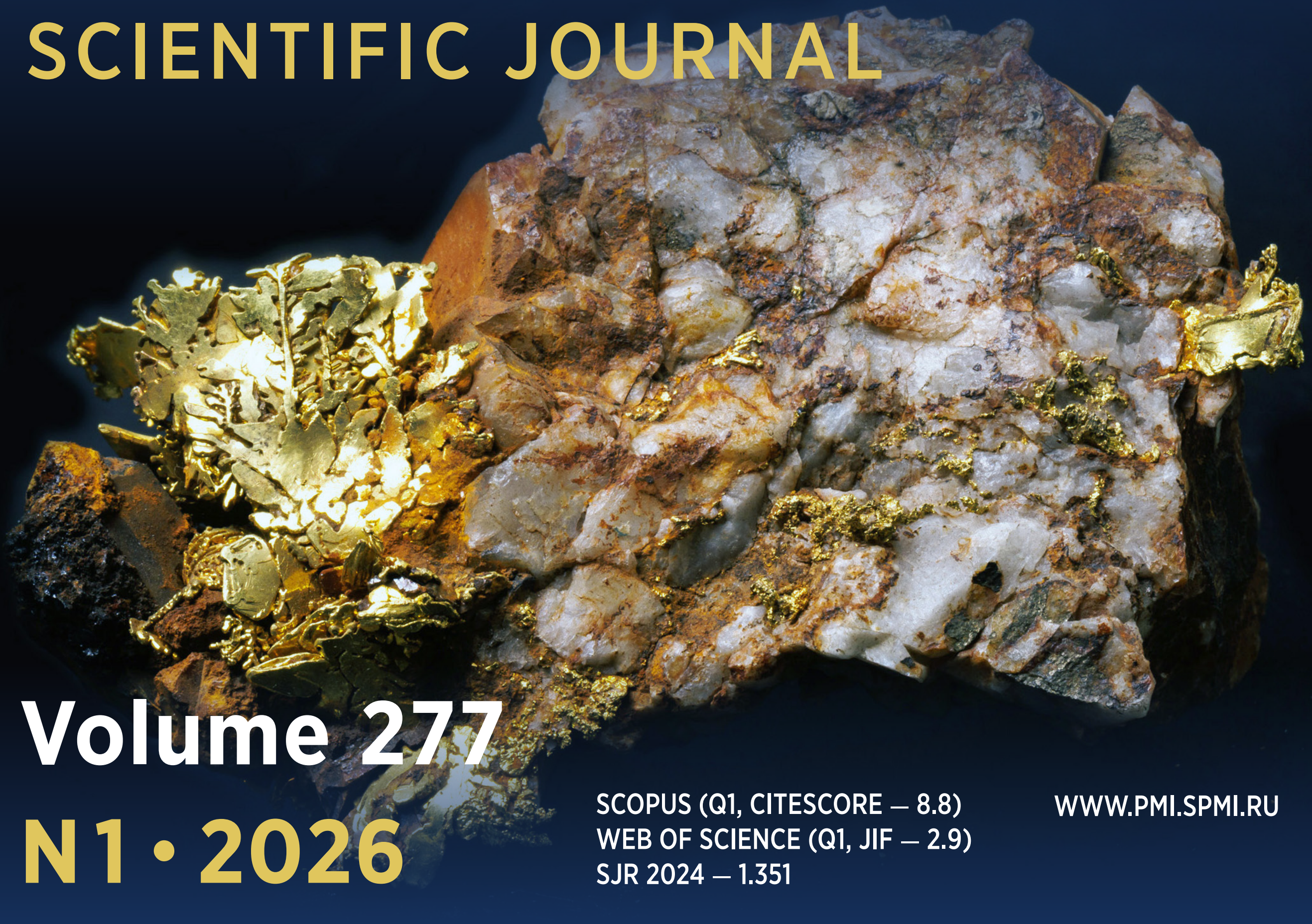

Volume 277
N1 • 2026

SCOPUS (Q1, CITESCORE – 8.8)
WEB OF SCIENCE (Q1, JIF – 2.9)
SJR 2024 – 1.351

WWW.PMI.SPMI.RU

Journal
of Mining Institute
Scientific journal

Empress Catherine II
Saint Petersburg
Mining University

The International
Competence Center
for Mining Engineering
Education under the
auspices of **UNESCO**

The peer-reviewed scientific periodical “Journal of Mining Institute” is published since 1907 by Empress Catherine II Saint Petersburg Mining University – the first higher technical educational institution in Russia, founded in 1773 by the decree of Catherine II as the embodiment of the ideas of Peter I and M.V.Lomonosov on the training of engineers for the development of mining business.

The International Competence Center for Mining Engineering Education under the auspices of UNESCO operates on the basis of Empress Catherine II Saint Petersburg Mining University and contributes to active interaction of the Journal with the international scientific community.

The purpose of the Journal is to create an information space in which Russian and foreign scientists can present results of their theoretical and empirical research on the problems of the mining sector. The journal invites the leading specialists to publish scientific articles and promotes them in the international scientific community.

Published articles cover the issues of geology, geotechnical engineering and engineering geology, mining and petroleum engineering, mineral processing, energy, geoecology and life safety, economics of raw materials industries.

The Journal is indexed by Scopus (Q1, CiteScore – 8.8), Web of Science (JCR – Q1, JIF – 2.9), SJR 2024 – 1.351, DOAJ, RSCI, GeoRef, Islamic World Science Citation Database (ISC), Google Scholar. It is included in the White list of the Ministry of Education and Science of the Russian Federation.

The Journal is published six times a year. The average first decision time is one month.

Articles are published free of charge. Translation is provided by the author.

The cover shows an exhibit of the Mining Museum – lamellar dendritic gold formations in fractured veined milky-white quartz with goethite, California, USA. Gift of Emperor Alexander II. Gold is one of the first known metals since ancient times due to its occurrence in native state. In Latin, the name for gold, *aurum*, means “yellow”.

The Mining Museum is the world’s third largest natural-science exposition, it contains more than 230 thousand exhibits, including precious metals and stones, unique collections of minerals, ores, rocks, paleontological remains, meteorites, a collection of models and prototypes of mining equipment, pieces of stone-cutting and jewelry art.

JOURNAL OF MINING INSTITUTE

ZAPISKI GORNOGO INSTITUTA

PEER-REVIEWED SCIENTIFIC JOURNAL

Published since 1907

ISSN 2411-3336
e-ISSN 2541-9404

Volume 277

N 1 • 2026

ST. PETERSBURG

Journal founder: Empress Catherine II Saint Petersburg Mining University

CHIEF EDITOR
V.S.Litvinenko, Doctor of Engineering Sciences, Professor, Member of the International Academy of Higher Education, RANS, RAHS, MANEB, Rector (Empress Catherine II Saint Petersburg Mining University, Saint Petersburg, Russia)

DEPUTY CHIEF EDITOR
S.G.Skublov, Doctor of Geological and Mineralogical Sciences, Professor, Member of the Russian Mineralogical Society, Expert of the RSF and RAS (Empress Catherine II Saint Petersburg Mining University, Saint Petersburg, Russia)

EXECUTIVE SECRETARY
S.V.Sinyavina, Candidate of Engineering Sciences, Director of the Publishing House (Empress Catherine II Saint Petersburg Mining University, Saint Petersburg, Russia)

EDITORIAL TEAM

O.E.Aksyutin, Doctor of Engineering Sciences, Corresponding Member of the RAS, Board Member, Head of Department (PAO Gazprom, Moscow, Russia)
A.A.Baryakh, Doctor of Engineering Sciences, Professor, Member of the RAS, Director (Perm Federal Research Center Ural Branch RAS, Perm, Russia)
V.N.Brichkin, Doctor of Engineering Sciences, Professor, Head of Department “Basics of Scientific Expertise” (Empress Catherine II Saint Petersburg Mining University, Saint Petersburg, Russia)
S.G.Gendler, Doctor of Engineering Sciences, Professor, Member of the RANS, Head of Department of Occupational Safety (Empress Catherine II Saint Petersburg Mining University, Saint Petersburg, Russia)
O.M.Ermilov, Doctor of Engineering Sciences, Professor, Member of the RAS, RAHS, Deputy Engineer-in-Chief of Science Programmes (OOO Gazprom Development Nadym, Nadym, Russia)
V.P.Zubov, Doctor of Engineering Sciences, Professor, Head of Department of Underground Mining (Empress Catherine II Saint Petersburg Mining University, Saint Petersburg, Russia)
G.B.Kleiner, Doctor of Economics, Professor, Corresponding Member of the RAS, Deputy Director (Central Research Institute of Economics and Mathematics of the RAS, Moscow, Russia)
A.V.Kozlov, Doctor of Geological and Mineralogical Sciences, Member of the Russian Mineralogical Society, Head of Department of Geology and Exploration of Mineral Deposits (Empress Catherine II Saint Petersburg Mining University, Saint Petersburg, Russia)
A.D.Kuranov, Candidate of Engineering Sciences, Director of Design of Technological Disciplines (Gipronickel Institute LLC, Saint Petersburg, Russia)
Yu.B.Marin, Doctor of Geological and Mineralogical Sciences, Professor, Corresponding Member of the RAS, Honorary President (Russian Mineralogical Society, Saint Petersburg, Russia)
V.A.Morenov, Candidate of Engineering Sciences, Associate Professor (Empress Catherine II Saint Petersburg Mining University, Saint Petersburg, Russia)
M.A.Pashkevich, Doctor of Engineering Sciences, Professor, Head of Department of Geoecology (Empress Catherine II Saint Petersburg Mining University, Saint Petersburg, Russia)
T.V.Ponomarenko, Doctor of Economics, Professor (Empress Catherine II Saint Petersburg Mining University, Saint Petersburg, Russia)
O.M.Prishchepa, Doctor of Geological and Mineralogical Sciences, Professor, Member of the RANS, Vice-Rector for Research (Empress Catherine II Saint Petersburg Mining University, Saint Petersburg, Russia)
A.G.Protosenya, Doctor of Engineering Sciences, Professor, Head of Department of Construction of Mining Enterprises and Underground Structures (Empress Catherine II Saint Petersburg Mining University, Saint Petersburg, Russia)
V.E.Somov, Doctor of Economics, Candidate of Engineering Sciences, Member of the RANS, Director (OOO Kinef, Kirishi, Russia)
A.A.Tronin, Doctor of Geological and Mineralogical Sciences, Director (Saint Petersburg Scientific-Research Centre for Ecological Safety RAS, Saint Petersburg, Russia)
V.L.Trushko, Doctor of Engineering Sciences, Professor, Member of the International Higher Education Academy of Sciences, RANS, RAHS, MANEB, Head of Department of Mechanics (Empress Catherine II Saint Petersburg Mining University, Saint Petersburg, Russia)
P.S.Tsvetkov, Candidate of Economics, Head of Department for Publishing Activity (Empress Catherine II Saint Petersburg Mining University, Saint Petersburg, Russia)
A.E.Cherepovitsyn, Doctor of Economics, Professor, Head of Department of Economics, Organization and Management (Empress Catherine II Saint Petersburg Mining University, Saint Petersburg, Russia)
Ya.E.Shklyarskii, Doctor of Engineering Sciences, Professor, Head of the Department of General Electric Engineering (Empress Catherine II Saint Petersburg Mining University, Saint Petersburg, Russia)
Oleg Antzutkin, Professor (University of Technology, Luleo, Sweden)
Gabriel Weiss, Doctor of Sciences, Professor, Pro-Rector for Science and Research (Technical University, Kosice, Slovakia)
Hal Gurgenci, Professor (School of Mining Machine-Building in University of Queensland, Brisbane, Australia)
Edwin Kroke, Doctor of Sciences, Professor (Institute of Inorganic Chemistry in Freiberg Mining Academy, Freiberg, Germany)
Zhou Fubao, Doctor of Sciences, Professor, Vice President (China University of Mining and Technology, Beijing, PR China)
Zhao Yuemin, Doctor of Sciences, Professor, Director of Academic Committee (China University of Mining and Technology, Beijing, PR China)

Sections

- Geology
- Geotechnical Engineering and Engineering Geology
- Economic Geology
- Energy

The journal invites the leading specialists to publish scientific articles and promotes them in the international scientific community
Registration Certificate PI N FS 77-70453 dated 20 July 2017

PH License N 06517 dated 09.01.02

Editorial staff: Head of the Editorial Center V.L.Lebedev, Editors E.S.Dribinskaya, M.G.Khachirova, L.V.Nabieva, A.I.Yakovleva, E.D.Bokareva
Bibliographer A.A.Belova. Computer Design N.N.Sedykh, V.I.Kashirina, E.A.Golovinskaya

© Empress Catherine II Saint Petersburg Mining University, 2026

Publishing date 27.02.2026. Format 60 × 84/8. Academic Publishing Division 40.
Circulation: 100 copies. Order 97. Printed by RIC of Empress Catherine II
Saint Petersburg Mining University. Free sale price.

Editorial and publisher address 2, 21st Line, St. Petersburg, 199106, Russia
Phone: +7 (812) 328-8416; +7 (812) 328-8216
E-mail: pmi@spmi.ru
Journal website: pmi.spmi.ru

CONTENTS

ISSN 2411-3336; e-ISSN 2541-9404

JOURNAL OF MINING INSTITUTE

Zapiski Gornogo instituta

Journal homepage: pmi.spmi.ru

Research article *Geotechnical Engineering and Engineering Geology*

Development of a composition and evaluation of the effectiveness of a bio-based product for cleaning oil-contaminated soils

Aleksandr S. Danilov[1]✉, **Irina D. Sosnina**[2], **Elizaveta A. Serdyukova**[1]
[1] *Empress Catherine II Saint Petersburg Mining University, Saint Petersburg, Russia*
[2] *Lengiprorechtrans JSC, Saint Petersburg, Russia*

How to cite this article: Danilov A.S., Sosnina I.D., Serdyukova E.A. Development of a composition and evaluation of the effectiveness of a bio-based product for cleaning oil-contaminated soils. Journal of Mining Institute. 2026. Vol. 277, p. 3-12.

Abstract
Soil pollution by oil and petroleum products is a serious environmental problem, especially relevant for industrialized regions. Microbiological remediation based on the use of oil-oxidizing microorganisms is a promising method of restoring polluted soils. The aims of the study are to develop a composition and assess the effectiveness of a specialized bio-based product adapted to the climatic conditions of northwest Russia. Bacterial strains capable of utilizing petroleum products as the only carbon source have been selected and cultivated. Based on laboratory tests, a consortium of microorganisms was selected, including strains of *Acinetobacter* sp. (VKM B-3202), *Rhodococcus erythropolis* (VKM Ac-858 T) and *Pseudomonas alcaligenes* (VKM B-1295), and their growth activity was evaluated. Three biologics compositions have been developed, differing in the proportions of bacterial suspensions by volume, and the technology of their application to oil-contaminated soils has been determined. The effectiveness of cleaning soils contaminated with oil and petroleum products (gasoline, diesel fuel, oil products from a spill at the Tammisuo railway station (Vyborg) at temperatures of 10-20 °C, typical for the climate of the region, was studied in laboratory conditions. At a temperature regime of 20±1 °C and natural soil moisture, after 60 days of the experiment, the maximum concentration reduction rates reached 75.59 % for crude oil, 71.97 % for oil products from the spill, 90.53 % for diesel fuel, 75.81 % for gasoline. At a temperature of 10±1 °C – 40.62 % for crude oil, 49.58 % for oil products from the spill, 69.06 % for diesel fuel, 68.10 % for gasoline. The results of the study confirm the effectiveness of the developed bio-based product for oil-contaminated soil purification in the climatic conditions of northwestern Russia.

Keywords
microbiological remediation; oil products; pollution; hydrocarbon-oxidizing microorganisms; reclamation; bacteria

Funding
This work was carried out within the framework of the state contract of the Ministry of Science and Higher Education of the Russian Federation (FSRW-2024-0005).

Received: 03.03.2025 ***Accepted: 16.07.2025*** ***Online: 21.01.2026*** ***Published: 27.02.2026***

Introduction

The oil industry is the leading industry in Russia, while significant production volumes are associated with a large proportion of waste generated as a result of the activities of oil companies [1, 2]. Petroleum products enter the environment for various reasons – accidents on pipelines, spills from shipping vessels, violations of drilling techniques, etc. [3, 4]. Soils, water, vegetation, and atmospheric air are susceptible to pollution due to the volatility of petroleum product components [5].

Russia has recorded 14 accidents at freshwater facilities, 12 of which occurred as a result of spills from ships and from a fuel oil pipeline in 2023[1]. In December 2024, the largest accident occurred in

---

[1] On the state and protection of the environment of the Russian Federation in 2023. State report. Moscow: Ministry of Natural Resources and Environment of the Russian Federation; Intellectual Analytics LLC; FGBU Directorate of Scientific and Technical Progress; Foundation for Environmental Monitoring and International Technological Cooperation, 2024, p. 707.

the Kerch Strait of the Black Sea, as a result of which, according to various estimates, from 3700 to 5000 t of oil entered the marine environment. Soil resources are equally susceptible to oil product contamination. According to Rosprirodnadzor, the area of disturbed land due to leaks during the transit of oil, gas, and refined petroleum products in 2023 amounted to 122 hectares[2]. According to the data of oil and gas producing companies, in comparison with 2022, the area of all disturbed lands increased by 4.6 %[3].

The negative impact on the soil cover from the ingress of petroleum products is associated with a reduction in biodiversity, death of animals and plants, the entry of toxic chemicals into the soil and atmospheric air [6], fertility degradation [7], and other dangerous consequences for the environment [8]. For the Northwestern Federal District, the problem of soil pollution with petroleum products is relevant due to the large length of pipeline, shipping and automobile transport in the region, as well as the presence of the largest oil loading terminals [9].

Various methods of restoring disturbed lands have been developed to eliminate the consequences of oil and petroleum products entering the soil: mechanical, physico-chemical, biological, thermal, electrical, etc. [10]. Microbiological remediation, based on the ability of microorganisms to absorb pollutants, is considered the most promising method in terms of the degree of purification and economic costs [11, 12]. Microorganisms with a petro-destructive ability include bacteria (*Pseudomonas*, *Flavobacterium*, *Acinetobacter* and others) [13, 14], fungi (*Alternaria*, *Aspergillus*, *Candida* and others) [15, 16] and microalgae (*Chlorella vulgaris*) [17]. Microorganisms are mainly used to remove oil pollution from soils and some types of wastewater. The method is carried out both directly at the site of contamination (*in situ*) [18], and with excavation of soil for placement in bioreactors (*ex situ*) [19], in some cases these methods are combined [20].

To introduce microorganisms into a polluted environment, biologics are used from three components necessary for their functioning:

- strains of microorganisms adapted to specific environmental conditions and contributing to the degradation of hydrocarbons (main component);
- sorbent carrier of both natural (peat, zeolite) and synthetic (polymers) origin [21, 22];
- a complex of nutrients (nitrogen, phosphorus, potassium, sulfur) that creates a favorable environment for the development of microorganisms [23, 24].

Natural sorbents, in addition to their main function, contribute to the improvement of the physico-mechanical and physico-chemical properties of soils [25, 26]. A number of biologics have been developed that differ in composition and properties [27-29], but their use is limited by the climatic conditions of the environment [30]. The Leningrad Region is characterized by moderate temperatures in summer, on average not exceeding 20 °C, which is not suitable for the development of most types of microorganisms [31]. In this regard, a significant part of the patented biological products cannot be used in the Northwestern Federal District, and most of the developments adapted for this region have not been put into practice [32].

The aims of the study are to develop a composition and assess the effectiveness of a specialized bio-based product adapted to the climatic conditions of northwest Russia.

Objectives of the work: scientific review on the research topic, selection and cultivation of psychrophilic bacterial strains, assessment of the growth activity of strains in the presence of petroleum products as the only carbon source, development of options for the composition of bio-based products and technology for applying biological products to oil-contaminated soils, evaluation of the effectiveness of purification of oil-contaminated soils with the proposed formulations in laboratory conditions.

---

[2] Environmental protection in Russia. 2024. Statistical collection. Moscow: Federal State Statistics Service (Rosstat), 2024, p. 118. URL: http://ssl.rosstat.gov.ru/storage/mediabank/Oxrana_okruj_sredi_2024.pdf (accessed 03.03.2025).

[3] On the state and protection of the environment of the Russian Federation in 2023. State report. Moscow: Ministry of Natural Resources and Environment of the Russian Federation; Intellectual Analytics LLC; FGBU Directorate of Scientific and Technical Progress; Foundation for Environmental Monitoring and International Technological Cooperation, 2024, p. 707.

Methods

For the study, a site was selected in the area of the Tammisuo railway station (Vyborg, Leningrad Region), where a massive spill of petroleum products occurred as a result of a leak in transport tanks located underground. The characteristic features of the territory are podzolic alluvial low-humus soils and vegetation cover, represented by shrubby plants, weedy herbaceous vegetation and mossy. During the reconnaissance survey of the spill site and adjacent territories, signs of a negative impact on the components of the natural environment were recorded – the suppression of herbaceous plant communities, the death of representatives of the animal world, and the blackening of shrub leaves.

Fig.1. Map-scheme of soil sampling. Blue contour – localization of the spill; P.1- P.5 – Sampling sites

Oil-contaminated soil was sampled using the envelope method at five test sites near the spill (Fig.1). From each site, samples were taken from two layers, from depths of 0-0.05 and 0.05-0.2 m, after which they were combined into one common sample for subsequent analysis. The choice of trial sites is determined by the uniformity of vegetation cover and different levels of pollution (Fig.2). The thickness of the oil-contaminated soil layer varied from 5-20 cm. Also for modeling pollution in laboratory conditions from the spill site according to GOST 2517-2012 “Oil and petroleum products. Sampling methods” the samples of pure petroleum product (without impurities of water and soil) and pure soil (without contamination with petroleum products) were taken.

Further sample preparation and experimental studies were carried out in the laboratory of the Scientific Research Center “Ecosystem” of the Mining University, where the selected samples were transported in a marked hermetically sealed container made of dark glass. To prepare the soil for analysis, inclusions were removed from the samples, the samples were crushed in a mortar, dried to an air-dry state and sifted through a sieve with a hole diameter of 1 mm. The samples were stored at a temperature of 4±2 °C. The preparation of water extracts for pH determination was carried out by adding 150 cm^3 of distilled water to pre-dried and crushed soil samples weighing 30 g. For X-ray fluorescence analysis (XFA), the working samples obtained by quartering the initial sample were ground to a powder state.

Fig.2. Sampling sites: *a* – N 1; *b* – N 3; *c* – N 4

The concentration of petroleum products was determined by fluorimetric analysis using a Fluorat-02-3M liquid analyzer for soil samples from the spill at the beginning of the study and subsequently to evaluate the effectiveness of the developed biological product [33]. Before the study, the purity of hexane was checked, calibration solutions were prepared, and the analyzer was calibrated. After extraction of petroleum products from the soil, the fluorescence intensity of the purified extract was measured on the specified liquid analyzer. The concentration of petroleum products in the sample was determined by the ratio of the mass concentration of petroleum products in the hexane solution of C_m, the final volume of the hexane solution and the dilution coefficient of the extract K to the mass of the soil sample m. The result X is shown in Table 1.

Table 1

Concentration of petroleum products in the soil according to the results of fluorimetric analysis

Sample	m, g	K	C_m	X, mg/kg
1	0.206	5	5.24	3180±800
2	0.201	40	5.96	>25,000 (29,652)*
3	0.202	5	5.72	3540±885
4	0.200	1	3.94	492±120
5	0.223	1	1.43	160±64

---

* The value obtained exceeds the measurement limit.

Based on the results of determining the pH of aqueous extracts from soils with a pH meter pH-150MI, it was decided to exclude the influence of the acidity of soil samples on the oil-oxidizing activity of bacteria and the indicators of soil purification efficiency obtained during further research due to minor differences in the pH values obtained.

To determine the content of heavy metals in samples that can affect the activity of oil-oxidizing microorganisms, a chemical analysis of soil composition was performed using X-ray fluorescence analysis using a portable X-ray fluorescence spectrometer NITON XLt. The elemental composition of sample N 2, obtained from the results of the RFA, is presented in Table 2. According to the results of a semi-quantitative analysis, exceedances of the maximum permissible concentration established by SanPiN 1.2.3685-21 for zirconium, zinc, chromium, and vanadium were revealed.

Table 2

The elemental composition of sample N 2 according to the results of the RFA

Element	Concentration, mg/kg	PCL, mg/kg*	Hazard class
Mo	32.1±3.2	50	3
Zr	37.2±4.3	6	3
Sr	12.6±2.0	200	2
Zn	102.4±10.9	55	1
Fe	169.4±27.6	–	4
Cr	175.8±65.8	100	1
V	343.0±117.6	150	3
Ca	2021±403	–	
K	1651±428	–	

---

* Sanitary Rules And Normatives 1.2.3685-21 “Hygienic standards and requirements for ensuring the safety and (or) harmlessness of environmental factors for humans”.

The determination of the elemental composition of pure petroleum products from the spill was carried out by gas chromatography-mass spectrometry (GCMS), which combines the functions of gas chromatography and mass spectrometry [34]. The study was performed on a Shimadzu GCMS-QP2010 SE gas chromatography-mass spectrometer with a helium carrier gas. A sample of 1 g of petroleum product was taken for analysis, from which a sample in the amount of 1 µl was inserted into the chromatograph evaporator with a micro-syringe. Based on the results of the GCMS, a chromatogram was obtained and the hydrocarbon components of the petroleum product were identified, most of which have from 15 to 26 carbon atoms, a linear structure and are typical components of heavy fuels such as fuel oil, diesel fuel, etc.

The experimental study on the creation of a bio-based product for soil purification from oil and petroleum products included five stages:

- selection and cultivation of bacterial strains;
- determination of the number of cells in bacterial suspensions;
- assessment of the growth activity of bacterial strains on nutrient media with the addition of petroleum products;
- development of the composition of a bio-based product;
- assessment of the effectiveness of oil-contaminated soil treatment.

The basis of the bio-based product was selected from the strains from the All-Russian collection of microorganisms (VKM IBFM RAS, Pushchino, Russia) – *Acinetobacter* sp. (catalog number B-3202, hereinafter – 3202), *Rhodococcus erythropolis* (Ac-858 T, hereinafter – 858), *Pseudomonas alcaligenes* (B-1295, hereinafter – 1295).

The selected strains of microorganisms are representatives of psychrophilic aerobic bacteria, have the ability to oxidize petroleum hydrocarbons and other organic substances, which is an important criterion for selecting strains for effective bioremediation of oil-contaminated soils [35]. Bacterial strains were obtained as a culture on mown agar. For culture re-sowing, a nutrient medium, HMS-agar, was prepared in Petri dishes, on the surface of which seed was introduced with zigzag-shaped movements ("stroke" sowing), after which the Petri dishes were placed upside down in a thermostat at 28±2 °C for three days. Thus, a sufficient amount of culture was obtained for further research.

To determine the number of cells, bacterial suspensions were prepared by washing them off the surface of the nutrient medium and 10 dilutions of the initial bacterial suspension, for which the optical density was determined on a Hach-Lange DR 5000 spectrophotometer. The number of tubes for the preparation of the initial cell suspension was selected experimentally for each bacterial strain. The cell concentration in the initial suspension was chosen with the condition of non-zero optical density of the suspensions of the latest dilutions, taking into account the nonlinear relationship between the optical density of the suspension and the number of bacterial cells in it. The sowing was carried out using the Drigalsky method. After three days, the number of colonies in Petri dishes for each strain was calculated. Based on the data obtained, calibration curves were constructed, which were used to determine the number of cells in bacterial suspensions (Fig.3).

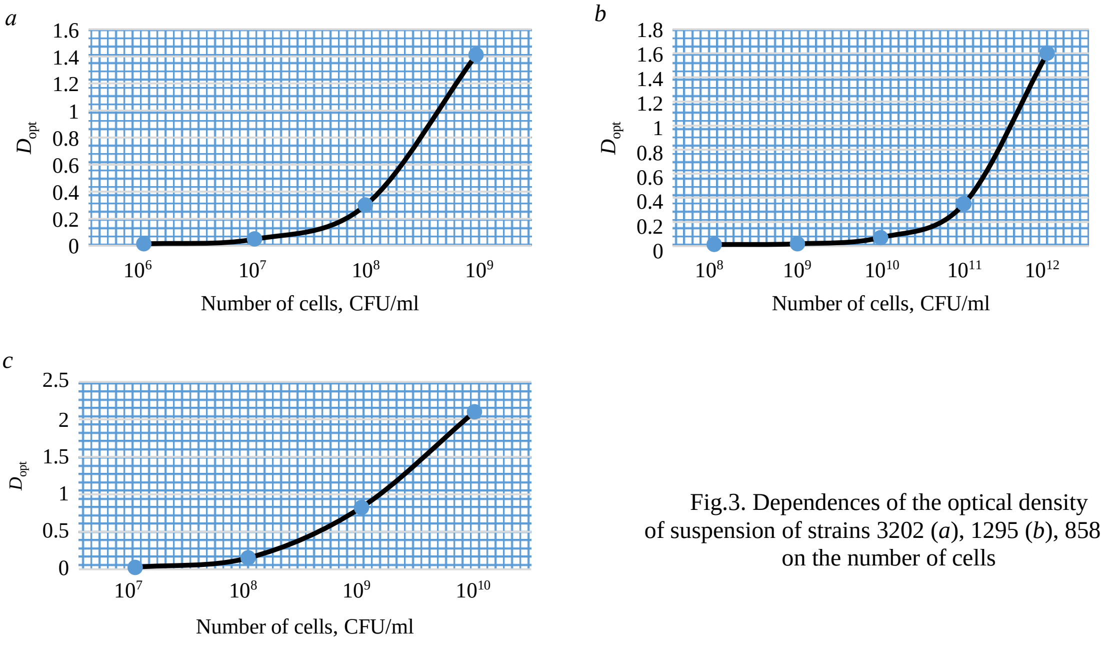

Fig.3. Dependences of the optical density of suspension of strains 3202 (*a*), 1295 (*b*), 858 (*c*) on the number of cells

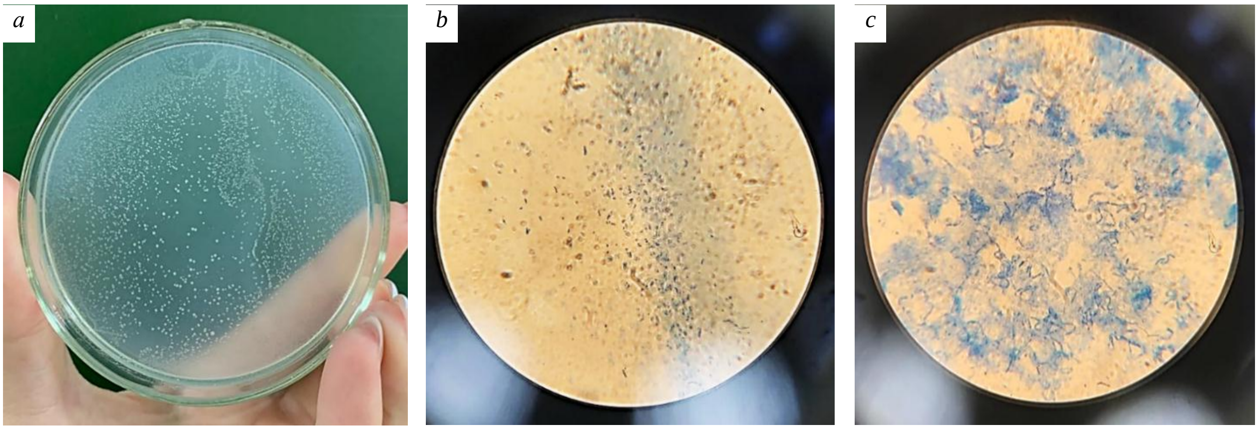

Fig.4. Microscopic pictures of cells of strain 3202 on Voroshilova – Dianova nutrient medium with the addition of a carbon source (*a*); strain 858 (magnification ×400) (*b*); strain 1295 on a nutrient medium with the addition of glucose (magnification ×400) (*c*)

To determine the proportions of strain culture application to the soil, the growth activity of the strains on mineral nutrient media was preliminarily determined in the presence of oil and petroleum products as the only carbon source, including crude oil, diesel fuel, gasoline, and petroleum products from the spill [36]. In the control sample, glucose served as the carbon source. Surface cultivation of the strains was carried out at a temperature of 26±2 °C for seven days. The growth activity of the strains was assessed both visually and by microscopy of fixed preparations (Fig.4).

The assessment of the growth of the 3202 strain culture was carried out visually due to the good distinctness of the colonies on the nutrient medium: small colonies have the appearance of a solid cloudy coating, larger colonies are convex, round, white, shiny (Fig.4, *a*).

Colonies of strain 858 on all nutrient media had the appearance of a continuous cloudy-white coating. To identify the growth of the culture, fixed preparations of colony cells grown on nutrient medium in Petri dishes were prepared. The presence of a large number of bacterial cells in smears from the surface of the nutrient medium for strain 858 was recorded at an increase of 400 times (Fig.4, *b*).

Despite the absence of visual differences in cultural properties, polymorphism of strain 1295 cells was revealed in the microscopic picture. When growing on a nutrient medium with the addition of glucose (a rich substrate), a significantly larger number of bacterial cells are observed, they are shortened, lined up in chains (Fig.4, *c*). On a nutrient medium with the addition of petroleum products (poor substrate), there are significantly fewer cells in the field of view, they are connected in stellate structures and have different lengths.

The results of the evaluation of the growth activity of strains on nutrient media with petroleum products and glucose are presented in Table 3.

Table 3

Growth activity of strains on nutrient media with the addition of petroleum products

Strain	Glucose	Oil	Oil product	Gasoline	Diesel fuel
3202	++	+	–	++	–
858	++	+	+	+	+
1295	+	+	+	+	++

Note. + low growth activity; ++ high growth activity; – no growth.

As can be seen from Table 3, the growth activity of the strains was recorded for almost all experiments based on the evaluation results. The exception was the experience with the addition of petroleum products and diesel fuel for strain 3202, where there was no growth.

Based on the data obtained, variants of the composition of the bio-based product with different proportions of bacterial suspensions are proposed (Table 4).

The following samples were prepared to evaluate the effectiveness of cleaning oil-contaminated soils using the developed formulations:

- soil with the introduction of crude oil (O) 5 wt.%;
- soil with diesel fuel (DF) 5 wt.%;
- soil with gasoline (G) 5 wt.%;
- soil with petroleum products (PP) from the spill.

Table 4

Variants of bio-based product compositions

Strain	Composit 1	Composit 2	Composit 3
	Proportions of application of bacterial suspensions		
3202	1	1	1
858	1	2	2
1295	2	1	2

Bacterial suspensions were prepared by flushing to introduce bioremediation compounds into the soil. The optical density of bacterial suspensions and the concentration of bacterial cells in suspensions (CFU/ml) were determined by the spectrophotometric method based on the calibration dependences obtained, and in all bacterial suspensions the cell concentration was in the range of 10^7-10^{12} CFU/ml. Next, the soil samples were packaged in isolated 200 g cuvettes in accordance with the proportions of bacterial suspensions (Table 4) in the amount of 20 ml for each soil sample. Soil samples without bacterial suspensions were used as controls (Table 5).

Table 5

Sample matrix

Pollutant	Temperature							
	20±1 °C				10±1 °C			
	Composition 1	Composition 2	Composition 3	C	Composition 1	Composition 2	Composition 3	C
G	G/1	G/2	G/3	G/C	G/1	G/2	G/3	G/C
O	O/1	O/2	O/3	O/C	O/1	O/2	O/3	O/C
DF	DF/1	DF/2	DF/3	DF/C	DF/1	DF/2	DF/3	DF/C
PP	PP/1	PP/2	PP/3	PP/C	PP/1	PP/2	PP/3	PP/C

The simulation of the climatic conditions of the warm season, typical for the Leningrad Region, was carried out at temperatures of 20±1 and 10±1 °C for 60 days using the Klimatostat R-2 equipment. The studied soil samples were periodically moistened and mixed with a sterile spatula. Then, for 60 days, soil samples were taken to determine the concentration of oil and petroleum products using the fluorimetric method.

Discussion

The evaluation of the effectiveness of soil purification from petroleum products using the developed biological product was carried out through mathematical processing of the data obtained. Diagrams reflecting the dynamics of the decrease in the concentration of petroleum products under the action of biologics compositions relative to the initial values (IV) are shown in Fig.5, 6.

The results of evaluating the effectiveness of soil purification with various compositions of the developed biological product for 60 days at temperatures of 20±1 and 10±1 °C are presented in the Table 6.

Conclusion

Soil pollution by oil and petroleum products remains an urgent environmental problem requiring comprehensive study and development of new effective cleaning technologies. Among the numerous methods of removing pollutants from soils, microbiological remediation is the most promising, the advantages of which include waste-free, high efficiency, low cost, and the possibility of restoring the fertile properties of the soil.

As part of the study, a new biological product was developed, which includes the bacterial consortium *Acinetobacter* sp. (VKM B-3202), *Rhodococcus erythropolis* (VKM Ac-858 T), *Pseudomonas alcaligenes* (VKM B-1295), which has a recycling activity against petroleum hydrocarbons. Three variants of the composition of this biological product have been prepared, differing in the volume ratio of bacterial suspensions (1:1:2, 1:2:1, 1:2:2 for compositions 1, 2, 3). It was found that all bacterial strains exhibit high growth activity in the presence of oil, gasoline, diesel fuel, and petroleum products from the spill as

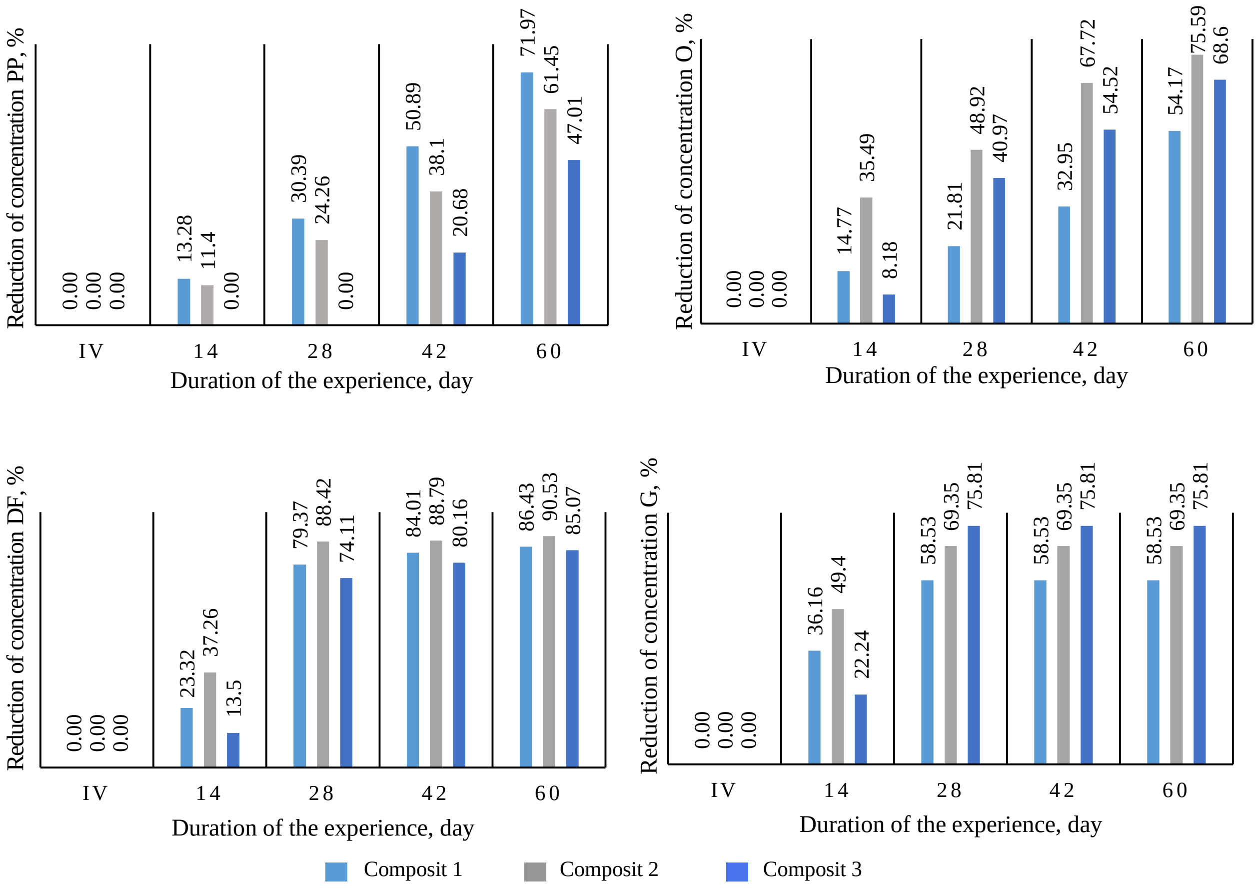

Fig.5. The dynamics of the concentration of oil and petroleum products at 20±1 °C

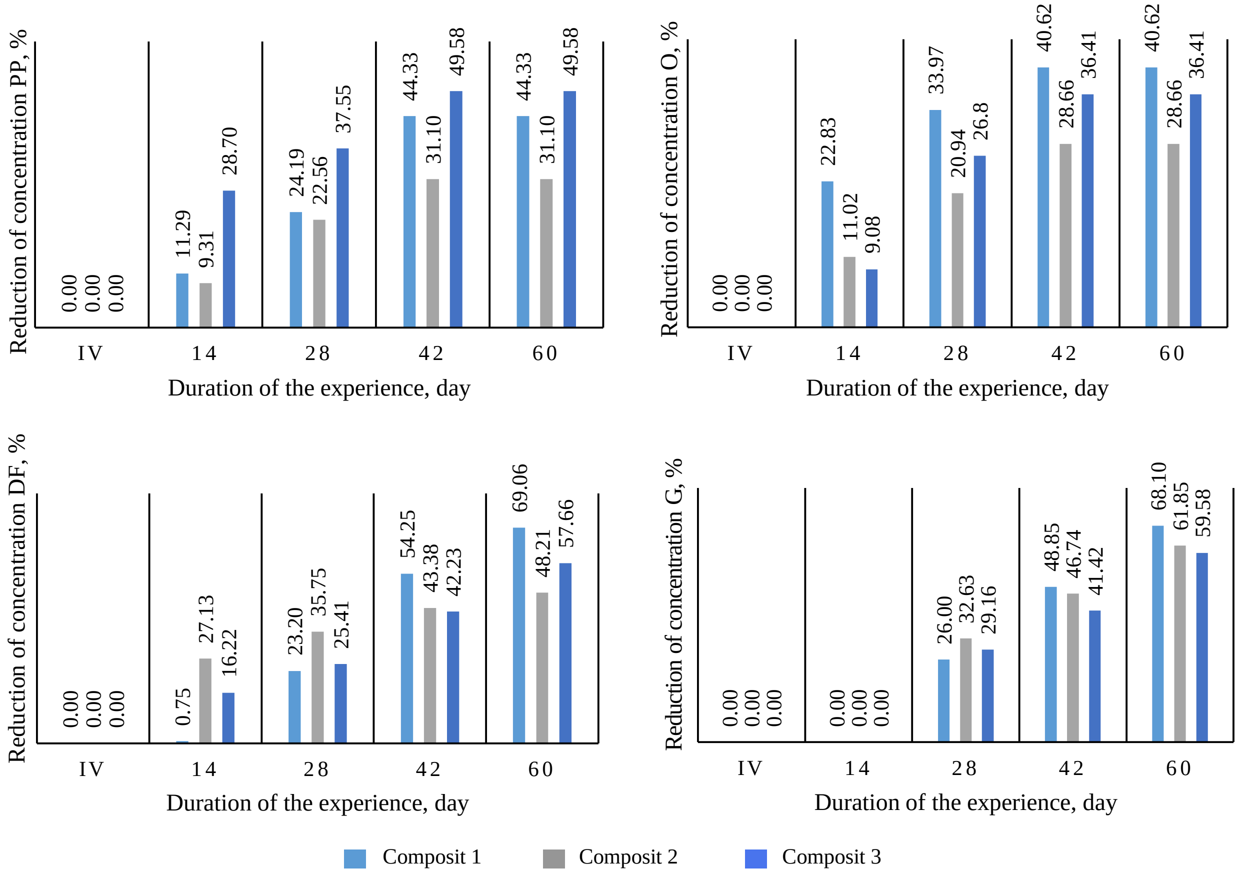

Fig.6. The dynamics of the concentration of oil and petroleum products at 10±1 °C

Table 6

Efficiency of soil purification from petroleum products

Pollutant	The composition with the highest efficiency	The proportion of bacterial suspension application	Reducing the concentration of pollutants in 60 days, %
20±1 °C			
PP	1	1:1:2	71,97
O	2	1:2:1	75,59
DF	2	1:2:1	90,53
G	3	1:2:2	75,81
10±1 °C			
PP	3	1:2:2	49,58
O	1	1:1:2	40,62
DF	1	1:1:2	69,06
G	1	1:1:2	68,10

the only carbon source in nutrient media, with the exception of strain B-3202 because in the experimental variants with diesel fuel and petroleum products, bacterial growth on nutrient media was not recorded.

According to the results of evaluating the effectiveness of cleaning oil-contaminated soils with the application of the developed biological product at a temperature of 20±1 °C and natural soil moisture after 60 days of the experiment, the following maximum concentration reduction rates were obtained: for crude oil – 75.59 %; for oil products from the spill – 71.97 %; for diesel fuel – 90.53 %; for gasoline – 75.81 %. At a temperature of 10±1 °C: for crude oil – 40.62 %; for oil products from the spill – 49.58 %; for diesel fuel – 69.06 %; for gasoline – 68.10 %.

The developed biological product can be used to clean oil-contaminated soils in the Northwestern Federal District, including in the area of the Tammisuo railway station (Vyborg, Leningrad Region) or in regions with similar soil and climatic conditions.

The direction of further research is to evaluate the effectiveness of the developed technology for reclamation of oil-contaminated soils in the field.

The results presented in this study are protected by a patent [37].

REFERENCES

1. Ponomarenko T.V., Gorbatyuk I.G., Cherepovitsyn A.E. Industrial clusters as an organizational model for the development of Russia petrochemical industry. *Journal of Mining Institute*. 2024. Vol. 270, p. 1024-1037.
2. Strizhenok A.V., Korelskiy D.S., Choi Y. Assessment of the Efficiency of Using Organic Waste from the Brewing Industry for Bioremediation of Oil-Contaminated Soils. *Journal of Ecological Engineering*. 2021. Vol. 22. Iss. 4, p. 66-77. DOI: 10.12911/22998993/133966
3. Batukova D.V. Geoecological problems associated with the supervision and operation of oil production facilities. Treshnikov readings – 2022. Modern geographical global picture and technology of geographic education. Materialy vserossiiskoi nauchno-prakticheskoi konferentsii s mezhdunarodnym uchastiem, posvyashchennoi pamyati znamenitogo rossiiskogo okeanologa, issledovatelya Arktiki i Antarktiki, akademika Alekseya Fedorovicha Treshnikova i 90-letiyu FGBOU VO “UlGPU im. I.N.Ulyanova”, 14-15 aprelya 2022, Ulyanovsk, Rossiya. Ulyanovsk: Ulyanovskii gosudarstvennyi pedagogicheskii universitet imeni I.N.Ulyanova, 2022, p. 23-24 (in Russian). DOI: 10.33065/978-5-907216-88-4-2022-23-24
4. Chukaeva M.A., Zaytseva T.A., Matveeva V.A., Sverchkov I.P. Purification of Oil-Contaminated Wastewater with a Modified Natural Adsorbent. *Ecological Engineering and Environmental Technology*. 2021. Vol. 22. N 2, p. 46-51. DOI: 10.12912/27197050/133331
5. Strizhenok A.V., Ivanov A.V. Monitoring of Air Pollution in the Area Affected by the Storage of Primary Oil Refining Waste. *Journal of Ecological Engineering*. 2021. Vol. 22. Iss. 1, p. 60-67. DOI: 10.12911/22998993/128873
6. Shulaev N.S., Kadyrov R.R., Pryanichnikova V.V. Combined method of phytoremediation and electrical treatment for cleaning contaminated areas of the oil complex. *Journal of Mining Institute*. 2024. Vol. 265, p. 147-155.
7. Volosnikova G.A., Sokolov A.S. Identification of the source of territory pollution with petroleum products and justification for the choice of technology for its environmental rehabilitation. *Ekonomika stroitelstva*. 2024. N 6, p. 240-245 (in Russian).
8. Minnikova T.V., Kolesnikov S.I. Environmental assessment of biochar application for remediation of oil-contaminated soils under various economic uses. *Journal of Mining Institute*. 2025. Vol. 271, p. 84-94.
9. Tishin A.S., Tishina Yu.R. A comparison of foreign and domestic experience in cleaning soils contaminated with petroleum products. *International Research Journal*. 2021. N 10 (112), p. 106-112 (in Russian). DOI: 10.23670/IRJ.2021.112.10.018
10. Polyak Y.M., Bakina L.G., Chugunova M.V., Gerasimov A.O. Diagnostics of the effeciency of remediation methods of oil-polluted agricultural podzolic soil by the complex of agrochemical and biological indicators. *Agrochemistry and ecology problems*. 2024. N 3, p. 47-52 (in Russian). DOI: 10.26178/AE.2024.83.31.007

11. Meredov E.N., Veldzhanova A.N., Khatamova M.Ch. The use of biotechnologies for the restoration of degraded lands prone to desertification and salinization: methods of phytoremediation and microbiological remediation. *Mezhdunarodnyi zhurnal gumanitarnykh i estestvennykh nauk*. 2024. N 10-3 (97), p. 153-155. DOI: 10.24412/2500-1000-2024-10-3-153-155

12. Sotnikova Yu.M., Grigoriadi A.S., Fedyaev V.V. et al. Application of microbiological preparations and lucern plants for phytoremediating activities on oil contaminated soils. *Journal of Agriculture and Environment*. 2022. N 5 (25), p. 6. DOI: 10.23649/jae.2022.5.25.02

13. Korshunova T.Yu., Kuzina E.V., Sharipov D.A., Rafikova G.F. Bacteria of the genera *Acinetobacter* and *Ochrobactrum* in the processes of bioremediation of oil-contaminated objects (review). *Theoretical and Applied Ecology*. 2021. N 3, p. 13-20 (in Russian). DOI: 10.25750/1995-4301-2021-3-013-020

14. Yang H., Kim G., Cho K.-S. Bioaugmentation of diesel-contaminated soil with *Pseudomonas* sp. DTF1. *International Journal of Environmental Science and Technology*. 2023. Vol. 20. Iss. 11, p. 12499-12510. DOI: 10.1007/s13762-023-04846-4

15. Kulikova N.A., Klein O.I., Landesman E.O. The effect of humic substances on the degradation of aromatic hydrocarbons of oil by basidial fungi in soil and peat at low temperature. *Agrochemistry and ecology problems*. 2024. N 3, p. 37-46 (in Russian). DOI: 10.26178/AE.2024.73.22.006

16. Kuyukina M.S., Glebov G.G., Osipenko M.A., Elkin A.A. Interspecies Interactions of *Rhodococcus* Beneficial for Bioremediation as Revealed by Ecological Modeling. *Science and Global Challenges of the 21st Century – Science and Technology*, p. 427-433. DOI: 10.1007/978-3-030-89477-1_43

17. Korchagina Yu.S., Shchemelinina T.N. Patent N 2764305 RF. Method for purifying soils from petroleum contamination by the method of hydroseeding a biological mixture using microalgae Chlorella vulgaris globosa IPPAS C-2024. Publ. 17.01.2022. Bul. N 2 (in Russian).

18. Haque S., Srivastava N., Pal D.B. et al. Functional microbiome strategies for the bioremediation of petroleum-hydrocarbon and heavy metal contaminated soils: A review. *Science of The Total Environment*. 2022. Vol. 833. N 155222. DOI: 10.1016/j.scitotenv.2022.155222

19. Decesaro A., Rempel A., Machado T.S. et al. Bacterial biosurfactant increases ex situ biodiesel bioremediation in clayey soil. *Biodegradation*. 2021. Vol. 32. Iss. 4, p. 389-401. DOI: 10.1007/s10532-021-09944-z

20. Glyaznetsova Yu.S., Lifshits S.Kh., Zueva I.N., Chalaya O.N. Issues of recultivation of oil-contaminated areas. *Regional Environmental Issues*. 2021. N 5, p. 109-112 (in Russian). DOI: 10.24412/1728-323X-2021-5-109-112

21. Serzhantov V.G., Khaptsev Z.Yu. Patent N 2779935 RF. Means based on glauconite for immobilization of living bacterial cells. Publ. 15.09.2022. Bul. N 26 (in Russian).

22. Qun Luo, Dengyong Hou, Dingwen Jiang, Wei Chen. Bioremediation of marine oil spills by immobilized oil-degrading bacteria and nutrition emulsion. *Biodegradation*. 2021. Vol. 32. Iss. 2, p. 165-177. DOI: 10.1007/s10532-021-09930-5

23. Chao Zhang, Daoji Wu, Huixue Ren. Bioremediation of oil contaminated soil using agricultural wastes via microbial consortium. *Scientific Reports*. 2020. Vol. 10. N 9188. DOI: 10.1038/s41598-020-66169-5

24. Minnikova T.V., Ruseva A.S., Revina S.Yu. et al. Assessment of the efficiency of bioremediation by oil-contaminated eutric cambisols in the Republic of Kalmykia (model experiment). *Aridnye ekosistemy*. 2023. Vol. 29. N 4 (97), p. 166-176 (in Russian). DOI: 10.24412/1993-3916-2023-4-166-176

25. Galiullina Y.R., Kulagin A.A. Determination of the degree of water purification after application of oil-absorbent sorbents. *Ecology of Urban Areas*. 2021. N 1, p. 29-32 (in Russian). DOI: 10.24412/1816-1863-2021-1-29-32

26. Petrova T.A., Rudzisha E. Utilization of sewage sludge as an ameliorant for reclamation of technogenically disturbed lands. *Journal of Mining Institute*. 2021. Vol. 251, p. 767-776. DOI: 10.31897/PMI.2021.5.16

27. Mazlova E.A., Kherrera-Alvarado L.A. Patent N 2568063 RF. Biological preparation for decontamination of soil and slimes from oil and oil products. Publ. 10.11.2015. Bul. N 31 (in Russian).

28. Tretyakova M.S., Belovezhets L.A., Markova Yu.A. Patent N 2705290 RF. Microbial preparation for bioremediation of soil contaminated with oil and oil products. Publ. 06.11.2019. Bul. N 31 (in Russian).

29. Gamzaeva R.S. Application of the Bak-Verad biodestructor on soddy-podzolic soil contaminated with oil products. *Izvestiya Saint-Petersburg State Agrarian University*. 2019. N 2 (55), p. 38-45 (in Russian). DOI: 10.24411/2078-1318-2019-12038

30. Bykova M.V., Pashkevich M.A. Assessment of oil pollution of soils of production facilities of different soil and climatic zones of the Russian Federation. *News of the Tula State University. Sciences of Earth*. 2020. Iss. 1, p. 46-59 (in Russian). DOI: 10.46689/2218-5194-2020-1-1-46-59

31. Evseeva E.A., Golov V.I., Zakharova E.B., Panasyuk A.N. Impact of effective microorganisms on reduction of soil pathogenicity in different soil and climatic conditions. *Dalnevostochnyj agrarnyj vestnik*. 2023. Vol. 17. N 4, p. 25-38 (in Russian). DOI: 10.22450/1999-6837-2023-17-4-25-38

32. Sozina I.D., Danilov A.S. Microbiological remediation of oil-contaminated soils. *Journal of Mining Institute*. 2023. Vol. 260, p. 297-312. DOI: 10.31897/PMI.2023.8

33. Pashkevich M.A., Bykova M.V. Methodology for thermal desorption treatment of local soil pollution by oil products at the facilities of the mineral resource industry. *Journal of Mining Institute*. 2022. Vol. 253, p. 49-60. DOI: 10.31897/PMI.2022.6

34. Temerdashev Z.A., Musorina T.N., Kiseleva N.V. et al. Gas Chromatography–Mass Spectrometry Determination of Polycyclic Aromatic Hydrocarbons in Surface Water. *Journal of Analytical Chemistry*. 2018. Vol. 73. N 12, p. 1154-1161. DOI: 10.1134/S1061934818120109

35. Chaporgina A.A., Korneykova M.V. Evaluation of the microorganisms consortium efficiency to cleaning soils polluted by oil products in the Kola North conditions. *Theoretical and Applied Ecology*. 2020. N 2, p. 136-142 (in Russian). DOI: 10.25750/1995-4301-2020-2-136-142

36. Pashkevich M.A., Bykova M.V. Improvability of measurement accuracy in determining the level of soil contamination with petroleum products. *Mining Informational and Analytical Bulletin*. 2022. N 4, p. 67-86 (in Russian). DOI: 10.25018/0236_1493_2022_4_0_67

37. Danilov A.S., Duka A.A., Ivanchenko O.B., Sozina I.D. Patent N 2808248 RF. Composition for bioremediation of soil contaminated with oil and petroleum products. Publ. 28.11.2023. Bul. N 34 (in Russian).

***Authors*: Aleksandr S. Danilov,** *Candidate of Engineering Sciences, Associate Professor (Empress Catherine II Saint Petersburg Mining University, Saint Petersburg, Russia), Danilov_AS@pers.spmi.ru, https://orcid.org/0000-0003-2108-2781*, **Irina D. Sosnina,** *Environmental Engineer (Lengiprorechtrans JSC, Saint Petersburg, Russia), https://orcid.org/0000-0001-5521-862X*, **Elizaveta A. Serdyukova,** *Researcher (Empress Catherine II Saint Petersburg Mining University, Saint Petersburg, Russia), https://orcid.org/0009-0001-2711-7693*.

The authors declare no conflict of interests.

ISSN 2411-3336; e-ISSN 2541-9404

JOURNAL OF MINING INSTITUTE

Zapiski Gornogo instituta

Journal homepage: pmi.spmi.ru

Research article *Geology*

Physical properties of Paleozoic-Mesozoic deposits from wells in the South Barents Basin

Vadim L. Ilchenko[1]✉, **Igor V. Chikirev**[2]

[1] *Geological Institute of the KSC RAS, Apatity, Russia*

[2] *Apatity Branch of Murmansk Arctic University, Apatity, Russia*

***How to cite this article*:** Ilchenko V.L., Chikirev I.V. Physical properties of Paleozoic-Mesozoic deposits from wells in the South Barents Basin. Journal of Mining Institute. 2026. Vol. 277, p. 13-25.

Abstract

The Arctic shelf zone is an important research target due to its significant hydrocarbon potential. A study of the physical properties (density, elasticity, elastic anisotropy index, specific acoustic impedance, and porosity) was conducted for core samples from six wells in the South Barents Basin: Admiralteyskaya-1, Krestovaya-1, Ludlovskaya-1, Shtokmanskaya-1, Arkticheskaya-1, and Severo-Kildinskaya-82. The sample collection consists of sandstones, siltstones, and limestones. Core analysis revealed that rocks from non-productive wells (Arkticheskaya-1, Admiralteyskaya-1, and Krestovaya-1), located in the central part of the South Barents Basin and within the Admiralty High, differ in their physical and petrographic properties from rocks in gas and gas-condensate wells (Shtokmanskaya-1, Severo-Kildinskaya-82, and Ludlovskaya-1), located near the boundaries of the South Barents Basin. Core samples from productive wells (Shtokmanskaya-1, Severo-Kildinskaya-82, Ludlovskaya-1) exhibit lower average P-wave velocities, lower specific acoustic impedance, and higher open porosity and/or elastic anisotropy index compared to non-productive wells (Arkticheskaya-1, Admiralteyskaya-1, Krestovaya-1). This combination of petrophysical parameters provides the reservoir properties of rocks prospective for hydrocarbons. The petrographic variation of the reservoir properties of the studied rocks from productive to non-productive wells is associated with a decrease in grain size and a transition from pore-filling cement to thin-film and basal cement. The sandstones from the Shtokmanskaya well have a larger grain size (0.1-0.5 mm), whereas the sandstones from the Arkticheskaya-1 and Krestovaya-1 wells are finer-grained (0.1-0.2 mm). The Shtokmanskaya-1 well is characterized by pore-filling cement, the Arkticheskaya-1 – by thin-film cement, and the Krestovaya-1 – by cement of the basal type. The established physical properties of sedimentary rocks, suitable for the development of productive strata, will allow for the screening out of empty areas at the preliminary stage of analyzing geophysical materials during the search for geological and tectonic structures prospective for hydrocarbon accumulations.

Keywords

Barents Sea shelf; hydrocarbons; wells; core; lithology; physical properties of rocks

Funding

The work was carried out in the framework of the State contract of GI KSC RAS N FMEZ-2024-0006.

Received:* *24.10.2024 ***Accepted:* *02.07.2025*** ***Online:* *14.11.2025*** ***Published:* *27.02.2026***

Introduction

The importance of hydrocarbon resources today can hardly be overestimated. The Russian Federation holds approximately one-third of the world's natural gas reserves. In terms of oil reserves, Russia is second only to five countries, which is sufficient reason to develop this industry. According to some estimates, up to 30 % of the world's gas and 13 % of oil may be located on the shelves of the Eastern Arctic marginal seas at depths not exceeding 500 m [1]. The search, exploration, and development of these accumulations in the Arctic regions are associated with solving complex technical and technological challenges [2, 3]. The depletion of the hydrocarbon resource base under modern conditions necessitates the creation of new effective and environmentally friendly technologies for developing fields with hard-to-recover reserves, primarily those with low-permeability reservoirs [4, 5].

A major achievement was the discovery of the global Arctic Petroleum Belt. Geological exploration on the shelves of the Barents, Pechora, and Kara seas has mapped numerous local features and identified 22 hydrocarbon fields [6]. Oil, gas, and gas-condensate fields have been discovered in the Barents Sea. Oil fields (Varandey-more, Prirazlomnoye, etc.) have been found in its southeastern part (Pechora Sea), directly adjacent to the Timan-Pechora Basin. Five fields have been discovered in the South Barents Basin – the Shtokmanskoye and Ledovoye (gas-condensate), and the Severo-Kildinskoye, Murmanskoye, and Ludlovskoye (gas) [7]. Within the boundaries of the Barents Sea, coal deposits have been found (Timan-Pechora Basin, Svalbard Archipelago), coal-bearing strata [8] and rare earth element deposits [9] are known on Franz Josef Land. A substantial amount of drilling and geophysical data has been accumulated over a vast area, enabling the integrated interpretation of results from regional seismic exploration and the re-interpretation of archival seismic data to delineate and identify prospective zones of oil and gas accumulation and targets for further geological exploration in areas with ambiguous forecasts and a lack of commercial petroleum potential [10].

The South Barents and North Barents basins are unique areas of crustal subsidence with geological features favorable for the formation of large oil and gas accumulations: an enormous thickness of the sedimentary cover, rifted geodynamic conditions, and a wide range of rocks that can act as both fluid seals and reservoirs [11]. The South Barents gas-condensate and gas fields are directly associated with Triassic and Jurassic deposits and are confined to the peripheral and boundary zones of the basin [12].

Fundamental studies of the physical properties of rocks (core samples) from shelf deposits and geothermal investigations of marine muds in the Barents-Kara region have been conducted at the Geological Institute of the KSC RAS for many years [13-15]. With modern drilling and oil and gas production technologies, core studies are not always performed [7]. Nevertheless, it is core analysis that provides information on the reservoir properties of rocks, which is one of the key issues in identifying prospective structures and petroleum objects. Core material is used in experimental and theoretical studies of applicability of the method of directional reservoir depressurization in fields with low-permeability reservoirs [3], of efficiency of water-gas injection for condensate recovery from low-pressure reservoirs [16], of overburden pressure influence on the permeability of sandstones and other hydrocarbon reservoirs [17, 18], and estimating the compressibility coefficients of fractures and intergranular pores in hydrocarbon reservoirs [19]. Digital models also rely on a large number of parameters obtained from lithological and petrographic studies of thin sections and well cores [20].

An important aspect of well core studies is research into the changes in the physical properties of rocks during the retrieval of samples from great depths [21] and specifically, changes in the mechanical properties, porosity, and fracturing of reservoir rocks during core retrieval from depth to the surface [22, 23]. The use of refined data on the mechanical properties of retrieved rock samples enhances the accuracy of digital geological models, which are necessary for conducting geological exploration, determining reservoir properties, assessing oil and gas saturation of fields, and developing oil and gas deposits.

This paper presents a petrographic characterization and the results of a study of the physical properties of core (density, elasticity, elastic anisotropy index, specific acoustic impedance, and porosity) from wells in the South Barents Basin: Admiralteyskaya-1, Krestovaya-1, Ludlovskaya-1, Shtokmanskaya-1, Arkticheskaya-1, Severo-Kildinskaya-82 (Fig.1). The rocks are represented by Paleozoic-Mesozoic deposits of the interval from the Lower Permian to the Lower Cretaceous.

The value of the open porosity index serves as the primary criterion for the reservoir properties of sedimentary rocks. In this work, we examine which combinations of physical parameters can be characteristic of reservoir rocks. Information on the physical properties of sedimentary rocks from the shelf deposits of the South Barents Basin (and indeed from all offshore wells, in principle) appears

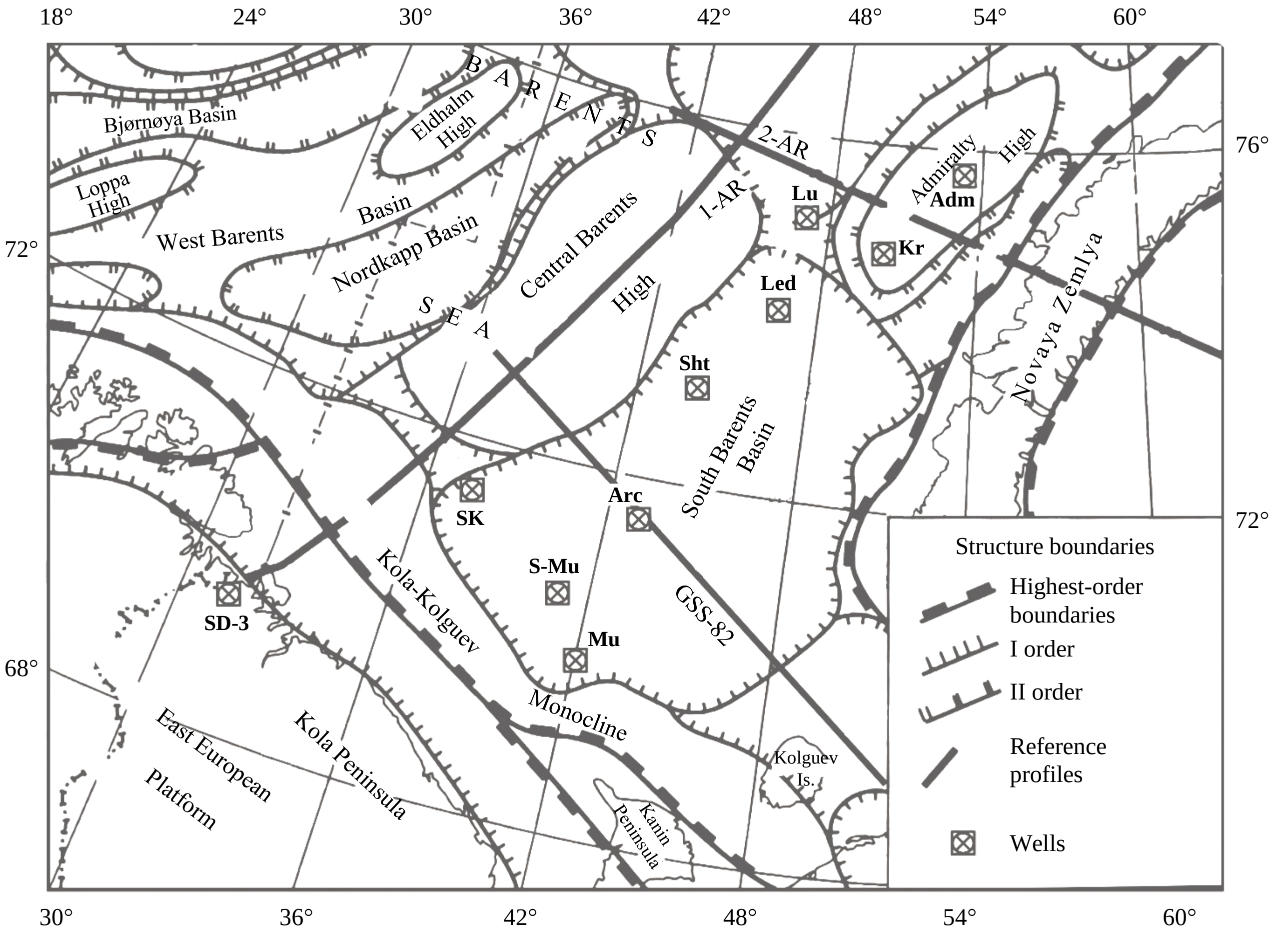

Fig.1. Geological schematic map of the southern part of the Barents Sea [24] with location of wells: SD-3 – Kola Superdeep; SK – Severo-Kildinskaya-82; S-Mu – Severo-Murmanskaya; Mu – Murmanskaya-24; Arc – Arkticheskaya-1; Led – Ledovaya-1; Kr – Krestovaya-1; Sht – Shtokmanskaya-1; Lu – Ludlovskaya-1; Adm – Admiralteyskaya-1. Reference seismological profiles: GSS-82, 1-AR, 2-AR

infrequently in open publications, and this material may be useful for lithologists, petroleum geologists, marine geologists, and engineers.

Methods

Core samples (42 specimens) were studied in petrographic thin sections using POLAM RP-1 (“LOMO” JSC) and Amplival (Carl Zeiss Jena) polarizing microscopes. The methodologies of V.N.Shvanov and V.T.Frolov [25] were used for sandstone classification and determination of their granulometric composition, specifically V.N.Shvanov's diagram for sandy rocks, which considers the ratio of different clastic components (quartz, feldspars, rock fragments) in sandstones. Grain size was determined using an eyepiece with a scale ruler on the polarizing microscope.

The material for petrophysical studies was prepared as follows: cube-shaped samples (edge length 25-30 mm) were cut from the core, with their faces (wave propagation directions) marked as x, y, z; the normal to face z coincides with the core axis, while directions x and y are arbitrary and mutually orthogonal. Elastic properties (longitudinal wave velocities V_x, V_y, V_z) were measured in the three respective directions in dry samples using a standard GSP UK-10PMS ultrasonic device. The instrumental error of the time interval was ±0.5 %, the duration of a single measurement – 0.5 min, the operating frequency – 45-60 kHz. A concentrated polysaccharide solution was used as a coupling agent to ensure wave transmission from the sensor to the sample surface. The number of measurements in each of the three directions of a cubic sample ranged from 5 to 10.

Subsequently, the elastic anisotropy index was calculated using the formula

$$A=\frac{1}{V_m}\sqrt{\left(V_x-V_m\right)^2+\left(V_y-V_m\right)^2+\left(V_z-V_m\right)^2}\cdot 100\ \%,$$

where V_m is the average propagation velocity of longitudinal waves, $V_m = (V_x + V_y + V_z)/3$.

The anisotropy of the elastic properties of a rock is determined by the geometry of its fracture system and, like permeability anisotropy, is one of the key petrophysical parameters important for reservoir rocks.

Density ρ was determined by hydrostatic weighing of the samples (Archimedes' method) in air-dry and water-immersed states, using the formula $\rho = \rho_w m_{dry}/(m_{dry} - m_{wet})$, where $\rho_w = 1$ g/cm^3 is the density of water; m_{dry} is the weight of the dry sample in air; m_{wet} is the weight of the sample immersed in water.

Specific acoustic impedance was determined by the formula $R = \rho V_m$. Variations in the R parameter indicate the alternation of rock layers with different physical properties in the section[1].

The open porosity coefficient was determined for each sample in the collection by impregnating initially dry core samples with kerosene. The porosity coefficient was calculated using the formula $C_p = (V_{por}/V_{sample})\cdot 100$ %, where V_{por} is the pore volume, cm^3; V_{sample} – the sample volume, cm^3. Porosity is one of the primary factors controlling reservoir quality [26, 27].

Results

The measurement and calculation results are presented in Table. All samples were described macroscopically and in thin sections (Fig.2). Figure 3 shows the core measurement results for the most representative wells in terms of the number of samples: Shtokmanskaya-1, Arkticheskaya-1, and Krestovaya-1.

Core description in thin sections. The studied core collection is represented by sedimentary rocks: sandstones, siltstones, and limestones, often with interlayers of carbonaceous material. Quartz grains are ubiquitous in the rocks – colorless, with low relief, gray interference colors, and typical undulatory extinction. Microcline fragments, identified by their gridiron twinning, and acidic plagioclases – colorless, with low relief, gray interference colors, and polysynthetic twins with thin twin lamellae – are widely distributed. Mica is present everywhere, typically as separate colorless flakes, with characteristic low relief, bright interference colors, and sparkling extinction. Individual zircon grains are common, characterized by high relief and bright interference colors with zoning. Sericite, which forms small yellowish flakes, and rarely chlorite with typical dirty-gray interference colors, typically develops on individual feldspar grains.

Many samples (sandstones, siltstones, etc.) are very similar to each other in thin sections, minor differences in the percentage content and size of fragments of individual minerals. A brief description of sample compositions is given in Table. Mineral alterations in thin sections show that most of the studied sediments exhibit features typical of late catagenesis (mesocatagenesis) or early metagenesis (apocatagenesis) phases.

Physical properties of well core. *Shtokmanskaya-1 well*. Rock density ρ varies slightly through the section from 2.26 to 2.6 g/cm^3 and tends to gradually increase with depth (Table, Fig.3, *a*). The average longitudinal wave velocity V_m does not depend on density but also varies slightly and gradually increases with depth. Density directly influences specific acoustic impedance, which changes significantly through the section and mirrors the variations in V_m.

---

[1] Glikman A.G. Physics and practice of spectral seismic exploration. 2002. URL: http://newgeophys.spb.ru/ru/book2/ (accessed 24.10.2024)

Physical properties of the core samples

Sample	Depth, m; age	Rock, composition	Longitudinal waves velocity V_x; V_y; V_z, km/s	Average velocity V_m, km/s	Density ρ, g/cm^3	Specific acoustic impedance R, g/cm^2·s	Elastic anisotropy index A, %	Open porosity, C_p, %
Shtokmanskaya-1 well								
1Sht	1437; K_1	Fine-grained arkose sandstone (0.1-0.5 mm, predominantly 0.15 mm) thin-layered; pore-filling cement of chlorite-sericite composition, locally ferruginous	2.92; 2.80; 1.14	2.29	2.31	5.29	61.44	10.8
2Sht	1557; K_1	Fine-grained arkose sandstone (0.1-0.5 mm, predominantly 0.15 mm); pore-filling cement of chlorite-sericite composition, locally ferruginous	2.25; 2.78; 1.17	2.07	2.31	4.78	56.06	10.5
3Sht	1705; K_1	Fine-grained arkose sandstone (0.1-0.5 mm, predominantly 0.15 mm) thinly horizontally layered; pore-filling cement of chlorite-sericite composition, locally ferruginous	3.12; 2.92; 1.40	2.48	2.50	6.20	53.64	6.1
4Sht	1810; K_1	Massive limestone	2.20; 3.30; 0.93	2.14	2.51	5.37	78.38	4.4
5Sht	1900; J_3	Fine-grained arkose sandstone (0.1-0.5 mm, predominantly 0.15 mm) thin-layered with open fractures; pore-filling cement of chlorite-sericite composition, locally ferruginous	2.64; 3.52; 1.77	2.64	2.51	6.63	46.87	5.2
6Sht	2066; J_2	Fine-grained arkose sandstone (0.1-0.5 mm, predominantly 0.15 mm) thin-layered, bioturbite structure; pore-filling cement of chlorite-sericite composition, locally ferruginous	2.98; 3.01; 1.88	2.62	2.29	6.00	34.76	13.1
7Sht	2177; J_2	Fine-grained arkose sandstone (0.1-0.5 mm, predominantly 0.15 mm) thin-layered, bioturbite structure; pore-filling cement of chlorite-sericite composition, locally ferruginous	3.03; 3.07; 2.33	3.02	2.36	7.13	22.91	11.8
8Sht	2246; J_2	Medium-grained quartz sandstone (0.1-1.2 mm, predominantly 0.4-0.5 mm); film cement of chlorite-sericite composition, locally quartz regenerative	1.79; 1.95; 1.73	1.72	2.26	3.89	8.84	13.2
9Sht	2303; J_2	Fine-grained arkose sandstone (0.1-0.5 mm, predominantly 0.15 mm) cross-bedded, bioturbite structure; pore-filling cement of chlorite-sericite composition, locally ferruginous	3.01; 2.18; 1.72	2.30	2.50	5.75	40.20	6.1
10Sht	2452; J_1	Limestone thin-layered	3.56; 3.50; 1.33	2.80	2.57	7.19	64.17	2.8
11Sht	2710; J_1	Medium-grained quartz sandstone (0.1-1.2 mm, predominantly 0.4-0.5 mm) massive; film cement of chlorite-sericite composition, locally quartz regeneration cement	2.55; 2.46; 2.38	2.46	2.28	5.61	4.89	11.4

Continuation of Table

Sample	Depth, m; age	Rock, composition	Longitudinal waves velocity V_x; V_y; V_z, km/s	Average velocity V_m, km/s	Density ρ, g/cm^3	Specific acoustic impedance R, g/cm^2·s	Elastic anisotropy index A, %	Open porosity, C_p, %
12Sht	2806; T_3	Fine-grained arkose sandstone (0.1-0.5 mm, predominantly 0.15 mm); pore-filling cement of chlorite-sericite composition, locally ferruginous	3.05; 3.32; 1.79	2.72	2.39	6.50	42.93	9.7
13Sht	2907; T_3	Fine-grained arkose sandstone (0.1-0.5 mm, predominantly 0.15 mm); pore-filling cement of chlorite-sericite composition, locally ferruginous	2.94; 2.22; 1.53	2.23	2.33	5.20	53.82	11.5
14Sht	3007; T_3	Fine-grained arkose sandstone (0.1-0.5 mm, predominantly 0.15 mm) horizontally layered; pore-filling cement of chlorite-sericite composition, locally ferruginous	3.89; 4.06; 2.14	3.36	2.59	8.70	44.73	1.4
15Sht	3020; T_3	Fine-grained arkose sandstone (0.1-0.5 mm, predominantly 0.15 mm) cross-bedded; pore-filling cement of chlorite-sericite composition, locally ferruginous	2.53; 3.28; 1.61	2.47	2.57	6.35	47.89	3.5
16Sht	3057; T_3	Fine-grained arkose sandstone (0.1-0.5 mm, predominantly 0.15 mm) thin-layered, bioturbite; pore-filling cement of chlorite-sericite composition, locally ferruginous	2.61; 3.79; 1.83	2.74	2.64	7.23	50.93	3.5
17Sht	3073; T_3	Fine-grained arkose sandstone (0.1-0.5 mm, predominantly 0.15 mm) thin-layered; pore-filling cement of chlorite-sericite composition, locally ferruginous	3.72; 3.82; 2.86	3.47	2.49	8.64	21.51	7.5
18Sht	3103; T_3	Fine-grained arkose sandstone (0.1-0.5 mm, predominantly 0.15 mm) micaceous, cross-bedded; pore-filling cement of chlorite-sericite composition, locally ferruginous	2.79; 3.66; 2.26	2.90	2.60	7.54	34.48	2.6
			Average values	2.43	2.43	5.9	42.69	7.5
		Arkticheskaya-1 well						
1Arc	2040; K_1	Fine-grained arkose sandstone (0.1-0.5 mm, predominantly 0.15 mm); pore-filling cement of chlorite-sericite composition, locally ferruginous	3.73; 3.52; 2.20	3.15	2.56	8.06	37.24	5.4
2Arc	2616; J_2	Silt-clay rock, thin-layered with shell fragments	3.32; 3.26; 2.30	2.96	2.09	6.19	27.34	0.0
3Arc	2872; J_2	Fine-grained arkose sandstone (0.1-0.5 mm, predominantly 0.15 mm) cross-bedded; pore-filling cement of chlorite-sericite composition, locally ferruginous	3.45; 3.48; 2.28	3.07	2.53	7.77	31.52	3.3
4Arc	3323; J_1	Fine-medium-grained arkose sandstone (0.1-0.5 mm, predominantly 0.2-0.3 mm) massive; film chlorite-sericite cement, locally regenerated quartz	3.51; 3.61; 2.69	3.27	2.45	8.01	21.83	6.1

Continuation of Table

Sample	Depth, m; age	Rock, composition	Longitudinal waves velocity V_x; V_y; V_z, km/s	Average velocity V_m, km/s	Density ρ, g/cm^3	Specific acoustic impedance R, g/cm^2·s	Elastic anisotropy index A, %	Open porosity, C_p, %
5Arc	3625; T_3	Medium-grained arkose sandstone (0.1-0.8 mm, predominantly 0.4-0.5 mm) massive; film chlorite-sericite cement, locally regenerated quartz	2.87; 2.93; 1.83	2.54	2.41	6.12	34.44	7.3
6Arc	4040; T_3	Limestone, grain size ≤ 0.1-0.15 mm, thin-layered	3.80; 3.87; 2.49	3.39	2.60	8.81	32.43	1.3
			Average values	3.06	2.44	7.47	30.75	3.9
		Krestovaya-1 well						
1Kr	2417; T_1	Fine-grained arkose sandstone (0.1-0.2 mm) thinly horizontally layered; carbonate cement of basal type	3.93; 4.18; 2.22	3.4	2.68	9.22	43.86	0.6
2Kr	3099; T_1	Fine-grained arkose sandstone (0.1-0.2 mm); carbonate cement of basal type	4.25; 3.24; 3.47	3.65	2.70	9.85	20.40	0.4
3Kr	3402; T_1	Fine-grained arkose sandstone (0.1-0.5 mm, predominantly 0.15 mm); pore-filling cement of chlorite-sericite composition, locally ferruginous	4.48; 4.64; 2.91	4.01	2.69	10.79	33.71	0.1
4Kr	3616; T_1	Fine-grained arkose sandstone (0.1-0.2 mm) thin-layered; carbonate cement of basal type	2.98; 4.51; 1.67	3.05	2.74	8.36	65.91	0.5
5Kr	3817; T_1	Fine-grained arkose sandstone (0.1-0.2 mm) thin-layered; carbonate cement of basal type	4.40; 4.10 2.19	3.56	2.74	9.75	47.62	0.7
6Kr	3806; T_1	Fine-grained arkose sandstone (0.1-0.2 mm) thin-layered; carbonate cement of basal type	2.94; 3.21; 2.50	2.88	2.72	7.83	17.60	0.4
7Kr	3910; P_2	Silt-clay rock, thin-layered	3.07; 4.31; 1.77	3.05	2.70	8.23	58.89	0.5
			Average values	3.38	2.71	9.16	41.14	0.4
		Admiralteyskaya-1 well						
1Adm	1845; P_2	Massive carbonaceous limestone	4.16; 3.23; 3.97	3.79	2.70	10.23	18.33	1.2
2Adm	2047; P_2	Thin-layered limestone	3.11; 4.67; 2.34	3.37	2.65	8.93	49.82	7.0
3Adm	2330; P_{1-2}	Massive limestone	4.60; 4.40; 3.49	4.16	2.73	11.36	20.11	0.7
4Adm	2640; P_1	Massive limestone	4.38; 3.92; 1.56	3.31	2.72	9.00	65.19	1.1
			Average values	3.66	2.7	9.88	38.36	2.5
		Ludlovskaya-1 well						
1Lu	1717; J_2	Fine-grained arkose sandstone (0.1-0.5 mm, predominantly 0.15 mm) thinly cross-bedded; pore-filling cement of chlorite-sericite composition, locally ferruginous	3.91; 3.31; 2.16	3.13	2.57	8.04	40.18	4.1

End of Table

Sample	Depth, m; age	Rock, composition	Longitudinal waves velocity V_x; V_y; V_z, km/s	Average velocity V_m, km/s	Density ρ, g/cm^3	Specific acoustic impedance R, g/cm^2·s	Elastic anisotropy index A, %	Open porosity, C_p, %
2Lu	2218; J_1	Fine-grained arkose sandstone (0.1-0.5 mm, predominantly 0.15 mm); pore-filling cement of chlorite-sericite composition, locally ferruginous	3.44; 3.72; 1.36	2.84	2.56	7.27	64.20	4.2
3Lu	2881; T_3	Fine-grained arkose sandstone (0.1-0.5 mm, predominantly 0.15 mm) cross-bedded; pore-filling cement of chlorite-sericite composition, locally ferruginous	3.74; 3.52; 2.13	3.13	2.57	8.04	39.44	1.5
			Average values	3.03	2.57	7.79	47.94	3.3
		Severo-Kildinskaya-82 well						
1SK	3413; T_1	Fine-grained arkose sandstone (0.1-0.5 mm, predominantly 0.15 mm) massive; pore-filling cement of chlorite-sericite composition, locally ferruginous	3.61; 3.45; 2.01	3.02	2.67	8.04	41.27	1.6
2SK	3774; T_1	Fine-grained arkose sandstone (0.1-0.5 mm, predominantly 0.15 mm) massive; pore-filling cement of chlorite-sericite composition, locally ferruginous	2.74; 2.82; 1.47	2.34	2.50	5.85	45.77	5.9
3SK	3875; T_1	Fine-grained arkose sandstone (0.1-0.5 mm, predominantly 0.15 mm) massive; pore-filling cement of chlorite-sericite composition, locally ferruginous	2.87; 2.27; 1.82	2.32	2.47	5.73	32.11	5.3
4SK	4007; T_1	Arkose sandstone, fine-medium-grained (0.1-0.5 mm, predominantly 0.2-0.3 mm) massive; film cement of chlorite-sericite composition, locally regenerated quartz	4.19; 4.29; 3.13	3.87	2.54	9.83	23.49	5.8
			Average values	2.89	2.54	7.34	35.66	4.6

The elastic anisotropy index A decreases down the section, varies substantially, and does not always align in the direction of change with the previous parameters. Porosity C_p exhibits the strongest variation, from 1.4 to 13.2 %, and in most cases is inversely proportional to the elastic parameters (V_m, R, A). The productive interval of this field with unique gas-condensate reserves is located within the depth range of 1813-2479 m [28]. According to [12], the Shtokmanskaya-1 well penetrated two gas-condensate intervals, at depths of ~1850-1900 m and ~2100-2200 m. Apparently, the samples 6Sht-8Sht with the highest porosity values C_p = 11.5-13.2 % belong to the second interval (2100-2200 m), although high porosity is also noted for samples 1Sht, 2Sht and 11Sht-13Sht (see Table, Fig.3).

Arkticheskaya-1 well. Rock density, as in the Shtokmanskaya well, changes weakly with depth from 2.4 to 2.6 g/cm^3, decreasing to 2.09 g/cm^3 at a depth of 2616 m (sample 2Arc, see Table, Fig.3, *b*). The average longitudinal wave velocity V_m and specific acoustic impedance R change synchronously through the section, not increasing with depth. The elastic anisotropy index A changes synchronously with R for the upper samples (1Arc-3Arc) and is in antiphase with R for the lower ones (4Arc-6Arc). The porosity coefficient C_p varies significantly from 0 to 7.1 %, increasing in the three lower samples. Data on the productivity of this well and the Arkticheskaya area in general are not available in open publications.

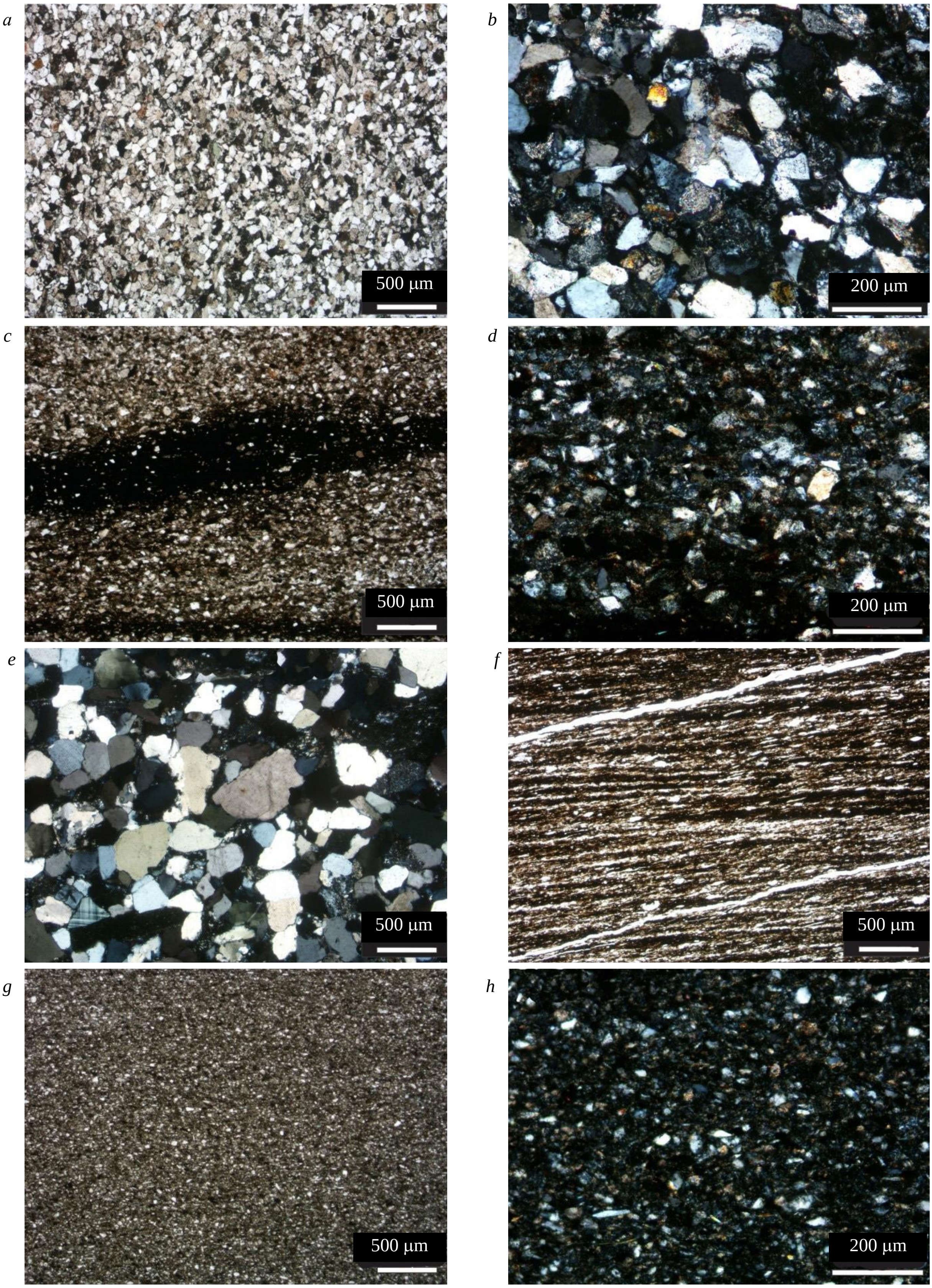

Fig.2. Photographs of thin sections of some rock samples: *a*, *b* – 4SK (fine-medium-grained arkose sandstone); *c*, *d* – 3Kr (fine-grained poorly sorted arkose sandstone); *e* – 8Sht (medium-grained quartz sandstone); *f* – 2Arc (silt-clay rock with distinct layering); *g*, *h* – 7Kr (silt-clay rock)

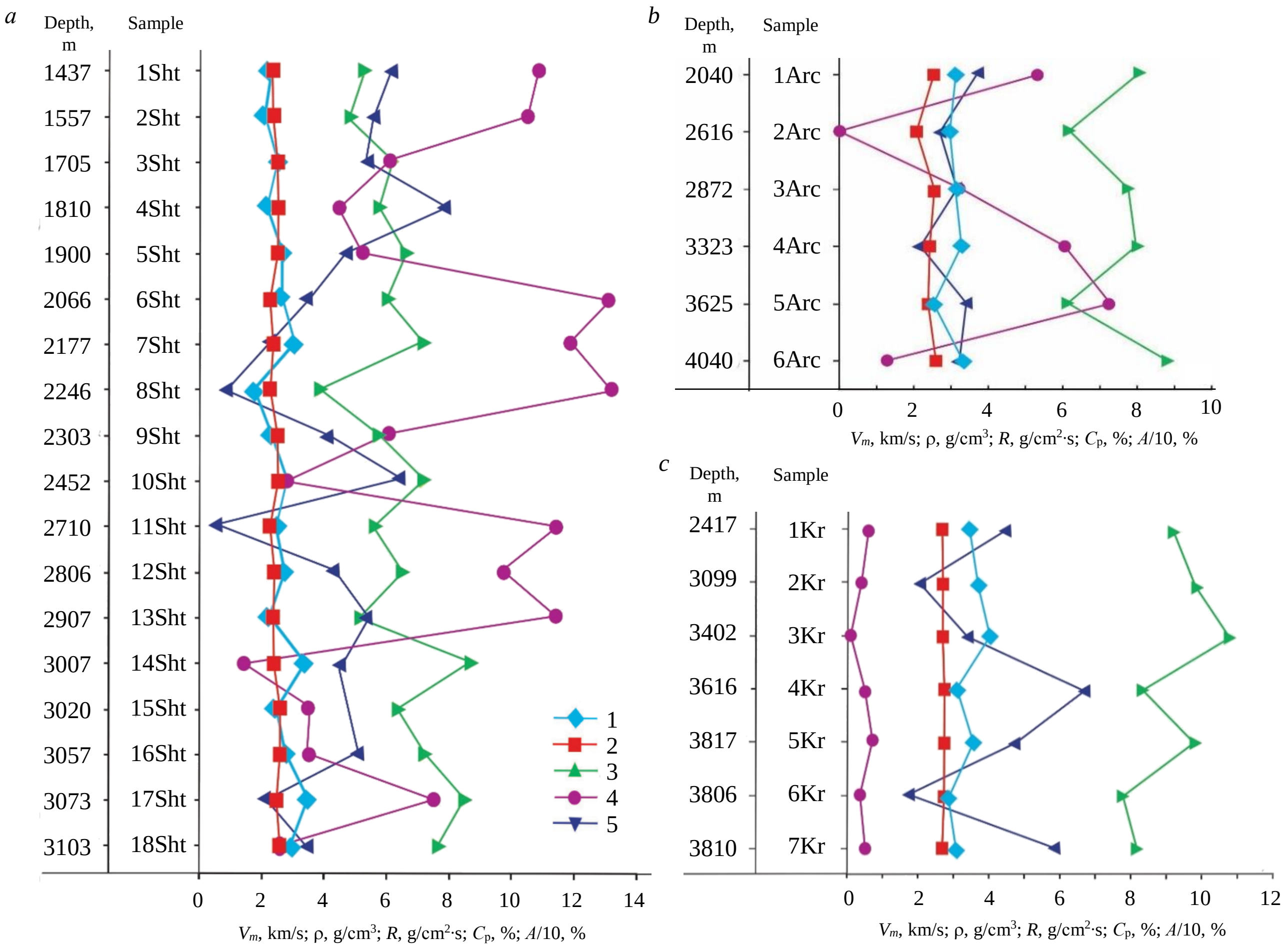

Fig.3. Variations in the physical properties of core along the section: *a* – Shtokmanskaya-1 well; *b* – Arkticheskaya-1 well; *c* – Krestovaya-1 well

1 – average velocity V_m, km/s; 2 – density ρ, g/cm^3; 3 – specific acoustic impedance *R*, g/cm^2·s; 4 – porosity coefficient C_p, %; 5 – elastic anisotropy index *A*/10, %

Krestovaya-1 well. Sample density falls within a narrow range (2.68-2.74 g/cm^3) due to rock homogeneity (see Table). The average velocity of longitudinal waves V_m and specific acoustic impedance *R* gradually decrease with depth. The elastic anisotropy index *A* varies significantly, being in antiphase with *R* for the upper samples (1Kr-5Kr), and changing synchronously with *R* for the lower samples (6Kr and 7Kr). The porosity coefficient C_p is low (0.1-0.7 %) in all samples, raising doubts about the possible presence of hydrocarbon accumulations here.

Discussion

Physical properties of core from the Kola Superdeep Borehole (SD-3) and a number of other wells drilled in ancient metamorphic rocks, as well as measurements of core from Cretaceous deposits of the Leningradskaya area (the Kara Sea shelf) [15], have shown that the elastic anisotropy of rocks, as a physical property related to the composition, structure, and fracture-pore system of the rock, reflects the tectonics of the object (rock massif) and is primarily caused by geodynamic processes [15, 29]. Recent studies [30] have obtained new information on the geological structure of the northern part of the Kara Sea shelf near the Severnaya Zemlya Archipelago. In general, the physical properties of rocks not only provide necessary information about their reservoir properties but also indicate the hydrocarbon potential of shelf deposits. Moreover, the formation of such a property of a sedimentary basin as hydrocarbon potential is ultimately determined by the evolution of the dynamic system of the basin itself [12, 31].

Figure 4 shows the average values of physical properties for each studied well (see Table), which represent characteristic points along a conditional profile oriented from southwest to northeast.

Despite the small number of studied samples, based on the average values of physical properties calculated for all wells (see Table, Fig.3), and using additional information, some conclusions can be drawn. According to [8, 28], three areas are productive: Severo-Kildinskaya-1 – gas, Shtokmanskaya-1 – gas-condensate, and Ludlovskaya-1 – gas. In terms of their geological position, productive wells are located at the boundaries of the basins, while non-productive ones are in the center of the South Barents Basin (Arkticheskaya-1) and within the Admiralty High (Krestovaya-1 and Admiralteyskaya-1, see Fig.1).

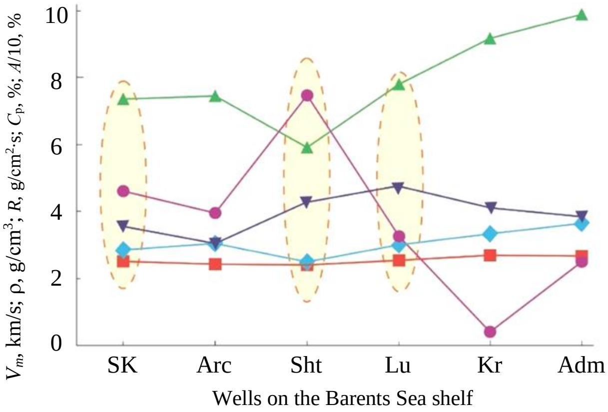

Fig.4. Average values of physical properties of wells core (from southwest to northeast). Productive wells are highlighted by ellipses

For legend, see Fig.3

The physical properties of core samples from Severo-Kildinskaya, Shtokmanskaya, and Ludlovskaya gas wells (Fig.4) are similar in their relatively low V_m and R values and higher C_p and A values. All these parameters depend on the presence of pores and fractures. The development of a fracture-pore system leads to an increase in open porosity coefficients and (or) elastic anisotropy, while simultaneously reducing the average velocity of longitudinal waves and decreasing specific acoustic impedance. The highest open porosity values are noted in the Shtokmanskaya-1 well, which has unrivalled reservoir properties. In the Ludlovskaya-1 well, with low open porosity, the value of the elastic anisotropy index increases, which may be associated with the presence of fracture systems. It is known that the role of fracturing in fluid filtration increases especially in dense, low-porosity rock varieties with low intergranular permeability [32]. Such rocks can form fracture-pore, pore-fracture, and in some cases, purely fracture reservoirs, where fluid filtration occurs primarily through fractures. The reservoir properties of low-productivity wells (Arkticheskaya-1, Krestovaya-1, Admiralteyskaya-1) are inferior in this respect to gas wells (Ludlovskaya, Severo-Kildinskaya-82, Fig.4), expressed in low values of open porosity and elastic anisotropy index, but elevated R and V_m parameters.

Thus, the physical properties of the studied core samples differ noticeably between productive and non-productive wells.

If we consider the petrographic properties of rocks using the example of the Shtokmanskaya-1 well (productive) and Arkticheskaya-1 and Krestovaya-1 wells (non-productive), then with the same rock type (arkose sandstones), a difference is observed both in the granulometric composition of the rocks and in the cementation type. The sandstones of the Shtokmanskaya well are characterized by a larger grain size (0.1-0.5 mm), while the sandstones from the Arkticheskaya-1 and Krestovaya-1 wells are fine-grained (0.1-0.2 mm). The Shtokmanskaya-1 well features pore-filling cement, the Arkticheskaya-1 well has thin-film cement, and the Krestovaya-1 well has cement of the basal type. The reservoir properties of sandstones decrease during the transition from pore-filling to thin-film and basal cement [33]. In the Shtokmanskaya well, against the background of sandstones, two limestone samples (4Sht and 10Sht) stand out in the section, which are characterized by the lowest porosity but high anisotropy, which may indicate the presence of internal fractures. Similar thinly laminated or massive limestones with very low porosity and low anisotropy are also noted in the Arkticheskaya-1 well (2Arc and 6Arc, see Table, Fig.3). Possibly, the absence of pores in the limestones is related to the small grain size $\leq$ 0.1-0.15 mm, since the decrease in reservoir properties of terrigenous (clastic) rocks can be directly related to the reduction in the size of their granulometric composition.

Based on the data presented in the article, it can be argued that hydrocarbon fields in the subsurface of the South Barents Basin should be sought at a relatively short distance from its tectonic boundaries. It is believed that during gas generation in the South Barents thermal chamber, these vast volumes of gas migrated to relatively elevated areas, such as the Shtokman-Ludlovskaya area [11]. From another point of view, fluids were squeezed towards the edges of the basin due to powerful lithostatic pressure; fluids migrated from areas of overpressure to peripheral zones of decompaction [12]. In any case, the gas-condensate and gas fields discovered in the South Barents Basin – Murmanskoye, Severo-Kildinskoye, Shtokmanskoye, Ledovoye, Ludlovskoye are confined to peripheral zones [8].

The obtained results can be useful in studying geotectonic structures prospective for hydrocarbons. Petrophysical methods can be applied to promptly screen out potentially empty areas at the preliminary stage of analyzing geophysical (seismological) materials. Lithological and petrophysical data from core samples of deep wells in oil and gas fields can also be used in mathematical modeling methods for constructing digital core models [34, 35], which are applied in studies of complex reservoir rocks that are difficult to experiment on or in assessing oil and gas reserves [20].

Conclusion

Based on the analysis of core from six wells in the South Barents Basin according to five different physical properties (density, elasticity, elastic anisotropy index, specific acoustic impedance, and porosity) and petrographic features, the following conclusions can be drawn.

Rocks from non-productive wells Arkticheskaya-1, Admiralteyskaya-1, and Krestovaya-1, located in the central part of the South Barents Basin and within the Admiralty High, differ in their physical properties from rocks of gas and gas-condensate wells Shtokmanskaya-1, Severo-Kildinskaya-82, and Ludlovskaya-1, located near the boundaries of the South Barents Basin. Core samples from productive wells have lower values of V_m and R and higher values of C_p and/or A than non-productive wells. It is this combination of petrophysical parameters that provides the reservoir properties of rocks prospective for hydrocarbons. The petrographic variation of the reservoir properties of the studied rocks in productive and non-productive wells is reflected in the decrease in the granulometric composition of the rocks and in the transition from pore-filling to thin-film and basal cement.

When searching for geotectonic structures prospective for hydrocarbons, petrophysical methods can be used to promptly screen out potentially empty areas at the preliminary stage of analyzing geophysical (seismological) materials.

REFERENCES

1. Tectostratigraphic Atlas of the Eastern Arctic. Ed. by O.V.Petrov, M.Smelror. St. Petersburg: VSEGEI, 2020, p. 152 (in Russian).

2. Gusev E.A. Results and prospects of geological mapping of the Arctic shelf of Russia. *Journal of Mining Institute*. 2022. Vol. 255, p. 290-298. DOI: 10.31897/PMI.2022.50

3. Karev V., Kovalenko Y., Ustinov K. Directional Unloading Method is a New Approach to Enhancing Oil and Gas Well Productivity. Geomechanics of Oil and Gas Wells. Springer, 2020, p. 155-166. DOI: 10.1007/978-3-030-26608-0_10

4. Dvoinikov M.V., Leusheva E.L. Modern trends in the development of hydrocarbon resources. *Journal of Mining Institute*. 2022. Vol. 258, p. 879-880 (in Russian).

5. Dmitrieva D., Romasheva N. Sustainable Development of Oil and Gas Potential of the Arctic and Its Shelf Zone: The Role of Innovations. *Journal of Marine Science and Engineering*. 2020. Vol. 8. Iss. 12. N 1003. DOI: 10.3390/jmse8121003

6. Archegov V.B., Nefedov Y.V. Oil and gas exploration strategy in evaluation of fuel and energy potential of Russian Arctic shelf. *Journal of Mining Institute*. 2015. Vol. 212, p. 5-13 (in Russian).

7. Innovative development vector of JSC MAGE. Ed. by G.S. Kazanin, G.I. Ivanov. St. Petersburg, 2017, p. 263 (in Russian).

8. Shipilov E.V., Murzin R.R. Hydrocarbon fields of Russia's West Arctic shelf: geology and distribution regularities. *Geologiya nefti i gaza*. 2001. N 4, p. 6-19 (in Russian).

9. Evdokimov A.N., Smirnov A.N., Fokin V.I. Mineral resources in Arctic islands of Russia. *Journal of Mining Institute*. 2015. Vol. 216, p. 5-12 (in Russian).

10. Prischepa O., Nefedov Y., Nikiforova V. Arctic Shelf Oil and Gas Prospects from Lower-Middle Paleozoic Sediments of the Timan-Pechora Oil and Gas Province Based on the Results of a Regional Study. *Resources*. 2022. Vol. 11. Iss. 1. N 3. DOI: 10.3390/resources11010003
11. Margulis E.A. Factors of forming the unique Shtokman-Ludlov knot of gas accumulation in the Barents Sea. *Neftegazovaya Geologiya. Teoriya i praktika.* 2008. Vol. 3. N 2, p. 9 (in Russian).
12. Shipilov E.V. Hydrocarbons fields of the Russian Arctic shelf: Geology and regularities of the disposal. *Vestnik of MSTU.* 2000. Vol. 3. N 2, p. 339-351 (in Russian).
13. Tsybulya L.A., Levashkevich V.G. Thermal field of the Barents Sea region. Apatity: Kolskii nauchnyi tsentr RAN, 1992, p. 112 (in Russian).
14. Ilchenko V.L. Fission tracks analysis to determine the paleotemperature regime of the Barents Sea sediments. *Litologiya i poleznye iskopaemye*. 1995. N 5, p. 552-557 (in Russian).
15. Ilchenko V.L., Chikirev I.V. Some Physical Properties of Cretaceous Rocks in the Southwestern Part of the Kara Sea Shelf. *Lithology and Mineral Resources.* 2009. Vol. 44. N 4, p. 328-338. DOI: 10.1134/S0024490209040026
16. Drozdov A., Gorbyleva Y., Drozdov N., Gorelkina E. Perspectives of application of simultaneous water and gas injection for utilizing associated petroleum gas and enhancing oil recovery in the Arctic fields. *IOP Conference Series: Earth and Environmental Science*. 2021. Vol. 678. N 012039. DOI: 10.1088/1755-1315/678/1/012039
17. Kozhevnikov E.V., Turbakov M.S., Riabokon E.P., Poplygin V.V. Effect of Effective Pressure on the Permeability of Rocks Based on Well Testing Results. *Energies*. 2021. Vol. 14. Iss. 8. N 2306. DOI: 10.3390/en14082306
18. Dasgupta T., Mukherjee S. Sediment Compaction and Applications in Petroleum Geoscience. Springer, 2020, p. 122. DOI: 10.1007/978-3-030-13442-6
19. Zhukov V.S., Kuzmin Yu.O. Experimental evaluation of compressibility coefficients for fractures and intergranular pores of an oil and gas reservoir. *Journal of Mining Institute.* 2021. Vol. 251, p. 658-666. DOI: 10.31897/PMI.2021.5.5
20. Belozerov I.P., Gubaidullin M.G. Concept of technology for determining the permeability and porosity properties of terrigenous reservoirs on a digital rock sample model. *Journal of Mining Institute.* 2020. Vol. 244, p. 402-407. DOI: 10.31897/PMI.2020.4.2
21. Kozlovsky Y.A. The Superdeep Well of the Kola Peninsula. Springer-Verlag, 1987, p. 571. DOI: 10.1007/978-3-642-71137-4
22. Baker R.O., Yarranton H.W., Jensen J.L. Practical Reservoir Engineering and Characterization. Elsevier, 2015, p. 534. DOI: 10.1016/C2011-0-05566-7
23. Peng Xiang, Hongguang Ji, Jingming Geng, Yiwei Zhao. Characteristics and Mechanical Mechanism of In Situ Unloading Damage and Core Discing in Deep Rock Mass of Metal Mine. *Shock and Vibration*. 2022. Vol. 2022. N 5147868. DOI: 10.1155/2022/5147868
24. Sakulina T.S., Roslov Yu.V., Ivanova N.M. Deep seismic investigations in the Barents and Kara seas. *Izvestiya, Physics of the Solid Earth.* 2003. Vol. 39. N 6, p. 438-452.
25. Systematics and classification of sedimentary rocks and their analogues. Ed. by V.N.Shvanov. St. Petersburg: Nedra, 1998, p. 352 (in Russian).
26. Yang Gao, Zhizhang Wang, Yuanqi She et al. Mineral characteristic of rocks and its impact on the reservoir quality of He 8 tight sandstone of Tianhuan area, Ordos Basin, China. *Journal of Natural Gas Geoscience*. 2019. Vol. 4. Iss. 4, p. 205-214. DOI: 10.1016/j.jnggs.2019.07.001
27. Barletta A. Fluid Flow in Porous Media. Routes to Absolute Instability in Porous Media. Springer, 2019, p. 121-133. DOI: 10.1007/978-3-030-06194-4_6
28. Kozlov S.A. Engineering geology of the Western Arctic shelf of Russia. St. Petersburg: VNIIOkeangeologiya, 2004, p. 147 (in Russian).
29. Artyushkov E.V. On the origin of the seismic anisotropy of the lithosphere. *Geophysical Journal International*. 1984. Vol. 76. Iss. 1, p. 173-178. DOI: 10.1111/j.1365-246X.1984.tb05033.x
30. Gusev E.A., Krylov A.A., Urvantsev D.M. et al. Geological structure of the northern part of the Kara Shelf near the Severnaya Zemlya archipelago according to recent studies. *Journal of Mining Institute.* 2020. Vol. 245, p. 505-512. DOI: 10.31897/PMI.2020.5.1
31. Lavrenova E.A., Shcherbina Yu.V., Mamedov R.A. Modeling of hydrocarbon systems and quantitative assessment of the hydrocarbon potential of Eastern Arctic seas. *Proceedings of higher educational establishments. Geology and Exploration.* 2020. Vol. 63. N 4, p. 23-38 (in Russian). DOI: 10.32454/0016-7762-2020-63-4-23-38
32. Belonovskaya L.G., Bulach M.H., Gmid L.P. The role of fracture in the formation of capacitive-filtration space of complex reservoirs. *Neftegazovaya Geologiya. Teoriya i praktika.* 2007. Vol. 2, p. 18 (in Russian).
33. Smirnova N.V. Types of cement and their effect on the permeability of sandy rocks. *Geologiya nefti i gaza*. 1959. N 7, p. 33-38 (in Russian).
34. Samylovskaya E., Makhovikov A., Lutonin A. et al. Digital Technologies in Arctic Oil and Gas Resources Extraction: Global Trends and Russian Experience. *Resources*. 2022. Vol. 11. Iss. 3. N 29. DOI: 10.3390/resources11030029
35. Esiri A.E., Jambol D.D., Ozowe C. Enhancing reservoir characterization with integrated petrophysical analysis and geostatistical methods. *Open Access Research Journal of Multidisciplinary Studies*. 2024. Vol. 7. Iss. 2, p. 168-179. DOI: 10.53022/oarjms.2024.7.2.0038

***Authors*: Vadim L. Ilchenko,** *Candidate of Geological and Mineralogical Sciences, Senior Researcher* (*Geological Institute of the KSC RAS, Apatity, Russia*), *v.ilchenko@ksc.ru*, *https://orcid.org/0000-0003-2086-4722*, **Igor V. Chikirev,** *Candidate of Geological and Mineralogical Sciences, Head of Department* (*Apatity Branch of Murmansk Arctic University, Apatity, Russia*), *https://orcid.org/0000-0002-4208-4332*.

The authors declare no conflict of interests.

ISSN 2411-3336; e-ISSN 2541-9404

JOURNAL OF MINING INSTITUTE

Zapiski Gornogo instituta

Journal homepage: pmi.spmi.ru

Research article *Geology*

High-alumina gneisses of the Chupa Formation in the Belomorian Mobile Belt: metamorphic conditions, partial melting, and the age of migmatites

Anastasiya V. Yurchenko[1]✉, **Shauket K. Baltybaev**[1,2], **Tatyana A. Myskova**[1]

[1] *Institute of Precambrian Geology and Geochronology RAS, Saint Petersburg, Russia*

[2] *Saint Petersburg State University, Institute of Earth Sciences, Saint Petersburg, Russia*

How to cite this article: Yurchenko A.V., Baltybaev Sh.K., Myskova T.A. High-alumina gneisses of the Chupa Formation in the Belomorian Mobile Belt: metamorphic conditions, partial melting, and the age of migmatites. Journal of Mining Institute. 2026. Vol. 277, p. 26-44.

Abstract

Migmatized gneisses of the Chupa paragneiss Formation in the Belomorian Mobile Belt (BMB) of the Fennoscandian Shield have been studied, and the conditions of partial melting during high-grade metamorphism of the rocks were determined. The melting temperatures and pressures, the amount and composition of the melt formed during the anatexis of gneisses in a closed system, were assessed through direct thermodynamic computer modeling of mineral formation and the construction of pseudosections in pressure-temperature coordinates. The mineral formation calculations are based on the principle of Gibbs energy minimization and were performed using the PERPLE_X software package. The bulk compositions of the migmatized rocks from the Chupa Formation, previously classified and grouped based on their major components, were used for the calculations. It is shown that water-saturated partial melting of compositionally diverse gneisses produces granitic or granodiorite-tonalitic melts within a temperature range of 680-730 °C at moderate to moderately high pressures. The study reveals that the key factor controlling the appearance of kyanite in the investigated rocks is a high Al_2O_3/CaO ratio (at least 5:1) in the protolith, combined with a total alkali content (Na_2O + K_2O) exceeding CaO. According the Chemical Index of Alteration (CIA), the protoliths of the gneisses contained detrital material of varying sedimentary maturity. The source rocks were likely weakly to moderately weathered. U-Pb ID-TIMS dating of monazite from two samples of garnet-kyanite-biotite migmatite (whole-rock analysis) indicates Paleoproterozoic migmatization of the Chupa gneisses at 1854 ± 5 Ma. This phase of Paleoproterozoic endogenic activity is widely recorded in the BMB and may be associated with the formation of the Lapland-Kola or Svecofennian orogens, located to the northeast and southwest of the belt, respectively.

Keywords

migmatites; Belomorian Mobile Belt; protolith; kyanite; Chupa gneisses; partial melting; dating; modeling

Funding

The research was carried out at the expense of a grant from the Russian Science Foundation N 25-27-00117.

Received: 29.01.2025 ***Accepted: 02.07.2025*** ***Online: 11.12.2025*** ***Published: 27.02.2026***

Introduction

The reconstruction of the formation and evolution mechanisms of continental crust remains one of the most pressing challenges in modern geology [1-3]. Granitoids play a key role in crustal formation processes [4-6], which cover significant areas and contain strategically important gold, iron, copper, rare metals, and rare earth elements, as well as other minerals [7-9]. Therefore, studying of granitoids, the mechanisms of their formation, and their role in crust formation is essential for expanding the country's strategic mineral resource base.

The formation of granitic material through the partial melting of metamorphic rocks plays an important role in tectonics [10-12], as the emergence and subsequent migration of anatectic melt significantly affects the rheology of the migmatized sequences by reducing their mechanical strength and increasing the volume of the metamorphic rocks. The volume, composition, and *PT* conditions of the granitic melt formation directly depend on the composition of the source rocks, the fluid regime of metamorphism, the closed or open nature of the system with respect to major components and liquid phases, including the mobility of the newly formed melt itself.

The *PT* melting conditions, quantity, and composition of the melt formed by melting metasedimentary rocks in closed or open systems can be determined through direct thermodynamic modeling by constructing pseudosections in "pressure – temperature" coordinates. For such calculations, the bulk compositions of the migmatized rocks are used. The success of this approach has been demonstrated in recent years in a number of scientific studies [13-15].

In this study, we turned to the analysis of the conditions for the manifestation of partial melting (anatexis) of rocks in the Chupa paragneiss Formation within the Belomorian Mobile Belt (BMB). For this analysis, we used the most diverse possible compositions of the protoliths of the Chupa Formation, allowing us to reveal the specifics of their melting. In addition to the protolith composition, we examined in detail the PTX regime at the onset of the melting process, the fluid regime, and the dependence of anatectic melt compositions on external parameters. Furthermore, to determine the timing of anatexis, U-Pb isotopic dating of monazite extracted from migmatized garnet-kyanite-biotite gneisses of the Chupa Formation was performed. The use of the obtained data makes a significant contribution to understanding the problem of crustal granitoid formation under conditions of elevated lithostatic pressure, which is necessary for reliable tectonic-metamorphic and geodynamic reconstructions.

Brief characteristics of the study area

The BMB is a complex nappe-fold structure, located in the northeastern part of the Fennoscandian Shield. It extends for 700 km along the White Sea as a belt 100-150 km wide, up to the border with Finland, and is bounded to the southwest by the Karelian and to the northeast by the Kola Archean cratons [16]. The BMB consists predominantly of Archean granitoids and migmatized gneisses, with subordinate amounts of Paleoproterozoic meta-intrusive mafic-ultramafic bodies and pegmatites. It represents a system of shallowly northeast-dipping Archean and Proterozoic tectonic nappes [17], complicated by domes. Proterozoic supracrustal formations are absent [16, 18, 19].

In the axial part of the BMB lies the Chupa tectonic nappe (Fig.1), as it is sometimes referred to in the literature, the Suite or Formation. As a Suite within the Belomorian Series, it was delineated during the 1951-1954 geological survey at a scale of 1:50,000 in the territory of the Chupa mica-bearing district. Other researchers, during subsequent geological mapping of the BMB, attributed lithologically similar sequences outside this area to the Chupa Formation. In this work, the neutral term "Formation" is used, as it does not define either the tectonic or stratigraphic nature of the geological unit under consideration, which in this case is not the subject of the study.

The Chupa Formation is considered by researchers as a tectonic nappe of metasedimentary rocks, which overlies the Khetolambina and Keret nappes and, together with them, is underthrust beneath the margin of the Karelian craton as a result of Late Archean subduction [16]. The Chupa tectonic nappe can be traced as a continuous belt or in the form of separate structures across the entire BMB [20]. According to the State Geological Map at a scale of 1:200,000 (Karelian Series, sheet Q-36-XV, XVI) [21], instead of the former Keret, Khetolambina, and Chupa Formations, the Kotozero migmatite-plagiogranite and Khetolambina ortho-amphibolite subcomplexes, as well as the Loukhi Formation, have been delineated. The Chupa Formation is assigned to the Loukhi Formation, the lower boundary of which is established by the abrupt change in rock associations compared to the underlying rocks of the Khetolambina and Kotozero subcomplexes of the Belomorian plutono-metamorphic complex. At the same time, the characteristic rocks of the Loukhi (Chupa) Formation, distinguishing it from others, are kyanite-bearing garnet-biotite, two-mica, and biotite gneisses with subordinate interlayers of amphibole-bearing schists and amphibolite bodies [16].

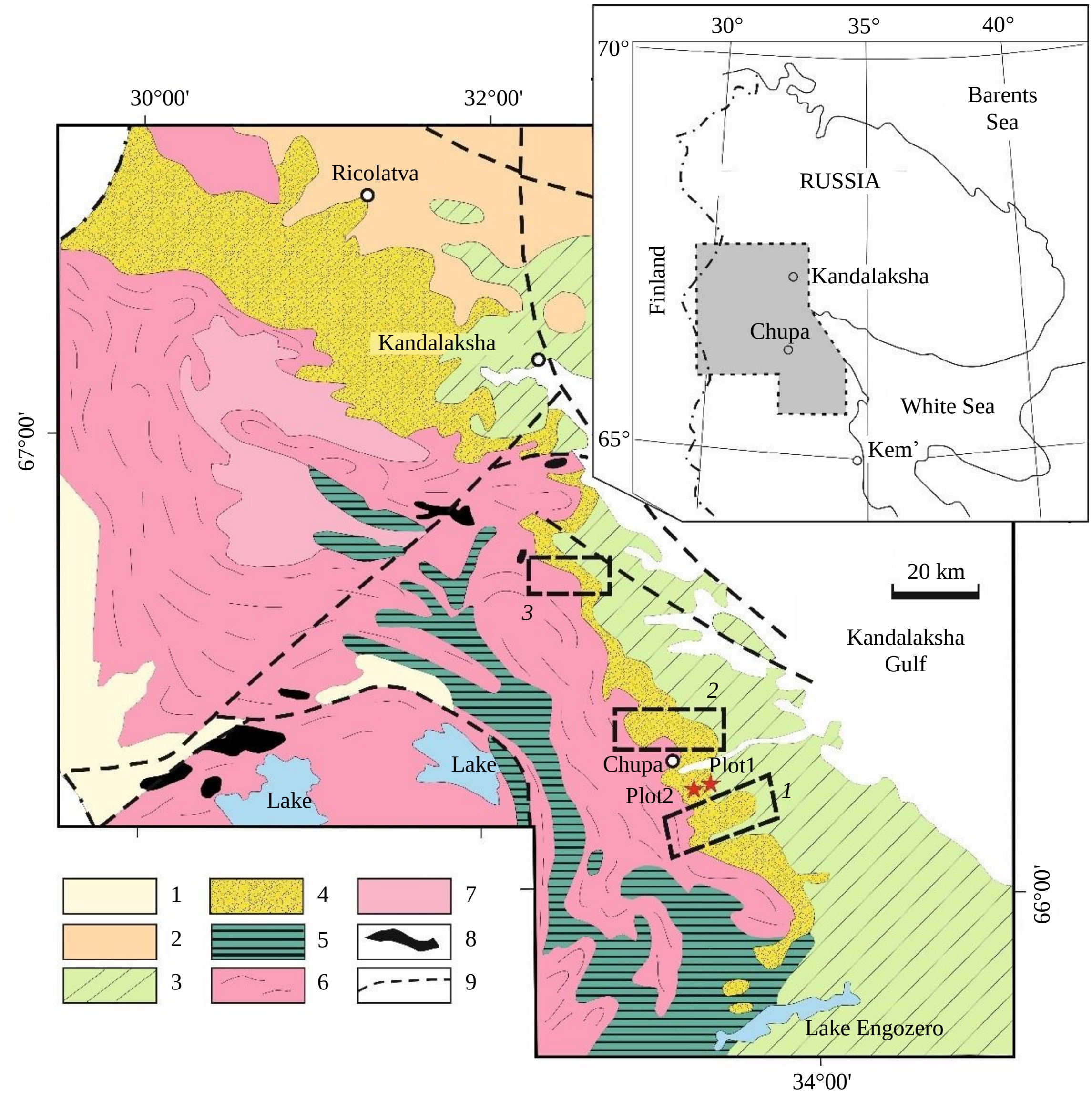

Fig.1. A schematic geological map of the study area indicating the location of the studied sample collection sites (compiled by Yu.V.Miller with modifications by the authors)

1 – Paleoproterozoic troughs; 2 – Svecofennian (Lapland) allochthon, Rikolatva nappe;
3-9 – Late Archean (Belomorian) allochthon: 3 – Khetolambina nappe – tonalites with included bands of mafic and ultramafic rocks, 4 – Chupa nappe – aluminous gneisses, injected by tonalities, 5, 6 – Kovdozero nappe (edge of the Karelian craton in allochthonous position): 5 – North Karelian System of greenstone belts – metabasalts and tuffs of intermediate composition, 6 – predominantly tonalitic infracrustal complex, 7 – Orijärvi nappe – tonalities, 8 – Paleoproterozoic gabbro-norite-lherzolite complex, 9 – faults.
Areas: *1* – Keleynogubsky; *2* – Pulonga-Chupa; *3* – Tupaya Guba – Seryak
Asterisks indicate the sample collection points (Plot1, Plot2) for isotopic dating

There are several hypotheses regarding the origin of the Chupa gneisses. Some researchers suggest that they are deeply metamorphosed sediments [22]. Some scientists [18] consider them as products of ultrametamorphic and metasomatic alterations of metavolcanics of intermediate, to a lesser extent felsic and mafic compositions. In a later study [20], it is proposed that the metamorphic rocks of the Chupa Formation formed from poorly differentiated graywackes, whose sources included felsic (predominant), mafic, and apparently, in small amounts, ultramafic components, which most likely were the products of erosion of volcanic complexes, including proto-ophiolites of mafic zones within young ensimatic island arcs 2.8-2.9 Ga, closely associated with graywackes in the sections.

PT regimes and stages of metamorphism of the Belomorian Mobile Belt

The BMB underwent two major stages of metamorphism: Archean (2.9-2.7 Ga) and Paleoproterozoic (2.0-1.7 Ga) [16, 19], under elevated pressures (8-14 kbar). These metamorphic episodes in the Chupa Formation and adjacent amphibolites of the Central Belomorian greenstone belt are associated with two distinct migmatite and leucogranite formation events. The Neoarchean melting episode (2710±15 and 2706±14 Ma, U-Pb zircon ages) is linked to the formation of the Neoarchean Belomorian collisional orogen, while the Paleoproterozoic episode (1944±12 and 1882±9 Ma, U-Pb zircon ages of leucosomes) corresponds to the development of the Paleoproterozoic Lapland-Kola orogen [19].

There are numerous estimates of the thermodynamic regime of metamorphism of rocks in the Belomorian region. The *PT* parameters of the earliest moderate-pressure granulite stage of metamorphism are: $T = 800$ °C, $P = 6\text{-}8$ kbar [18]; $T = 700\text{-}730$ °C, $P = 6\text{-}7$ kbar [23]. The later stage of high-pressure amphibolite-facies metamorphism, locally reaching granulite-facies conditions, has the following parameters: $T = 750\text{-}850$ °C, $P = 8\text{-}9$ kbar [24]; $T = 730\text{-}750$ °C, $P = 7\text{-}8.5$ kbar [23].

The timing of the granulite-facies metamorphism in the Tupaya Guba area is estimated by the U-Pb method on zircon from garnet-biotite gneiss as 2.85 Ga, and on zircon from metagabbro as 2.7 Ga [23]. The high-pressure amphibolite-facies metamorphism, following the granulite one and corresponding to the conditions of the kyanite-sillimanite facies series, occurred in the interval of 2.7-2.67 Ga: $T = 660\text{-}700$ °C, $P = 12\text{-}14$ kbar [18]; $T = 600\text{-}700$ °C, $P = 8\text{-}9$ kbar [24]. A Paleoproterozoic stage of amphibolite-facies metamorphism is also distinguished, locally manifested along shearing zones, having lower *PT* parameters compared to the previous Late Archean amphibolite stage: $T = 630\text{-}650$ °C, $P = 7.5$ kbar [18]; $T = 550\text{-}630$ °C, $P = 6\text{-}7$ kbar in the area of the Chupa muscovite deposits [24].

For kyanite-bearing gneisses of the Chupa Formation, *PT* conditions of formation are given for leucosomes of Archean age (~2.68 Ga): $P = 9\text{-}11$ kbar, $T = 700\text{-}780$ °C. At the same time, it is noted that non-migmatized garnet-biotite gneisses are characterized by higher metamorphic parameters: $P = 8.5\text{-}12.5$ kbar, $T = 720\text{-}840$ °C [19]. For the melanosome around an early Paleoproterozoic leucosome in amphibolites (~1.94 Ga), the following conditions have been calculated: $T = 625\text{-}700$ °C, $P = 9\text{-}11$ kbar, while for the late (also Paleoproterozoic, ~1.88 Ga) leucosome crosscutting the early one, peak values ($T = 800\text{-}830$ °C, $P = 14\text{-}15$ kbar) have been established, decreasing to $T = 670\text{-}700$ °C, $P = 10\text{-}12$ kbar.

Zircon dating of kyanite gneisses and amphibolites [25] revealed that the zircon cores from gneisses correspond to Neoarchean events with ages of 2700-2800 Ma, and from amphibolites – to the time of magmatic crystallization (2775±12 Ma). At the same time, the inner rims of zircon from amphibolites and gneisses are associated with Neoarchean metamorphic events with ages of 2650±8 and 2599±10 Ma, respectively, and the outer rims – with Paleoproterozoic metamorphism around 1890 Ma.

Methods and research data

The content of chemical elements in the rocks was analyzed by X-ray fluorescence spectrometry (XRF, Central Laboratory of the Karpinsky Institute). The analyzed sample was mixed with a flux (50 % lithium metaborate and 50 % lithium tetraborate) in a 1:9 ratio and then fused in gold-platinum crucibles. The analysis was performed on pressed fused pellets weighing 4 g. The quantitative content of each element is automatically calculated by comparing the element signals (mass spectra) of the working sample and the calibration mixture. The lower detection limit for oxides was 0.01-0.03 wt.%.

U-Pb isotopic dating. Monazite from the crushed samples of migmatized garnet-kyanite-biotite gneiss was extracted using heavy liquids. Then, the monazite grains were grouped under a binocular microscope taking into account their morphology and size. Each analyzed batch contained from 8 to

12 monazite grains. Chemical decomposition of monazite was carried out in a thermostat at a temperature of 220 °C for 24 h using concentrated HCl acid with Teflon inserts inside a stainless-steel jacket. Separation of U and Pb was performed using a modified T.E.Krogh technique. For quantitative determination of Pb and U, a mixed ^{208}Pb-^{235}U tracer was applied. Isotopic analysis of Pb and U was performed on a Triton TI multi-collector mass spectrometer (analyst N.G.Rizvanova, IPGG RAS) in a single filament mode on Re filaments, pre-heated for 30 min at a temperature of 2000±50 °C. For the measurements, a silica gel emitter mixed with H_3PO_4 was used. Mass fractionation factors, determined for Pb from measurements of the NBS standard SRM-982 and for U from measurements of a natural sample, amounted to 0.1 and 0.08 % per atomic mass unit, respectively. Blank contamination did not exceed 50 pg Pb and 10 pg U. Data processing was carried out using the PbDAT and ISOPLOT programs (author K.Ludwig). When calculating the age, the uranium decay constants from [26] were used. Corrections for common lead were introduced according to model values. All errors are reported at the 2σ level.

Computer modeling of phase equilibria was performed using the PERPLE_X v.7.19 program [27] (updated up to 2024) with a database of thermodynamic data for minerals and solid solutions of biotite, plagioclase, chlorite, garnet, spinel, orthopyroxene, white micas, chloritoid, staurolite, cordierite, ilmenite in the MnTiNCKFMASH ($MnO–TiO_2–Na_2O–CaO–K_2O–FeO–MgO–Al_2O_3–SiO_2–H_2O–CO_2$) hp62ver system [28]. The thermodynamic description of melt properties was done according to the paper [29].

The material for determining the compositions of the protoliths of the supracrustal rocks of the Chupa Formation included 100 samples; in addition to the authors' own data, data from the works of O.I.Volodichev and O.S.Sibelev were used (all of them can be provided upon request). These data were divided by cluster analysis and using various diagrams into five groups, which were then analyzed in detail using thermodynamic calculations of metamorphic mineral formation conditions. The analysis of the chemical composition of 152 samples of rock-forming minerals was also used. U-Pb dating of migmatites by monazite was performed for two samples of migmatized garnet-kyanite gneiss (from the whole rock).

Petrochemical characteristics of the studied rocks

The available data on the chemical composition of the rocks of the Chupa Formation, based on cluster analysis, were preliminarily divided into five groups (gr1-1 – gr2-3) and considered on diagrams. On the N.P.Semenenko[*] classification diagram, most of the figurative composition points are concentrated in the upper part of field II, which corresponds to ferromagnesian aluminosilicate protoliths (Fig.2, *a*). A smaller number of points are located in the fields of alkaline-earth aluminosilicate (III) and aluminosilicate (I) protoliths. At the same time, within the field of aluminosilicate protoliths (I), two rock groups are distinguished – one with an elevated aluminum content (gr2-1), and the other (gr1-2, gr2-2) tends towards the compositions of ferromagnesian aluminosilicate protoliths (II).

On the classification diagram [30], which is used to determine sediment maturity, the compositions of the Chupa Formation gneisses fall into the field of immature sediments – greywackes (Fig.2, *b*). Weak and moderate sediment maturity is also illustrated by the Al_2O_3 – ($CaO + Na_2O + K_2O$) – (FeO_t + MgO) diagram (Fig.2, *c*), proposed in the work [31]. The compositions of these samples form a compact field between vectors A and B, elongated towards the apex of the triangle in the direction of increasing weathering intensity. This indicates uneven chemical weathering of a wide spectrum of terrigenous material in the source area. A small part of the points forms a trend in the direction of composition change of acid igneous rocks (A) that underwent chemical weathering; at the same time, this could also be the result of a high degree of migmatization of the gneisses [32].

---

[*] Efremova S.V., Stafeev K.G. Petrochemical Methods for the Study of Rocks. A Reference Guide. Moscow: Nedra, 1985, p. 511.

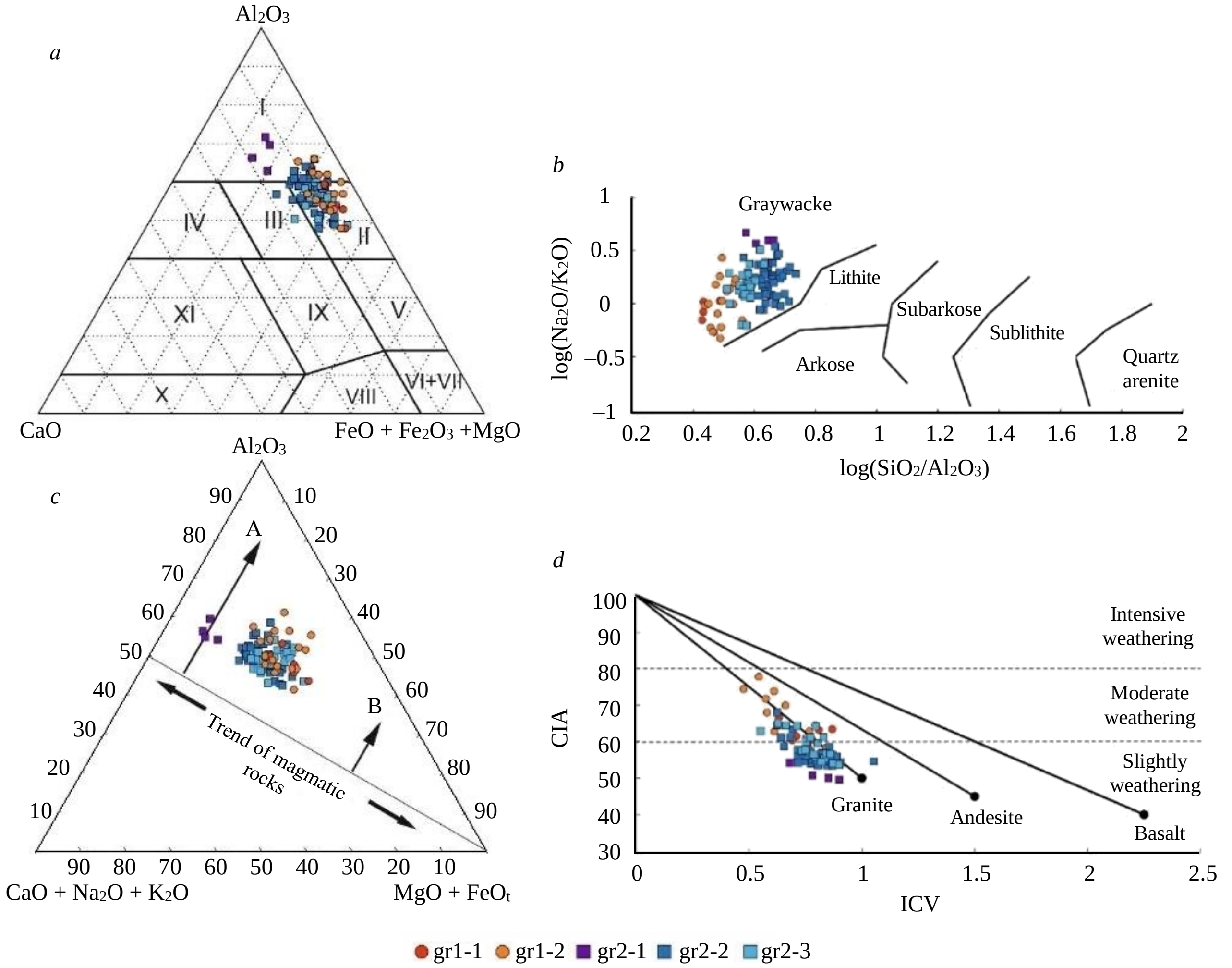

Fig.2. Position of figurative points representing chemical compositions of Chupa Formation gneisses on classification diagrams: *a* – A–C–FM; *b* – $\log(Na_2O/K_2O) – \log(SiO_2/Al_2O_3)$ [30]; *c* – Al_2O_3 – (CaO + Na_2O + K_2O) – (MgO + FeO_t), mol. % [31] (arrows indicate compositional trends during chemical weathering of acidic (A) and basic (B) igneous rocks); *d* – CIA-ICV [31, 33]

Field names according to N.P.Semenenko: I – aluminosilicate; II – iron-rich-magnesian aluminosilicate; III – alkali-earth-aluminosilicate, orthoseries; IV – calcic-aluminosilicate; V – aluminous-magnesian-iron-rich-siliceous; VI – iron-rich-siliceous; VII – magnesian ultramafic; VIII – alkali-earth-Al-poor, ultramafic orthoseries; IX – alkali-earth-aluminous, mafic othoseries; X – calc-carbonate; XI – aluminous-calcic

The Index of Compositional Variability (ICV) varies in the range from 0.5 to 1.1 and reflects the presence of clastic material of varying degrees of sedimentary maturity in the metasedimentary rocks (Fig.2, *d*, Table 1). The figurative points on the CIA-ICV diagram [31, 32] tend towards the lower part of the granite trend, while the points of aluminous gneisses have a higher ICV value and tend towards the central granite line. The Chemical Index of Alteration (CIA) indicates that the rocks of the Chupa Formation generally had weakly and moderately weathered source materials. The high-alumina gneisses, containing a noticeable amount of kyanite, have CIA values from 60 to 78 and are slightly more mature than the garnet-biotite gneisses, in which this index ranges from 50-60 (Fig.2, *d*).

The compositions of the studied rocks, based on the values of the hydrolyzate modulus (HM) [34], belong to siallites and siferlites (the latter predominate), as well as silites (Fig.3, *a*). In half of the samples, the MgO content exceeds or is close to 3 wt.%, which allows them to be considered as pseudosiallites and pseudosilites. The negative correlation on the HM-NAM diagram (Fig.3, *a*) and the positive correlation in the coordinates of TM-IM (Fig.3, *b*), along with AlkM > 1 and elevated values of IM and HM, indicate the primary erosion of igneous rocks with a noticeable admixture of basic-composition pyroclastics (volcaniclastics) [34].

Table 1

Petrochemical indices of Chupa Formation gneisses

Group of gneisses	N analyses	HM	AM	FM	TM	AlkM	NAM	IM	ASM
gr1-1	5	0.52-0.58 (0.54)	0.32-0.37 (0.37)	0.21-0.30 (0.27)	0.04-0.06 (0.04)	0.54-1.04 (0.84)	0.25-0.33 (0.27)	0.37-0.56 (0.49)	4.5-5.9 (5.5)
gr1-2	17	0.27-0.36 (0.47)	0.27-0.36 (0.32)	0.13-0.25 (0.20)	0.03-0.06 (0.05)	0.60-2.69 (1.00)	0.17-0.40 (0.26)	0.24-0.49 (0.40)	3.8-7.0 (5.2)
gr2-1	4	0.26-0.32 (0.29)	0.22-0.27 (0.24)	0.05-0.07 (0.06)	0.02-0.03 (0.02)	3.68-4.63 (3.92)	0.32-0.44 (0.33)	0.15-0.23 (0.16)	5.0-6.8 (5.7)
gr2-2	46	0.28-0.35 (0.32)	0.18-0.27 (0.23)	0.09-0.19 (0.12)	0.03-0.05 (0.04)	0.87-3.42 (1.76)	0.20-0.41 (0.32)	0.26-0.57 (0.36)	3.0-6.3 (4.9)
gr2-3	29	0.36-0.44 (0.39)	0.23-0.31 (0.27)	0.15-0.19 (0.17)	0.03-0.09 (0.04)	0.62-3.18 (1.39)	0.19-0.45 (0.29)	0.32-0.45 (0.39)	3.5-7.6 (5.1)

Group of gneisses	N analyses	Petrochemical parameters after A.N.Neelov [35]				CIA	ICV
		a, at. qty	*b*, at. qty	*n*, at. qty	*k*, at. qty		
gr1-1	5	0.38-0.44 (0.43)	0.25-0.35 (0.30)	0.12-0.18 (0.14)	0.38-0.55 (0.44)	61-67 (63)	0.63-0.87 (0.79)
gr1-2	17	0.32-0.42 (0.38)	0.19-0.32 (0.24)	0.10-0.19 (0.14)	0.20-0.55 (0.40)	55-78 (63)	0.48-0.88 (0.68)
gr2-1	4	0.26-0.31 (0.28)	0.12-0.16 (0.14)	0.10-0.17 (0.17)	0.12-015 (0.14)	50-54 (50)	0.68-0.91 (0.78)
gr2-2	46	0.22-0.32 (0.27)	0.14-0.25 (0.19)	0.10-0.19 (0.14)	0.15-0.40 (0.27)	51-69 (55)	0.63-1.05 (0.78)
gr2-3	29	0.27-0.36 (0.31)	0.19-0.30 (0.23)	0.10-0.18 (0.14)	0.17-0.51 (0.32)	51-65 (58)	0.66-0.90 (0.79)

Notes. Petrochemical modules: hydrolyzate HM – [(Al_2O_3 + TiO_2 + FeOt + MnO)/SiO_2]; aluminum-silica AM – [Al_2O_3/SiO_2]; femic FM – [(FeOt + MnO + MgO)/SiO_2]; titanium TM – [TiO_2/Al_2O_3]; alkaline AlkM – [Na_2O/K_2O]; normalized alkalinity modulus NAM – [(Na_2O + K_2O)/Al_2O_3]; iron IM – [(FeOt + MnO)/(TiO_2 + Al_2O_3)]; total alkalinity ASM – [Na_2O + K_2O] [34]. Petrochemical parameters: *a* – Al/Si, *b* – (Fe^{2+} + Fe^{3+} + Mn + Ca + Mg)/1000, vector length *n* – K + Na, vector slope *k* – K/(K + Na) [35]. CIA – [Al_2O_3/(Al_2O_3 + CaO + Na_2O + K_2O)]·100 [31], ICV – [(Fe_2O_3 + K_2O + Na_2O + CaO + MgO + TiO_2)/Al_2O_3] [32]. Median values of compositions are given in parentheses.

On the FM-NAM diagram [34], designed for the separation of clayey deposits, most of the rocks are localized in the field of essentially chloritic clay compositions with a subordinate role of Fe-hydromicas. The more leucocratic gneisses fall into the uncertainty field. A part of the compositions is located in the field of predominantly kaolinitic clays, while the high-alumina gneisses tend towards the upper part of field (V) and enter the overlap fields – montmorillonite-kaolinite-illitic clays (Fig.3, *c*).

To determine the nomenclatural classification of the rocks, the classification diagram of A.N.Neelov [35], developed for metamorphosed sedimentary-volcanogenic formations, was used. On the diagram (Fig.3, *d*), parameter *a* – the alumina modulus – reflects two mechanisms of material differentiation: the intensity of chemical weathering and granulometric sorting; parameter *b* characterizes the overall melanocratic index of the rocks; and the alkalinity of the rocks is expressed by vectors *n* and *k*. The main cluster of points is concentrated in the field of siltstones and aleuropelites. Fewer compositions fall into the field of sandstones and pelites. In accordance with this, it can be concluded that the distribution of rock composition points is related to a greater extent to the granulometric differentiation of the material. It should be noted that a part of the points (gr2-1) is characterized by a gentler slope of vector *k* (0.12-0.15) compared to other rock groups (0.20-0.55) due to the predominance of Na_2O over K_2O. At the same time, these compositions are shifted leftward along the *b* axis relative to the majority of other compositions due to the lower content of FeO and MgO in the rock. It is also characteristic that a part of the points (gr1-1) is shifted rightward along the *b* axis because of the higher content of FeO and MgO in the rock, while this rock group has the maximum values of parameter *k* (0.38-0.55) due to the predominance of K_2O over Na_2O.

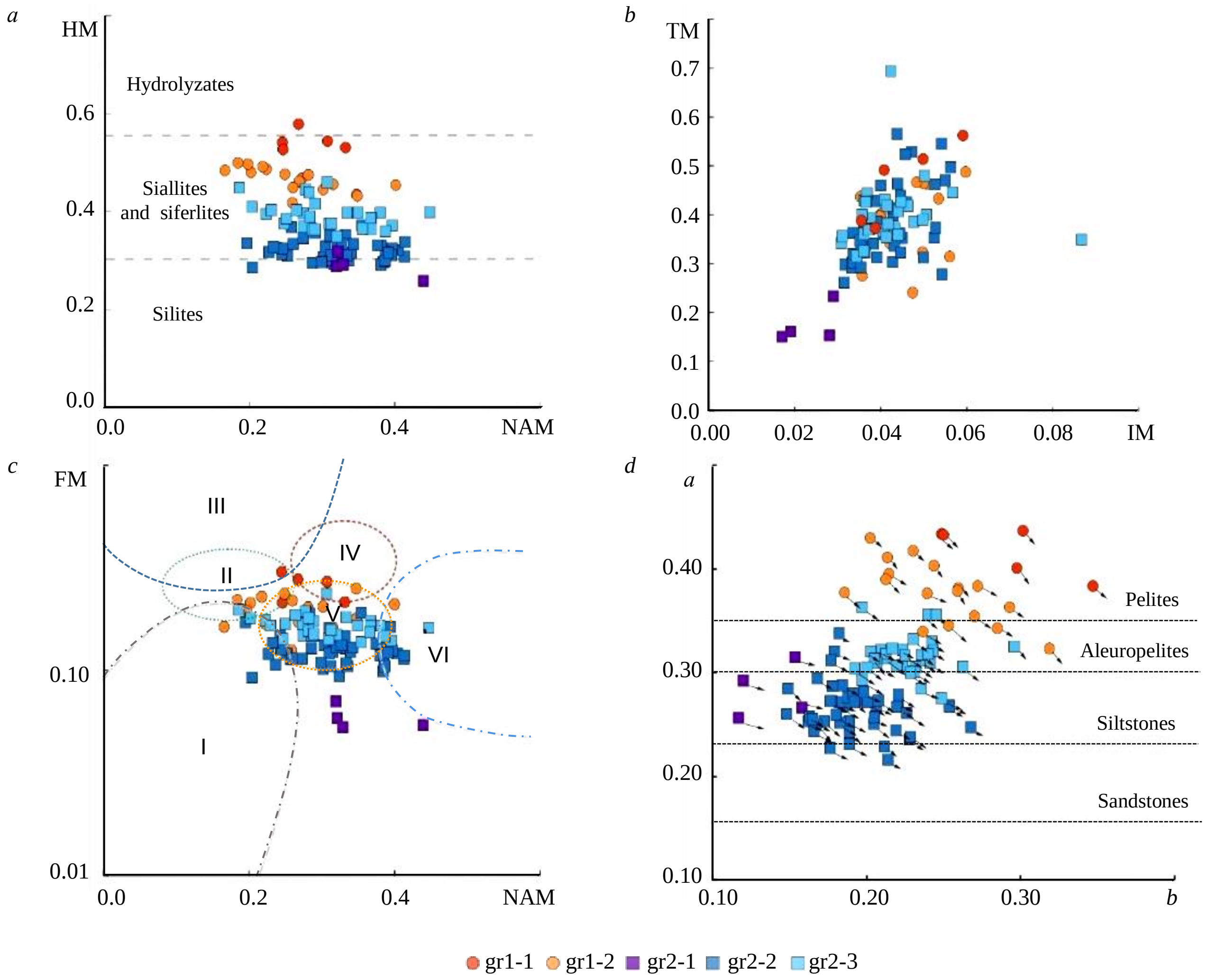

Fig.3. Compositional plots of studied metasedimentary rocks from the Chupa Formation on modulus diagrams FM-NAM (*a*), TM-IM (*b*) и HM-NAM (*c*) [34], *a-b* diagram (*d*)

Clay composition fields: I – predominantly kaolinitic clays; II – montmorillonite-kaolinite-hydromica clays; III – essentially chloritic clays with subordinate Fe-hydromicas; IV – chlorite-hydromica clays; V – chlorite-montmorillonite clays; VI – predominantly hydromica clays with significant feldspar admixture

Petrographic features of the Chupa gneisses

Based on petrographic composition, four varieties of gneisses are confidently distinguished: garnet-biotite; kyanite-garnet-biotite, with the kyanite content ranging from single grains to 20 vol.%; leucocratic essentially quartz-plagioclase gneisses, in which mafic minerals (garnet, biotite, single grains of kyanite) do not exceed 10 vol.%; and muscovite-bearing gneisses, in which muscovite is in association or paragenesis with the described mafic minerals. All gneisses are characterized by both fine-grained and coarse-grained porphyrolepidogranoblastic, lepidogranoblastic, and granoblastic structures, as well as massive, more often banded textures (Fig.4). As a rule, porphyroblasts are represented by garnet, much more rarely by kyanite. Garnet has a pyrope-almandine composition ($(\mathrm{Alm}_{60\text{-}73}\mathrm{Py}_{17\text{-}30}\mathrm{Grs}_{6\text{-}9}\mathrm{Sps}_{1\text{-}4})$)[*] and contains inclusions of both matrix minerals – quartz, biotite, kyanite – and accessory phases – apatite, monazite, zircon, rutile. Garnet grains exhibit retrograde zoning – from the core to the rim of the grains, the content of the pyrope component decreases and the proportion of the almandine component increases.

---

[*] Mineral abbreviations are given according to [36].

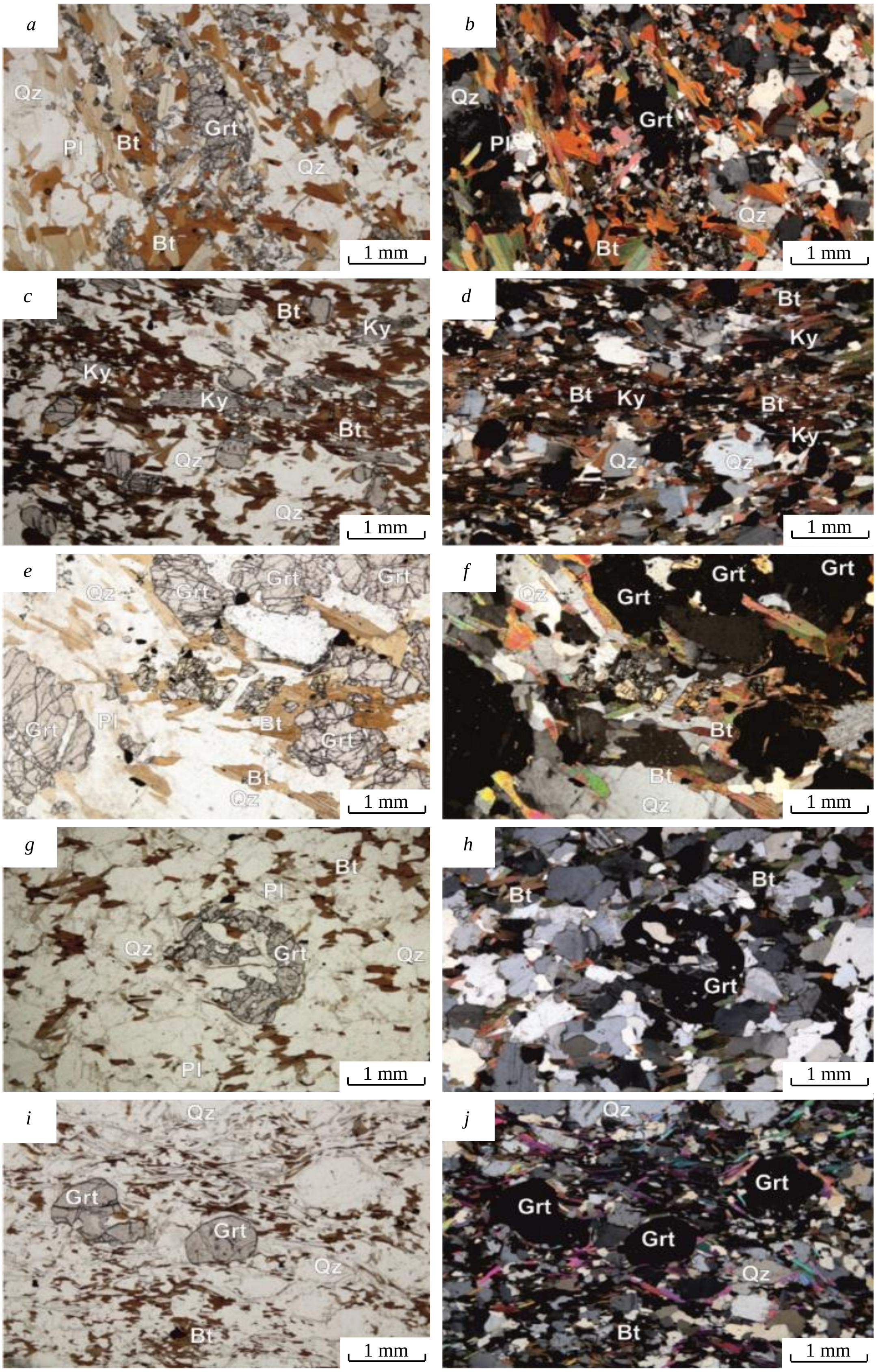

Fig.4. Petrographic characteristics of rocks from the Chupa Formation: kyanite-garnet-biotite gneiss (*a*, *b*); garnet-kyanite-biotite gneiss (*c*, *d*); coarse-grained kyanite-garnet-biotite gneiss (*e*, *f*), kyanite partially replaced by staurolite; leucocratic garnet-biotite gneiss (*g*, *h*); garnet-muscovite-biotite gneiss (*i*, *j*).
Photographs on the left were taken in plane-polarized light (PPL), on the right – in cross-polarized light (XPL)

Biotite belongs to magnesian varieties (Mg# 0.58-0.67) with a predominance of the phlogopite component in its composition and contains 2.6-4.0 wt.% TiO_2. It is the second most common and second largest in grain size, as a rule, tends to melanocratic layers, exhibits pleochroism in brown colors, has practically no secondary alterations, and contains inclusions of zircon.

Plagioclase (An 23-30 %) often has polysynthetic twins and is located in leucocratic layers, being locally subjected to secondary alterations. Quartz occurs together with plagioclase, its grain sizes vary widely, and fine grains or rims adjacent to garnet and around kyanite grains are often observed.

Kyanite most often occurs in paragenesis with garnet and biotite; its association with the boundaries of layers is observed, which, most likely, emphasizes the heterogeneity of the primary protolith of the metasedimentary rock. During retrograde changes, this early metamorphic kyanite is replaced by staurolite. Along with metamorphic kyanite, kyanite with reaction rims of muscovite and quartz is found in migmatites. Kyanite porphyroblasts may contain inclusions of quartz, biotite, apatite, and rutile.

Muscovite is the second most significant mica in the Chupa gneisses, occurs in association with biotite, and develops along cracks in kyanite, more rarely being present in the rock matrix. The muscovite content varies strongly and sometimes reaches 30 vol.%. Potassium feldspar is practically absent in the studied rocks but has been found as inclusions in garnet and in some types of migmatite leucosomes.

Migmatization in the studied gneisses is manifested unevenly – rocks are encountered across a wide spectrum – from those unaffected by migmatization to highly migmatized ones, containing up to 50-70 vol.% leucosomes. The thickness of the leucosomes varies from a few millimeters to a few centimeters. They are represented mainly by plagioclase-quartz aggregates with single grains of biotite, muscovite, and garnet; potassium feldspar varieties with muscovite are also occasionally found.

Determination of *PT* conditions of migmatization

The metamorphic mineral parageneses observed in the studied rocks are well reproduced during computer modeling of mineral formation in the PERPLE_X program (Fig.5). The paragenesis consisting of garnet, plagioclase, kyanite, biotite, and rutile occupies areas of high-temperature amphibolite and granulite facies of medium- to moderately high-pressure metamorphism on these diagrams. The best results for mineral formation during computer modeling were obtained using a carbonic-aqueous fluid with a ratio $CO_2:H_2O = 0.2:0.8$. With a greater amount of carbonic acid in the fluid, carbonate minerals (dolomite, ankerite, etc.) become widespread, which does not correspond to natural observations.

The kyanite-free mineral paragenesis is also adequately reproduced by modeling if the protoliths are characterized by an elevated calcium content (Fig.5, *b*). This can be demonstrated using binary diagrams with varying amounts of a series of components (Fig.6). The diagrams show that kyanite-bearing mineral parageneses, at the same *PT* parameters, can arise only in relatively high-alumina protoliths but with a low calcium content. While the first condition is obvious – alumina is the main component of kyanite – the increase in calcium content involves an increase in the amount of plagioclase in the metamorphic rock, which leads to the complete consumption of alumina during the formation of this feldspar. An additional condition to the specified parameters is the excess of the sum of alkalis ($Na_2O + K_2O$) over CaO in the protolith. However, in the considered examples, favorable protolith compositions for kyanite formation were those in which the sum of FeO + MgO contents usually did not exceed 10 wt.% (in rare cases, slightly higher).

The initial temperature of appearance of the granitic melt in rocks of different composition differs somewhat on average and indicates the possibility of anatectic leucosome formation in the temperature range of 680-730 °C. The most important parameter, besides the protolith composition, affecting the position of the granite liquidus line is the proportion (activity) of water in the metamorphic fluid. For example, a decrease in the molar fraction of water from 1 to 0.6 in a carbonic-aqueous fluid causes an increase in the initial melting temperature of the Chupa gneisses by 50-70 °C.

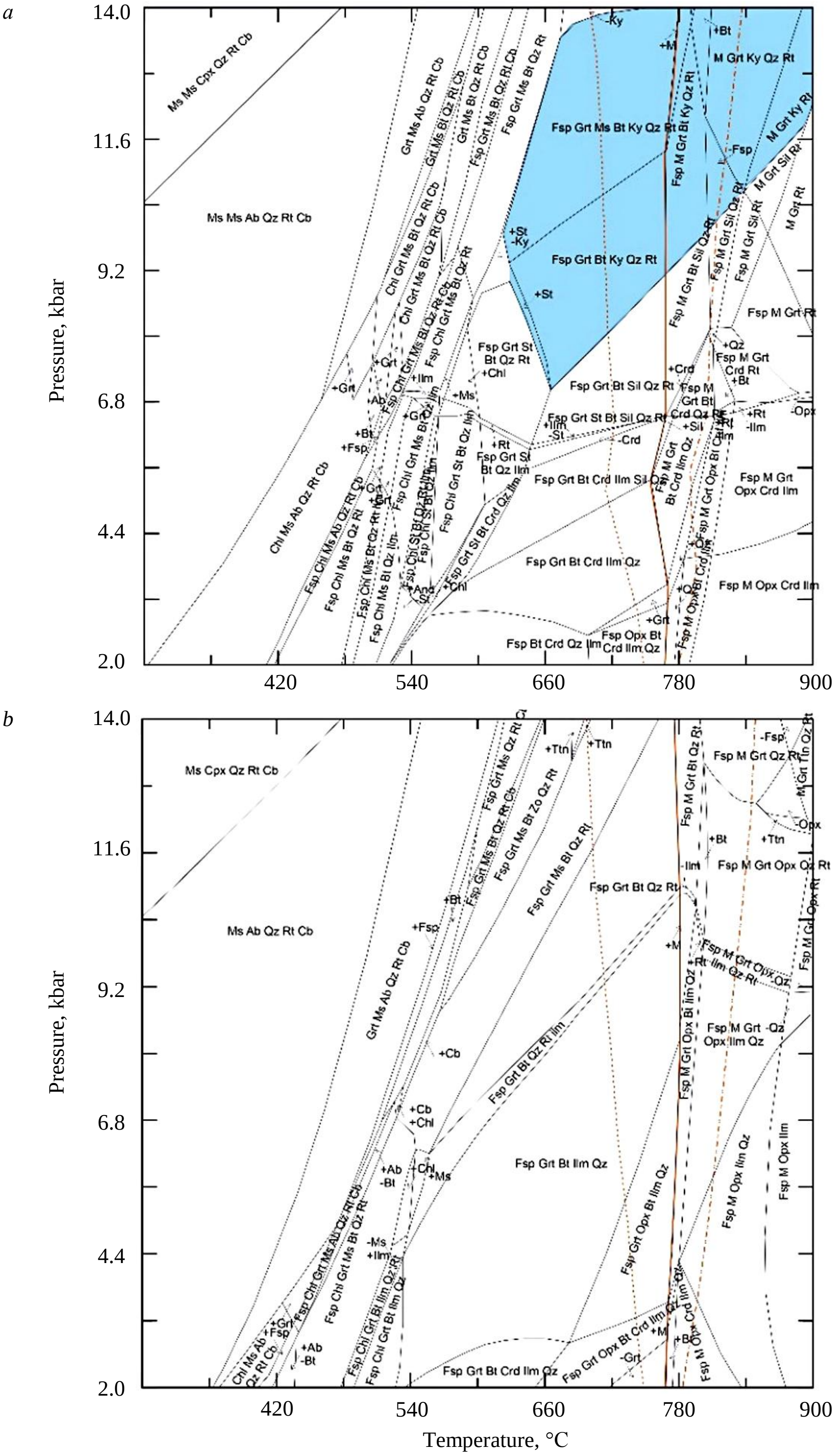

Fig.5. *PT* phase equilibrium diagrams calculated by Gibbs free energy minimization for rocks of the Chupa Formation: gneisses (gr1-2), having a protolith with compositions transitional between groups I (aluminosilicate) and II (ferromagnesian aluminosilicate) with elevated Fe and Mg contents (*a*); gneisses (gr2-1) with a protolith – aluminosilicate (I), but with a high CaO content (*b*); gneisses with protolith compositions between groups I and II, belonging to siltstones (gr2-2) (*c*) and aleuropelites (gr2-3) (*d*). The field of presence of kyanite-bearing mineral parageneses is shown in blue. The position of the granite liquidus at different CO_2:H_2O ratios in the fluid is indicated by red lines: dashed line – $CO_2 = 0.0$, solid line – $CO_2 = 0.2$, dash-dotted line – $CO_2 = 0.4$

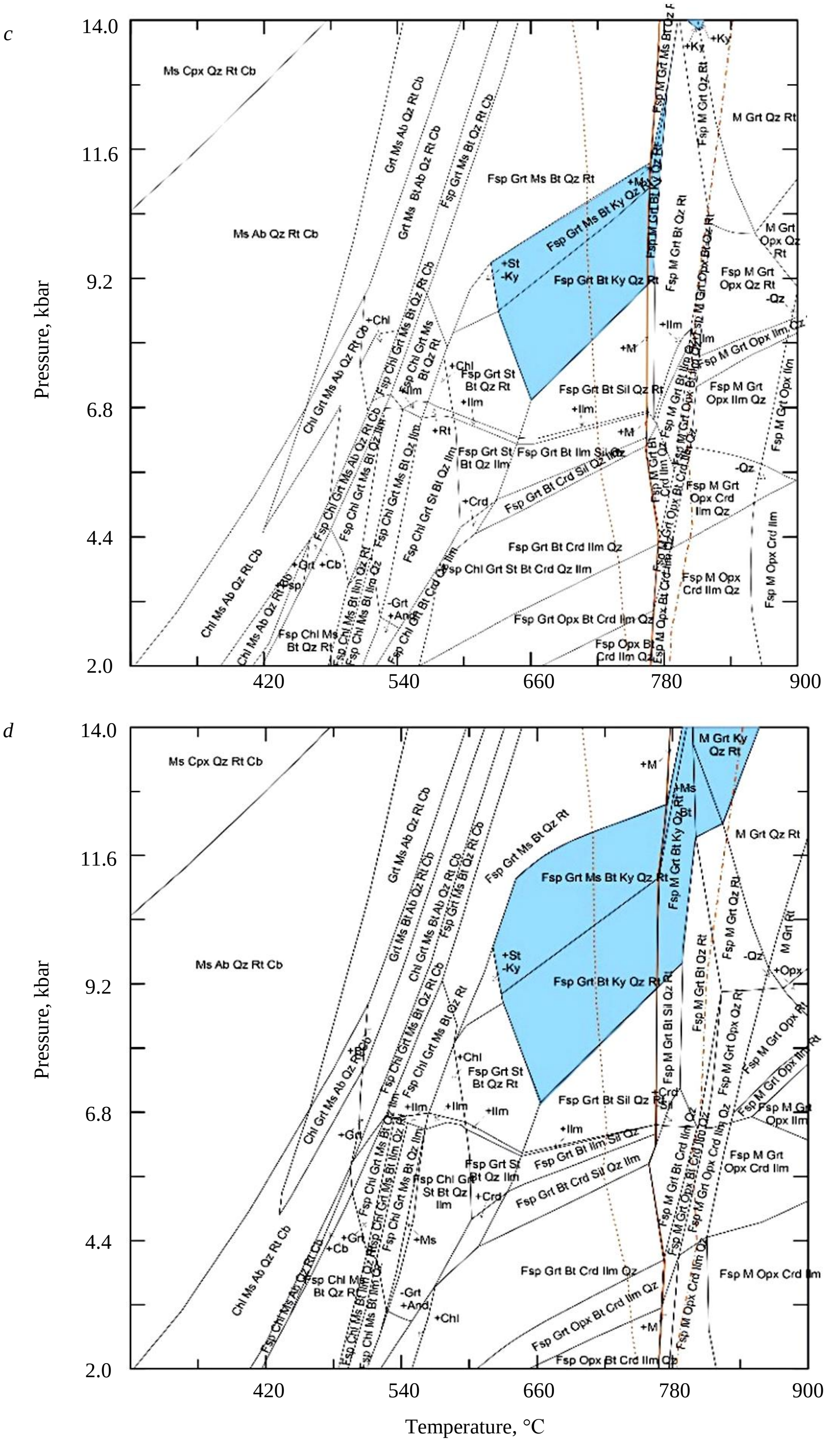

Fig.5. Completion

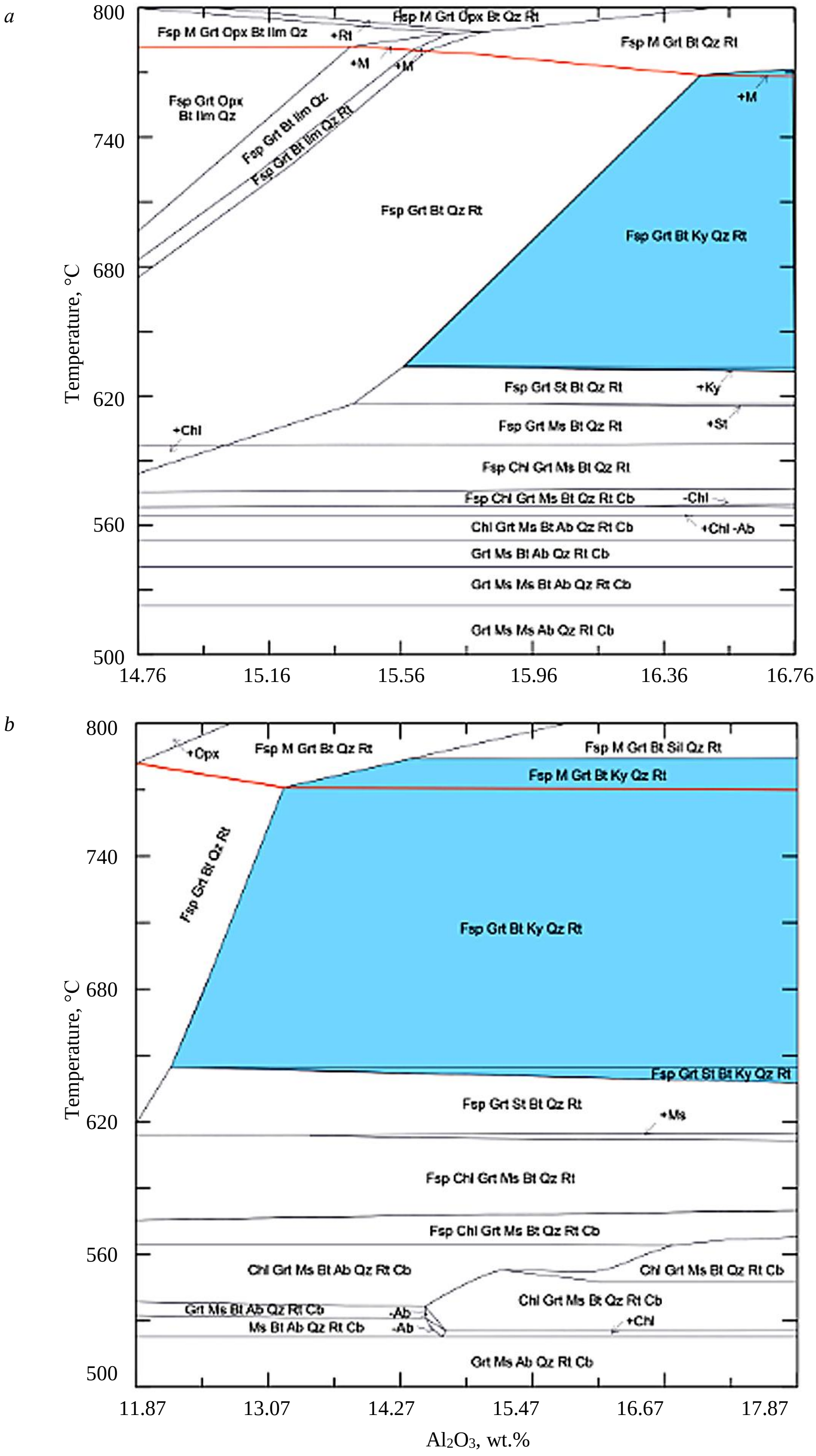

Fig.6. Binary phase diagrams “Temperature – Composition”, calculated by the Gibbs free energy minimization method to determine compositions favorable for the appearance of kyanite with variations in the protolith contents of Al_2O_3 (*a*, *b*) and CaO (*c*, *d*). The field of presence of kyanite-bearing mineral parageneses is shown in blue, the position of the granite liquidus at a fluid ratio of CO_2:H_2O = 0.2:0.8 is indicated by a red line

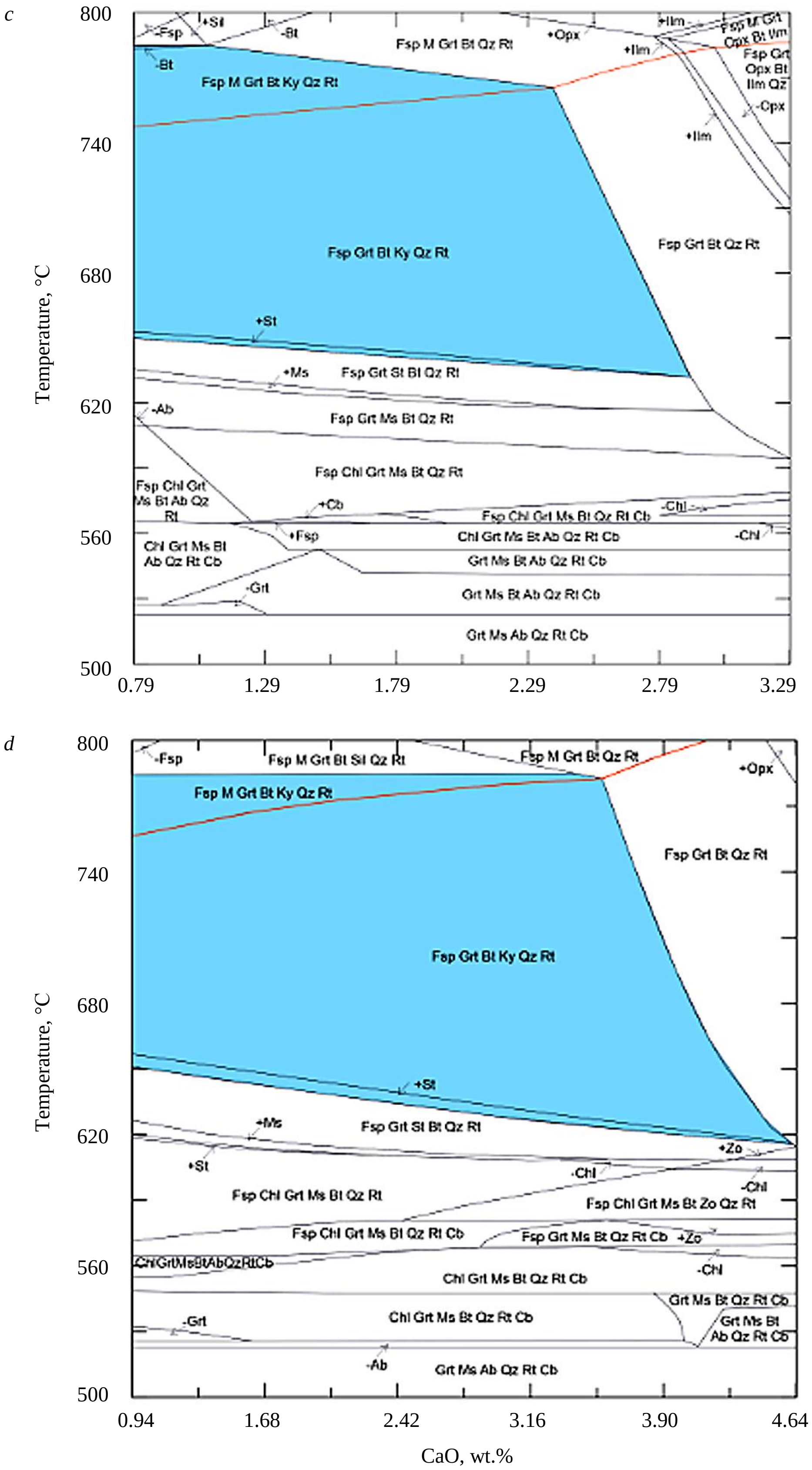

Fig.6. Completion

U-Pb dating of monazite

Isotopic U-Pb analysis of monazite from two samples (Plot1 and Plot2, see Fig.1) of migmatized garnet-kyanite-plagioclase gneiss is presented in Table 2. The figurative points of monazite on the Concordia diagram (Fig.7) are located with a slight deviation from the concordia curve of the two isotopic subsystems of the U-Pb system, which indicates the absence of its disturbance after the crystallization of the studied minerals.

Table 2

Results of U-Pb isotopic studies of monazite

Sample	N grains	$^{206}Pb^a/^{204}Pb$	$^{207}Pb^b/^{206}Pb$	$^{208}Pb^b/^{206}Pb$	$^{207}Pb/^{235}U$	$^{206}Pb/^{238}U$	Th/U	Rho	Age, Ma			Concordant age	MSWD/P
									$^{206}Pb/^{238}U$	$^{207}Pb/^{235}U$	$^{207}Pb/^{206}Pb$		
Plot1	8 grains	4290	0.11313	2.2409	5.211	0.3341	6.2	0.94	1858.0	1854.4	1850.3	1853±5	2/0.16
Plot2	12 grains	7590	0.11329	2.1725	5.214	0.3338	6.0	0.94	1856.9	1855.0	1852.9	1854±5	0.48/0.48

The concordant age values were for sample Plot1 1853±5 Ma, MSWD = 2 with a concordance probability of 0.16, and for sample Plot2 – 1854±5 Ma, MSWD = 0.48 with a probability of 0.49. Given the practical identity of the calculated age values, as well as their overlap within analytical error, the age of monazites from the two samples is taken as 1854±5 Ma.

Discussion

Metamorphic mineral parageneses in the studied rocks of the Chupa Formation have a sufficiently wide stability field in temperature and pressure coordinates. Data from previous studies (e.g. [19]) indicate that mineral parageneses corresponding to peak high-pressure granulite facies conditions are preserved in leucosomes of amphibolites, and their retrograde transformations occurred under medium- and high-temperature amphibolite facies conditions of high pressure. However, it remains unclear to which time of the endogenous evolution of the rocks these PT parameters relate, since in the migmatites, these authors dated only Archean-age zircons, while younger (e.g., Paleoproterozoic) zircons were not detected in the samples. This is strange, since Paleoproterozoic processes are very intensely manifested in the BMB [16, 23, 37], which is confirmed by numerous

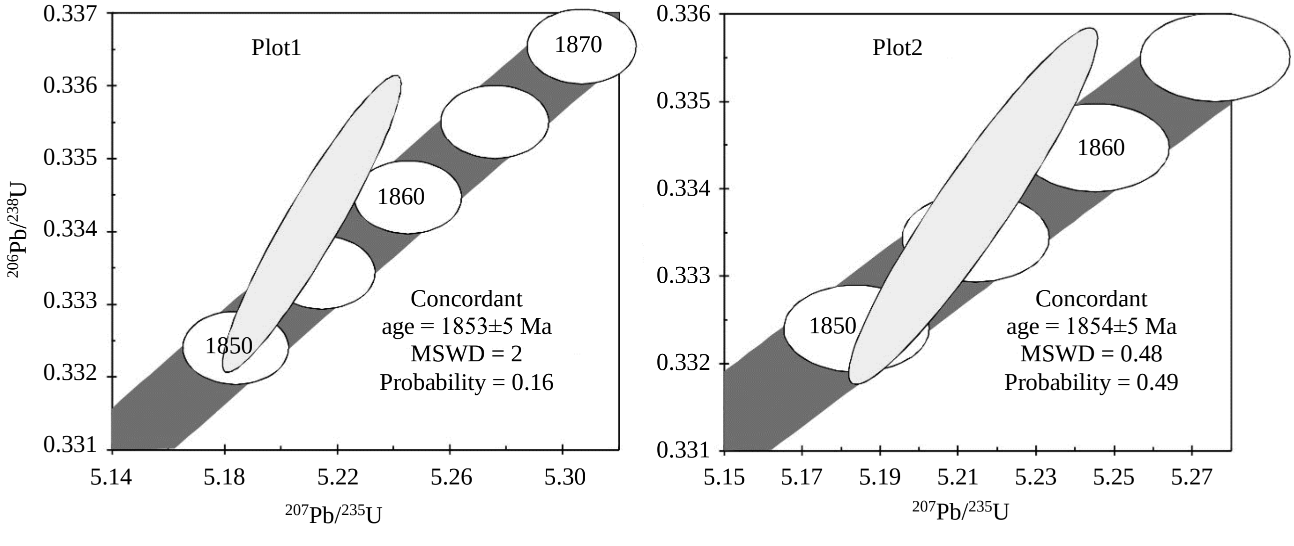

Fig.7. Concordia diagram for two monazite samples from garnet-kyanite-plagioclase gneiss of the Chupa Formation. Age values are calculated at 2σ confidence level

geochronological studies [38-40]. In particular, in the rocks of the Voche-Lambina area in the northwestern part of the BMB, a leucosome with east-dipping transpressional lineations has an age of 1898±2 Ma and is associated with Paleoproterozoic collisional events [38]. Further south, in the Chupa-Loukhi area, the last collisional metamorphism and migmatization took place between 1840 and 1875 Ma (according to U-Pb SIMS studies of zircon [41]). Taking these geochronological data into account, a suggestion has been made [38] that within the BMB, the collision of the Archean Kola and Karelian cratons led to the formation of a regional complex of shearing zones (plastic shear flow) under amphibolite-facies metamorphic conditions, which was accompanied by migmatization of the rocks [38, 41,42]. Metamorphism does not always lead to noticeable migration of chemical elements in rocks, as follows from a number of works on structures adjacent to the Chupa Formation [43, 44].

Metamorphic conditions corresponding to moderate or elevated pressures of the amphibolite facies are very characteristic both for the BMB and for structures directly adjacent to the belt. In particular, *PT* parameters of moderate-pressure amphibolite facies metamorphism have been established in intrusions of peridotites, as well as acidic and intermediate metavolcanics aged 1923-1926 Ma of the Kaskama structure of the Inari terrane, located north of the Lapland Granulite Belt [45]. Paleoproterozoic progressive amphibolite facies metamorphism at $T = 625\text{-}660$ °C and $P = 7\text{-}9$ kbar is also described in the rocks of the Korvatundra structure underlying the Lapland Granulite Belt [46].

The compositions of most protoliths of the Chupa gneisses turned out to be favorable for the formation of kyanite. The key factor determining the appearance of kyanite in the studied rocks is the elevated Al_2O_3/CaO ratio in the protoliths, which must be at least 5:1 with a content of the sum of alkalis ($Na_2O + K_2O$) exceeding the content of CaO. In such protoliths, kyanite forms both above and below the water-saturated solidus temperature. This determines the widespread presence of this mineral both in migmatized varieties and in gneisses that do not contain leucosomes.

Judging by the ICV values in the range of 0.5-1.1, the protoliths contained clastic material of varying sedimentary maturity. Weakly and moderately weathered rocks of granitic composition could have served as the protoliths.

Zones of gentle foliation and shearing (plastic shear flow), associated with the formation of gently dipping (5-30°) subhorizontal or northwest-striking thrusts, are considered as an important benchmark of the Paleoproterozoic stage of evolution of the BMB [38, 39, 42]. S.Yu.Kolodiazhnyi also believes that the widely developed, gently dipping thrust zones within the BMB formed as a result of the emplacement of the Porya Guba granulite protrusion [47]. Based on the geological relationships of Paleoproterozoic dikes and metagabbro masses with sheared rocks, as well as geochronological data obtained from metamorphic rocks in zones of gentle shearing and foliation, it is suggested that these zones formed around 1855 Ma [39].

According to U-Pb dating of titanite and rutile [37], during the period from approximately 1.94 to 1.82 Ga, the rocks of the BMB experienced slow cooling. The last metamorphic event 1900-1800 Ma, which led to the resetting of the U-Pb system in titanites and local zircon growth, was associated with zones of migmatization and pegmatite formation, where the most intensive circulation of aqueous-alkaline fluids is assumed [37, 41].

The obtained data on the *PT* parameters of metamorphism and the timing of migmatization in the Chupa Formation should be considered as one of the stages of Paleoproterozoic tectono-thermal activity, reaching conditions of partial rock melting in intensity. The place of this event in the overall sequence of tectonic events in the region, as well as the nature of the involvement of geological structures formed by that time, requires further study. Possibly, in the tectonic scenario explaining the evolution of Paleoproterozoic endogenous events within the BMB, one should take into account processes associated with the formation of the Svecofennian orogen and, accordingly, the Svecofennian orogeny.

Conclusion

The conducted studies of the mineral and petrographic composition, together with the determination of the lithochemical parameters of the rocks of the Chupa Formation (BMB), U-Pb dating of metamorphic monazite, and petrogenetic modeling, allow us to draw the following conclusions:

- The *PT* metamorphic parameters and the U-Pb isotopic age of 1854±5 Ma for monazite from migmatized gneisses of the Chupa Formation correspond to one of the stages of Paleoproterozoic tectonothermal activity in the BMB. The nature of this activity in the context of the development and formation of large structures of the Belomorian region in the Paleoproterozoic requires further study.
- The metamorphic mineral parageneses, consisting of garnet, plagioclase, kyanite, biotite, and rutile, are well reproduced during computer modeling of mineral formation in the field of high-temperature amphibolite and granulite facies of medium- to moderately high-pressure metamorphism.
- The key factor determining the appearance of kyanite in the Chupa rocks is the elevated Al_2O_3/CaO ratio, which must be at least 5:1 at a weight content of alkalis, the sum ($Na_2O + K_2O$) of which must exceed CaO.
- Judging by the value of the ICV parameter, the protoliths contained clastic material of varying sedimentary maturity. Such protoliths could have been weakly and moderately weathered granites.

The authors thank O.L.Galankina (IPGG RAS, Saint Petersburg) for assistance in the analytical investigations of mineral compositions and N.G.Rizvanova (IPGG RAS, Saint Petersburg) for assistance in the isotopic studies of monazite.

REFERENCES

1. Mingguo Zhai, Xiyan Zhu, Yanyan Zhou et al. Continental crustal evolution and synchronous metallogeny through time in the North China Craton. *Journal of Asian Earth Sciences*. 2020. Vol. 194. N 104169. DOI: 10.1016/j.jseaes.2019.104169
2. Emo R.B., Kamber B.S. Evidence for highly refractory, heat producing element-depleted lower continental crust: Some implications for the formation and evolution of the continents. *Chemical Geology*. 2021. Vol. 580. N 120389. DOI: 10.1016/j.chemgeo.2021.120389
3. Touret J.L.R., Santosh M., Huizenga J.M. Composition and evolution of the continental crust: Retrospect and prospect. *Geoscience Frontiers*. 2022. Vol. 13. Iss. 5. N 101428. DOI: 10.1016/j.gsf.2022.101428
4. Marimon R.S., Hawkesworth C.J., Dantas E.L. et al. The generation and evolution of the Archean continental crust: The granitoid story in southeastern Brazil. *Geoscience Frontiers*. 2022. Vol. 13. Iss. 4. N 101402. DOI: 10.1016/j.gsf.2022.101402
5. Sakyi P.A., Kwayisi D., Nunoo S. et al. Crustal evolution of alternating Paleoproterozoic belts and basins in the Birimian terrane in southeastern West African Craton. *Journal of African Earth Sciences*. 2024. Vol. 220. N 105449. DOI: 10.1016/j.jafrearsci.2024.105449
6. Wen-Bin Xue, Shao-Cong Lai, Yu Zhu et al. Generation of Neoproterozoic granites of the Huangling batholith in the northern Yangtze Block, South China: Implications for the evolution of the Precambrian continental crust. *Journal of Asian Earth Sciences*. 2025. Vol. 277. N 106395. DOI: 10.1016/j.jseaes.2024.106395
7. Alekseev V.I. Deep structure and geodynamic conditions of granitoid magmatism in the Eastern Russia. *Journal of Mining Institute*. 2020. Vol. 243, p. 259-265. DOI: 10.31897/PMI.2020.3.259
8. Marin Yu.B., Smolensky V.V., Beskin S.M. Classification of Rare-Metal Alkali Granites. *Geology of Ore Deposits*. 2024. Vol. 66. N 7, p. 905-913. DOI: 10.1134/S1075701524700132
9. Lehmann B. Formation of tin ore deposits: A reassessment. *Lithos*. 2021. Vol. 402-403. N 105756. DOI: 10.1016/j.lithos.2020.105756
10. Yong-Fei Zheng, Peng Gao. The production of granitic magmas through crustal anatexis at convergent plate boundaries. *Lithos*. 2021. Vol. 402-403. N 106232. DOI: 10.1016/j.lithos.2021.106232
11. Qiong-Xia Xia, Meng Yu, Er-Lin Zhu et al. Two generations of crustal anatexis in association with two-stage exhumation of ultrahigh-pressure metamorphic rocks in the Dabie orogen. *Lithos*. 2023. Vol. 446-447. N 107146. DOI: 10.1016/j.lithos.2023.107146
12. Shaoji Yang, Yanru Song, Haijin Xu et al. Paleoproterozoic ultrahigh-temperature metamorphism and anatexis of the pelitic granulites in the Kongling terrane, South China. *Precambrian Research*. 2024. Vol. 414. N 107591. DOI: 10.1016/j.precamres.2024.107591
13. Guangyu Huang, Jinghui Guo, Richard Palin. Phase equilibria modeling of anatexis during ultra-high temperature metamorphism of the crust. *Lithos*. 2021. Vol. 398-399. N 106326. DOI: 10.1016/j.lithos.2021.106326

14. Haobo Wang, Shuyun Cao, Junyu Li et al. High-pressure granulite-facies metamorphism and anatexis of deep continental crust: New insights from the Cenozoic Ailao Shan–Red River shear zone, Southeast Asia. *Gondwana Research*. 2022. Vol. 103, p. 314-334. DOI: 10.1016/j.gr.2021.10.010

15. Guangyu Huang, Hao Liu, Jinghui Guo et al. Partial melting mechanisms of peraluminous felsic magmatism in a collisional orogen: An example from the Khondalite belt, North China craton. *Journal of Metamorphic Geology*. 2024. Vol. 42. Iss. 6, p. 817-841. DOI: 10.1111/jmg.12774

16. Early Precambrian of the Baltic shield. Ed. by V.A.Glebovitskii. Saint-Petersburg: Nauka, 2005, p. 711 (in Russian).

17. Glebovitskii V.A., Sedova I.S., Larionov A.N., Berezhnaya N.G. Isotopic Timing of the Magmatic and Metamorphic Events at the Turn of the Archean and Proterozoic within the Belomorian Belt, Fenno-Scandinavian Shield. *Doklady Earth Sciences*. 2017. Vol. 476. Part 2, p. 1143-1146. DOI: 10.1134/S1028334X1710004X

18. Volodichev O.I. Belomorian Complex of Karelia. Geology and Petrology. Leningrad: Nauka, 1990, p. 245 (in Russian).

19. Slabunov A.I., Azimov P.Ya., Glebovitskii V.A. et al. Archaean and Palaeoproterozoic Migmatizations in the Belomorian Province, Fennoscandian Shield: Petrology, Geochronology, and Geodynamic Settings. *Doklady Earth Sciences*. 2016. Vol. 467. Part 1, p. 259-263. DOI: 10.1134/S1028334X16030077

20. Myskova T.A., Glebovitskii V.A., Miller Yu.V. et al. Supracrustal Sequences of the Belomorian Mobile Belt: Protoliths, Age, and Origin. *Stratigraphy and Geological Correlation*. 2003. Vol. 11. N 6, p. 535-549.

21. State Geological Map of the Russian Federation, Scale 1:200000. Izdanie 2-e. Seriya Karelskaya. List Q-36-XV, XVI (Loukhi). Obyasnitelnaya zapiska. Moscow: Moskovskii filial “VSEGEI”, 2021, p. 109 (in Russian).

22. Ruchev A.M. On the protolith of the North Karelian gneisses of the Chupa Formation, Belomorian Complex. *Geologiya i poleznye iskopaemye Karelii*. Petrozavodsk: Karelskii nauchnyi tsentr RAN, 2000. Iss. 2, p. 12-25 (in Russian).

23. Bibikova E.V., Borisova E.Yu., Drugova G.M., Makarov V.A. Metamorphic History and Age of Aluminous Gneisses of the Belomorian Mobile Belt on the Baltic Shield. *Geokhimiya*. 1997. N 9, p. 883-893 (in Russian).

24. Drugova G.M. Peculiarities of the early Precambrian metamorphism in Eastern and Western parts of the Belomorsky folded belt (Baltic shield). *Zapiski Vserossiiskogo mineralogicheskogo obshchestva*. 1996. Vol. 125. N 2, p. 24-38 (in Russian).

25. Skublov S.G., Azimov P.Ya., Li X.-H. et al. Polymetamorphism of the Chupa шддшеу of the Belomorian Mobile Belt (Fennoscandia): Evidence from the Isotope-Geochemical (U-Pb, REE, O) Study of Zircon. *Geochemistry International*. 2017. Vol. 55. N 1, p. 47-59. DOI: 10.1134/S0016702917010098

26. Steiger R.H., Jäger E. Subcommission on geochronology: Convention on the use of decay constants in geo- and cosmochronology. *Earth and Planetary Science Letters*. 1977. Vol. 36. Iss. 3, p. 359-362. DOI: 10.1016/0012-821X(77)90060-7

27. Connolly J.A.D. Multivariable Phase Diagrams: An Algorithm Based on Generalized Thermodynamics. *American Journal of Science*. 1990. Vol. 290. Iss. 6, p. 666-718. DOI: 10.2475/ajs.290.6.666

28. Holland T.J.B., Powell R. An improved and extended internally consistent thermodynamic dataset for phases of petrological interest, involving a new equation of state for solids. *Journal of Metamorphic Geology*. 2011. Vol. 29. Iss. 3, p. 333-383. DOI: 10.1111/j.1525-1314.2010.00923.x

29. White R.W., Powell R., Holland T.J.B. et al. New mineral activity–composition relations for thermodynamic calculations in metapelitic systems. *Journal of Metamorphic Geology*. 2014. Vol. 32. Iss. 3, p. 261-286. DOI: 10.1111/jmg.12071

30. Pettijohn F.J., Potter P.E., Siever R. Sand and Sandstone. Springer-Verlag, 1972, p. 634.

31. Nesbitt H.W., Young G.M. Early Proterozoic climates and plate motions inferred from major element chemistry of lutites. *Nature*. 1982. Vol. 299. Iss. 5885, p. 715-717. DOI: 10.1038/299715a0

32. Yurchenko A.V., Baltybaev S.K., Volkova Yu.R., Malchushkin E.S. The Mineralogical Composition, Metamorphic Parameters, and Protoliths of Granulites from the Larba Block of the Dzhugdzhur–Stanovoy Fold Area. *Russian Journal of Pacific Geology*. 2024. Vol. 18. N 2, p. 130-149. DOI: 10.1134/S181971402402009X

33. Cox R., Lowe D.R., Cullers R.L. The influence of sediment recycling and basement composition on evolution of mudrock chemistry in the southwestern United States. *Geochimica et Cosmochimica Acta*. 1995. Vol. 59. Iss. 14, p. 2919-2940. DOI: 10.1016/0016-7037(95)00185-9

34. Yudovich Ya.E., Ketris M.P. Principles of lithogeochemistry. Saint-Petersburg: Nauka, 2000, p. 479 (in Russian).

35. Neelov A.N. Petrochemical classification of metamorphosed sedimentary and volcanic rocks. Leningrad: Nauka, 1980, p. 100 (in Russian).

36. Warr L.N. IMA–CNMNC approved mineral symbols. *Mineralogical Magazine*. 2021. Vol. 85. Iss. 3, p. 291-320. DOI: 10.1180/mgm.2021.43

37. Bibikova E., Skiöld T., Bogdanova S. et al. Titanite-rutile thermochronometry across the boundary between the Archaean Craton in Karelia and the Belomorian Mobile Belt, eastern Baltic Shield. *Precambrian Research*. 2001. Vol. 105. Iss. 2-4, p. 315-330. DOI: 10.1016/S0301-9268(00)00117-0

38. Daly J.S., Balagansky V.V., Timmerman M.J., Whitehouse M.J. The Lapland–Kola orogen: Palaeoproterozoic collision and accretion of the northern Fennoscandian lithosphere. European Lithosphere Dynamics. Geological Society of London, 2006. Vol. 32, p. 579-598. DOI: 10.1144/GSL.MEM.2006.032.01.35

39. Kozlovskii V.M., Travin V.V., Savatenkov V.M. et al. Thermobarometry of Paleoproterozoic Metamorphic Events in the Central Belomorian Mobile Belt, Northern Karelia, Russia. *Petrology*. 2020. Vol. 28. N 2, p. 183-206. DOI: 10.1134/S0869591120010038

40. Dokukina K.A., Konilov A.N., Bayanova T.B. et al. Metamorphosed Plagiogranite Veins In Salma Eclogites, Belomorian Eclogite Province. *Precambrian Research*. 2024. Vol. 400. N 107248. DOI: 10.1016/j.precamres.2023.107248

41. Bibikova E.V., Bogdanova S.V., Glebovitsky V.A. et al. Evolution of the Belomorian Belt: NORDSIM U-Pb Zircon Dating of the Chupa Paragneisses, Magmatism, and Metamorphic Stages. *Petrology*. 2004. Vol. 12. N 3, p. 195-210.

42. Balaganskii V.V. Main stages of tectonic development of the Northeastern Baltic Shield in the Paleoproterozoic: Avtoref. dis. … d-ra geol.-mineral. nauk. Saint Petersburg: Institut geologii i geokhronologii dokembriya RAN, 2002, p. 32 (in Russian).

43. Krylov D.P., Klimova E.V. Origin of carbonate-silicate rocks of the Porya Guba (the Lapland-Kolvitsa Granulite Belt) revealed by stable isotope analysis ($\delta^{18}O$, $\delta^{13}C$). *Journal of Mining Institute.* 2024. Vol. 265, p. 3-15.

44. Salimgaraeva L.I., Skublov S.G., Berezin A.V., Galankina O.L. Fahlbands of the Keret archipelago, White Sea: the composition of rocks and minerals, ore mineralization. *Journal of Mining Institute.* 2020. Vol. 245, p. 513-521. DOI: 10.31897/PMI.2020.5.2

45. Vrevsky A.B., Kuznetsov A.B., Lvov P.A. Age and Stratigraphic Position of a Supracrustal Complex (Kaskama Block, Inari Terrane, Northeastern Kola–Norwegian Region of the Fennoscandian Shield). *Doklady Earth Sciences.* 2023. Vol. 511. Part 2, p. 645-651. DOI: 10.1134/S1028334X23600950

46. Nitkina E.A., Belyaev O.A., Dolivo-Dobrovolskii D.V. et al. Metamorphism of the Korvatundra Structure of the Lapland – Kola Orogen (Arctic Zone of the Fennoscandian Shield). *Russian Geology and Geophysics.* 2022. Vol. 63. N 4, p. 503-518. DOI: 10.2113/RGG20214404

47. Kolodiazhnyi S.Yu. Paleoproterozoic structural-kinematic evolution of the South-East Baltic Shield. Moscow: GEOS, 2006, p. 332 (in Russian).

***Authors*: Anastasiya V. Yurchenko,** *Candidate of Geological and Mineralogical Sciences, Researcher* (*Institute of Precambrian Geology and Geochronology RAS, Saint Petersburg, Russia*), *yurchenko-nastya@yandex.ru*, *https://orcid.org/0000-0002-3999-5151*, **Shauket K. Baltybaev,** *Doctor of Geological and Mineralogical Sciences, Chief Researcher* (*Institute of Precambrian Geology and Geochronology RAS, Saint Petersburg, Russia*), *Professor* (*Saint Petersburg State University, Institute of Earth Sciences, Saint Petersburg, Russia*), *https://orcid.org/0000-0002-6484-2042*, **Tatyana A. Myskova,** *Candidate of Geological and Mineralogical Sciences, Senior Researcher* (*Institute of Precambrian Geology and Geochronology RAS, Saint Petersburg, Russia*), *https://orcid.org/0000-0001-6911-7694*.

The authors declare no conflict of interests.

ISSN 2411-3336; e-ISSN 2541-9404

JOURNAL OF MINING INSTITUTE

Zapiski Gornogo instituta

Journal homepage: pmi.spmi.ru

Research article *Geology*

Prospects for rare earth element mineralization in the weathering crusts developed on granite-gneisses of the Souktal Plutonic Complex (Northern Kazakhstan)

Medet A. Junussov[1], **Kamal R. Regmi**[1], **Ekaterina V. Klimova**[2]✉, **Aleksandr V. Reznik**[3]
[1] *Nazarbayev University, Astana, Kazakhstan*
[2] *Institute of Precambrian Geology and Geochronology RAS, Saint Petersburg, Russia*
[3] *N.A.Chinakal Institute of Mining Siberian Branch RAS, Novosibirsk, Russia*

How to cite this article: Junussov M.A., Regmi K.R., Klimova E.V., Reznik A.V. Prospects for rare earth element mineralization in the weathering crusts developed on granite-gneisses of the Souktal Plutonic Complex (Northern Kazakhstan). Journal of Mining Institute. 2026. Vol. 277, p. 45-54.

Abstract

This study investigates unique weathering crust samples from the most altered sections (30-43 m) of the weathering profile within the Souktal Plutonic Complex, Northern Kazakhstan. The samples, obtained from two drill cores, consist of quartz, kaolinite, microcline, muscovite, and plagioclase, as identified through polarized light microscopy and confirmed by X-ray diffraction analysis. Sequential extraction of rare earth elements (REE) was performed using inductively coupled plasma mass spectrometry (ICP-MS) following a two-step leaching procedure with hydroxylamine hydrochloride (0.2 mol $NH_2OH{\cdot}HCl$) and sodium hydroxide (1 mol NaOH) solutions. The extraction process effectively recovered REE, indicating their presence in an ion-exchangeable form, with total extraction rates (REE + Sc + Y) ranging from 4.1 to 7.8 ppm. The total light REE content varies from 3.5 to 5.9 ppm, while heavy REE content ranges from 0.2 to 0.7 ppm across all samples. Petrological and geochemical analyses suggest that the studied area represents an ion-adsorption-type REE weathered deposit. These findings enhance the understanding of ionic-adsorbed REE within weathering crusts and highlight the effectiveness of sequential extraction methods for REE determination. Moreover, the study suggests that this area holds promising potential as a future REE ion-adsorption site, contributing to the development of Kazakhstan's national REE industry.

Keywords

rare earth elements; weathering crust; REE deposits; Souktal; Kazakhstan

Funding

The work was performed within the framework of topic 064.01.00 (SPG) of Nazarbayev University and the research topic of the IPGG RAS FMUW 2025-0003 (FMUW 2022-0004).

Received: 09.12.2024 ***Accepted: 02.07.2025*** ***Online: 25.11.2025*** ***Published: 27.02.2026***

Introduction

The interest in rare earth elements (REE) has been steadily increasing due to their crucial role in various industries, including electronics, aviation, automotive manufacturing, energy production, and many others. Despite their occurrence in various minerals, the average concentration of REE in the Earth's crust is relatively low, and the number of known REE deposits remains limited [1, 2]. Rare earth elements play a vital role in modern industry and have significant potential for advancing new technologies and innovations. Hence, there is a growing emphasis on identifying sources of REE and improving their extraction and processing methods. REE play a crucial role in deciphering the genesis of various geological processes, including those at the mineral scale [3-5]. Recent studies have demonstrated that trace elements can be highly sensitive indicators of rare-metal mineralization [6, 7]. Thus, studying the distribution of rare and rare earth elements provides valuable data for identifying mineral deposits and analyzing their genesis. This method is applicable to both scientific research and practical applications in geosciences, including mineral exploration and extraction [8]. The primary sources of REE include minerals such as bastnasite, monazite, loparite, xenotime, and ion-adsorption clays [9].

Weathering processes lead to the leaching of REE from minerals, followed by their adsorption, resulting in the formation of ion-adsorption-type weathering crusts [10]. These deposits are widely distributed in Southern China and represent one of the world's main sources of heavy rare earth elements (HREE) [11]. In addition to REE fractionation through the dissolution of REE-bearing minerals [12] other mechanisms of deposit formation include complexation with organic and inorganic ligands [13], mineral adsorption [14], surface precipitation [15], and redox reactions [16]. These characteristics make REE valuable indicators for studying the geochemical properties of rocks. Global REE reserves are estimated at approximately 120 million t, with the majority located in China, Brazil, Russia, India, and Australia. The most productive REE deposits are associated with carbonatites, alkaline rocks, and weathering crusts [17, 18].

Significant advancements in REE separation have been achieved through ion exchange [19, 20] and extraction methods [21]. Sequential chemical leaching or extraction is a highly effective technique for studying REE behavior [22, 23], widely applied in fractionating these elements in soils and sediments [24, 25].

Kazakhstan holds significant potential for REE deposit discoveries due to its substantial unexplored resources. The country has registered 384 deposits across 160 sites, including carbonatite, alkaline, magmatic, metamorphic, metasomatic, sedimentary, and weathering crust-type deposits [26]. One of the poorly studied weathering crust deposits is Souktal, located in the northern part of the country. Therefore, determining REE concentrations in the weathering crust over the Souktal granitic-gneisses using a two-stage sequential chemical extraction method is a relevant research objective.

Geological settings

The study area is located along the southeastern boundary of the Kostanay Region in Northern Kazakhstan. It lies within a tectonomagmatically reactivated zone at the junction of a regional submeridional compression zone and deep-seated fault structures of both sublatitudinal and submeridional orientations. These structures have contributed to the development of quartz-feldspar metasomatism with rare-metal (Sn, W, Be, Ta, Nb, etc.) and the formation of linear weathering crusts. Proterozoic granitic gneisses (γ_2 PR_2) represent the oldest rocks of the Souktal Massif. The massif's granitoids exhibit diverse compositions, though coarse-grained granitic gneisses predominate. These gneisses are encircled by a halo of banded microcline gneisses [27]. Proterozoic formations (PR) form the core of the Mesozoic Ulytau Anticline, where the exhumation and weathering of the Souktal granitic-gneiss complex have occurred [27]. The weathering crust over the granitic gneisses varies in thickness from 23 to 85 m [27]. The region also contains Lower to Middle Proterozoic ($PR_{1\text{-}2}$) green schists and tuffs, with the total Proterozoic sequence reaching 5400-5700 m in thickness. The Proterozoic and Palaeozoic formations comprise the folded basement, while Mesozoic and Cenozoic unconsolidated deposits form the platform cover. Palaeozoic strata are relatively scarce. Devonian terrigenous sequences consist of red-coloured arkose sandstones, siltstones, coarse-grained sandstones, and conglomerates, with the upper portion characterized by interbedded fine-grained red sandstones, siltstones, and pinkish-gray calcareous sandstones (total thickness – 150 m). The Devonian strata exhibit a sharp angular unconformity with Palaeozoic mafic intrusions (gabbro) and Proterozoic schists [27].

The weathering profile is divided into four distinct zones: granitic-gneiss zone – characterized by fractures filled with manganese oxides and iron hydroxides; kaolinite-montmorillonite zone – composed of variegated clays, predominantly light green, greenish-light gray, gray, and black;

reddish-gray kaolinite zone – consists of kaolinite, quartz, iron, and hydroxides; white kaolinite zone – primarily composed of kaolinite and quartz. Supergene formations are overlain by Cenozoic and Quaternary deposits. The sedimentary cover mainly consists of sands, loams, silts, and aeolian and alluvial deposits, reaching a thickness of up to 70 m [27].

Sampling and analytical methods

Sampling was conducted from two boreholes, labeled C-15 (N49°31'32.82"-E66°38'18.72") and C-18 (N49°31'32.84"-E66°38'24.30"), due to the lack of surface exposures. Borehole C-15 reached a depth of 43 m, while borehole C-18 extended to 30 m. Each collected sample weighed approximately 1 kg.

The mineral composition of the weathering crust was determined using a transmitted light microscope (Zeiss Primotech), for preliminary optical diagnostics and subsequently determined using X-ray diffraction (XRD). X-ray diffraction (XRD) analysis was performed using a Rigaku Smart Lab instrument with a CuKα X-ray source for samples at 30 kV X-ray tube voltage, 15 mA current, with a fixed slit system, a scanning range of 3 to 90°, a minimum step of 0.020 and a scanning speed of 2 rpm. Samples of the weathering crust from boreholes were carefully crushed, pulverized, and homogenized in a laboratory ball mill (Retsch, TM 300 DrumMill) at 80 rpm for 10-20 min, and then sieved using a sieve shaker (Retsch, AS 300 Control) to obtain powders with a particle size of 74 μm. 25 g of distilled water was added to 10 g of each sample, and the mixtures were left in sealed graduated cylinders at room temperature for two days to reach equilibrium. The pH of the resulting solutions was measured with a pH meter (ISOLAB). Subsequently, the samples were dried in an oven at 60 °C and ground in an agate mortar.

The two-step sequential leaching of REE in the samples was performed following the methods described in references [28, 29] as outlined:

1. A 10 ml solution of NH_2 OH·HCl (0.2 mol, pH = 5.0) was added to 1 g of powdered samples (74 μm) [30, 31] and shaken for 3 h. The suspension was then heated in a water bath at 95 °C for 4 h while being continuously mixed with a magnetic stirrer at 250 rpm. After centrifugation and filtration, the supernatant was collected.

2. The residue was transferred into a glass beaker, and 10 ml of 1 mol NaOH was added. The mixture was then stirred at 350 rpm using a heating magnetic stirrer while being heated in a water bath at 75 °C for 1 h.

The liquid extracts from both steps were further analyzed for REE concentrations using inductively coupled plasma mass spectrometry (ICP-MS). The concentrations of REE were determined using a single quadrupole-based ICP-MS (Thermo Fisher Scientific iCAP RQ). The calibration standard IV-STOCK-26-125ML was used to construct calibration curves and evaluate the reliability of the obtained results. The detection limits for all elements were calculated based on the calibration curves and were less than 0.0005 μg/l.

All analytical studies were conducted at Nazarbayev University (Astana, Kazakhstan).

Results

Mineral composition of rocks. In hand specimens, the sample C-15 occurs as a slightly sticky reddish-brown, while the sample C-18 is yellowish brown, light and brittle. Both specimens are highly weathered granitic gneisses. The petrographic study revealed that they are composed of muscovite, K-feldspar, quartz, plagioclase, kaolinite, and Fe hydroxides (Fig.1). However, XRD patterns confirmed the presence of K-feldspar, quartz, plagioclase with minor muscovite and kaolinite but Fe hydroxides was never detected in XRD spectra (Fig.2). The average mineral contents show that the sample C-15 has, vol.%: 42.7 quartz, 54.3 kaolinite; and 3 hydroxides Fe; while sample C-18 has, vol.%: 47.8 quartz, 35 kaolinite, 8.3 K-feldspar, 5.4 muscovite, 3.5 plagioclase, and a small amount of amorphous materials.

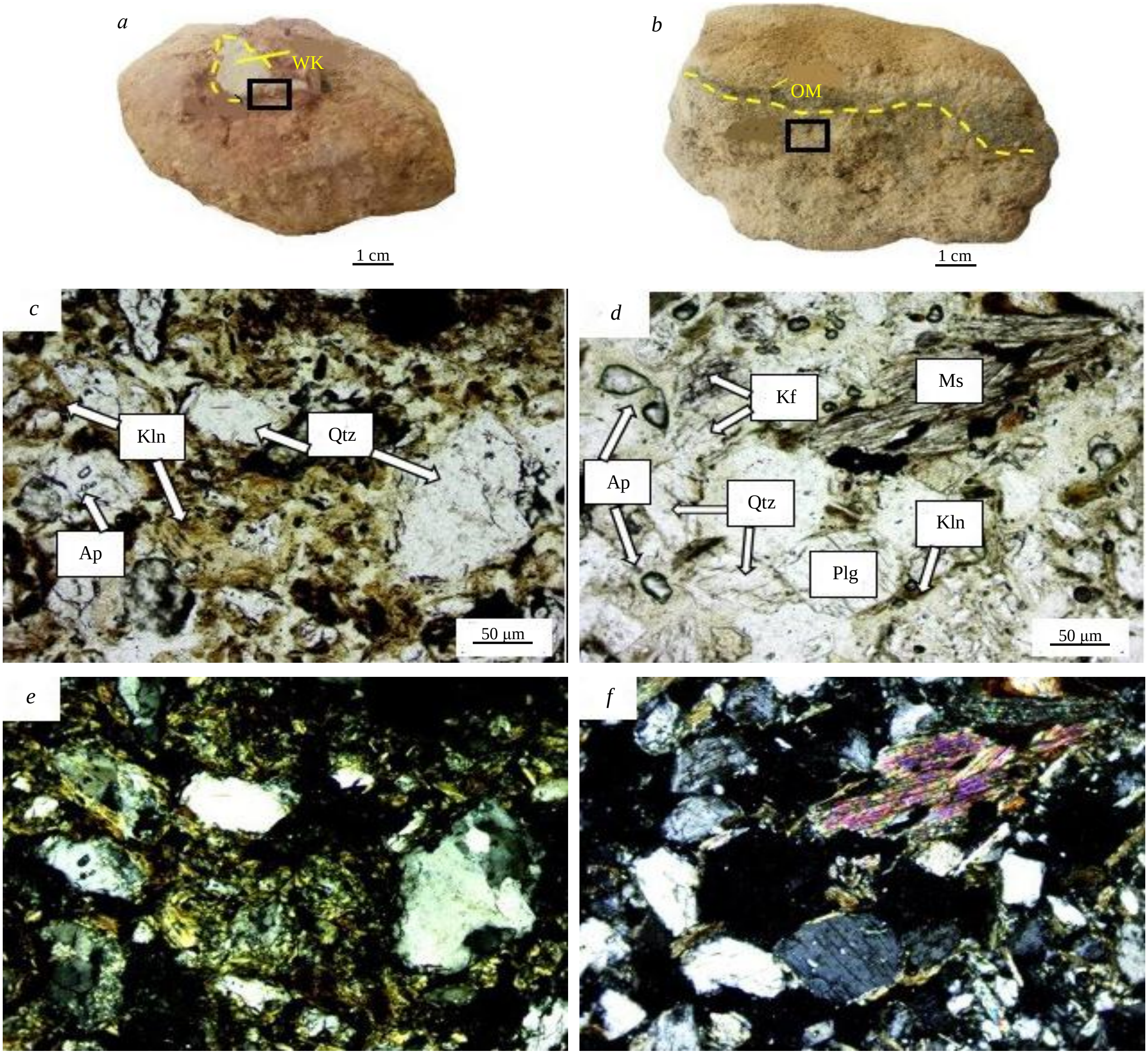

Fig.1. Weathering crust fragments, sample C-15 – note-white kaolinite (WK) fragments in reddish brown fragile clay (*a*); sample C-18 – yellowish-grey fragile clay interbedded with organic matter (OM) (*b*); micrographs without analyzer (*c*, *d*); with analyzer (*e*, *f*); quartz grains cemented by kaolinite with iron hydroxide (*c*, *e*); grains of quartz, feldspar, apatite, kaolinite and muscovite (*d*, *f*). Mineral abbreviations after R.Kretz [32]

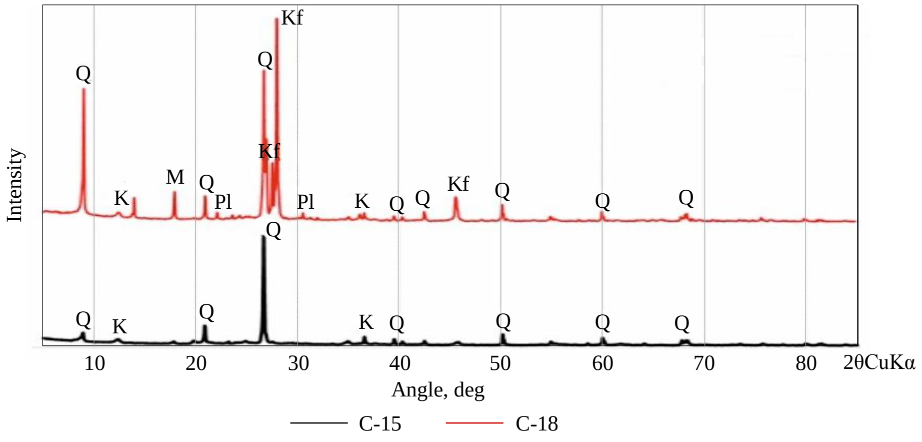

Fig.2. X-ray diffraction (XRD) spectra of the samples:
M – muscovite; Kf – K-feldspar; Q – quartz; K – kaolinite; Pl – plagioclase

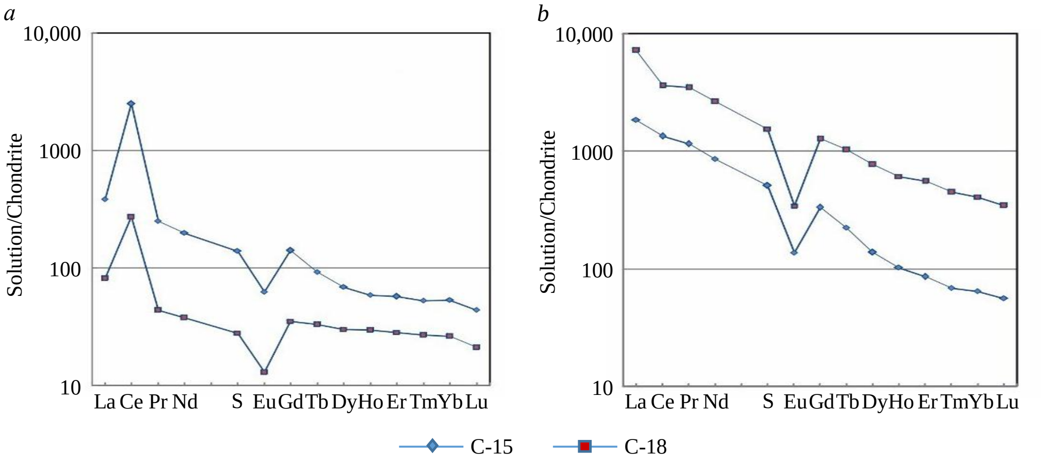

Fig.3. Distribution of REE in experimental solutions at the first stage of leaching (*a*); at the second stage of leaching (*b*)

Sequential experimental leaching. All REE, including Y and Sc, with the exception of Pm, were successfully extracted in the sequential leaching process (Fig.3).

In the first step of the leaching, Ce, La, Nd, Y, Sc, Gd and Sm were extracted in relatively high amounts, while Eu, Tb, Dy, Ho, Er, Yb, and Tm were in much smaller quantities from the sample C-15 (see Table). On the other hand, sample C-18 released comparatively low amounts.

REE concentrations in the extracted solutions (ICP-MS)

Element	Sample C-15		Sample C-18	
	1st step $NH_2OH{\cdot}HCl$, ppb	2nd step NaOH, ppb	1st step $NH_2OH{\cdot}HCl$, ppb	2nd step NaOH, ppb
Sc	26.71	98.11	Below the detection limit	146.32
Y	59.16	116.88	38.32	1072.88
La	90.27	435.86	19.16	1692.78
Ce	1513.07	815.03	165.15	2214.96
Pr	23.08	106.18	4.04	320.80
Nd	90.50	391.20	17.22	1195.81
Sm	20.64	75.11	4.13	227.78
Eu	3.51	7.72	0.72	19.31
Gd	27.88	65.88	7.02	251.70
Tb	3.32	8.07	1.19	37.05
Dy	16.89	33.81	7.40	188.67
Ho	3.21	5.59	1.61	33.33
Er	9.09	13.67	4.53	88.54
Tm	1.30	1.69	0.66	11.04
Yb	8.55	10.42	4.20	65.73
Lu	1.07	1.38	0.52	8.48
ΣРЗЭ	1812	1971	237	6351
La/Yb	10.55	41.83	4.56	25.76
Ce/Ce*	2.83	0.96	2.13	0.85
Σ sample, ppm	1.8	2.3	0.2	6.3
Total Σ REE, ppm	4.1		6.5	
ΣРЗЭ + Sc + Y	4.1		7.8	

In the second leaching step (remnant of REE from the 1st step of extraction), the high concentration of Ce, La, Nd, Y, Pr, Sc, and Lu was leached in sample C-15; while sample C-18 liberated even higher quantity (see Table).

The most abundant extracted element is Ce in the 1st step leaching, followed by Nd and La, in C-15 whereas in C-18 the order is Ce > Y > La. In the 2nd step of leaching, the extracted amount is Ce > La > Nd > Y in both samples (see Table). Ce has the highest extracted values while Tm has the lowest.

The results of laboratory experiments showed that the obtained solutions are characterized by elevated values of light rare earth elements (LREE) relative to HREE. The La/Yb ratio in the experimental solutions at the first leaching stage was 10.5 and 4.6 in samples C-15 and C-18, respectively. The La/Yb ratio in C-15 and C-18 at the second leaching stage is higher, at 41.8 and 25.8. The total extraction of REE, including Sc and Y, during the two-stage sequential leaching was 4.1 ppm from sample C-15 and 7.8 ppm from sample C-18 (see Table).

The experimental solutions from the first leaching stage showed maximum Ce-anomaly values of 2.83 in the sample from borehole C-15 and 2.13 in the sample from borehole C-18. The minimum Ce/Ce* values were obtained at the second leaching stage – 0.96 and 0.85 from the samples of boreholes C-15 and C-18, respectively (see Table).

The results of laboratory experiments showed a negative Eu-anomaly at two stages of the experiment (Fig.3).

The pH measurements indicate a higher value of 5.03 in C-18 and a lower value of 4.85 in C-15.

Discussion

Origin of REE in ion-adsorption form in the weathering crust of granite-gneisses. The weathered granitic gneiss from the Souktal Plutonic Complex is characterized as a clay-rich REE deposit, where feldspars undergo kaolinization due to crustal weathering and deposition from detrital sedimentary rocks. Quartz, the most stable mineral, is present in all weathering crust zones. It is often leached, angular, and contains traces of mica with clay aggregates adhering to its surface, and occasionally has inclusions of black, iron-rich minerals [27]. Feldspars and platy-angular fragments of light and greenish micas are predominantly found in clay-mica zones, with feldspars being replaced by kaolinite. The minerals are frequently impregnated with iron and manganese hydroxides [27]. In both samples, kaolinite is closely associated with Fe hydroxides (see Fig.1). However, Fe hydroxides were not detected in the XRD spectra due to their amorphous or poorly crystalline state [33]. The results of the studies showed that the main minerals concentrating REE in the weathering crust are kaolinite, micas, iron hydroxides, feldspars, and apatite. Our results show that the REE in the Souktal are of a typical ion-adsorption origin. Ion-adsorption-type REE deposits refer to the phenomenon where REE bind to clay minerals and sediment particles through electrostatic attraction in their ionic form [34]. This type of deposit was first discovered in China (in 1969), in the weathered granitic crust in Longnan, Jiangxi Province [35, 36]. Later, similar deposits were subsequently found in other places. Several authors have attributed the formation of these deposits to the enrichment of REE through the weathering of magmatic parent rocks. The content of clay minerals in the weathering crusts of deposits ranges from 40 to 70 %, and the content of ion-exchangeable REE in samples typically ranges from 50 to 70 % [37-39].

REE-bearing minerals in rocks can be broadly classified into two categories: REE-bearing accessory and ore minerals (including silicates such as zircon, allanite, titanite, and garnet; phosphates such as xenotime, apatite, and monazite; fluoro-carbonates such as bastnasite, synchysite, and parisite; as well as niobates, tantalates, and fluorite) and rock-forming minerals (such as feldspar, quartz, muscovite, biotite, and amphibole, and others) [40-42]. Approximately 78 % of REE originate from the decomposition of REE-bearing minerals, while the breakdown of rock-forming minerals contributes around 22 % [12, 24]. The increase in REE concentrations is primarily driven by the decomposition of accessory minerals and the extent of mineral weathering within the weathering profile [24, 40]. In the weathering crust deposits of Northern Kazakhstan, cerium-group REE generally dominate over yttrium-group REE [43]. Although REE are relatively widespread, their distribution is highly uneven along both the strike and dip within the weathering profile [27]. In the weathering crust of the Souktal Massif, the primary REE- and Y-bearing minerals are kaolinite, muscovite, and, to a lesser extent, plagioclase [25].

Additionally, clay minerals act as indicators of the degree of rock weathering, with fully weathered layers primarily characterized by the transformation of feldspar into kaolinite [24, 44]. Within the weathering profile, as rock transitions to clay, REE are initially leached from the parent material and, with increasing pH, become adsorbed in the most intensely weathered horizons. The total extracted REE content is 6.5 ppm in sample C-18, whereas it is lower in sample C-15, at 4.1 ppm. These findings may help identify more enriched weathering crust zones within the study area.

The reliability of selected reagents for leaching. Primary REE-bearing minerals break down during weathering, thus releasing soluble REE ions [45]. These ions interact mainly with clay minerals and other sediments, forming ion-exchangeable complexes that can be easily leached or extracted [38, 39]. To enhance the efficiency of REE extraction, extensive research has been conducted on the extraction processes of REE from weathering crusts, which have formed because of leaching from parent rocks [46]. The extraction of REE ions adsorbed on clay minerals can be desorbed through ion exchange by cations, including Na^+, Ca^{2+}, and NH_4 [20, 38, 47]. The results of two-stage leaching experiments on weathering crust samples from the granitic-gneisses of the Souktal Plutonic Complex in Northern Kazakhstan demonstrated successful REE extraction using $NH_2OH \cdot HCl$ and NaOH. Therefore, the leaching procedure with these reagents is a reliable method for extracting ion-exchangeable REE.

Distribution characteristics of REE. The LREE (La, Ce, Pr, Nd, Sm, Eu, and Sc) are released at a rate five times higher than the HREE (Y, Tb, Dy, Ho, Er, Tm, Yb, Lu, and Gd) in both of the samples. A similar LREE-enriched mineral deposit has been observed in the granite porphyry of the Jiangxi Region, China [48]. A key indicator of chemical weathering is the enrichment of REE in the weathering crust relative to the parent substrate [49]. In weathering crusts formed on granitoid protoliths, HREE are generally more enriched [50]. However, this study demonstrates that LREE dominate in solution after leaching, with La/Yb ratios of 10.5 and 4.6 in samples C-15 and C-18, respectively, during the first leaching stage, and increasing to 41.8 and 25.8 in samples C-15 and C-18 in the second leaching stage (see Table). Research conducted at the Institute of Precambrian Geology and Geochronology of the RAS confirms the preferential removal of LREE from the weathering profile during the leaching of Precambrian granitoids from the Fennoscandian Shield. Furthermore, the study revealed that when weakly acidic sulfuric acid interacts with Paleoproterozoic granitic gneisses of the Fennoscandian Shield, progressive LREE enrichment relative to HREE occurs with increasing interaction time [51]. Similar findings have been reported in previous studies on the selective leaching of REE from marine sediments using hydrochloric acid [52].

Among REE, europium can exist in multiple oxidation states. A negative Eu-anomaly (Fig.3) is characteristic of highly weathered rocks, where Eu^{3+} is leached under oxidizing conditions [52].

Cerium can exist as Ce^{3+} and Ce^{4+} under supergene conditions. The presence of Ce in both forms within modern natural aquatic systems is evident, as indicated by a negative Ce-anomaly in oxygenated waters. In contrast, anoxic waters exhibit a positive Ce-anomaly, indicating Ce enrichment relative to La and Nd (including Pd). Since the pH of oceanic water remains relatively stable and can be measured or calculated, the partial oxygen pressure can be determined based on Ce content. However, in the drainage solutions of the supergene zone, pH values are more variable and fluctuate across different stages of continental weathering [51, 52]. Numerous factors influence Ce behaviour [13, 53, 54], with pH-Eh conditions being the primary controls on Ce partitioning between solid and liquid phases [55]. Another key factor affecting Ce behaviour is the intensity of drainage within the weathering profile [52]. Our results indicate that the Ce-anomaly is positive during the first leaching stage but becomes negative in the second stage, likely due to variations in pH conditions. Additionally, Ce exhibits a relatively high concentration among REE (Fig.3). During the first leaching stage, a positive Ce-anomaly is observed, whereas the second, alkaline leaching stage results in a negative Ce-anomaly. Petrographic studies reveal that Fe hydroxides are closely associated with kaolinite (see Fig.1). Previous research [45, 56, 57] has shown that Fe hydroxides play a critical role in forming positive Ce-anomalies across various geological settings. These Fe hydroxides account for approximately 95 % of the total Ce content, as Fe oxides can adsorb REE and are typically associated with clay minerals [50, 52]. Studies on REE sorption and co-precipitation onto Fe hydroxides have demonstrated a positive Ce-anomaly in solutions due to its oxidation in the solid phase [50]. These findings align with our data, which show positive Ce-anomalies (Ce/Ce* = 2.83 and 2.13) during the first leaching stage.

Conclusion

Petrographic and geochemical analyses suggest that the weathering profile of the Souktal Massif holds significant potential for further REE exploration. The findings confirm that the deposit belongs to the ion-adsorption type of REE deposits formed in the weathering crust of granitic-gneisses. Sequential leaching effectively extracted REE, with total recovery of REE + Sc + Y ranging from 4.1 to 7.8 ppm. The total content of LREE varies from 3.5 to 5.9 ppm, while HREE range from 0.2 to 0.7 ppm. The observed positive Ce-anomaly in the weathering profile is attributed to the association of kaolinite with Fe hydroxides. Based on these results, further investigations are recommended to a depth of approximately 100 m.

These findings not only enhance our understanding of geological processes in the formation of ion-adsorption deposits but also hold practical significance for the industrial development of REE resources in the region.

Authors extend gratitude to the School of Mining and Geosciences and Core Facilities at Nazarbayev University for providing the necessary resources to conduct this analytical work. We sincerely appreciate the assistance of D.Bralina, Ye.Satay, and K.Gudun in sample preparation and chemical reagent preparation. Special thanks to E.Sugurbekov for his support in the X-ray laboratory during analysis; to K.Akhmetova and A.Beldeubayev for their assistance in measuring REE in the ICP-MS laboratory. Lastly, the authors thank an industrial company for generously providing samples and field data.

REFERENCES

1. Binnemans K., Jones P.T. Rare Earths and the Balance Problem. *Journal of Sustainable Metallurgy*. 2015. Vol. 1. Iss. 1, p. 29-38. DOI: 10.1007/s40831-014-0005-1
2. Takeda O., Okabe T.H. Current Status on Resource and Recycling Technology for Rare Earths. *Metallurgical and Materials Transactions E*. 2014. Vol. 1. Iss. 2, p. 160-173. DOI: 10.1007/s40553-014-0016-7
3. Rogova I.V., Stativko V.S., Petrov D.A., Skublov S.G. Trace Element Composition of Zircons from Rapakivi Granites of the Gubanov Intrusion, the Wiborg Massif, as a Reflection of the Fluid Saturation of the Melt. *Geochemistry International*. 2024. Vol. 62. N 11, p. 1123-1136. DOI: 10.1134/S0016702924700630
4. Skublov S.G., Petrov D.A., Galankina O.L. et al. Th-Rich Zircon from a Pegmatite Vein Hosted in the Wiborg Rapakivi Granite Massif. *Geosciences*. 2023. Vol. 13. Iss. 12. N 362. DOI: 10.3390/geosciences13120362
5. Salimgaraeva L., Berezin A., Sergeev S. et al. Zircons from Eclogite-Associated Rocks of the Marun–Keu Complex, the Polar Urals: Trace Elements and U–Pb Dating. *Geosciences*. 2024. Vol. 14. Iss. 8. N 206. DOI: 10.3390/geosciences14080206

6. Skublov S.G., Hamdard N., Ivanov M.A., Stativko V.S. Trace element zoning of colorless beryl from spodumene pegmatites of Pashki deposit (Nuristan province, Afghanistan). *Frontiers in Earth Science*. 2024. Vol. 12. N 1432222. DOI: 10.3389/feart.2024.1432222

7. Levashova E.V., Skublov S.G., Hamdard N. et al. Geochemistry of Zircon from Pegmatite-bearing Leucogranites of the Laghman Complex, Nuristan Province, Afghanistan. *Russian Journal of Earth Sciences*. 2024. Vol. 2. Iss. 2. N ES2011 (in Russian). DOI: 10.2205/2024ES000916

8. Evdokimov A.N., Pharoe B.L. Indicator role of rare and rare-earth elements of the Northwest manganese ore occurrence (South Africa) in the genetic model of supergene manganese deposits. *Journal of Mining Institute*. 2021. Vol. 252, p. 814-825. DOI: 10.31897/PMI.2021.6.4

9. Shijie Wang. Rare Earth Metals: Resourcefulness and Recovery. *JOM*. 2013. Vol. 65. Iss. 10, p. 1317-1320. DOI: 10.1007/s11837-013-0732-y

10. Yan Hei Martin Li, Wen Winston Zhao, Mei-Fu Zhou. Nature of parent rocks, mineralization styles and ore genesis of regolith-hosted REE deposits in South China: An integrated genetic model. *Journal of Asian Earth Sciences*. 2017. Vol. 148, p. 65-95. DOI: 10.1016/j.jseaes.2017.08.004

11. Zhiwei Bao, Zhenhua Zhao. Geochemistry of mineralization with exchangeable REY in the weathering crusts of granitic rocks in South China. *Ore Geology Reviews*. 2008. Vol. 33. Iss. 3-4, p. 519-535. DOI: 10.1016/j.oregeorev.2007.03.005

12. Bosia C., Chabaux F., Pelt E. et al. U–Th–Ra variations in Himalayan river sediments (Gandak river, India): Weathering fractionation and/or grain-size sorting? *Geochimica et Cosmochimica Acta*. 2016. Vol. 193, p. 176-196. DOI: 10.1016/j.gca.2016.08.026

13. Davranche M., Pourret O., Gruau G., Dia A. Impact of humate complexation on the adsorption of REE onto Fe oxyhydroxide. *Journal of Colloid and Interface Science*. 2004. Vol. 277. Iss. 2, p. 271-279. DOI: 10.1016/j.jcis.2004.04.007

14. Piasecki W., Sverjensky D.A. Speciation of adsorbed yttrium and rare earth elements on oxide surfaces. *Geochimica et Cosmochimica Acta*. 2008. Vol. 72. Iss. 16, p. 3964-3979. DOI: 10.1016/j.gca.2008.05.049

15. Dardenne K., Schäfer T., Lindqvist-Reis P. et al. Low Temperature XAFS Investigation on the Lutetium Binding Changes during the 2-Line Ferrihydrite Alteration Process. *Environmental Science & Technology*. 2002. Vol. 36. Iss. 23, p. 5092-5099. DOI: 10.1021/es025513f

16. Bau M., Koschinsky A. Oxidative scavenging of cerium on hydrous Fe oxide: Evidence from the distribution of rare earth elements and yttrium between Fe oxides and Mn oxides in hydrogenetic ferromanganese crusts. *Geochemical Journal*. 2009. Vol. 43. Iss. 1, p. 37-47. DOI: 10.2343/geochemj.1.0005

17. Tkachev A.V., Rundqvist D.V., Vishnevskaya N.A. Main Features of the REE Metallogeny through Geological Time. *Geology of Ore Deposits*. 2022. Vol. 64. N 3, p. 41-77. DOI: 10.1134/S1075701522030060

18. Yufeng Huang, Hongping He, Xiaoliang Liang et al. Characteristics and genesis of ion adsorption type REE deposits in the weathering crusts of metamorphic rocks in Ningdu, Ganzhou, China. *Ore Geology Reviews*. 2021. Vol. 135. N 104173. DOI: 10.1016/j.oregeorev.2021.104173

19. Spedding F.H., Voigt A.F., Gladrow E.M, Sleight N.R. The Separation of Rare Earths by Ion Exchange. I. Cerium and Yttrium. *Journal of the American Chemical Society*. 1947. Vol. 69. Iss. 11, p. 2777-2781. DOI: 10.1021/ja01203a058

20. Spedding F.H., Voigt A.F., Gladrow E.M. et al. The Separation of Rare Earths by Ion Exchange. II. Neodymium and Praseodymium. *Journal of the American Chemical Society*. 1947. Vol. 69. Iss. 11, p. 2786-2792. DOI: 10.1021/ja01203a060

21. Zimina G.V., Nikolaeva I.I., Tauk M.V., Tsygankova M.V. Extraction schemes of rare-earth metals' separation. *Tsvetnye metally*. 2015. N 4, p. 23-27 (in Russian). DOI: 10.17580/tsm.2015.04.04

22. Land M., Öhlander B., Ingri J., Thunberg J. Solid speciation and fractionation of rare earth elements in a spodosol profile from northern Sweden as revealed by sequential extraction. *Chemical Geology*. 1999. Vol. 160. Iss. 1-2, p. 121-138. DOI: 10.1016/S0009-2541(99)00064-9

23. Estrade G., Marquis E., Smith M. et al. REE concentration processes in ion adsorption deposits: Evidence from the Ambohimirahavavy alkaline complex in Madagascar. *Ore Geology Reviews*. 2019. Vol. 112. N 103027. DOI: 10.1016/j.oregeorev.2019.103027

24. Denys A., Janots E., Auzende A.-L. et al. Evaluation of selectivity of sequential extraction procedure applied to REE speciation in laterite. *Chemical Geology*. 2021. Vol. 559. N 119954. DOI: 10.1016/j.chemgeo.2020.119954

25. Zhenxiao Wu, Yu Chen, Yang Wang et al. Review of rare earth element (REE) adsorption on and desorption from clay minerals: Application to formation and mining of ion-adsorption REE deposits. *Ore Geology Reviews*. 2023. Vol. 157. N 105446. DOI: 10.1016/j.oregeorev.2023.105446

26. Mihalasky M.J., Tucker R.D., Renaud K., Verstraeten I.M. Rare earth element and rare metal inventory of central Asia: Fact Sheet 2017–3089. U.S. Department of the Interior, U.S. Geological Survey, 2018, p. 4. DOI: 10.3133/fs20173089

27. Isayeva L.D., Dyussembayeva K.Sh., Kembayev M.K., Yusupova U. Rare earth elements and their forms of occurrence in the weathering crust of ore talayryk (the North Kazakhstan). *News of the National Academy of Sciences of the Republic of Kazakhstan. Series of geology and technical sciences*. 2015. Vol. 6. N 414, p. 57-65 (in Russian).

28. Setiawan I. The sequential REE (Rare Earth Elements) extraction of weathered crusts of granitoids from Sibolga, Indonesia. *IOP Conference Series: Earth and Environmental Science*. 2021. Vol. 882. N 012020. DOI: 10.1088/1755-1315/882/1/012020

29. Junussov M., Mádai F., Földessy J., Hámor-Vidó M. The Role of Organic Matter in Gold Occurrence: Insights from Western Mecsek Uranium Ore Deposit. *Economic and Environmental Geology*. 2024. Vol. 57. Iss. 4, p. 371-386. DOI: 10.9719/EEG.2024.57.4.371

30. Junussov M., Mustapayeva S. Preliminary XRF Analysis of Coal Ash from Jurassic and Carboniferous Coals at Five Kazakh Mines: Industrial and Environmental Comparisons. *Applied Sciences*. 2024. Vol. 14. Iss. 22. N 10586. DOI: 10.3390/app142210586

31. Junussov M., Madai F., Kristály F. et al. Preliminary analysis on roles of metal–organic compounds in the formation of invisible gold. *Acta Geochimica*. 2021. Vol. 40. Iss. 6, p. 1050-1072. DOI: 10.1007/s11631-021-00494-y

32. Kretz R. Symbols for rock-forming minerals. *American Mineralogist*. 1983. Vol. 68. N 1-2, p. 277-279.

33. Shi-Yong Wei, Fan Liu, Xiong-Han Feng et al. Formation and Transformation of Iron Oxide–Kaolinite Associations in the Presence of Iron(II). *Soil Science Society of America Journal*. 2011. Vol. 75. Iss. 1, p. 45-55. DOI: 10.2136/sssaj2010.0175

34. Sababa E., Essomba Owona L.G., Temga J.P., Ndjigui P.-D. Petrology of weathering materials developed on granites in Biou area, North-Cameroon: implication for rare-earth elements (REE) exploration in semi-arid regions. *Heliyon*. 2021. Vol. 7. Iss. 12. N e08581. DOI: 10.1016/j.heliyon.2021.e08581

35. Deng-hong Wang, Zhi Zhao, Yang Yu et al. Exploration and research progress on ion-adsorption type REE deposit in South China. *China Geology*. 2018. Vol. 1. Iss. 3, p. 415-424. DOI: 10.31035/cg2018022

36. Wang Zhen, Chen Zhen Yu, Zhao Zhi et al. REE mineral and geochemical characteristics of Neoproterozoic metamorphic rocks in South Jiangxi Province. *Mineral Deposits*. 2019. Vol. 38. N 4, p. 837-850 (in Chinese). DOI: 10.16111/j.0258-7106.2019.04.010

37. Sanematsu K., Kon Y. Geochemical characteristics determined by multiple extraction from ion-adsorption type REE ores in Dingnan County of Jiangxi Province, South China. *Bulletin of the Geological Survey of Japan*. 2013. Vol. 64. N 11/12, p. 313-330.

38. Li M.Y.H., Mei-Fu Zhou, Williams-Jones A.E. The Genesis of Regolith-Hosted Heavy Rare Earth Element Deposits: Insights from the World-Class Zudong Deposit in Jiangxi Province, South China. *Economic Geology*. 2019. Vol. 114. N 3, p. 541-568. DOI: 10.5382/econgeo.4642

39. Li M.Y.H., Mei-Fu Zhou. The role of clay minerals in formation of the regolith-hosted heavy rare earth element deposits. *American Mineralogist*. 2020. Vol. 105. N 1, p. 92-108. DOI: 10.2138/am-2020-7061

40. Yuejun Wang, Weiming Fan, Guowei Zhang, Yanhua Zhang. Phanerozoic tectonics of the South China Block: Key observations and controversies. *Gondwana Research*. 2013. Vol. 23. Iss. 4, p. 1273-1305. DOI: 10.1016/j.gr.2012.02.019

41. Bern C.R., Shah A.K., Benzel W.M., Lowers H.A. The distribution and composition of REE-bearing minerals in placers of the Atlantic and Gulf coastal plains, USA. *Journal Geochemical Exploration*. 2016. Vol. 162, p. 50-61. DOI: 10.1016/j.gexplo.2015.12.011

42. Xiangping Zhu, Bin Zhang, Guotao Ma et al. Mineralization of ion-adsorption type rare earth deposits in Western Yunnan, China. *Ore Geology Reviews*. 2022. Vol. 148. N 104984. DOI: 10.1016/j.oregeorev.2022.104984

43. Isayeva L.D., Dyussembayeva K.Sh., Kembayev M.K. et al. Forms of occurrence of rare earth elements in the weathering crust of the Kundybay deposit (North Kazakhstan). *News of the National Academy of Sciences of the Republic of Kazakhstan. Series of geology and technical sciences*. 2015. Vol. 2. N 410, p. 23-30 (in Russian).

44. Alshameri A., Hongping He, Chen Xin et al. Understanding the role of natural clay minerals as effective adsorbents and alternative source of rare earth elements: Adsorption operative parameters. *Hydrometallurgy*. 2019. Vol. 185, p. 149-161. DOI: 10.1016/j.hydromet.2019.02.016

45. Meijun Yang, Xiaoliang Liang, Lingya Ma et al. Adsorption of REEs on kaolinite and halloysite: A link to the REE distribution on clays in the weathering crust of granite. *Chemical Geology*. 2019. Vol. 525, p. 210-217. DOI: 10.1016/j.chemgeo.2019.07.024

46. Zhenyue Zhang, Changyu Zhou, Wendou Chen et al. Effects of Ammonium Salts on Rare Earth Leaching Process of Weathered Crust Elution-Deposited Rare Earth Ores. *Metals*. 2023. Vol. 13. Iss. 6. N 1112. DOI: 10.3390/met13061112

47. Lifen Yang, Cuicui Li, Dashan Wang et al. Leaching ion adsorption rare earth by aluminum sulfate for increasing efficiency and lowering the environmental impact. *Journal of Rare Earths*. 2019. Vol. 37. Iss. 4, p. 429-436. DOI: 10.1016/j.jre.2018.08.012

48. Zhi Zhao, Denghong Wang, Leon Bagas, Zhenyu Chen. Geochemical and REE mineralogical characteristics of the Zhaibei Granite in Jiangxi Province, southern China, and a model for the genesis of ion-adsorption REE deposits. *Ore Geology Reviews*. 2022. Vol. 140. N 104579. DOI: 10.1016/j.oregeorev.2021.104579

49. Nesbitt H.W. Chapter 6 – Diagenesis and metasomatism of weathering profiles, with emphasis on Precambrian paleosols. Developments in Earth Surface Processes. Elsevier, 1992. Vol. 2: Weathering, Soils & Paleosols, p. 127-152. DOI: 10.1016/B978-0-444-89198-3.50011-8

50. Chaoxi Fan, Cheng Xu, Aiguo Shi et al. Origin of heavy rare earth elements in highly fractionated peraluminous granites. *Geochimica et Cosmochimica Acta*. 2023. Vol. 343, p. 371-383. DOI: 10.1016/j.gca.2022.12.019

51. Felitsyn S.B., Alfimova N.A., Klimova E.V. Fractionation of Rare Earth Elements in the Acid Treatment of Granitoids. *Lithology and Mineral Resources*. 2011. Vol. 46. N 4, p. 391-394. DOI: 10.1134/S0024490211040031

52. Dubinin A.V. Geochemistry of rare earth elements in the ocean. Moscow: Nauka, 2006, p. 360.

53. Developments in Geochemistry. Ed. by P.Henderson. Elsevier, 1984. Vol. 2: Rare Earth Element Geochemistry, p. 522.

54. Matrenichev V.A., Klimova E.V. Experimental modeling of the conditions for the formation of Precambrian weathering profiles. Composition of solutions and redistribution of lanthanides. *Vestnik of Saint-Petersburg University. Earth Sciences*. 2017. Vol. 62. N 4, p. 389-408 (in Russian). DOI: 10.21638/11701/spbu07.2017.405

55. De Baar H.J.W., Bacon M.P., Brewer P.G., Bruland K.W. Rare earth elements in the Pacific and Atlantic Oceans. *Geochimica et Cosmochimica Acta*. 1985. Vol. 49. Iss. 9, p. 1943-1959. DOI: 10.1016/0016-7037(85)90089-4

56. Li M.Y.H., Mei-Fu Zhou, Williams-Jones A.E. Controls on the Dynamics of Rare Earth Elements During Subtropical Hillslope Processes and Formation of Regolith-Hosted Deposits. *Economic Geology*. 2020. Vol. 115. N 5, p. 1097-1118. DOI: 10.5382/econgeo.4727

57. Ni Su, Shouye Yang, Yulong Guo et al. Revisit of rare earth element fractionation during chemical weathering and river sediment transport. *Geochemistry, Geophysics, Geosystems*. 2017. Vol. 18. Iss. 3, p. 935-955. DOI: 10.1002/2016GC006659

***Authors*: Medet A. Junussov,** *PhD, Postdoctoral Scholar (Nazarbayev University, Astana, Kazakhstan), https://orcid.org/0000-0002-1379-5952,* **Kamal R. Regmi,** *PhD, Associate Professor (Nazarbayev University, Astana, Kazakhstan), https://orcid.org/0000-0003-1207-9118,* **Ekaterina V. Klimova,** *Junior Researcher (Institute of Precambrian Geology and Geochronology RAS, Saint Petersburg, Russia), katya_kli@list.ru, https://orcid.org/0000-0002-9771-9518,* **Aleksandr V. Reznik,** *Candidate of Engineering Sciences, Senior Researcher (N.A.Chinakal Institute of Mining Siberian Branch RAS, Novosibirsk, Russia), http://orcid.org/0000-0002-0077-3404.*

The authors declare no conflict of interests.

ISSN 2411-3336; e-ISSN 2541-9404

JOURNAL OF MINING INSTITUTE
Zapiski Gornogo instituta
Journal homepage: pmi.spmi.ru

Research article *Energy*

Development of an engineering methodology for determining the standard consumption of electricity by air coolers

Daria E. Filimoshina
GCE-energo LLC, Saint Petersburg, Russia

How to cite this article: Filimoshina D.E. Development of an engineering methodology for determining the standard consumption of electricity by air coolers. Journal of Mining Institute. 2026. Vol. 277, p. 55-67.

Abstract
The issue of reducing electricity consumption costs is becoming relevant for industrial enterprises, taking into account the growing demand for electricity every year. The electricity consumption of air coolers at a gas processing plant was considered in the framework of this study. The change in ambient temperature (during the day and depending on the season) is the main disturbing factor affecting the performance of air coolers. With such significant seasonal changes in air temperature, its density changes, which causes fluctuations in the power consumed by the electric motor by up to 30 %. The issues of increasing energy efficiency, forecasting and determining the power consumption rate of air coolers, depending on changing external conditions, therefore become important. A methodology has been developed to determine the standard power consumption of air coolers depending on two factors – the ambient temperature and the load of the gas processing plant. A two-factor power-law approximation of the values was carried out due to nonlinear dependencies on plant loading and ambient temperature. The dependence of power consumption on ambient temperature and the loading of the installation on raw materials for any type of air cooler is determined with high accuracy (the root-mean-square error of the calculated and approximating values does not exceed 1 %). The formula for calculating the standard consumption of electric power of the air cooler at the considered installation was determined based on the results of the study. The methodology can be used by employees of gas processing enterprises to determine the standard electricity consumption of air coolers under changing climatic and technological factors.

Keywords
air cooler; gas processing plant; electricity consumption; energy efficiency; standardization; ambient temperature

Received: 26.03.2025 ***Accepted: 09.10.2025*** ***Online: 27.11.2025*** ***Published: 27.02.2026***

Introduction

One of the priorities for all types of production in Russia and the world due to the high energy intensity [1] is the reduction and optimization of fuel and energy resources costs [2], including electrical energy, which is highlighted in one of the trends of the 4D concept [3]. Thus, the “decrease” trend means a reduction in the consumption of all types of resources and materials, including the amount of waste produced. At the same time, industrial electricity consumption in the world is projected to increase by 83 % in 2022-2050.[1]

There has been a decrease in gas production and transportation due to external factors in recent years. The development of the industry depends both on foreign supplies of equipment (which makes it difficult to introduce new capacities) and on the demand for energy resources, while the cost of electricity increases [4, 5]. In this regard, a lot of research is being conducted in the direction of peak load coverage by means of electricity storage systems to reduce costs at gas industry facilities [6-8].

---

[1] Scenarios for the development of global energy until 2050. URL: https://rosenergo.gov.ru/press-center/news/stsenarii-razvitiya-mirovoy-energetiki-do-2050-goda/ (accessed 26.03.2025).

A significant amount of electrical energy costs at gas production, transportation and processing facilities is determined by the operation of pumps [9], compressors [10], various traction, ventilation and air coolers [11], which are the objects of this study, as well as their design features and degree of wear. The operating mode of the specified equipment may depend on many factors that affect energy consumption to varying degrees. Thus, air coolers are operated on the territory of the Russian Federation in a wide temperature range: from –45 to +50 °C [12]. Changes in ambient temperature (during the day and depending on the season) are the main disturbing factor affecting the operation of air coolers and their operability [13, 14]. The heat flow changes with such significant seasonal changes in ambient temperature and there is a need to increase air consumption, which causes corresponding fluctuations in the power consumed by the electric motor – up to 30 % [15, 16]. At the same time, at subzero ambient temperatures (in winter in the northern regions), air coolers may not be switched on at all.

On the other side, the electrical consumption of the air cooler is affected by the loading of the gas processing plant, which includes the air cooler. Depending on the technological process (volume of transported or pumped gas), the need to turn on the air cooler occur in stages, even in summer. In this regard, at the next stage of the work, it is necessary to take into account and classify industrial facilities as typical according to several parameters combined (technological process, location of the region, type of technology, etc.).

According to the article [17], the efficiency of each type of air cooler is not constant during operation, but is characterized by a certain dynamics, which is caused by a change in the operating mode of the technological site/plant, as well as changes in climatic conditions. Reducing unit costs per unit of produced and processed products, i.e. gas or gas condensate, including in the transportation and distribution sector (at gas transportation facilities – compressor stations) [18-20], is an important scientific and technical research area for the development of the gas industry [21].

One of the relevant directions is the use of digital twins of technological equipment at oil and gas industry facilities [22, 23]. The digital twin of an air cooler is a virtual model that is an exact copy of a real device used for modeling, analyzing, and optimizing its operation. The digital twin of an air cooler can include physical parameters, heat transfer characteristics, aerodynamics and other important factors and be used for the following purposes:

- optimization of operation – modeling of various scenarios of operation of the air cooler, determining optimal operating modes to increase efficiency and reduce energy consumption [24];
- fault prediction based on data collected from real equipment, the digital twin can predict possible breakdowns and malfunctions, which allows for preventive maintenance and avoiding equipment downtime [25];
- design improvement – testing new design solutions and optimizing the shape and size of the air cooler elements to increase its efficiency;
- staff training to work with air coolers without putting real equipment at risk;
- lifecycle management – monitoring the condition of the air cooler from design to disposal.

The methodology presented in this study can serve as a basis for the creation, implementation, and use of modern solutions in the field of digitalization at enterprises.

The issue of increasing energy efficiency [26, 27], modeling [28-30], forecasting [31, 32] and determining the rate of power consumption by air coolers, depending on changing external conditions such as ambient temperature and plant loading, is becoming relevant. However, in the research of Russian authors, for example in [33, 34], mathematical models are proposed that describe the operation of air coolers and are designed to develop methods for controlling the operating modes of air coolers to reduce electricity consumption, in which only one factor (ambient temperature) is reflected as influencing fluctuations in the power consumption of air coolers. The influence of wind speed on the cooling process by air coolers, in addition to temperature, is taken into account in the studies of foreign authors [35, 36].

The purpose of this study is to develop a methodology for determining the standard electricity consumption of air coolers depending on two changing factors – ambient temperature and the load of the gas processing plant.

The research methodology includes solving the following tasks:

- determination of the availability of initial data, such as the technical characteristics and parameters of air coolers, the thermal load of air coolers based on the results of preliminary modeling of the gas processing plant;
- calculation of the mass air flow through the air cooler;
- calculation of the standard power consumption of the air cooler, taking into account the efficiency of the engines;
- approximation of values by the smallest polynomial function of standard electricity consumption with a deviation of the approximated and calculated values of no more than 5 %;
- determination of the coefficients of two-factor approximation for the formation of the final dependence of the standard of electricity consumption by the air cooler on the ambient temperature and the loading of the gas processing plant.

Methods

The consumption of fuel and energy resources by technological and auxiliary equipment of industrial enterprises depends on several factors, the main of which is the volume of production.

The initial data for the development of formulas for calculating the standard consumption of fuel and energy complex by technological equipment is a list of equipment, as well as statistical data on its operating modes. This data is recorded at the enterprises and used when planning production volumes. The following can be used as initial data on the operating modes of technological equipment: unloading from the accounting system, time sheets, maps, technological regulations, design data. Statistical data in the development of formulas for calculating the standard consumption of fuel and energy complex are used only to determine the technological parameters that affect the energy consumption of production and equipment.

One of the tasks in developing this methodology for determining standard consumption values is to use simple formulas for calculating that do not require the use of specialized equipment or software, with the possibility of further application of the methodology by specialists of gas processing enterprises. Mathematical modeling of technological plants and processes using specialized software is a laborious process and is not the optimal solution to achieve the objectives of this study. For this reason, upon completion of the calculation of the theoretically required volume of fuel and energy resources consumption, depending on the volume of output/processing of raw materials and ambient temperature, the results of the calculations are approximated to develop formulas for calculating consumption without using specialized tools.

Approximation is a scientific method that consists in replacing some mathematical objects with others that are close to the original ones [37]. In particular, it is the basis for the analytical representation of tabular data by a function of a given type with unknown parameters, the values of which are determined so that the graph of the functions is as close as possible to the specified points. To simplify the calculation formulas, minimum degree polynomials are used in the approximation, which ensures the necessary calculation accuracy. The algorithm for developing calculation formulas for the absolute consumption of technological equipment is shown in Fig.1. The above algorithm is applied for each piece of equipment.

It is possible to use two methods for determining the thermal load of air coolers, depending on the availability of initial data and the scope of application of each equipment item:

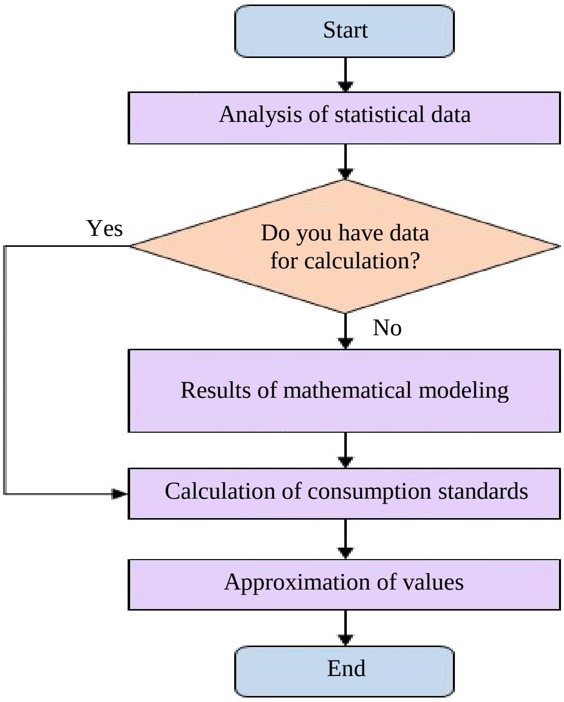

Fig.1. An algorithm for developing calculation formulas for electricity consumption standards

- according to the mathematical modeling of technological plants;
- according to the flow rate, the temperature of the cooled medium at the inlet and the maximum allowable temperature at the outlet of the air cooler.

The article discusses a technique based on mathematical modeling of technological plants, suitable for use by engineering and technical personnel and using two variable parameters, which allows to obtain the most accurate result. The methodology for developing calculation formulas for the standard consumption of electric energy by air coolers is presented using the example of a gas condensate stabilization unit (GCSU) at a gas processing plant. Further calculations were performed in the Microsoft Office Excel software, which is sufficient to complete the task.

The AC-101 air cooler, which is located as part of the GCSU of the condensate stabilization plant, was considered as the object under study. The main parameter determining the performance of the GCSU is the volume of raw materials – the processed oil and gas condensate mixture. Figure 2 shows a block diagram of a gas condensate stabilization unit.

The oil and gas condensate mixture enters the processing train of the plant from a common collector and passes sequentially through the tube space of the E-101/1-3 heat exchangers, where it is heated to a temperature of 80-120 °C by a reverse flow of stable condensate coming out of the cubic part of the C-101/1 stabilization column. The oil and gas condensate mixture, heated to a temperature of 80-120 °C, enters the 20th plate in the middle part of the C-101/1 stabilization column. The C-101/1 stabilization column is designed for separating an oil and gas condensate mixture into stable condensate (SC) and a wide fraction of light hydrocarbons by rectification. The C-101/1 column is a vertical cylindrical apparatus of variable cross-section, inside which 38 mass-exchange valve plates are located. The SC is withdrawn to the raw materials park or to the substandard product line.

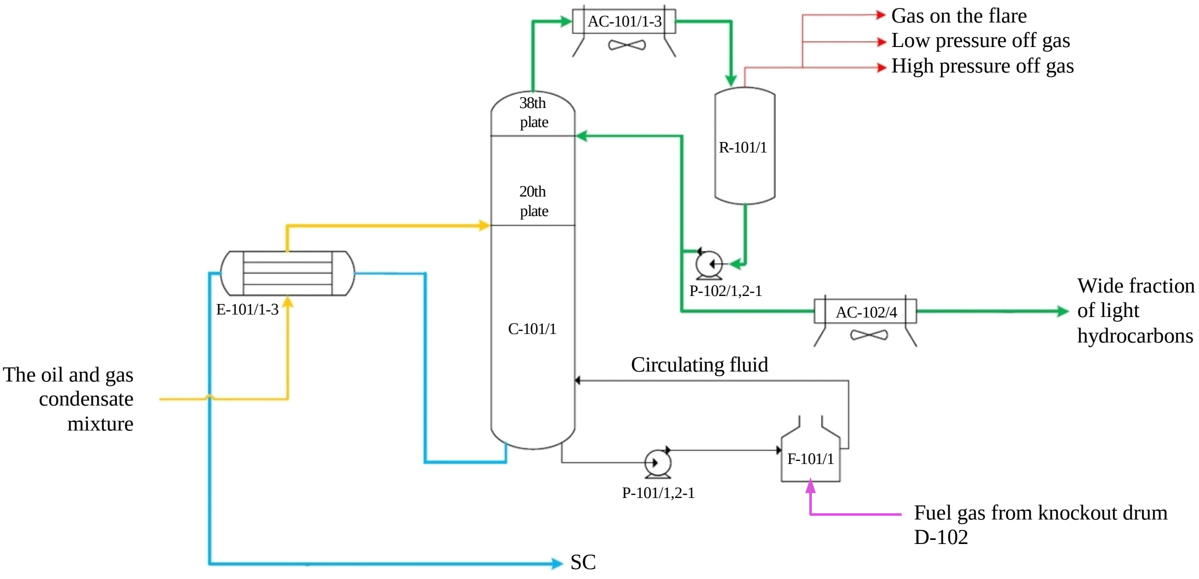

Fig.2. Technological block diagram of a gas condensate stabilization unit

Vapors of a wide fraction of light hydrocarbons from the top of the C-101/1 stabilization column are sent to the parallel-operating air coolers AC-101/1-3, where they are cooled to a temperature of 25-60 °C, partially condensed and fed into the reflux drum R-101/1.

An reflux system for tube bundles with chemically purified water is installed on the air coolers in the summer to reduce the amount of waste gases. A partially condensed wide fraction of light hydrocarbons from the reflux drum R-101/1 is supplied to the pumps P-102/1,2-1, with which a portion of the wide fraction of light hydrocarbons is supplied to the upper plate of the stabilization column C-101/1 as live reflux to maintain the temperature regime of the top of the stabilization column. The balance amount of a wide fraction of light hydrocarbons passes through the AC-102/4 air cooler, where it is pre-cooled to a temperature of no more than 40 °C and sent for further processing or output as finished products to the parks of the raw material base or to the line of substandard product.

A constant amount of cubic liquid is circulated by pumps P-101/1-1, P-101/2-1 through the furnace F-101/1 and the return of the vapor-liquid mixture to the lower part of the stabilization column under the lower plate to maintain the required temperature regime of the stabilization column C-101/1. A balanced amount of stable condensate is removed from the cube of the C-101/1 stabilization column under its own pressure, which sequentially passes through the shell side of the E-101/1-3 heat exchangers, gives off heat to the oil and gas condensate mixture and cools to a temperature not exceeding 40 °C, enters the common collector, through which it is discharged. Stable condensate is discharged into the line of substandard product during start-up and stop operations of technological lines, as well as if the quality of stable condensate does not meet the requirements.

The AC-101/1-3 air cooler is a condenser of the upper product of the column. An air cooler of type AVZ-20-2.5-B1/8-4-6 is installed at the specified position. Zigzag type AVZ air coolers are designed for condensation and cooling of vaporous, gaseous and liquid media [38]. The main parameters of the air cooler are in accordance with the data of the technological regulations for the condensate stabilization unit, as well as OST 26-02-537-79[2], necessary for the development of a standard for electricity consumption (initial data): type – AVZ-20-2,5-B1/8-4-6; heat exchange surface of a tubes area – 440 m^2, finned – 5300 m^2; size – 6.0×6.47 m; number of sections – 3; fan power – 90 kW.

The consumption of air coolers includes the consumption of electrical energy for the fan drive, which is determined by the required air flow through the fan. The required air consumption is determined by the thermal load of the air cooler (heat output into the atmosphere), as well as the temperature difference between the cooled medium and the ambient air.

Results

When developing a methodology for rationing basic indicators, it is necessary to ensure that calculations are linked to these factors, i.e. to identify the dependence of the productivity of individual equipment, such as a furnace [39, 40] or a column reboiler, on the volume of output or processing of raw materials by a technological plant. Mathematical modeling of technological installations in Aspen Hysys software can be used to calculate the theoretically required amount of energy consumption by technological equipment of enterprises.

During the simulation, the operating modes of plants and individual equipment are assumed in accordance with the available statistical data. The simulation is carried out under operating conditions of installations and individual equipment at several performance values, which makes it possible to determine the theoretically required energy consumption. The result of the mathematical modeling of technological installations is the elementwise theoretically necessary loads of technological equipment.

---

[2] OST 26-02-537-79 “The air coolers are zigzag-shaped with two fans. Basic parameters and sizes”.

An additional calculation is carried out based on the results of mathematical modeling, depending on the type of equipment under study, the purpose of which is to determine the dependencies of the theoretical consumption of fuel and energy resources on the plant's performance and ambient temperature, taking into account the characteristics of the equipment. Thus, for air coolers, an assessment of the electricity consumption by fans is carried out to ensure the necessary heat removal.

The estimated power consumption for the fan motor at the design stage should be increased by 10 % to ensure engine start-up. The design documentation calculates the maximum load of the installation, so there is no calculation of the power consumption of air coolers depending on the load of the installation. In this study, the obtained dependence allows us to determine the value of power consumption by the air cooler at a certain load of the installation at a specific time. The thermal load on the air cooler was determined based on the results of mathematical modeling of the column at different plant loads taking into account the use of a two-phase cooled medium (Fig.3). At a raw material consumption of 100 m^3/h, the thermal load is 252.9 (4860) kJ/kg (kW); at 150 m^3/h, the thermal load is 252.8 (7290) kJ/kg (kW); at 200 m^3/h, the thermal load is 252.8 (9718) kJ/kg (kW); at 250 m^3/h, thermal load 252.7 (12,145) kJ/kg (kW); at 300 m^3/h, thermal load 252.97 (14,570) kJ/kg (kW).

The temperatures of the cooled medium at the inlet and outlet of the air cooler, in accordance with the analysis of statistical data, are assumed to be equal to constant values for the operating mode of the plant. The temperature values of the cooled medium (the upper product of the columns) averaged for the operating mode of the installation are 70.0 °C at the inlet and 52.6 °C at the outlet.

The possibility of heat exchange of one section of the air cooler (heat release into the atmosphere) is calculated using the heat transfer equation

$$Q_{\text{air cooler}} = K_1 K F \theta_t,$$

where K_1 is the coefficient of normative deterioration of the technical condition of the air cooler over the period of operation; K is the heat transfer coefficient of this type of air cooler, J/kg ·°C; F is the area of the finned heat exchange surface, m^2; θ_t is the average logarithmic temperature difference.

Average logarithmic temperature difference

$$\theta_t = (\theta_1 - \theta_2)/LN(\theta_1/\theta_2);$$

$$\theta_1 = t_1 - T_2;$$

$$\theta_2 = t_2 - T_1,$$

where T_1 is the outside air temperature, °C; T_2 is the air temperature behind the air cooler, °C,

$$T_2 = T_1 + Q/(nG_a C_{hc});$$

n is the number of installed sections of the air cooler; G_a is the air flow rate through one section of the air cooler, kg/s; C_{hc} is the heat capacity of the air, J/kg·°C.

Based on the presented dependencies, the required air flow through the air cooler was calculated (Table 1). Based on the data in Table 1 and the typical dependence of the power consumption of the air cooler on the air flow (Fig.4), the calculation of the standard power consumption for the drive of the air cooler was carried out.

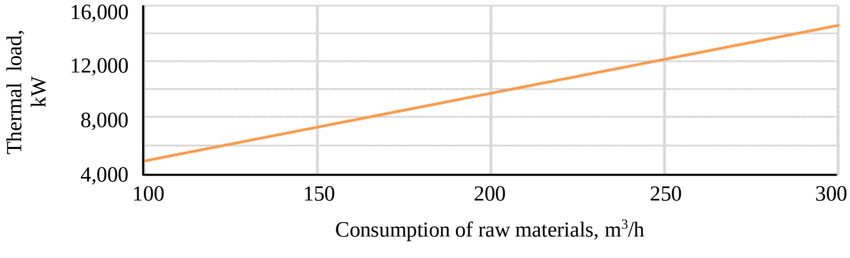

Fig.3. The calculated value of the thermal load of the air cooler, depending on the load and operating mode of the condensate stabilization plant

Table 1

Air consumption through the air cooler, kg/s

Consumption of raw materials, m^3/h	T_a, °C				
	–40	–20	0	20	30
100	50.7	64.2	87.6	137.6	192.6
150	76.0	96.3	131.3	206.4	288.9
200	101.4	128.4	175.1	275.1	385.2
250	126.7	160.4	218.8	343.8	481.3
300	152.0	192.5	262.5	412.5	577.5

Note. T_a – ambient temperature.

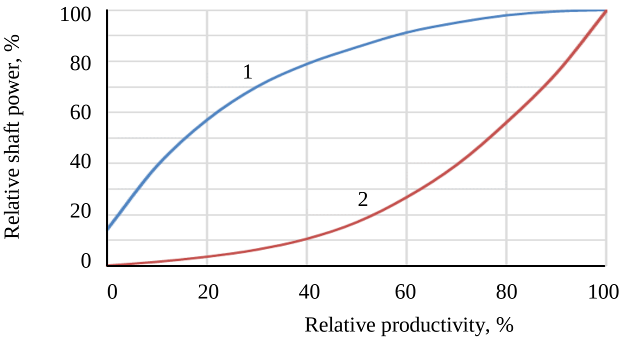

Fig.4. Typical dependence of the fan power consumption on its performance

1 – throttling; 2 – frequency control

The power of the electric drive of the fans of the air cooler is determined by the typical dependence in Fig.4 in the absence of a frequency-controlled drive. The power consumption of the electric fan drive of the air cooler in the presence of a frequency-controlled drive is calculated by the formula

$$N_{\text{air cooler}} = \frac{N_0}{\eta_{\text{em}}\eta_{\text{fc}}}\left(\frac{p_a}{p_{\text{st}}}\frac{T_{\text{st}}}{T_a}\right)\left(\frac{n}{n_{\text{nom}}}\right)^3,$$

where N_0 is the rated power of the air cooler according to the passport documentation, kW; η_{em} is the efficiency of the electric motor; η_{fc} is the efficiency of the frequency converter; p_a is the barometric pressure, MPa; p_{st}, T_{st} are pressure and temperature under standard conditions, respectively, p_{st} = = 101,325 Pa, T_{st} = 293.15 K; n_{nom}, n is the nominal and actual rotation speed of the electric motor shaft, respectively, rpm.

The following parameters were taken into account in the subsequent calculations:

- typical dependence of the fan power consumption on its performance;
- type of air flow control (no regulation, blinds, variable frequency drive);
- electric motor power of one section;
- number of sections;
- engine load factor in nominal mode (assumed to be 0.8);
- the method of turning on the fans (in parallel or in series).

The rated efficiency of the engine was determined according to the international IEC standard[3].

The results of the calculation of the standard power consumption for the drive of the air cooler are presented in Table 2.

The dependence of the power consumption of the air cooler is nonlinear both on the ambient temperature and on the loading of the installation (Fig.5), in Fig.6 the dependencies are presented in two-dimensional form.

The study calculated the operating modes of the air cooler at 25 points. Since the calculations are complex, their use directly at the enterprise in this form is impractical. Therefore, a polynomial two-factor approximation of the values of electricity consumption by an air cooler was carried out. Due to non-linear dependencies both in terms of installation load and ambient temperature, a power-law approximation of the values was carried out using the least squares method implemented in Microsoft Office Excel software. The degree of the polynomial was chosen to be minimal (to reduce the complexity of the function), giving an error of no more than 5 % at any of the calculated points.

---

[3] GOST IEC 60034-30-1-2016 Rotating electrical machines – Part 30-1: Efficiency classes for grid-connected AC motors (IE code). GOST IEC/TS 60034-30-2-2021 Rotating electrical machines. Part 30-2. Efficiency classes of AC motors with frequency inverter (IE code).

Table 2

Standard power consumption depending on performance and ambient temperature

Consumption of raw materials, m^3/h	T_a, °C				
	–40	–20	0	20	30
Mechanical power of the fan drive, taking into account alternate loading, kW					
100	63.42	71.73	85.15	109.34	130.77
150	78.70	89.81	106.61	135.54	159.08
200	92.41	105.30	124.36	155.74	177.64
250	104.53	118.74	139.64	170.47	192.57
300	115.34	130.72	152.49	182.02	203.40
The standard of power consumption of the air cooler, taking into account the efficiency of the engines, kW					
100	98.67	103.81	112.28	129.63	148.09
150	108.15	115.35	127.48	152.47	174.89
200	117.11	126.46	142.33	171.65	193.06
250	125.87	137.43	156.29	186.02	207.88
300	134.55	148.05	168.51	197.37	218.91

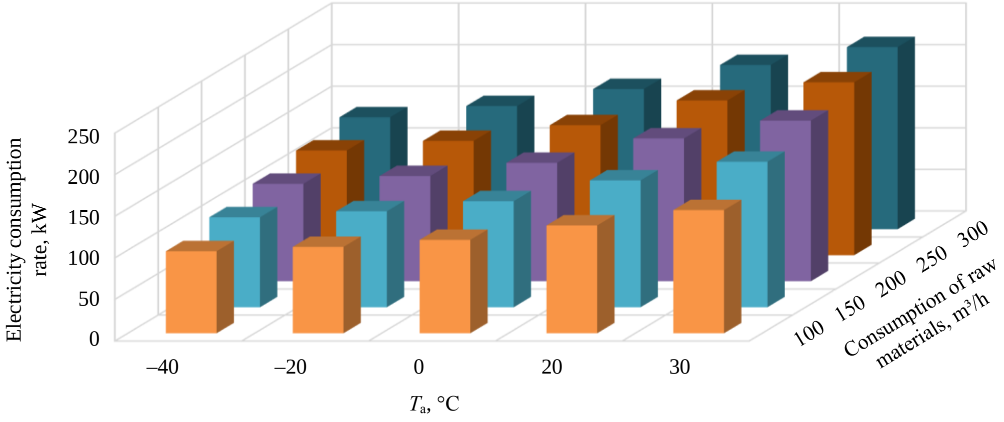

Fig.5. The dependence of the power consumption of the air cooler on the load of the installation and the ambient temperature

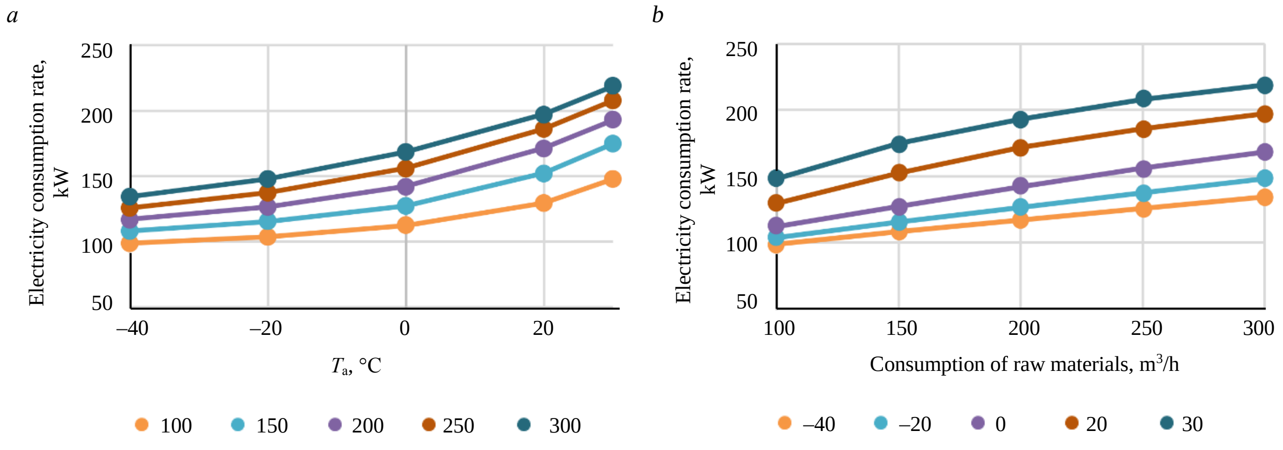

Fig.6. The dependence of the power consumption of the air cooler on the ambient temperature at different plant loads (*a*), on the plant load (*b*)

The minimum degrees of the polynomial obtained from the results of the analysis are as follows: in terms of loading Q, m^3/h – the 2nd degree, in terms of ambient temperature T_a, °C – the 2nd degree. The results of the selection of approximate values of the power consumption of the air cooler are presented in Table 3.

Table 3

The results of the selection of approximate values of the power consumption of the air cooler

Consumption of raw materials, m^3/h	T_a, °C				
	–40	–20	0	20	30
Electricity consumption rate, kW					
100	98.67	103.81	112.28	129.63	148.09
150	108.15	115.35	127.48	152.47	174.89
200	117.11	126.46	142.33	171.65	193.06
250	125.87	137.43	156.29	186.02	207.88
300	134.55	148.05	168.51	197.37	218.91
Approximate value of the standard of power consumption, kW					
100	99.78	101.50	112.51	132.80	146.42
150	108.97	113.18	128.42	154.68	171.95
200	117.89	124.70	143.06	172.99	192.29
250	126.54	136.04	156.44	187.72	207.45
300	134.92	147.22	168.54	198.88	217.43
Deviation of the approximated and calculated values, %					
100	1.117	–2.226	0.209	2.438	–1.128
150	0.753	–1.880	0.740	1.453	–1.682
200	0.663	–1.397	0.518	0.782	–0.397
250	0.532	–1.010	0.095	0.914	–0.203
300	0.274	–0.559	0.017	0.761	–0.676
Root-mean-square error (RMSE) – 0.301 %					

Based on the results of comparing the approximating curves and the calculated values of the electricity consumption standards, it was concluded that the approximation polynomial and the calculated values are satisfactorily convergent (the standard deviation at all points does not exceed 1 %). According to the approximation results, the resulting dependence will have the form:

$$f(Q, T_a) = (a2.1Q^2 + b2.1Q + c2.1)\,T_a^2 + (a1.1Q^2 + b1.1Q + c1.1)\,T_a + (a0.1Q^2 + b0.1Q + c0.1),$$

where Q – consumption of raw materials, m^3/h; a, b, c – coefficients of two-factor approximation, relative units (Table 4).

Table 4

Coefficients of two-factor approximation, rel. u.

Designation	Meaning	The physical meaning of coefficients
$a2.1$	$-3.012 \cdot 10^{-7}$	The coefficient at $x2$ (the coefficient at higher powers of x) reflects nonlinear components that may indicate the presence of curvature, fluctuations, or other complex dependencies in the process
$b2.1$	$1.189 \cdot 10^{-4}$	
$c2.1$	$2.724 \cdot 10^{-3}$	
$a1.1$	$-1.706 \cdot 10^{-5}$	The coefficient at $x1$ (linear coefficient) determines the rate of change of the function (slope) relative to the variable x (dependence of the consumption of the air cooler with proportional changes in the plant load and ambient temperature)
$b1.1$	$9.369 \cdot 10^{-3}$	
$c1.1$	0.01598	
$a0.1$	$-2.542 \cdot 10^{-4}$	The free term (coefficient at $x0$) is the initial value of the function at the point $x = 0$ or the base level (the base value of the consumption of the air cooler according to the initial technical parameters and equipment data)
$b0.1$	0.3818	
$c0.1$	76.87	

It is necessary to take into account the context of the problem, the physical meaning of variables and units of measurement when interpreting coefficients. Not all coefficients may have an obvious physical meaning in each particular case, some of them may simply be mathematical artifacts reflecting the complexity of the process being approximated. A formula for calculating the standard power consumption for the air cooler AVZ-20-2.5-B1/8-4-6 was formed based on the results of determining the coefficients of two-factor approximation

$$f(Q, T_a) = (-3.012\cdot10^{-7}Q^2 + 1.189\cdot10^{-4}Q + 2.274\cdot10^{-3})T_a^2 +$$
$$+ (-1.706\cdot10^{-5}Q^2 + 9.369\cdot10^{-3}Q + 0.01598)\,T_a + (-2.542\cdot10^{-4}Q^2 + 0.3818Q + 76.87).$$

The obtained dependence allows us to calculate the value of the power consumption of the air cooler at a specific time. Additionally, the sensitivity of the model to the input data is analyzed. When checking the model based on test values for plant loading (raw material consumption) and changes in ambient temperature for the calculation period, it was found that with various combinations of errors in setting the ambient temperature by ±2 °C and/or raw material consumption by ±5 %, the change in the calculated value of the power consumption standard was up to 1.5 %.

The resulting solution can be the basis (source data) for the formation of a database of statistical data for determining the standard of electricity consumption and subsequently used for the following purposes:

- planning the volume of electricity consumption and reducing energy consumption in the planning and economic processes of enterprises;
- identification of equipment and nodes with increased electricity consumption in order to develop plans for replacement, reconstruction, and modernization of installations;
- analysis of electric energy costs as part of the development of schedules for preventative and predictive maintenance and future energy conservation and energy efficiency programs;
- creation and implementation of digital twins at production facilities, models for forecasting electricity and power consumption, energy management systems with the integration of IoT sensors and other intelligent devices.

Conclusion

The issue of reducing the cost of electricity consumption for industrial enterprises with an annual growing demand for electricity and, as a result, the introduction of energy-saving and energy efficiency-enhancing measures is becoming urgent. However, the development of such measures is impossible without an accurate assessment of the power consumption of various types of equipment involved in the production process.

The electrical consumption of air coolers at a gas processing plant was considered in the framework of this study. A methodology has been developed that makes it possible to determine with high accuracy the standard consumption of electric power by an air cooler, depending on two changing factors – the ambient temperature and the load of the gas processing plant (the RMSE of the calculated and approximating values according to the results of the study does not exceed 1 %). The formula for calculating the standard electric power consumption for a specific air cooler in the installation under consideration was determined based on the results of the study.

The methodology can be used by employees of gas processing enterprises to determine the standard electricity consumption of air coolers under changing external and technological factors. This technique, developed and implemented in the Microsoft Office Excel software, allows its use by administrative, technical and production personnel without the use of specialized equipment or software, which would be a laborious process. In particular, it is possible to use the methodology in the R7-Office software for enterprises that have switched to the Russian office application package.

The further direction of the research work is to test the developed calculation methodology at gas processing and/or transportation enterprises, namely, comparing the obtained standard values with real statistical data recorded at the enterprise, conducting field measurements, assessing the factors affecting electricity consumption and the degree of their influence.

Such factors may include the following:

- geographical location and microclimate of the facility;
- physical obsolescence and deterioration of equipment;

- the absence or presence of seasonal changes in the fan blades impinging angle in spring and autumn due to changes in air density (the effect of temperature on the operating mode of the air cooler is only partially compensated because the adjustment is discrete, as a result, inaccurate maintenance of gas temperature and increased energy costs, since turning on the fans of the air cooler does not lead to the required temperature reduction, however, the possible savings in electrical energy are up to 10 %);
- irregular or untimely cleaning of the finned surface of the heat exchange pipes of the air cooler (hydrates form on the walls of the pipes of the heat exchange sections at low outdoor temperatures, as a result of which the gas cooling efficiency deteriorates, pressure losses in the heat exchange sections increase, mechanical deformation and destruction of the pipes of the heat exchange sections occur);
- design and operational features of the air cooler (lifting the structures of the units above ground level, the use of heat exchange pipes with a maximum finning coefficient, or, for example, the use of composite materials in the design of impellers, which will increase the efficiency of fans due to a more advanced aerodynamic shape of the blades and ensure the possibility of reducing the power consumption of the air cooler by up to 40 %);
- fan activation method (fans can be loaded in different ways depending on the switching method – in parallel, when all fans are turned on at the same time and work the same way, or sequentially, when one fan is loaded to 100 % first, then the next, etc.);
- air flow control, the degree of engine load (lack of regulation, regulation by means of blinds or a frequency-controlled drive, for example, reducing the power of a drive not designed to operate as part of a frequency-controlled drive, with frequency control by more than 30 % leads to overheating of the windings and reduced service life, while the presence of a frequency-controlled drive provides energy savings of up to 20 %);
- the quality of the source data (requires statistics on the electricity consumption of each piece of equipment installed at the research facility, in addition to the working documentation and equipment passports), etc.

Based on the results of testing the methodology at gas processing plants, studies can be conducted aimed at developing predictive analytics methods to identify signs of equipment wear at an early stage, and measures can be developed to save energy and increase energy efficiency, reduce electricity costs.

REFERENCES

1. Zhukovskiy Y.L., Batueva D.E., Buldysko A.D. et al. Fossil Energy in the Framework of Sustainable Development: Analysis of Prospects and Development of Forecast Scenarios. *Energies*. 2021. Vol. 14. Iss. 17. N 5268. DOI: 10.3390/en14175268
2. Khasanov I.I., Arduganov A.I. Modernization of fans of gas air cooling unit at compressor stations of main gas pipelines. *Transport and storage of Oil Products and hydrocarbons.* 2022. N 1-2, p. 29-34 (in Russian). DOI: 10.24412/0131-4270-2022-1-2-29-34
3. Zhukovskiy Y., Koshenkova A., Vorobeva V. et al. Assessment of the Impact of Technological Development and Scenario Forecasting of the Sustainable Development of the Fuel and Energy Complex. *Energies*. 2023. Vol. 16. Iss. 7. № 3185. DOI: 10.3390/en16073185
4. Morenov V. Advances in Oil and Gas Production: A Viewpoint. *Energies*. 2023. Vol. 16. Iss. 3. N 1379. DOI: 10.3390/en16031379
5. Zhukovskiy Y., Tsvetkov P., Koshenkova A. et al. A Methodology for Forecasting the KPIs of a Region's Development: Case of the Russian Arctic. *Sustainability*. 2024. Vol. 16. Iss. 15. N 6597. DOI: 10.3390/su16156597
6. Tokarev I.S. Development of parameters for an industry-specific methodology for calculating the electric energy storage system for gas industry facilities. *Journal of Mining Institute.* 2025. Vol. 272, p. 171-180.
7. Senchilo N.D., Ustinov D.A. Method for Determining the Optimal Capacity of Energy Storage Systems with a Long-Term Forecast of Power Consumption. *Energies*. 2021. Vol. 14. Iss. 21. N 7098. DOI: 10.3390/en14217098
8. Tokarev I.S., Yugay V.F., Tolmachev V.N. et al. Use of electric power storage systems as part of power generating equipment of PJSC Gazprom production facilities power supply systems. *Gas Industry.* 2023. Iss. S3 (853), p. 34-40 (in Russian).

9. Dubinina N.A., Michurina O.Y., Kudryavtseva O.V., Kushner A.A. The main directions of increasing energy efficiency at the enterprises of the oil and gas industry. *Engineering and Construction Bulletin of the Caspian Region*. 2021. N 4 (38), p. 80-85 (in Russian). DOI: 10.52684/2312-3702-2021-38-4-80-85

10. Pronin V.A., Tsvetkov V.A., Kovanov A.V. et al. Methods for regulating the performance of screw compressors. *Journal of International Academy of Refrigeration*. 2021. N 2 (79), p. 28-38 (in Russian). DOI: 10.17586/1606-4313-2021-20-2-28-38

11. Abakumov A.M., Zubkov Yu.V., Abakumov O.A. Electric drives control of gas cooling units taken into account of individual characteristics air cooling apparatus. *News of the Tula State University. Sciences of Earth*. 2024. Iss. 8, p. 567-571 (in Russian). DOI: 10.24412/2071-6168-2024-8-567-568

12. Yanvarev I.A., Vanyashov A.D., Krupnikov A.V. Improving Gas Cooling Technology at its Compression in the Booster Compressor Station. *Procedia Engineering*. 2016. Vol. 152, p. 233-239. DOI: 10.1016/j.proeng.2016.07.696

13. Kudina H.F., Prihodzko I.V., Karpenko V.V., Kuritsyn P.A. Influence of climatic factors on performance of electrical equipment. *Mining Mechanical Engineering and Machine-Building*. 2021. N 2, p. 55-64 (in Russian).

14. Ermishov K.V., Zharov A.Yu., Kopycheva U.N. Implementation of digital models for increasing of the efficiency of gas-processing enterprises: Simulation of air-cooling units. *Oil & Gas Chemistry*. 2021. N 3-4, p. 60-62 (in Russian). DOI: 10.24412/2310-8266-2021-3-4-60-62

15. Khvorov G.A., Yumashev M.V. Analysis of energy-saving technologies for gas cooling based on air cooling units for gas transport at Gazprom PJSC. *Oil and Gas Territory*. 2016. N 9, p. 127-132 (in Russian).

16. Arslanova A.F., Farukhshina R.R. Evaluation of the thermal efficiency of air-cooled gas devices of the “Iceberg” type. *Transport and Storage of Oil Products and Hydrocarbons*. 2023. N 2, p. 59-65 (in Russian). DOI: 10.24412/0131-4270-2023-2-59-65

17. Kalinin A.F., Merkuryeva Yu.S., Hallyev N.H. Operational Efficiency Estimate of Gas Air Coolers of New Generation. *Oil and Gas Territory*. 2018. N 9, p. 74-80 (in Russian).

18. Eremenko O.V. Towards the effectiveness of innovation in the selected sectors of activity of oil and gas producing enterprises. *Bulletin of Buryat State University. Economy and Management*. 2018. Iss. 1, p. 33-43 (in Russian). DOI: 10.18101/2304-4446-2018-1-33-43

19. Shoghl S.N., Pazuki G. Compressor/pump stations in natural gas transmission pipelines. Advances in Natural Gas: Formation, Processing, and Applications. Elsevier, 2024. Vol. 6: Natural Gas Transportation and Storage, p. 177-236. DOI: 10.1016/B978-0-443-19225-8.00006-8

20. Jiawei Zhang, Lin Li, Qizhi Zhang, Yanbin Wu. Optimization of Load Sharing in Compressor Station Based on Improved Salp Swarm Algorithm. *Energies*. 2022. Vol. 15. Iss. 15. N 5720. DOI: 10.3390/en15155720

21. Maskov L.R., Kornilov V.Yu. Development of a model of an electrical complex for gas air cooling devices of gas field N 1 Gazprom dobycha Yamburg LLC with a centralized power supply system in the MATLAB/SIMULINK program. *Power engineering: research, equipment, technology*. 2022. Vol. 24. N 2, p. 50-71 (in Russian). DOI: 10.30724/1998-9903-2022-24-2-50-71

22. Knebel F.P., Trevisan R., do Nascimento G.S. et al. A study on cloud and edge computing for the implementation of digital twins in the Oil & Gas industries. *Computers & Industrial Engineering*. 2023. Vol. 182. N 109363. DOI: 10.1016/j.cie.2023.109363

23. Egbumokei P.I., Dienagha I.N., Digitemie W.N. et al. The role of digital transformation in enhancing sustainability in oil and gas business operations. *International Journal of Multidisciplinary Research and Growth Evaluation*. 2024. Vol. 5. Iss. 5, p. 1029-1041. DOI: 10.54660/.IJMRGE.2024.5.5.1029-1041

24. Semenov P.V., Semishkur R.P., Diachenko I.A. Conceptual model of digital twin technology implementation for oil and gas industry. *Gas Industry*. 2019. N 7 (787), p. 24-30 (in Russian).

25. Yun J., Kim S., Kim J. Digital Twin Technology in the Gas Industry: A Comparative Simulation Study. *Sustainability*. 2024. Vol. 16. Iss. 14. N 5864. DOI: 10.3390/su16145864

26. Abakumov A.M., Antropov V.E., Vedernikov A.S., Abakumov O.A. The energy efficiency of cooling the natural gas with variable frequency drive fans. *Vestnik of Samara State Technical University. Technical Sciences Series*. 2019. N 3 (63), p. 94-104 (in Russian).

27. Kalinin A.F., Merkuryeva J.S., Fomin A.V. Performance Assessment of Variable Speed Electrical Drive for Gas Air Cooling Units on Trunk Pipeline Compressor Station. *Oil and Gas Territory*. 2019. N 11, p. 68-75 (in Russian).

28. Enbin Liu, Liuxin Lv, Yang Yi, Ping Xie. Research on the Steady Operation Optimization Model of Natural Gas Pipeline Considering the Combined Operation of Air Coolers and Compressors. *IEEE Access*. 2019. Vol. 7, p. 83251-83265. DOI: 10.1109/ACCESS.2019.2924515

29. Angjun Xie, Gang Xu, Chunming Nie et al. Operation Data Analysis and Performance Optimization of the Air-Cooled System in a Coal-Fired Power Plant Based on Machine Learning Algorithms. *Energies*. 2024. Vol. 17. Iss. 22. N 5571. DOI: 10.3390/en17225571

30. Mehrpooya M., Ghorbani B., Mousavi S.A., Zaitsev A. Proposal and assessment of a new integrated liquefied natural gas generation process with auto-Cascade refrigeration (exergy and economic analyses). *Sustainable Energy Technologies and Assessments*. 2020. Vol. 40. N 100728. DOI: 10.1016/j.seta.2020.100728

31. Klyuev R.V., Morgoev I.D., Morgoeva A.D. et al. Methods of Forecasting Electric Energy Consumption: A Literature Review. *Energies*. 2022. Vol. 15. Iss. 23. N 8919. DOI: 10.3390/en15238919

32. Babanova I.S., Prokhorova V.B., Tokarev I.S. Management of electricity consumption by oil and gas companies, taking into account the assessment of the technical condition of consumers and regulators. Moscow: Gornaya kniga, 2022, p. 372 (in Russian).

33. Shalygin A.V., Fetisov V.G., Karyakina I.V. Research of air cooler working in a main gas pipeline system. *Transport and Storage of Oil Products and Hydrocarbons*. 2023. N 2, p. 29-32 (in Russian). DOI: 10.24412/0131-4270-2023-2-29-32

34. Fahmy M.F.M., Nabih H.I. Impact of ambient air temperature and heat load variation on the performance of air-cooled heat exchangers in propane cycles in LNG plants – Analytical approach. *Energy Conversion and Management*. 2016. Vol. 121, p. 22-35. DOI: 10.1016/j.enconman.2016.05.013

35. Lei Chen, Lijun Yang, Xiaoze Du, Yongping Yang. A novel layout of air-cooled condensers to improve thermo-flow performances. *Applied Energy*. 2016. Vol. 165, p. 244-259. DOI: 10.1016/j.apenergy.2015.11.062

36. Yonghong Guo, Tongrui Cheng, Xiaoze Du, Lijun Yang. Anti-Freezing Mechanism Analysis of a Finned Flat Tube in an Air-Cooled Condenser. *Energies*. 2017. Vol. 10. Iss. 11. N 1872. DOI: 10.3390/en10111872

37. Nelyubin A.P., Podinovski V.V. Approximation of Functions Defined in Tabular Form: Multicriteria Approach. *Computational Mathematics and Mathematical Physics.* 2023. Vol. 63. N 5, p. 730-742. DOI: 10.31857/S0044466923050174

38. Silkina T.S., Lyamina N.F. Increasing energy efficiency of air cooler in associated petroleum gas disposal in oilfields. *Oil and gas technologies and environmental safety.* 2023. N 1, p. 51-58 (in Russian). DOI: 10.24143/1812-9498-2023-1-51-58

39. Arabov M.Sh., Arabov S.M. Energy efficiency of technological processes at the Astrakhan gas processing plant. *Equipment and technologies for oil and gas complex.* 2023. N 3 (135), p. 10-19 (in Russian). DOI: 10.33285/1999-6934-2023-3(135)-10-19

40. Arabov M.Sh., Gamzatova A.H., Arabova Z.M., Arabov S.M. Tubular furnace efficiency in the process of hydrocarbon condensate stabilization at the Astrakhan Gas Processing Plant. *Oil and gas technologies and environmental safety.* 2023. N 4, p. 62-69 (in Russian). DOI: 10.24143/1812-9498-2023-4-62-69

Author **Daria E. Filimoshina,** *Candidate of Engineering Sciences*, *Leading Specialist* (*GCE-energo LLC*, *Saint Petersburg*, *Russia*), *dariabatueva418@gmail.com*, *https://orcid.org/0000-0002-6945-2270*.

The author declares no conflict of interests.

ISSN 2411-3336; e-ISSN 2541-9404

JOURNAL OF MINING INSTITUTE
Zapiski Gornogo instituta
Journal homepage: pmi.spmi.ru

Research article

Geology

Experimental modeling of diamond dissolution in kimberlite within crustal cumulative centers

Anastasiya V. Kuzyura[1]✉, **Anna V. Spivak**[1], **Galina Yu. Kriulina**[2]
[1] *D.S.Korzhinskii Institute of Experimental Mineralogy of RAS, Chernogolovka, Russia*
[2] *Lomonosov Moscow State University, Moscow, Russia*

***How to cite this article*:** Kuzyura A.V., Spivak A.V., Kriulina G.Yu. Experimental modeling of diamond dissolution in kimberlite within crustal cumulative centers. Journal of Mining Institute. 2026. Vol. 277, p. 68-80.

Abstract

The main stages within the chemically active history of diamond genesis are proposed, from the upper-mantle chambers to the explosive ejections of diamonds and kimberlite material from cumulative centers to the surface. The paper focuses on the pre-final episode of diamond deposit genesis – the interaction of diamonds with carbonate-silicate kimberlite magmas in a crustal cumulate chamber. Such interactions are possible when the transport of diamonds by these magmas from the depths of the mantle primary chambers to the surface is stopped within crustal rock complexes with a strong roof. The cooling and solidification time of kimberlite melts in such cumulative centers is long enough to cause a significant mass loss of dissolving diamonds. The interaction of carbonate-silicate kimberlite melts with varying carbonate content with natural single-crystal diamonds was studied experimentally at a pressure of 0.15 GPa and a temperature of 1200 °C. Model carbonate, carbonate-fluid, natural kimberlite, and kimberlite-fluid systems were used as solvents. At experimental conditions, the solvents melted, and diamond crystals surface were underwent by dissolution. It was established that etching patterns are recorded on the growth planes, and diamonds lose mass: from 3-4.5 % after 2-hour exposure (the order of kimberlite transport time from the upper-mantle diamond-forming centers to the crustal cumulative centers) to 47.6 % after 10-day exposure (at the crustal cumulative center conditions). The results demonstrate that the dissolving ability of carbonate-silicate transport magmas is a factor that effectively reduces the diamond potential of kimberlite deposits.

Keywords

diamond genesis; diamond-forming capacity of kimberlites; diamond dissolution; kimberlite magmas; transport mantle – crust; cumulative crustal centers

Funding

The study is fulfilled under Research program N FMUF-2022-0001 of the IEM RAS.

Received: 30.04.2025 ***Accepted: 09.10.2025*** ***Online: 08.12.2025*** ***Published: 27.02.2026***

*This paper honors the memory of the eminent geochemist Yurii Andreevich Litvin,
building upon his ideas, schemes, and insights. The authors, his students
and followers, deeply appreciate and remember his scientific contribution
in diamond genesis theory and Earth's mantle geochemistry*

Introduction

There are approximately 2500 known kimberlite pipes on the Earth, and only 25 of them are currently commercial diamond deposits. This means that less than 2-3 % of kimberlite pipes are of interest for industrial diamond mining [1]. This must be taken into account when formulating public policy on the effectiveness of mineral resource management [2]. One of the main risk factors in the formation of primary diamond deposits in kimberlite pipes is the dissolving capacity of carbonate and silicate-carbonate kimberlite melts for kinetically stable metastable diamonds [3-6]. Therefore, comprehensive mineralogical and experimental studies assessing the scale of diamond potential losses during diamond dissolution at various stages remain relevant today [7-10].

According to modern views, diamond is a polygenic mineral, forming in nature under various physicochemical and geodynamic conditions [1]. Based on a physicochemical approach combining experimental, mineralogical, and computational data, Yu.A.Litvin proposed the mantle-carbonatite theory for the formation of natural diamonds and associated paragenetic and xenogenic mineral phases [7, 11]. Later developed geological-genetic models for the formation of diamond deposits [12] are based on published information about diamond-bearing kimberlite systems and original studies of the ontogenetic features of diamond crystals, and are in agreement with the aforementioned mantle-carbonatite concept. Based on the proposed models, the main stages in the origin and evolution of kimberlite diamond deposits can be identified (Fig.1).

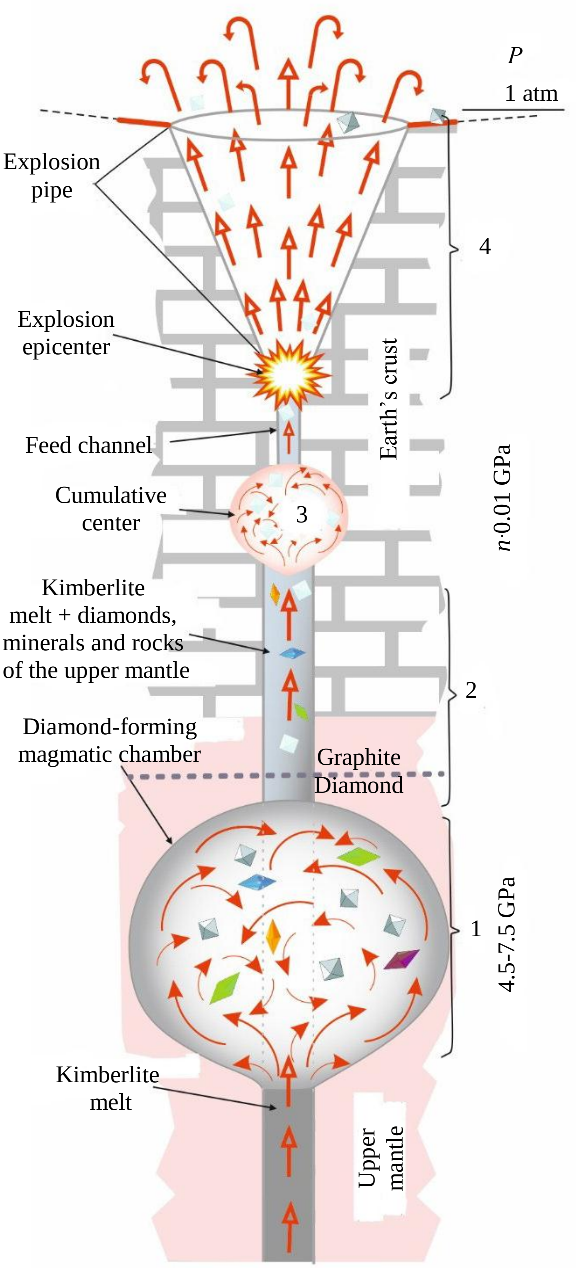

Fig.1. Schematic of diamond genesis and associated phases, and their evolution from route to the Earth's surface

Stages in the origin and evolution of kimberlite diamond deposits

1. Primary diamond crystallization. Approximately 90 % of diamonds form in the subcratonic lithospheric mantle [1]. Their nucleation and growth (in a thermodynamically stable form) occur in stationary upper-mantle magma chambers of parental melts, where the maximum diamond potential of primary diamond deposits in the explosion kimberlite pipes is established. The formed diamonds can remain in the parental magma chamber for millions of years, unchanged or altered in shape due to subsequent growth stages, partial dissolution, or mass transfer [11, 13, 14].

2. Transport of diamonds by kimberlites from the mantle magma chamber to the Earth's crust. Below the upper-mantle magma chamber, the sublithospheric mantle begins to melt due to fluids [15]. Under a subcontinental thermal regime, metasomatized zones form where the temperature increases by several hundred degrees, thus kimberlite melts form. The surfaces of the formed diamonds begin to be actively affected by high-temperature carbonate-bearing kimberlite and assimilated diamond-forming melts, which are effective diamond solvents [7, 9, 14]. As they move towards the surface, kimberlite flows carry diamonds (with inclusions) along with genetically associated minerals and diamond-bearing rocks towards the Earth's crust. The significantly carbonate (carbonatitic) composition of the liquid phase of kimberlite magma has been substantiated theoretically [3] and experimentally [16, 17].

Diamonds continue to partially lose mass in the transporting carbonate-bearing kimberlite melts during their ascent and emplacement to the continental crust. However, these losses are relatively small due to the short-term (up to several hours) dissolution of diamonds by magmas, with losses of up to 3.0-4.5 wt.% [7] during their transport into the Earth's crust. On their way to the surface, the kimberlite magma carrying xenoliths can stop temporarily, when encountering dense rocks on its way and form episodic cumulative centers [18, 19]. During this process, the rate of diamond dissolution in kimberlites increases with decreasing pressure and increasing oxygen fugacity, at least from 6.3 to 1 GPa [20].

3. The final stopping of the kimberlite flow can ultimately occur within the Earth's crust, in rock complexes with a strong roof, thus creating cumulative magma centers-chambers of kimberlite melts just before a kimberlite eruption. Here, at the lowest pressure of 0.15-0.20 GPa and still high temperatures of 1200-1250 °C [12, 21] the most favorable conditions for the dissolution of diamonds brought from the mantle depths are expected.

4. Formation of kimberlite explosion pipes. Most researchers agree on the explosive origin of diatremes as a result of the release of gases dissolved in the magma. At a depth of 1.5-3 km, regardless of temperature, the specific volume of dissolved water and CO_2 sharply increases at pressures of 0.4-0.8 kbar, resulting in the formation of an explosion center and, consequently, an explosive ejection of the highly compressed contents of the cumulative center, forming an explosion cone and filling it with kimberlite and materials displaced from the upper mantle and Earth's crust. As a result of the powerful explosion, kimberlite diamond deposits are created in the pipes, concentrating diamonds that survived after partial dissolution and were entrained by the explosion [6, 9]. At this final stage, we state the final diamond-bearing indicator of the deposit, but an additional damage to diamond content can be expected due to the incomplete removal of diamonds from the cumulative centers.

Therefore, one of the main risk factors at the formation of primary diamond deposits in kimberlite pipes is the dissolving ability of carbonate and silicate-carbonate kimberlite melts with respect to kinetically stable metastable diamonds. The extent of diamond loss due to dissolution can be determined experimentally.

The aim of this work was an experimental study of the interaction of carbonate-silicate melts with diamonds in crustal cumulative centers prior to kimberlite eruption, in order to assess the dissolving ability of carbonate and silicate-carbonate kimberlite melts, with application to the development of diamond crystal preservation factors and the determination of the productivity of primary diamond sources.

Experimental procedure

Experiments for investigation of the solubility of metastable but kinetically stable diamond were carried out on a high-pressure gas apparatus at $P = 0.15$ GPa and $T = 1200$ °C (IEM RAS, Chernogolovka). This temperature is consistent with the genetic geological model and geothermal studies [12, 21]. Solvent weight was 200 mg, along with a natural diamond crystal of various shapes (3-4 mm in size and weighing 30-50 mg), was placed in a Pt-capsule with a diameter of 7 mm, a height of 8 mm, and an ampoule wall thickness of 0.2 mm. The temperature was measured using a $Pt_{70}Rh_{30}$ (or $Pt_{94}Rh_{06}$) thermocouple and maintained by an automatic controller with an accuracy of ±2 °C. The duration of the experiments ranged from 2 to 12 days. Quenching cooling of the sample from 1200 to 800 °C occurred in 1.5-2.5 min. Reagents of analytical grade (99.5 %) were used as components for solvents of diamonds: $CaCO_3$, Na_2CO_3, oxalic acid dihydrate $H_2C_2O_4 \cdot 2H_2O$, and natural porphyritic kimberlite from the Nyurbinskaya pipe of the Yakutian diamond province (Kimb.Nyurb).

Model carbonate $CaCO_3$, $(CaCO_3)_{50}(Na_2CO_3)_{50}$, and carbonate-fluid $(CaCO_3)_{47.5}(Na_2CO_3)_{47.5}(H_2C_2O_4 \cdot 2H_2O)_5$, wt.% compositions were used as solvents in the first stage of the experiments – to understand the complete picture of diamond dissolution in complex multicomponent kimberlitic systems, ranging from predominantly carbonate to silicate-carbonate compositions. The kimberlite-carbonate mixture $(Kimb.Nyurb)_{80}(CaCO_3)_{20}$ served as the solvent at modeling the enrichment of kimberlite with Ca-carbonate just before an eruption (Table 1). To clarify the influence of the fluid on the diamond dissolution process another addition to the kimberlite was used – COH fluid in ratio 95:5 wt.%.

Analytical studies were performed at the IEM RAS. The experimental products were studied using scanning electron microscopy (SEM) and energy-dispersive X-ray spectroscopy on a Vega TS5130MM scanning electron microscope equipped with secondary and backscattered electron detectors and an INCA-PentaFET energy-dispersive X-ray detector for quantitative analysis. Microprobe analysis of the investigated samples were done at an accelerating voltage of 20 kV, an absorbed electron current of 0.1 nA, and a probe size of 0.1 μm. The analysis time per point (or area scan) was 70 s. The following were used as standards for quantitative analysis of the main elements: quartz, albite, MgO, Al_2O_3, wollastonite, as well as metals Mn, Cr, Ti, Fe.

Table 1

Starting chemical compositions of kimberlite-bearing media, wt.%

System	SiO_2	TiO_2	Al_2O_3	Cr_2O_3	Fe_2O_3	MnO	NiO	MgO	CaO	Na_2O	K_2O	P_2O_5	CO_2	H_2O	LOI*	Sum
Kimb.Nyurb	31.47	0.52	4.03	0.11	8.53	0.08	0.15	30.30	8.09	0.06	0.83	0.54			15.21	99.92
$(Kimb.Nyurb)_{80}$ $(CaCO_3)_{20}$	25.18	0.42	3.22	0.09	6.82	0.06	0.12	24.24	17.67	0.05	0.66	0.43	8.80	–	12.17	99.94
$(Kimb.Nyurb)_{95}$ $H_2C_2O_4{\cdot}2H_2O)_5$	29.90	0.49	3.83	0.10	8.10	0.08	0.14	28.79	7.69	0.06	0.79	0.51	2.50	2.5	14.45	99.92

*LOI – loss on ignition at 1100 °C for 1 day.

Raman scattering spectra of dissolved diamond crystals and the solvent medium after the experiments were obtained using a Renishaw RM1000 Raman spectrometer equipped with a Leica microscope (excitation wavelength 532 nm, power 20 mW). Spectra were recorded at 50x magnification for 100 s. The software used for data processing was Fytik 1.3.1 and OriginPro 2021. Phase identification of inclusions from Raman spectra was done using CrystalSleuth software and the RRUFF™ Project database [22]. After the experiments, the diamond crystals were cleaned with a sulfuric and nitric acid mixture, washed in alcohol, then in distilled water in an ultrasonic bath, and dried at a temperature of 120 °C. The loss of diamond mass was determined by precise weighing of the diamond crystals, with a measurement accuracy of 0.01 mg.

Experimental results on diamond dissolution at the conditions of crustal cumulative centers

Experiments on diamond dissolution at the conditions of crustal cumulative centers were conducted at a pressure of 0.15 GPa, a temperature of 1200 °C, and duration times ranging from 2 to 12 days. In the case of kimberlite and kimberlite-fluid systems samples after the experiments consisted of a dense mass with large and small pores (5-250 μm). The diamond crystal was separated with a little effort, leaving a smooth imprint in the quenching material. Carbonate and carbonate-fluid solvents after the experiments presented as a light, translucent, glassy, brittle mass. Sometimes, at opening the ampoule, spheres (50-200 μm) that appeared to be melted material could be found on its walls. The diamond crystal was easily extracted from the sample. Thus, the sample structures may indicate that the solvents were melted, and the diamond crystals were dissolved in the solvent melts.

Diamond crystals undergoing dissolution in carbonate systems become more rounded, with their surfaces becoming smoother and more uniform than they were before the experiment (Table 2). Crystals from kimberlite systems exhibit increased roughness, porosity, and cavernousness due to the formation of numerous, varied indentations (Table 3). The photographs in Table 2 and 3 were acquired using backscattered electron mode. For natural diamonds, ditrigonal and shield-shaped layers on relict faces {111} are common relief features of planar-curved forms. The layered structure of the crystal (trigonal shield-like layers) is well observed in the experimental diamond crystal from experiment KC-6 (Table 3). During the layer-by-layer growth of diamond and incomplete formation (undergrowth) of a face to the edge, striations appear along the crystal edges, formed by the ends of octahedral faces –

so-called parallel striations (run КС-12). Dissolution of the edges of octahedral faces produces sheaf-like (ditrigonal) striations. This texture can be observed on the faces of diamond crystals from the CNF-4 and KC-12 experiments (Table 2, 3).

Table 2

Experimental conditions for diamond dissolution in carbonate systems, diamond mass loss, and SEM images of diamond crystals before and after dissolution

Solvent	Sample number/ duration, days	Mass loss, %	Sample number/ duration, days	Mass loss, %
$CaCO_3$	C-2/2 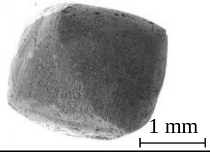 	1.71 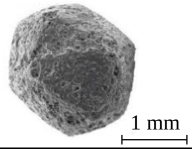 		
$(CaCO_3)_{50}(Na_2CO_3)_{50}$	CN-2/2 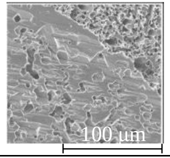 	12.40 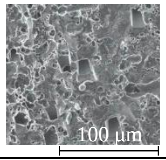 	CN-4/4 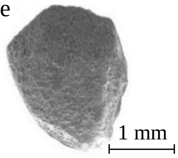 	13.42 
	CN-8/8 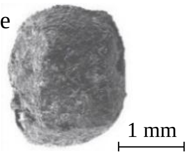 	32.44 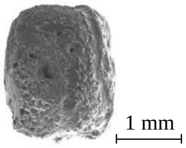 	CN-12/12 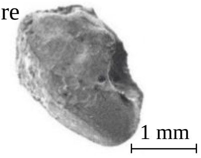 	40.00 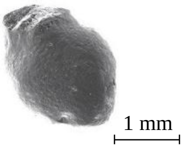
$[(CaCO_3)_{50}(Na_2CO_3)_{50}]_{95}$ $(COH)_5$	CNF-4/4  	21.34  	CNF-12/12 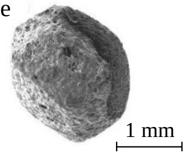 	47.63 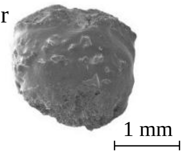

Table 3

Experimental conditions for diamond dissolution in kimberlite systems, diamond mass loss, and SEM images of diamond crystals before and after dissolution

Solvent	Sample number/ duration, days	Mass loss, %	Sample number/ duration, days	Mass loss, %
$(Kimb.Nyurb)_{80}$ $(CaCO_3)_{20}$	KC-6/6 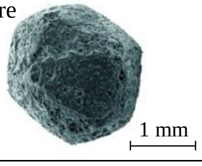 	15.92  	KC-9/9 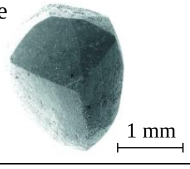 	30.51 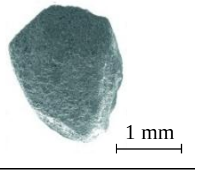
	KC-12/12 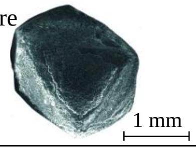 	47.62  		
$(Kimb.Nyurb)_{95}$ $(COH)_5$	KNF-10/10 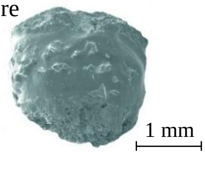 	58.78  		

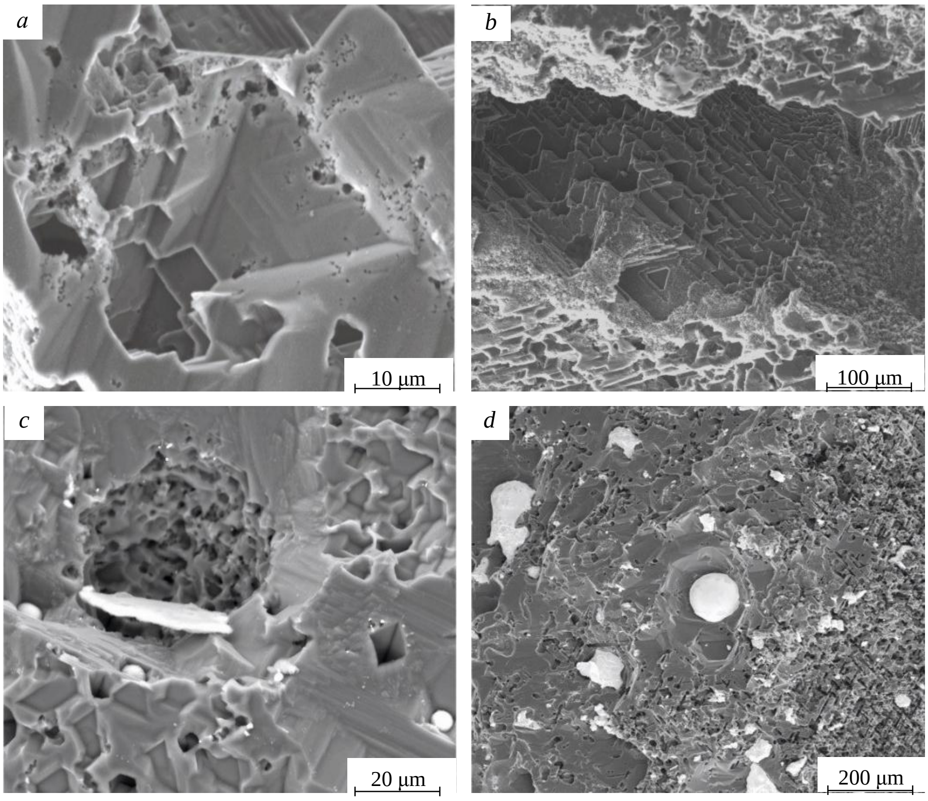

Fig.2. SEM images of etched diamond surfaces at backscattered electron mode: *a* – from experiment KC-9; *b* – from experiment CN-8; at mixed backscattered and secondary electron mode: *c* – from experiment CN-4; *d* – CNF-12

Another widely occured relief element on the {111} faces of natural diamonds are “negative trigons” [23]. Negative triangular features are evident on nearly all crystals after the experiments (Table 2, 3). Figure 2, *a*, *b* displays the magnified surface of etched facets, revealing clear negative trigons. Distinct spheres, presumably of quenched melt, are readily observed within the etch pyramids on the diamond surface (Fig.2, *c*, *d*). In the same images, it is evident that certain large triangular pits with truncated vertices have evolved into hexagonal forms.

There is a diamond crystal with a finely pitted etched surface after acid cleaning of solidified melt-solvent particles on the Fig.3, *a*, *b*. Raman spectroscopy of partially dissolved crystals demonstrated the presence of both diamond and graphite peaks (Fig.4), signifying surface graphitization of the diamonds. At using all types of solvents, the diamonds after experiments were covered with a graphite film of varying thickness. Rounded imprints of melt/fluid bubbles were observed on this film (Fig.5, *a*). Graphite formed spherical inclusions in carbonate and carbonate-fluid systems (Fig.5, *b*).

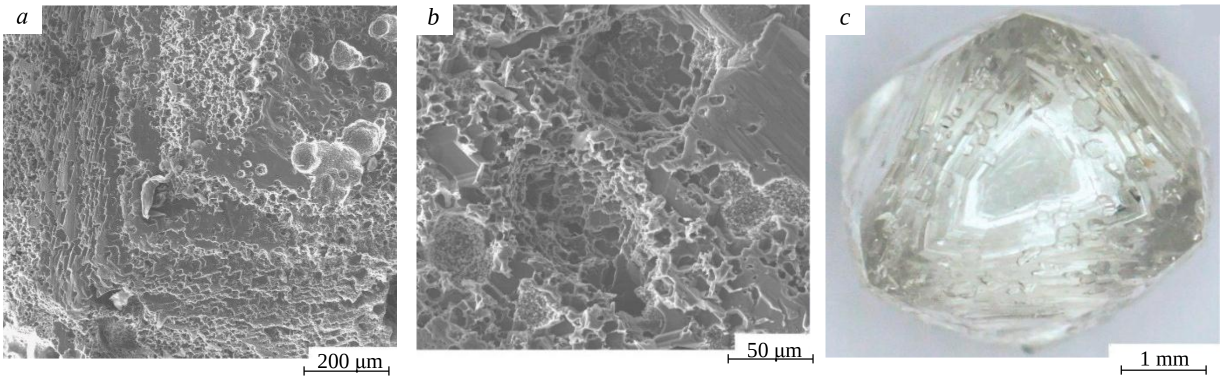

Fig.3. Micro-pitted etching morphology: *a* – on the surface of a diamond crystal from experiment CN-4; *b* – in a natural diamond crystal from the Zapolyarnaya kimberlite pipe (Yakutia, Russia); *c* – natural corrosion of a natural crystal (*b*). Photos were taken using an optical microscope at backscattered electron mode

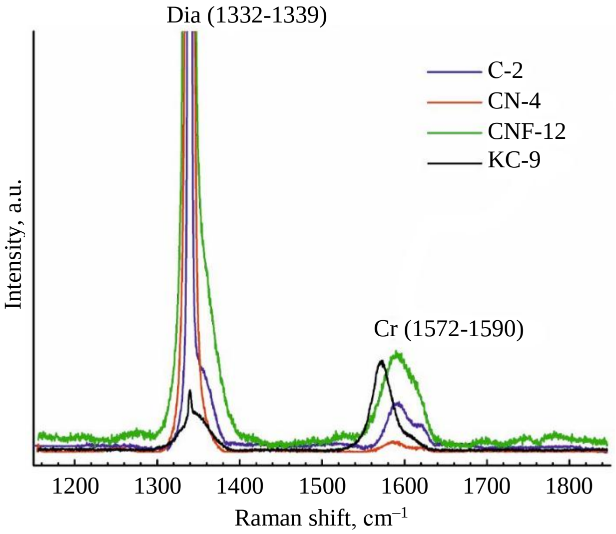

Fig.4. Raman spectra of dissolved diamonds after experiments, prior to acid purification

Figure 5, *d-f* demonstrates the process of "crust" formation at the interface between diamond and the carbonate medium. The "crust" consists of chains of graphite microspheres. The formation of graphite "dust" on the dissolving diamond crystal (Fig.5, *c*) was observed in runs with kimberlite solvent (KC-6, KC-12). Furthermore, Raman spectra of diamonds from these experiments often showed graphite peaks, despite the fact that visual inspection under an optical microscope revealed crystals that appeared "conditionally clean" without a graphite film.

The carbonate melt after the experimental procedures was a dense, white, glass-like substance. Its composition consisted of quenched dendritic crystals of calcium carbonates (in case of $CaCO_3$-solvent) or calcium and sodium carbonates (in case of a carbonate mixture $(CaCO_3)_{50}(Na_2CO_3)_{50}$) – nierite $Na_2Ca(CO_3)_2$, shortite $Na_2Ca_2(CO_3)_3$, and calcite $CaCO_3$, as confirmed by micro-X-ray spectral analysis and Raman spectroscopy (Fig.6, *a*). The sizes of the quenched crystals vary over a wide range from 1 to 100 μm. Numerous micro-voids are observed in the quenched mass, which are most likely related to the release of gaseous H_2O during quenching, this water originates from the atmosphere and is bound by hygroscopic sodium carbonate at the start of the experiment.

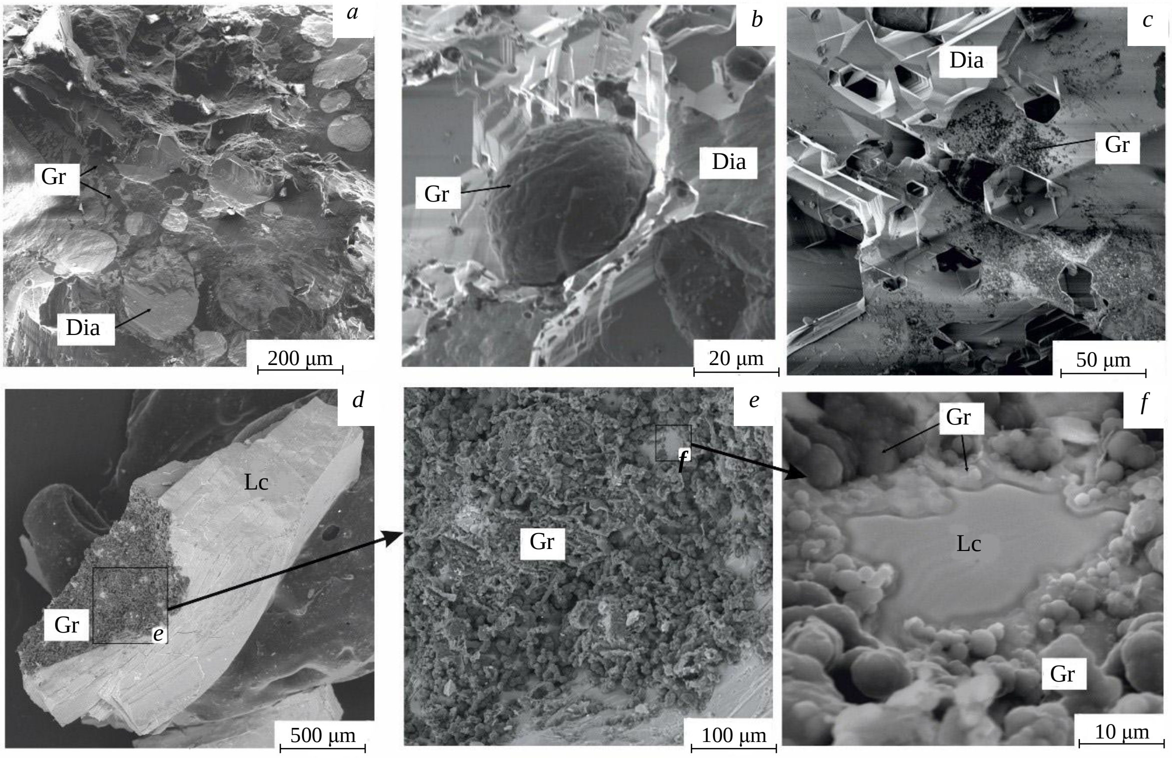

Fig.5. Graphite formation: *a* – diamond surface in a graphite film after experiment CN-4; *b* – graphite sphere on the diamond surface after experiment CNF-4; *c* – graphite "dust" on the diamond surface from experiment KC-6; *d-f* – graphite "crust" on the surface of a quenched carbonate melt at the interface with the dissolving diamond from experiment CNF-4. SEM photos of the samples at secondary electron mode (*a-c*), at mixed mode of reflected and secondary electrons (*d-f*)

Dia – diamond; Gr – graphite; Lc – carbonate melt

Experiments involving the carbonate-fluid system $(CaCO_3)_{47.5}(Na_2CO_3)_{47.5}(COH)_5$ did not reveal any substantial calcium phases. Areas with round micro-voids are found in the samples, where gas, H_2O and/or CO_2 contained in the starting composition was released during quenching. The size of the quenched crystallites is in the range of one to tens of micrometers.

During the experiments, the solvents in the experimental $(Kimb.Nyurb)_{80}(CaCO_3)_{20}$ system samples were predominantly heterogeneous, consisting of: melt ± solid phase (including olivine, clinopyroxene, and calcite) ± fluid (CO_2 and H_2O). In all experiments, after quenching, the majority of the kimberlite solvent consists of isometric, spherical quench formations, 5-25 µm in cross-section, that are in conformal contact with one another, similar to pillow lavas. The quenched melt within these "pillows" occupies 75-80 % of the sample. It is homogeneous (though fine-grained areas are also encountered), with a Ca-carbonate-silicate composition and a calculated CO_2 content of 15-22 wt.%. Relief phase relationships are evident on unpolished sample breaks. Large pores and channels indicate fluid presence in the melt during the experiment and its release during quenching. Furthermore, bubble imprints made of Ca-carbonate-silicate glasses are commonly found in the bulk of the samples.

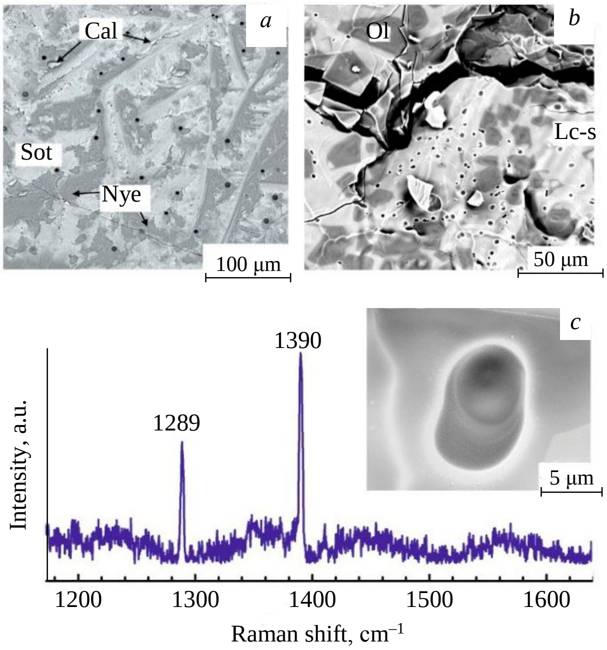

Fig.6. Formation of micro-voids in samples after experiments due to the release of gaseous H_2O and/or CO_2:
a – run CN-8; *b* – run KNF-10; *c* – CO_2-gas bubble in the experiment in quenched kimberlite melt and its Raman spectrum. SEM photos at secondary electrons mode

Ol – olivine; Cal – calcite; Nye – nyererite; Sot – shortite; Lc-s – carbonate-silicate melt

The experimental sample of the system $(Kimb.Nyurb)_{95}(COH)_5$ also showed the formation of a homogeneous miscible carbonate-silicate substance, likely a melt (Fig.6, *b*) and silicate minerals, including olivine 20-100 µm and clinopyroxene up to 400 µm. It should be noted that the KNF-10 experiment, representing a kimberlite-fluid system, was the only successful experiment in the series. In the other experiments with this start composition, the hermetically sealed ampoules could not withstand prolonged exposition and were exploded due to the large amount of free fluid. This is evidenced by the abundance of pores (bubbles) in the quenched mass. According to Raman spectroscopy data, gaseous CO_2 was detected in a closed bubble (Fig.6, *c*).

The experimental conditions and diamond mass loss are presented in Table 2, 3 and summarized in the graph (Fig.7). The lowest diamond mass loss (1.7 %) was recorded in Ca-carbonate melts after a 2-day duration. In the case of using a Ca,Na-carbonate solvent, diamond mass loss ranges from 12.40 to 39.97 % over duration periods of 2 to 12 days. Furthermore, the diamond mass loss for duration of 10 and 12 days is practically identical. The addition of 5 % fluid to the carbonate

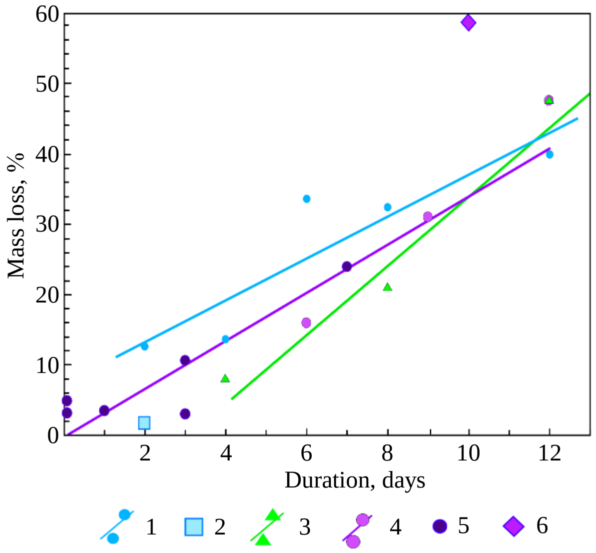

Fig.7. Dependence of diamond mass loss at their dissolution in carbonate, carbonate-fluid, kimberlite, and kimberlite-fluid solvents on duration time at P = 0.15 GPa, T = 1200-1250 °C
1 – $(CaCO_3)_{50}(Na_2CO_3)_{50}$; 2 – $CaCO_3$;
3 – $(CaCO_3)_{47.5}(Na_2CO_3)_{47.5}(COH)_5$; 4 – kimberlite of Nyurbinskaya pipe; 5 – kimberlite of Nyurbinskaya pipe by [7];
6 – $(Kimb.Nyurb)_{95}(COH)_5$

system, its influence is only evident after 12 days duration. In this carbonate-fluid melt, the mass loss reaches 47.63 %, representing an increase of 7.66 % over the mass loss observed in the “dry” carbonate melt. In experiments with kimberlite as a solvent, diamond mass loss ranged from 15.92 % after 6 days of duration to 47.62 % after 12 days of duration. Maximum losses of up to 58.79 % after 10 days of duration were recorded in the kimberlite-fluid solvent. It should be noted that after 12-day duration, the mass losses of diamonds demonstrate a very similar value for carbonate, carbonate-fluid, and kimberlite solvents.

Discussion

The results of this experimental study on diamond dissolution in carbonate and kimberlite melts in the presence of a fluid or in dry systems demonstrate that at crustal conditions, specifically within a crustal cumulative center of kimberlite melt (P = 0.15 GPa and T = 1200 °C with varying carbonate content), significant dissolution of transported diamond crystals is possible, up to 47.6 % after 10 days of duration.

Studies have demonstrated that in the crustal cumulative center, kimberlitic, kimberlite-fluid, carbonate, and kimberlite-carbonate mixtures melt, forming a melt that is the principal driver of diamond dissolution in the cumulative chamber. Solvent melting can be diagnosed by several indicators, both structural and analytical. The formation of carbonate spheres in dissolution pits on the diamond surface, the rounded pores within the dense but brittle carbonate material, and the diamond's own mass loss all suggest that these processes could only have taken place in a melt.

According to estimates based on experimental data, the primary melting temperature at the solidus of multicomponent kimberlites occurs between 800-1100 °C at pressures ranging from 0.1-0.2 GPa. The high porosity characterized by rounded pores and channels, the homogeneous chemical composition of the cement matrix between the rounded olivine grains, and the microstructures observed in the quenched samples all support the interpretation of melting. The kimberlite-carbonate mixture also melted, forming homogeneous carbonate-silicate melts and, upon quenching, these melts resulted in glasses with pores and impressions of released gas bubbles, in contrast to the alkali-carbonate-silicate immiscibility at 0.2 GPa and 1100-1250 °C [24].

The dissolution of diamonds in molten solvents led to morphological alterations, characterized by the formation of distinct dissolution morphologies. The fine pitting observed during the etching of diamond crystals in the experiment is analogous to the “corrosion” known in natural samples (see Fig.3, *c*). This phenomenon can be observed as scattered pits on the crystal’s surface, as well as a fine, net-like pattern across a surface area. Parallel hatching (as seen in experiment KC-12) can be revealed through the dissolution of diamond in metal-sulfide ± silicate solvents at 4.0-4.5 GPa and 1400-1450 °C [25, 26]. Rounded crystals are prevalent in natural diamonds [27], with the majority of their formation due to the interaction with kimberlite melt [28-30]. The conditions and mechanisms of this interaction have been the subject of long-standing scientific debate. Predominantly, they are characterized by a wide range of surface sculptures, such as trigonal or hexagonal pits, ditrigonal and shield-like layers, droplet-shaped tubercles, striations of varying intensity, and many other sculptural elements. Experimental investigations have revealed that surface sculptures on natural diamonds can be indicative of both dissolution conditions and the internal features of diamond crystals [31].

The results of experimental studies on the dissolution of diamond crystals (octahedral, pseudorhombo-dodecahedral ones, and cubes) in water-bearing carbonate and silicate melts at temperatures of 1100-1450 °C and pressures of 1-5.7 GPa [14] demonstrated that crystal dissolution can occur both during the ascent of diamonds from the mantle (upon contact with kimberlite and lamproite melts), as well as while diamonds are within the mantle. The authors demonstrated that the surface sculptural features observed on the experimental crystals are similar to those found on naturally dissolved crystals. In experiments, at a dissolution degree of 25 %, the octahedral faces are completely replaced by rounded surfaces. With further dissolution, the curvature of the surfaces changes, and at a weight loss of 45-50 %, the dissolution form of a pseudorhombo-dodecahedron becomes close to the dissolution form of an octahedron. At 50 % weight loss, cubic faces become tetrahexahedroidal and rounded, showing many quadrangular etch pits. Intensive dissolution creates deep etch channels at block boundaries, leading to a high chance of breaking along these channel’s line.

The research group experimentally found that the rate at which diamonds dissolve in kimberlitic magmas increases as pressure decreases from 6.3 to 1.0 GPa [8]. Therefore, the maximum diamond dissolution rate can be expected at the level of the Earth's crust. Previously, the interaction of Nyurbinskaya pipe kimberlite melts (Yakutia) with natural single-crystal diamonds was experimentally investigated at 0.15 GPa and 1200-1250 °C for 2 h (estimated time scale for kimberlite transport from upper-mantle diamond-forming sources to crustal cumulative centers) [7]. With weak surface dissolution of diamonds in Ca-carbonate-bearing kimberlite melt, diamond mass loss ranges from 3.0 to 4.5 %. This indicates that diamond dissolution occurs during transport, but it is insignificant due to the high ascent rate and, consequently, short residence time. The dissolution of a diamond crystal at all stages of its genesis and in the cumulative center, in particular, is discussed with reference to natural diamond “Matryoshka” [32].

Some models of kimberlite ascent suggest the upward movement of a localized, vertically constrained fracture filled with volatile-rich magma through the lithospheric mantle [12, 33]. Typical ascent rates for kimberlite magma are estimated to be between 10-30 m/s. Decarbonation and gas release are ongoing processes during the kimberlite magma's journey to the surface. As the melts rise, reactions between solid or liquid carbonates and silicates occur, leading to the release of CO_2. Furthermore, a decrease in the viscosity of the kimberlite melt by more than 3 times by the time it reaches the surface can also contribute to its rapid ascent [34].

According to E.A.Vasiliev [19], the dominance of a single diamond population in a kimberlite pipe (characterized by exceptional preservation and crystal quality, relative simplicity of their anatomy, uniformity of spectroscopic characteristics, and minimal dissolution of crystals, as observed, for example, in the Mir and Internatsionalnaya pipes) may indicate that, after the activation of kimberlite formation, a portion of the melt containing diamonds grown in a single crystallization cycle rapidly ascended to the surface, forming the kimberlite bodies. In more complex cases E.A.Vasiliev suggests the possibility of stopping that non-opening crack that drives the kimberlite melt containing diamonds at rheological boundaries, leading to the formation of an intermediate chamber where the melt cools and solidifies. In this process, some crystals are deformed and dissolved, while aggregation of defects in the crystalline structure occurs, forming complex shapes. The Zapolyarnaya diamond pipe and the M.V.Lomonosov deposit are examples of such objects, among others.

Experimental samples exhibited diamond graphitization. Diamond is known to be the thermodynamically stable phase at high pressures, while graphite is relatively stable at low pressures, down to ambient [7]. The boundary between the stability fields of diamond and graphite is defined by the graphite-diamond equilibrium curve. Graphite is kinetically stable and metastable in the diamond stability field, and diamond is kinetically stable and metastable in the graphite stability field. On the graphite-diamond equilibrium curve, the equilibrium solubilities of graphite and diamond in any solvent composition are equal. In the graphite stability region, the equilibrium solubility of diamond is greater than the solubility of the stable graphite phase. However, in a strictly isothermal experiment, the concentration of dissolved carbon in metastable diamond approaches, but cannot reach, its solubility value [35]. When the solution that dissolves metastable diamond (which has higher solubility) becomes oversaturated with respect to stable graphite (which has lower solubility), graphite crystallization happens automatically. The process can proceed until metastable diamond is completely dissolved, with continuous crystallization of stable graphite. This is the reason for the difficulties in experimentally measuring the “equilibrium” solubility of metastable diamond. This is also evidenced by the findings of graphite, and graphite films on diamond crystals of impact and metamorphic diamonds [36, 37]. Surface graphitization on diamonds from kimberlites and xenoliths occurs less frequently, in the form of very thin, semi-transparent to dense opaque graphite films [38]. Surface graphitization of diamond has been experimentally documented in undersaturated volatile silicate melts, including basaltic and kimberlitic compositions, even at high pressures [23, 39, 40].

Kimberlite pipe formation demands a huge quantity of gas, driving the melt to boil and mix with the pipe’s molten and solidified magmatic rocks [41]. Gases may start forming and accumulating in kimberlite magma right from the initial stage of the deep kimberlite melt's ascent from the mantle diamond-forming source. In addition to the original gas source, incongruent melting of carbonates occurs at various depths: magnesite $MgCO_3$ below 2.3 GPa [42], dolomite $CaMg(CO_3)_2$ at 0.5 GPa, siderite $FeCO_3$ between 0.05 and 1 GPa [43], calcite $CaCO_3$ at 0.1-0.7 GPa [44]. Moreover, the Earth's crust, where the cumulative centers form, contains carbonates and hydrous minerals, may be capable of supplying CO_2 and H_2O.

Crystallization of the liquidus silicate phases of olivine and clinopyroxene from kimberlitic magma increases the proportion of the carbonate component in residual kimberlitic melts. According to experimental data and thermodynamic modeling, the solubility of CO_2 in these melts decreases with decreasing temperature [10], which causes the separation of dissolved carbon dioxide in the form of a free fluid. As the kimberlitic system solidified upon quenching, the internal fluid pressure within the bubbles increased and grew, leading to the rupture of their envelopes. Internal fluid pressure increased when the kimberlite system solidified during quenching in bubbles, resulting in the disintegration of their shells. At low pressures, the solubility of the fluid in the kimberlite melt decreases, leading to their increasing separation from the melt. These gases, along with those produced by decomposition, accumulate in large volumes prior to eruption. The mechanism for accumulating free gases, particularly CO_2, could have also occurred within crustal cumulative kimberlite centers as they cooled. In the experiment, the presence of gas in this study is indicated by a large number of pores in the quenched samples (see Fig.6, *a*, *b*). Raman spectroscopy has detected gaseous CO_2 in these enclosed bubbles. Moreover, the accumulation of gases and the large volumes of the cumulative centers allow the kimberlite melt to mix actively, enhancing diamond dissolution.

In this way, if a kimberlite flow encounters an obstruction in form of a dense crust rocks, it will likely be stopped there for some time (day or more), resulting in the formation of a stationary crustal cumulative center. At these conditions, experimentally modelling in this work, significant dissolution of diamonds in kimberlitic fluidized melts is most probable and can reach up to ~45-50 % with a lifetime of such a center about 10 days.

Conclusion

Our experiments investigating diamond dissolution in carbonate and kimberlite melts, under both fluid-present and dry conditions, reveal that Ca,Na-carbonate melts display the highest solubility for hold times up to 6 days, when compared to kimberlite and carbonate-fluid (5 wt.% fluid) melts. For longer exposure times (up to 12 days), the aggressiveness of the experimental media and the solubility of diamond in them are practically the same under the conditions of a crustal cumulative chamber (0.15 GPa and 1200 °C). This allows for substantial dissolution of introduced diamond crystals, reaching up to 47.6 % after 10 days.

The role of crustal cumulative centers as the main risk factors for the reduction of diamondiferous potential in deposits is shown. If there are “stopping points” along the diamond’s path to the Earth’s surface, the final stop occurs in the crustal rocks just before the kimberlite eruption. The crystals brought into the chambers dissolve considerably within them, up to complete disappearance, depending on the lifetime of that cumulative center. The degree of dissolution of the deposit’s main crystal generation allows for an estimation of the probability of kimberlite magma containing diamonds being delayed in cumulative centers.

REFERENCES

1. Kaminsky F.V., Voropaev S.A. Modern Concepts on Diamond Genesis. *Geochemistry International.* 2021. Vol. 59. N 11, p. 1038-1051. DOI: 10.1134/S0016702921110033
2. Litvinenko V.S., Petrov E.I., Vasilevskaya D.V. et al. Assessment of the role of the state in the management of mineral resources. *Journal of Mining Institute.* 2023. Vol. 259, p. 95-111. DOI: 10.31897/PMI.2022.100
3. Golovin A.V., Kamenetsky V.S. Compositions of Kimberlite Melts: A Review of Melt Inclusions in Kimberlite Minerals. *Petrology.* 2023. Vol. 31. N 2, p. 143-178. DOI: 10.1134/S0869591123020030
4. Sokol A.G., Kruk A.N., Persikov E.S. Dissolution of Peridotite in a Volatile-Rich Carbonate Melt as a Mechanism of the Formation of Kimberlite-like Melts (Experimental Constraints). *Doklady Earth Sciences.* 2022. Vol. 503. Part 2, p. 157-163. DOI: 10.1134/S1028334X22040183

5. Litvin Yu.A., Spivak A.V., Kuzyura A.V. Physicogeochemical Evolution of Melts of Superplumes Uplift from the Lower Mantle to the Transition Zone: Experiment at 26 and 20 GPa. *Geochemistry International.* 2021. Vol. 59. N 7, p. 661-682. DOI: 10.1134/S0016702921070041

6. Giuliani A., Schmidt M.W., Torsvik T.H., Fedortchouk Y. Genesis and evolution of kimberlites. *Nature Reviews Earth & Environment*. 2023. Vol. 4. Iss. 11, p. 738-753. DOI: 10.1038/s43017-023-00481-2

7. Litvin Yu.A., Kuzyura A.V., Varlamov D.A. et al. Interaction of Kimberlite Magma with Diamonds Upon Uplift from the Upper Mantle to the Earth's Crust. *Geochemistry International.* 2018. Vol. 56. N 9, p. 881-900. DOI: 10.1134/S0016702918090070

8. Khokhryakov A.F., Kruk A.N., Sokol A.G., Nechaev D.V. Experimental Modeling of Diamond Resorption during Mantle Metasomatism. *Minerals*. 2022. Vol. 12. Iss. 4. N 414. DOI: 10.3390/min12040414

9. Smit K.V., Shirey S.B. Diamonds Are Not Forever! Diamond Dissolution. *Gems & Gemology*. 2020. Vol. 56. N 1, p. 148-155.

10. Fedortchouk Y., Liebske C., McCammon C. Diamond destruction and growth during mantle metasomatism: An experimental study of diamond resorption features. *Earth and Planetary Science Letters*. 2019. Vol. 506, p. 493-506. DOI: 10.1016/j.epsl.2018.11.025

11. Litvin Y.A. Genesis of Diamonds and Associated Phases. Springer, 2017, p. 51. DOI: 10.1007/978-3-319-54543-1

12. Kozlov A.V., Vasilev E.A., Ivanov A.S. et al. Genetic geological model of diamond-bearing fluid magmatic system. *Journal of Mining Institute.* 2024. Vol. 269, p. 708-720.

13. Gubanov N.V., Zedgenizov D.A., Vasilev E.A., Naumov V.A. New data on the composition of growth medium of fibrous diamonds from the placers of the Western Urals. *Journal of Mining Institute.* 2023. Vol. 263, p. 645-656.

14. Khokhryakov A.F., Palyanov Y.N. The evolution of diamond morphology in the process of dissolution: Experimental data. *American Mineralogist*. 2007. Vol. 92. Iss. 5-6, p. 909-917. DOI: 10.2138/am.2007.2342

15. Dasgupta R., Chowdhury P., Eguchi J. et al. Volatile-bearing Partial Melts in the Lithospheric and Sub-Lithospheric Mantle on Earth and Other Rocky Planets. *Reviews in Mineralogy and Geochemistry*. 2022. Vol. 87, p. 575-606. DOI: 10.2138/rmg.2022.87.12

16. Sharygin I.S., Litasov K.D., Shatskiy A. et al. Experimental constraints on orthopyroxene dissolution in alkali-carbonate melts in the lithospheric mantle: Implications for kimberlite melt composition and magma ascent. *Chemical Geology*. 2017. Vol. 455, p. 44-56. DOI: 10.1016/j.chemgeo.2016.09.030

17. Shatskiy A., Litasov K.D., Sharygin I.S., Ohtani E. Composition of primary kimberlite melt in a garnet lherzolite mantle source: constraints from melting phase relations in anhydrous Udachnaya-East kimberlite with variable CO_2 content at 6.5 GPa. *Gondwana Research*. 2017. Vol. 45, p. 208-227. DOI: 10.1016/j.gr.2017.02.009

18. Simakov S.K., Stegnitskiy Yu.B. On the presence of the postmagmatic stage of diamond formation in kimberlites. *Journal of Mining Institute.* 2022. Vol. 255, p. 319-326. DOI: 10.31897/PMI.2022.22

19. Vasilev E.A. Defects of diamond crystal structure as an indicator of crystallogenesis. *Journal of Mining Institute.* 2021. Vol. 250, p. 481-491. DOI: 10.31897/PMI.2021.4.1

20. Khokhryakov A.F., Kruk A.N., Sokol A.G. The effect of oxygen fugacity on diamond resorption in ascending kimberlite melt. *Lithos*. 2021. Vol. 394-395. N 106166. DOI: 10.1016/j.lithos.2021.106166

21. Kavanagh J.L., Sparks R.S.J. Temperature changes in ascending kimberlite magma. *Earth and Planetary Science Letters*. 2009. Vol. 286. Iss. 3-4, p. 404-413. DOI: 10.1016/j.epsl.2009.07.011

22. Lafuente B., Downs R.T., Yang H., Stone N. 1. The power of databases: The RRUFF project. Highlights in Mineralogical Crystallography. De Gruyter, 2016. P. 1-30. DOI: 10.1515/9783110417104-003

23. Fedortchouk Y., Zhuoyuan Li, Chinn I., Fulop A. Geometry of dissolution trigons on diamonds: Implications for the composition of fluid and kimberlite magma emplacement. *Lithos*. 2024. Vol. 470-471. N 107526. DOI: 10.1016/j.lithos.2024.107526

24. Shapovalov Yu.B., Kotelnikov A.R., Suk N.I. et al. Liquid Immiscibility and Problems of Ore Genesis: Experimental Data. *Petrology*. 2019. Vol. 27. N 5, p. 534-551. DOI: 10.1134/S0869591119050060

25. Chepurov A.I., Sonin V.M., Zhimulev E.I. et al. Dissolution of diamond crystals in a heterogeneous (metal–sulfide–silicate) medium at 4 GPa and 1400 °C. *Journal of Mineralogical and Petrological Sciences*. 2018. Vol. 113. Iss. 2, p. 59-67. DOI: 10.2465/jmps.170526

26. Sonin V.M., Zhimulev E.I., Chepurov A.A. et al. Incipient stages of transformation of round natural diamonds under dissolution in Fe-S melt at high pressure. *Lithosphere.* 2019. Vol. 19. N 6, p. 945-952 (in Russian). DOI: 10.24930/1681-9004-2019-19-6-945-952

27. Orlov Yu.L. Diamond Mineralogy (in Russian). Moscow: Nauka, 1984, p. 170.

28. Ragozin A., Zedgenizov D., Kuper K., Palyanov Y. Specific Internal Structure of Diamonds from Zarnitsa Kimberlite Pipe. *Crystals*. 2017. Vol. 7. Iss. 5. N 133. DOI: 10.3390/cryst7050133

29. Khokhryakov A.F., Nechaev D.V., Sokol A.G. Microrelief of Rounded Diamond Crystals as an Indicator of the Redox Conditions of Their Resorption in a Kimberlite Melt. *Crystals*. 2020. Vol. 10. Iss. 3. N 233. DOI: 10.3390/cryst10030233

30. Kostrovitsky S., Dymshits A., Yakovlev D. et al. Primary Composition of Kimberlite Melt. *Minerals*. 2023. Vol. 13. Iss 11. N 1404. DOI: 10.3390/min13111404

31. Palyanov Yu.N., Khokhryakov A.F., Kupriyanov I.N. Crystallomorphological and Crystallochemical Indicators of Diamond Formation Conditions. *Crystallography Reports.* 2021. Vol. 66. N 1, p. 142-155. DOI: 10.1134/S1063774521010119

32. Litvin Yu.A. Physicogeochemical Mechanisms of the Genesis of Matryoshka-Type Diamonds on the Basis of the Mantle-Carbonatite Theory. *Geochemistry International.* 2023. Vol. 61. N 3, p. 238-251. DOI: 10.1134/S0016702923030072

33. Barnes S.J., Yudovskaya M.A., Iacono-Marziano G. et al. Role of volatiles in intrusion emplacement and sulfide deposition in the supergiant Norilsk-Talnakh Ni-Cu-PGE ore deposits. *Geology*. 2023. Vol. 51. N 11, p. 1027-1032. DOI: 10.1130/G51359.1

34. Persikov E.S., Bukhtiyarov P.G., Sokol A.G. Change in the viscosity of kimberlite and basaltic magmas during their origin and evolution *(prediction)*. *Russian Geology and Geophysics.* 2015. Vol. 56. N 6, p. 885-892. DOI: 10.1016/j.rgg.2015.05.005

35. Litvin Yu.A. The physicochemical conditions of diamond formation in the mantle matter: experimental studies. *Russian Geology and Geophysics.* 2009. Vol. 50. N 12, p. 1188-1200. DOI: 10.1016/j.rgg.2009.11.017

36. Masaitis V.L., Futerhendler S.I., Gnevushev M.A. Diamonds in impactites of the Popigay meteoretic crator. *Zapiski Vsesoyuznogo mineralogicheskogo obshchestva*. 1972. Part 101, p. 108-112 (in Russian).

37. Korsakov A.V., Shatsky V.S. Origin of graphite-coated diamonds from ultrahigh-pressure metamorphic rocks. *Doklady Earth Sciences.* 2004. Vol. 399. N 8, p. 1160-1163.

38. Fedortchouk Y. A new approach to understanding diamond surface features based on a review of experimental and natural diamond studies. *Earth-Science Reviews*. 2019. Vol. 193, p. 45-65. DOI: 10.1016/j.earscirev.2019.02.013

39. Sonin V., Leech M., Chepurov A. et al. Why are diamonds preserved in UHP metamorphic complexes? Experimental evidence for the effect of pressure on diamond graphitization. *International Geology Review*. 2019. Vol. 61. Iss. 4, p. 504-519. DOI: 10.1080/00206814.2018.1435310

40. Korsakov A.V., Zhimulev E.I., Mikhailenko D.S. et al. Graphite pseudomorphs after diamonds: An experimental study of graphite morphology and the role of H_2O in the graphitisation process. *Lithos*. 2015. Vol. 236-237, p. 16-26. DOI: 10.1016/j.lithos.2015.08.012

41. Gernon T.M., Gilbertson M.A., Sparks R.S.J., Field M. The role of gas-fluidisation in the formation of massive volcaniclastic kimberlite. *Lithos*. 2009. Vol. 112. Suppl. 1, p. 439-451. DOI: 10.1016/j.lithos.2009.04.011

42. Sutao Zhao, Poli S., Schmidt M.W. et al. An experimental determination of the liquidus and a thermodynamic melt model in the $CaCO_3$-$MgCO_3$ binary, and modelling of carbonated mantle melting. *Geochimica et Cosmochimica Acta*. 2022. Vol. 336, p. 394-406. DOI: 10.1016/j.gca.2022.08.014

43. Kang N., Schmidt M.W., Poli S. et al. Melting of siderite to 20 GPa and thermodynamic properties of $FeCO_3$-melt. *Chemical Geology*. 2015. Vol. 400, p. 34-43. DOI: 10.1016/j.chemgeo.2015.02.005

44. Irving A.J., Wyllie P.J. Subsolidus and melting relationships for calcite, magnesite and the join $CaCO_3$-$MgCO_3$ 36 kb. *Geochimica et Cosmochimica Acta*. 1975. Vol. 39. Iss. 1, p. 35-53. DOI: 10.1016/0016-7037(75)90183-0

***Authors*: Anastasiya V. Kuzyura,** *Candidate of Geological and Mineralogical Sciences, Senior Researcher* (*D.S.Korzhinskii Institute of Experimental Mineralogy of RAS, Chernogolovka, Russia*), *shushkanova@iem.ac.ru*, *https://orcid.org/0000-0002-1769-8711*, **Anna V. Spivak,** *Doctor of Geological and Mineralogical Sciences, Chief Researcher* (*D.S.Korzhinskii Institute of Experimental Mineralogy of RAS, Chernogolovka, Russia*), *https://orcid.org/0000-0001-9688-520X*, **Galina Yu. Kriulina,** *Candidate of Geological and Mineralogical Sciences, Researcher* (*Lomonosov Moscow State University, Moscow, Russia*), *https://orcid.org/0009-0009-8495-9289*.

The authors declare no conflict of interests.

ISSN 2411-3336; e-ISSN 2541-9404

JOURNAL OF MINING INSTITUTE

Zapiski Gornogo instituta

Journal homepage: pmi.spmi.ru

Research article *Energy*

Assessment of reliability parameters for workshop power supply circuits in mining enterprises with single-transformer substations under various redundancy methods

Renata M. Petrova✉, **Elena I. Gracheva**
Kazan State Power Engineering University, Kazan, Republic of Tatarstan, Russia

***How to cite this article*:** Petrova R.M., Gracheva E.I. Assessment of reliability parameters for workshop power supply circuits in mining enterprises with single-transformer substations under various redundancy methods. Journal of Mining Institute. 2026. Vol. 277, p. 81-93.

Abstract

With the increasing complexity of electrical equipment in mining enterprises, the development and analysis of methods to enhance the reliability of technical devices within power supply systems are becoming increasingly relevant. This article focuses on assessing the reliability parameters of workshop network circuits in mining enterprises equipped with single-transformer substations operating at 10 and 0.4 kV, considering various redundancy methods. Research objective is to evaluate the reliability parameters of different redundancy methods for power supply circuits in facilities with transformer substations at medium voltage (MV) and low voltage (LV), with respect to low-voltage switchgear consumers in mining operations. Research target is the power supply system of an auxiliary production workshop at a mining enterprise (Kemerovo). The study examines the following network reliability parameters: probability of failure-free (normal) operation, $P(t)$; probability of failure occurrence, $Q(t)$; failure flow rate, ω_{circuit}; time between failures (TBF), T_{TBF}. The analysis covers the following circuit configurations: without redundancy; with redundancy at MV; with redundancy at LV; with dual redundancy (at both MV and LV). Estimation results indicate that the TBF for the nonredundant circuit is 2.04 times lower than for the LV redundancy circuit, 2.11 times lower than for the MV redundant circuit, and 2.8 times lower than for the dual redundant circuit. Redundancy proves to be a technically and economically justified method for improving the $P(t)$ parameter of the facility's power supply system. The obtained results can be integrated into power supply system design (to optimize structural circuits and select rational redundancy methods for components), maintenance program development (to develop justified maintenance and repair schedules), reliability monitoring system development (to enable continuous monitoring of equipment status in mining enterprise workshops).

Keywords

mining enterprise; workshop; looped circuit; circular circuit; reliability logic diagram; failure flow rate; time between failures; redundancy; dual redundancy

Received: 31.01.2025 ***Accepted: 02.07.2025*** ***Online: 23.12.2025*** ***Published: 27.02.2026***

Introduction

With the increasing complexity of process and electrical equipment in mining enterprises, the development and analysis of methods to enhance the reliability of technical devices within power supply systems (PSS) become topical issues. The reliability of PSS equipment operation can be assessed both at early stages (design, reconstruction) and after equipment commissioning [1-3]. A necessary condition for obtaining valid results in reliability parameter estimations is ensuring compliance with methodological and informational error requirements [4]. It is known that electrical equipment components of workshop PSS in mining enterprises can be either repairable after failure or non-repairable [5].

Ensuring the reliability and failure-free operation of electrical installations is achieved by complying with regulated storage conditions, normal operating modes, and requirements for maintenance and repair [6, 7].

The relevance of this issue stems from the continuous growth in electricity consumption at mining and dressing enterprises, coupled with the increasing complexity of structural and topological characteristics of PSS. This complexity manifests itself in a growing number of circuit elements and increasingly intricate functional interconnections between them. These factors create prerequisites for developing new methodologies to estimate the reliability of complex, highly interconnected systems [8, 9]. In particular, study [10] focuses on analysing the key reliability parameters and performance indicators of electrical equipment at industrial facilities in Kazan.

Methodological foundations for reliability analysis of electrotechnical complexes applied to load nodes involve developing algorithms to determine probabilities of failure occurrence and that of failure-free system operation [11-13]. As structural interconnections between elements become more complex, traditional methods of transforming design circuits into series-parallel or parallel-series configurations become inapplicable [14-16].

Specific features are inherent to “bridge” [17] and “double bridge” circuit types, for which the rules of series-parallel or parallel-series reliability circuit transformations do not apply. For such cases, special analysis methods are required, including logical-probabilistic methods, graph theory, matrix calculation methods, and numerical simulation via the Monte Carlo method [18, 19]. A promising direction is the development of combined algorithms that integrate analytical approaches and mathematical modelling. This is especially relevant for complex, multi-level PSS at mining enterprises.

The development of electrical system equipment necessitates improving the reliability of electrical installations and PSS as a whole [20]. This objective is achieved through refining design methods using software solutions as well as developing new types of electrical installations. An analysis of failure causes and defects in low-voltage equipment at mining enterprises reveals that ~40-45 % of total failures result from design errors, 20 % from manufacturing errors, 30 % are caused by harsh operating conditions, unacceptable operating modes, or improper maintenance, ~5-7 % are due to natural wear and equipment aging [9, 21].

The literature presents the following methods for assessing reliability parameters of single-transformer substations: development of a system model that integrates economic indicators and failure characteristics [22, 23]; method for evaluating the reliability of power supply to consumers, enabling electricity quality management based on network equipment condition data [24]; quantitative risk assessment method for power supply interruptions using Bayesian networks, which identifies factors affecting power system reliability [25]; implementation of automatic blocking in distribution networks through node optimization, along with reliability analysis of power supply in distribution networks by blocks [26]; creation of a comprehensive reliability management model for accurate prediction of power system behaviour [27]; optimization of PSS maintenance schedules, accompanied by analysis of reliability parameters for distribution network components [28, 29]; statistical method for power system reliability assessment, accounting for operational conditions through Monte Carlo simulation and development of probabilistic reliability models [30, 31].

Energy and resource conservation are among the priority tasks [32, 33] in managing energy-intensive mining production. Measures aimed at improving energy efficiency and conservation, which are being implemented in PSS of mining enterprises [34, 35], can be conventionally categorized into the following areas: electrical networks; electric drives; monitoring and accounting of electricity consumption [36, 37].

Research objective is to assess the reliability parameters of various redundancy methods for power supply circuits in PSS of facilities with transformer substations operating at medium voltage

(MV) and low voltage (LV), with respect to low-voltage switchgear consumers in mining enterprises [38-40]. Scientific novelty of the proposed method introduces development and construction of a reliability logic diagram that accounts for each type of equipment, simplification of the diagram in accordance with reliability theory, incorporating statistical data on probabilistic characteristics of each component, as well as estimation of the total failure flow rate and failure-free operation time for the circuit that differs from existing methods by explicitly considering elements of the 0.4 kV network, including low-voltage switching devices. Research target is the PSS of an auxiliary production workshop at a mining enterprise (Kemerovo).

Methods

The study examines the following types of electrical circuits:

1. Without redundancy.
2. With LV redundancy (by installing a 0.4 kV bypass jumper).
3. With MV redundancy (by installing disconnectors, S), without LV redundancy.
4. With dual redundancy at both MV and LV levels.

Analysis of failure statistics leads to the conclusion that the reliability parameters of the circuit conform to the exponential distribution law [5].

The key reliability indicators for PSS circuit elements include:

- failure flow rate

$$\omega(t) = \lim_{\Delta t \to 0} \frac{Q(t, t+\Delta t)}{\Delta t},$$

defined by the probability of failure occurrence $Q(t, \Delta t)$ in the time interval t, Δt;

- probability of failure-free (normal) operation

$$P = e^{-\omega(t)};$$

- probability of failure occurrence;

$$Q = 1 - P = 1 - e^{-\omega(t)};$$

- time between failures

$$T_{\text{TBF}} = \frac{1}{\omega(t)}.$$

Discussion

The study examines the reliability parameters of four possible variants of circuit redundancy.

Diagram of the network section without redundancy (Fig.1, *a*). Figure 1, *b*, *c* shows the structural reliability diagram without redundancy and its transformation. All elements are connected in series, and the failure of any one element leads to loss of operability of the entire system. The efficiency of such a circuit depends, firstly, on the initial state parameters and, secondly, on the probabilistic sequence of element (node) failures.

Failure flow rate for the power supply source-to-load circuit (Fig.1, *b*, *c*) for the nonredundant circuit section:

$$\omega_{\text{nonred}} = \omega_1 + \omega_2 + \omega_3 + \ldots + \omega_{20} = \omega_{\text{VCB}_1} + \omega_{\text{L}_1} + \omega_{\text{T}_1} + \omega_{\text{QF}_1} + \omega_{\text{QF}_2} + \omega_{\text{L}_2} + \omega_{\text{QF}_3} + \omega_{\text{Q}} + \omega_{\text{QF}_4} +$$

$$+ \omega_{\text{L}_3} + \omega_{\text{KM}_1} + \omega_{\text{QF}_5} + \omega_{\text{L}_4} + \omega_{\text{KM}_2} + \omega_{\text{QF}_6} + \omega_{\text{L}_5} + \omega_{\text{KM'}_1} + \omega_{\text{QF}_7} + \omega_{\text{L}_6} + \omega_{\text{KM'}_2} =$$

$$= \omega_{\text{VCB}} + \omega_{\text{L}_{10\text{kV}}} + \omega_{\text{T}} + 7\omega_{\text{QF}} + 5\omega_{\text{L}_{0.4\text{kV}}} + \omega_{\text{Q}} + 2\omega_{\text{KM}} + 2\omega_{\text{KM'}}.$$

The failure flow rate of the cable line $\omega_{\text{L}_{10\text{kV}}}$ (SKl-10 kV) depends on its length and is estimated based on the specific parameter per 1 km: $\omega_{\text{L}_1} = 0.01(100\ \text{m}/1000\ \text{m}) = 0.001$ failures/year.

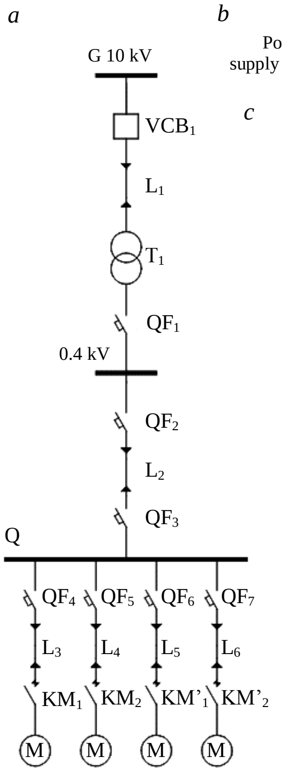

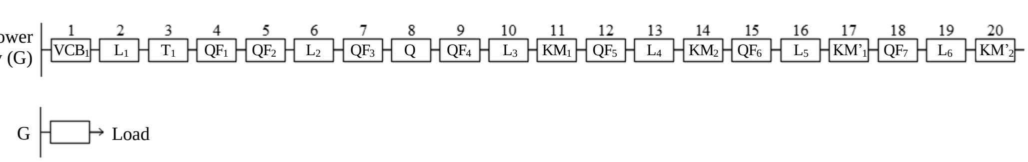

Fig.1. Diagram of a network section without redundancy (*a*), logical reliability diagram without redundancy (*b*), and its transformation (*c*)

The failure flow rate of the $\omega_{L0.4kV}$ cable line (AVVG-0.4 kV) is estimated similarly:

- for L_2

$$\omega = 0.026\,(10\text{ m}/100\text{ m}) = 0.0026\text{ failures/year};$$

- for $L_3...L_6$

$$\omega = 0.026\,(5\text{ m}/100\text{ m}) = 0.0013\text{ failures/year}.$$

Table 1 presents the basic and estimated characteristics of the equipment (Fig.1, *a*), based on an analysis of product catalogues from companies manufacturing high-voltage electrical equipment and apparatus: Vysokovoltnyy Soyuz LLC; Unkomtech Trading House LLC (cable and wiring products); ELTECHKOM LLC (high-voltage equipment); KEAZ JSC (electrical products); "Absolutenergo" (electrical products); EXPERT CABLE (cable and wiring products).

Table 1

Specifications of the equipment and estimation results for the failure flow rate ω of the circuit elements

Elements	Grade, manufacturer	ω, failures/year
VCB_1	VRS-10, Vysokovoltnyy Soyuz LLC[1]	0.015
L_1	SKl-10kV, cross-section 70 mm², length 100 m, Unkomtekh Trading House LLC[2]	0.001
T_1	TM-1600/10/0.4, ELTECHKOM LLC[3]	0.015
QF_1, QF_2, QF_3	VA51-39, Kursk Electrical Equipment Plant JSC (KEAZ)[4]	0.051
QF_4, QF_5, QF_6, QF_7	VA51-35, KEAZ JSC[4]	0.051
Q	ShRS-1, "Absolutenergo"[5]	0.001
L_2	AVVG-0.4 kV, cross-section 16 mm², length 10 m, EXPERT CABLE[6]	0.026
L_3, L_4, L_5, L_6	AVVG-0.4 kV, cross-section 4 mm², length 5 m, EXPERT CABLE[6]	0.0013
KM_1, KM_2	PML-1100, KEAZ JSC[4]	0.095
KM'_1, KM'_2	KT-6000, KEAZ JSC[4]	0.098

Thus,

$$\omega_{\text{nonred}} = 0.015 + 0.01 + 0.015 + 7\cdot0.051 + (0.0026 + 4\cdot0.0013) + 0.001 + 2\cdot0.095 + 2\cdot0.098 = 0.7828;$$

$$T_{\text{TBF}} = \frac{1}{\omega} = \frac{1}{0.7828} = 1.2775.$$

Diagram of a network section with LV redundancy (*with a 0.4 kV bypass jumper*) (Fig.2). Redundancy is a method for increasing the reliability of electrical installations, based on replacing a failed unit with a backup one. The main redundancy methods:

- Element-level (component-level) – redundancy of individual system components (transformers, circuit breakers, cable lines, etc.).

---

[1] Vysokovoltnyy Soyuz LLC catalogue. URL: https://www.vsoyuz.com/ (accessed 31.01.2025).

[2] Unkomtekh Trading House LLC catalogue. URL: https://www.uncomtech.ru/ (accessed 31.01.2025).

[3] ELTECHKOM LLC catalogue. URL: https://eltexkom.com/silovye-transformatory/ (accessed 31.01.2025).

[4] KEAZ JSC catalogue. URL: https://keaz.ru/catalog (accessed 31.01.2025).

[5] Absolutenergo LLC catalogue. URL: https://absolutnrg.ru/catalog/elektrochit/nickovol.html (accessed 31.01.2025).

[6] EXPERT CABLE catalogue. URL: https://expert-cable.ru/catalog/ (accessed 31.01.2025).

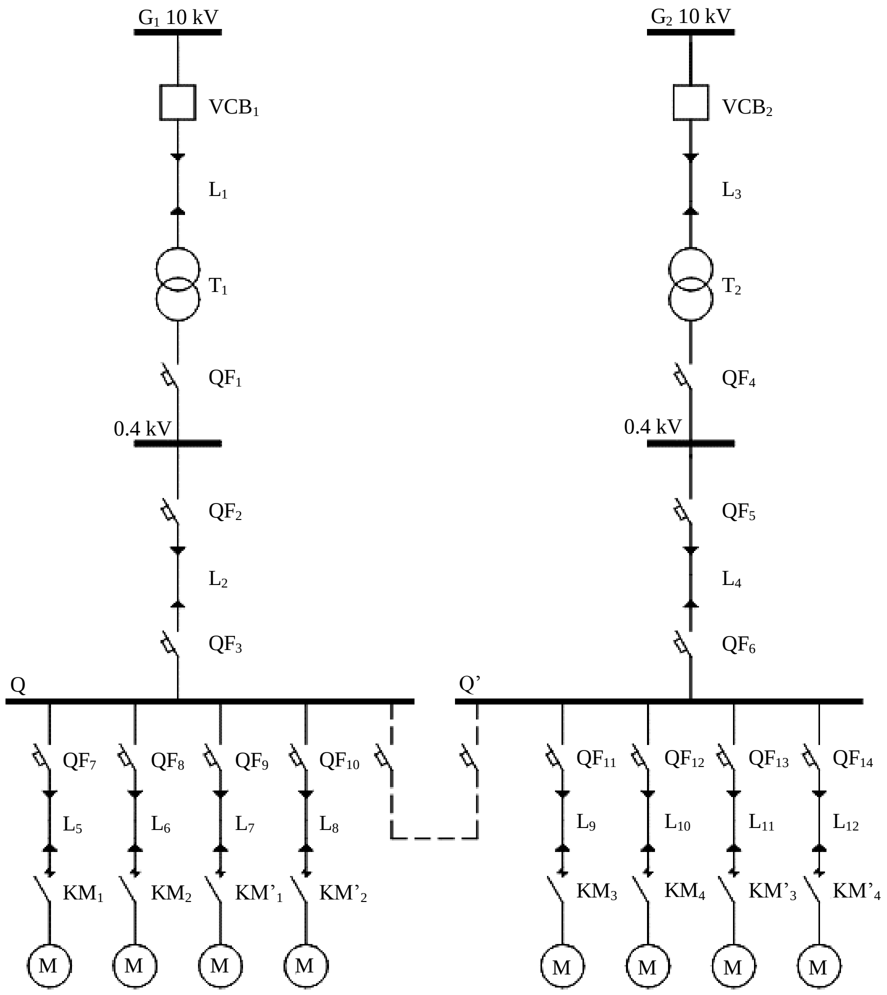

Fig.2. Diagram of a network section with LV redundancy

- Group (modular) – redundancy of functional equipment groups (transformer, circuit breaker, cable line).
- General (system-wide) redundancy – full duplication of the PSS.

For the electrical supply circuit of the first bus section with an installed LV 0.4 kV bypass jumper (b/jump) (Fig.2), the reliability logic diagram consists of two series operational circuits connected in parallel by the b/jump element (Fig.3).

The first stage involves transforming the series branches (Fig.3, *b*).

The failure flow rate for the G_1-b/jump circuit is:

$$\omega_{G_1\text{-b/jump}} = \omega_1 + \ldots + \omega_8 = \omega_{VCB_1} + \omega_{L_1} + \omega_{T_1} + \omega_{QF_1} + \omega_{QF_2} + \omega_{L_2} + \omega_{QF_3} + \omega_Q =$$

$$= 0.015 + 0.001 + 0.015 + 3\cdot 0.051 + 0.0026 + 0.001 = 0.1876.$$

The failure flow rate for the G_2-b/jump circuit is

$$\omega_{G_2\text{-b/jump}} = \omega_{21} + \ldots + \omega_{28} + \omega_{\text{b/jump}}.$$

The bypass jumper includes two automatic circuit breakers and a 0.4 kV cable line. The failure flow rate of the b/jump is:

$$\omega_{\text{b/jump}} = \omega_{QF} + \omega_{L_{0.4\text{kV}}} + \omega_{QF} = 2\omega_{QF} + \omega_{L_{0.4\text{kV}}} = 2\cdot 0.051 + 0.0013 = 0.1033;$$

$$\omega_{G_2\text{-b/jump}} = \omega_{VCB_2} + \omega_{L_3} + \omega_{T_2} + \omega_{QF_4} + \omega_{QF_5} + \omega_{L_4} + \omega_{QF_6} + \omega_{Q'} + \omega_{\text{b/jump}} =$$

$$= 0.015 + 0.001 + 0.015 + 3\cdot 0.051 + 0.0026 + 0.001 + 0.1033 = 0.2909.$$

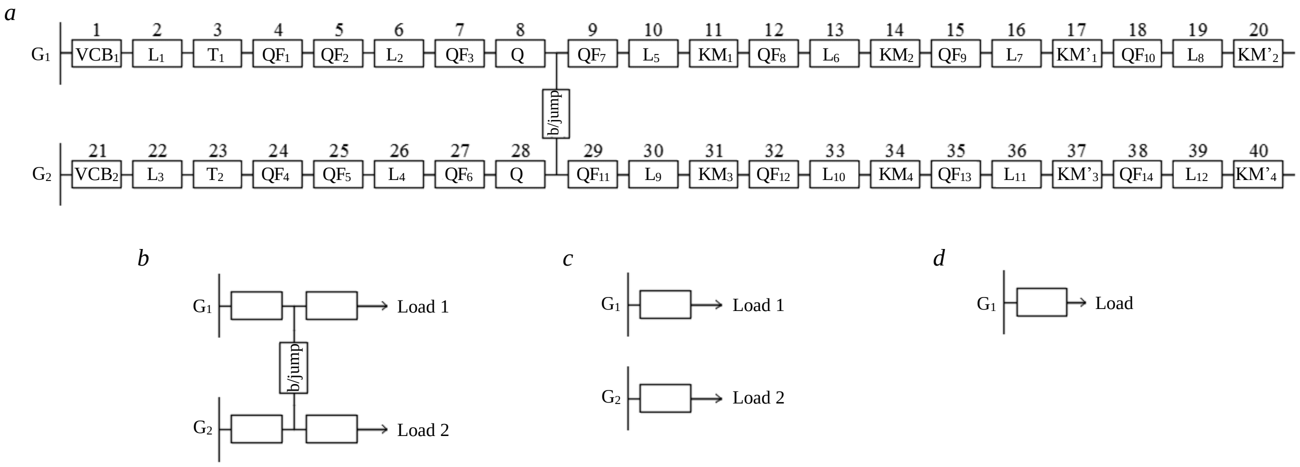

Fig.3. Logical reliability diagram for a network section with LV redundancy (*a*), transformation stages: first (*b*), second (*c*), and third (*d*)

Failure flow rate of the b/jump-load$_1$ circuit:

$$\omega_{\text{b/jump-load}_1} = \omega_9 + \ldots + \omega_{20} = \omega_{\text{QF}_7} + \omega_{\text{L}_5} + \omega_{\text{KM}_1} + \omega_{\text{QF}_8} + \omega_{\text{L}_6} + \omega_{\text{KM}_2} + \omega_{\text{QF}_9} + \omega_{\text{L}_7} + \omega_{\text{KM'}_1} + \omega_{\text{QF}_{10}} +$$

$$+ \omega_{\text{L}_8} + \omega_{\text{KM'}_2} = 4\omega_{\text{QF}} + 4\omega_{\text{L}} + 2\omega_{\text{KM}} + 2\omega_{\text{KM'}} = 4\cdot 0.051 + 4\cdot 0.0013 + 2\cdot 0.095 + 2\cdot 0.098 = 0.5952.$$

Failure flow rate of the b/jump-load$_2$ parallel circuit:

$$\omega_{\text{b/jump-load}_2} = \omega_{29} + \ldots + \omega_{40} = 0.5952.$$

The second stage is presented in Fig.3, *c*.

Failure flow rate of the G$_1$-load$_1$ circuit:

$$\omega_{\text{G}_1\text{-load}_1} = \omega_{\text{G}_1\text{-b/jump}} + \omega_{\text{b/jump-load}_1} = 0.1876 + 0.5952 = 0.7828.$$

Failure flow rate of the G$_2$-load$_2$ parallel circuit:

$$\omega_{\text{G}_2\text{-load}_2} = \omega_{\text{G}_2\text{-b/jump}} + \omega_{\text{b/jump-load}_2} = 0.2909 + 0.5952 = 0.8861.$$

At the third stage, it is necessary to estimate the probabilities of failure occurrence for the series branches. Probabilities of failure-free operation of the circuits:

$$P_{\text{G}_1\text{-load}_1} = e^{-0.7828} = 0.4571;$$

$$P_{\text{G}_2\text{-load}_2} = e^{-0.8861} = 0.4123.$$

Probabilities of failure occurrence for the circuits:

$$Q_{\text{G}_1\text{-load}_1} = 1 - e^{-0.7828} = 0.5429;$$

$$Q_{\text{G}_2\text{-load}_2} = 1 - e^{-0.8861} = 0.5877.$$

The third stage involves transforming the parallel branches G$_1$-load$_1$ and G$_2$-load$_2$.

Probability of failure occurrence for a circuit with two parallel-connected elements:

$$Q_{\text{circuit}} = Q_{\text{G}_1\text{-load}_1} Q_{\text{G}_2\text{-load}_2} = 0.5429\cdot 0.5877 = 0.319.$$

Probability of failure-free operation of the circuit:

$$P_{\text{circuit}} = 1 - Q_{\text{circuit}} = 1 - 0.319 = 0.681.$$

Knowing P_{circuit}, one can determine the failure flow rate for a system with two parallel-connected elements, as well as the time between failures:

$$\omega_{\text{circuit}} = -\ln(P_{\text{circuit}}) = -\ln(0.681) = 0.3842;$$

$$T_{\text{TBF}} = 1/0.3842 = 2.6028.$$

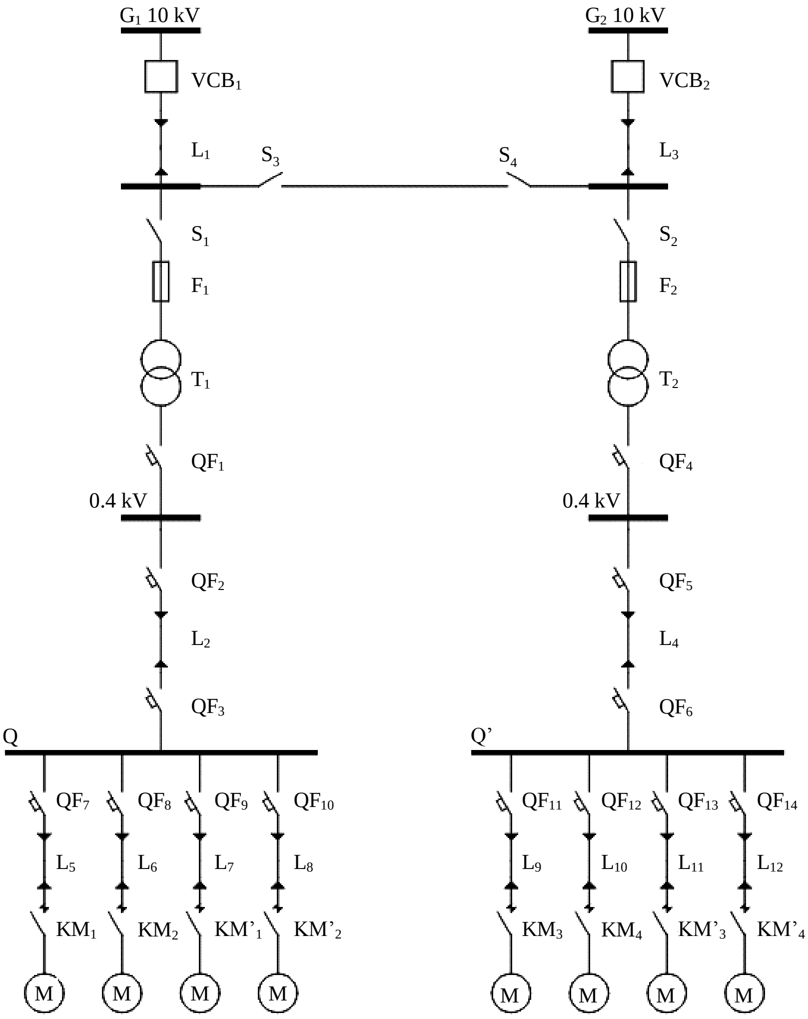

Fig.4. Circuit with MV redundancy and no LV redundancy

Logic diagram with redundancy at the MV line (*with disconnectors S_3 and S_4 installed*), *without redundancy at LV.* Figure 4 shows a looped circuit variant. In cases of low power supply source (G) capacity, remote location, or uneconomical operation, the power supply source is considered a backup one and is activated when the main power source is disconnected. If the power sources are equivalent, power is supplied from each source.

In case of a fault on one of the lines, power to the consumers of that line is disconnected via disconnectors S_3 and S_4, while the adjacent sections of the circuit remain operational.

The reliability probabilistic logic diagram (Fig.5) comprises two series operational circuits (G_1-load$_1$, G_2-load$_2$) connected by a parallel branch of elements S_3-L-S_4.

The reliability logic diagram and transformation stages are similar to those presented in Fig.3.

Redundancy of the MV line is provided by two disconnectors (S_3, S_4) and a cable line (L). The failure flow rate of the bypass jumper (b/jump):

$$\omega_{\text{redund}} = \omega_{45} + \omega_{46} + \omega_{47} = \omega_{S3} + \omega_{L} + \omega_{S4}.$$

The probabilities of failure occurrence and failure-free operation for the circuit (Fig.5, *c*):

$$Q_{\text{circuit}} = Q_{G_1\text{-load}_1} Q_{G_2\text{-load}_2} = 0.5371\cdot 0.5773 = 0.31;$$

$$P_{\text{circuit}} = 1 - Q_{\text{circuit}} = 1 - 0.31 = 0.69.$$

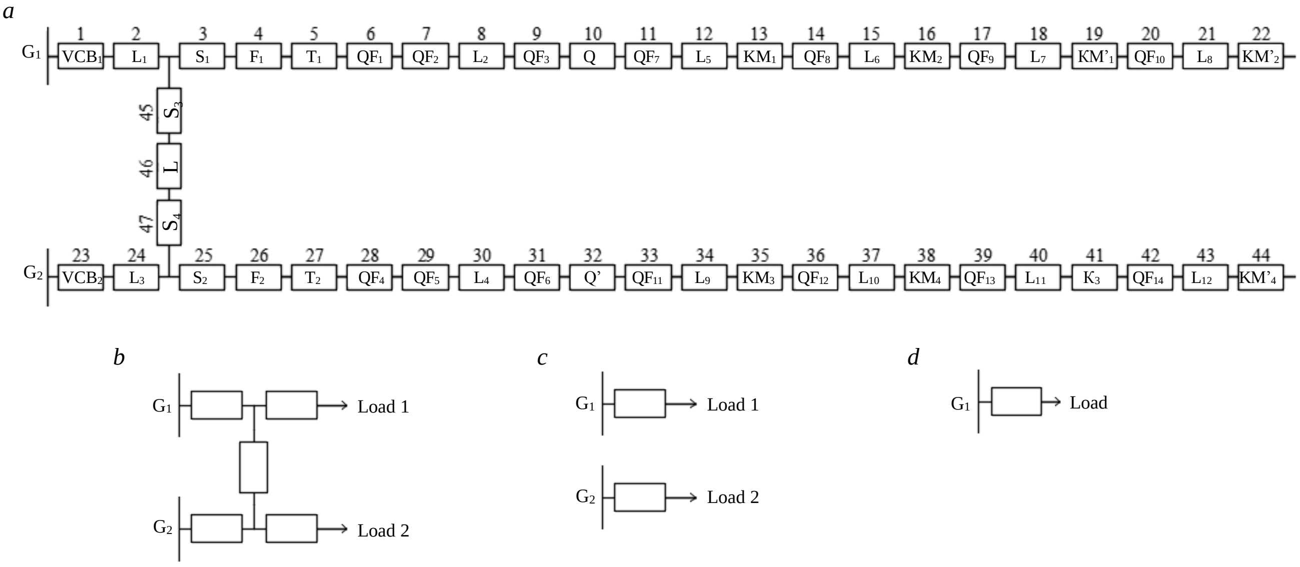

Fig.5. Reliability logic diagram for a network section with MV line redundancy and no LV redundancy (*a*), transformation stages: first (*b*), second (*c*), and third (*d*)

The failure flow rate and time between failures:

$$\omega_{\text{circuit}} = -\ln(P_{\text{circuit}}) = -\ln(0.69) = 0.3711;$$

$$T_{\text{TBF}} = 1/0.3711 = 2.6947.$$

Diagram of a network section with double redundancy (*with redundancy at MV and LV, installation of disconnectors S_3 and S_4, and a 0.4 kV bypass jumper*). Figure 6 shows a section of a circular circuit. The circular circuit must be connected to at least two geographically remote, independent power sources. The circular circuit ensures reliable power supply and allows for future network expansion as consumer loads increase. For power supply to consumers of reliability categories I and II, looped, circular, and combined circuits are used; a single transformer may be installed at the transformer substation (Fig.6, T_1, T_2). For power supply to areas with consumers of reliability category I and II, a combined loop circuit is recommended; for areas with consumers of category III, a looped circuit is used (see Fig.2, 4).

In the normal operation mode of the circular circuit (Fig.6), the MV line is open via disconnectors S_3 and S_4, and each section of the circuit is powered independently from the power source. The 0.4 kV bypass jumper must remain energized when the MV section is open.

Figure 7 shows the reliability logic diagram for the double-redundancy configuration.

The first transformation stage consists of equivalent substitution of the series branches of the original circuit (Fig.7, *a*):

$$\omega_{\text{G}_1\text{-L}_1} = \omega_1 + \omega_2;$$

$$\omega_{\text{G}_2\text{-redund}} = \omega_{23} + \omega_{24} + \omega_{\text{redund}} = \omega_{23} + \omega_{24} + \omega_{45} + \omega_{46} + \omega_{47};$$

$$\omega_{\text{S}_1\text{-Q}} = \omega_3 + \omega_4 + \omega_5 + \omega_6 + \omega_7 + \omega_8 + \omega_9 + \omega_{10};$$

$$\omega_{\text{S}_2\text{-b/jump}} = \omega_{25} + \omega_{26} + \omega_{27} + \omega_{28} + \omega_{29} + \omega_{30} + \omega_{31} + \omega_{32} + \omega_{\text{b/jump}} =$$

$$= \omega_{25} + \omega_{26} + \omega_{27} + \omega_{28} + \omega_{29} + \omega_{30} + \omega_{31} + \omega_{32} + \omega_{48} + \omega_{49} + \omega_{50};$$

$$\omega_{\text{b/jump-load}_1} = \omega_{11} + \omega_{12} + \ldots + \omega_{22};$$

$$\omega_{\text{b/jump-load}_2} = \omega_{33} + \omega_{34} + \ldots + \omega_{44}.$$

The probability of failure-free operation is then estimated:

$$P_{\text{G}_1\text{-L}_1} = e^{-\omega\text{G}_1\text{-L}_1};$$

$$P_{\text{G}_2\text{-redund}} = e^{-\omega\text{G}_2\text{-redund}},$$

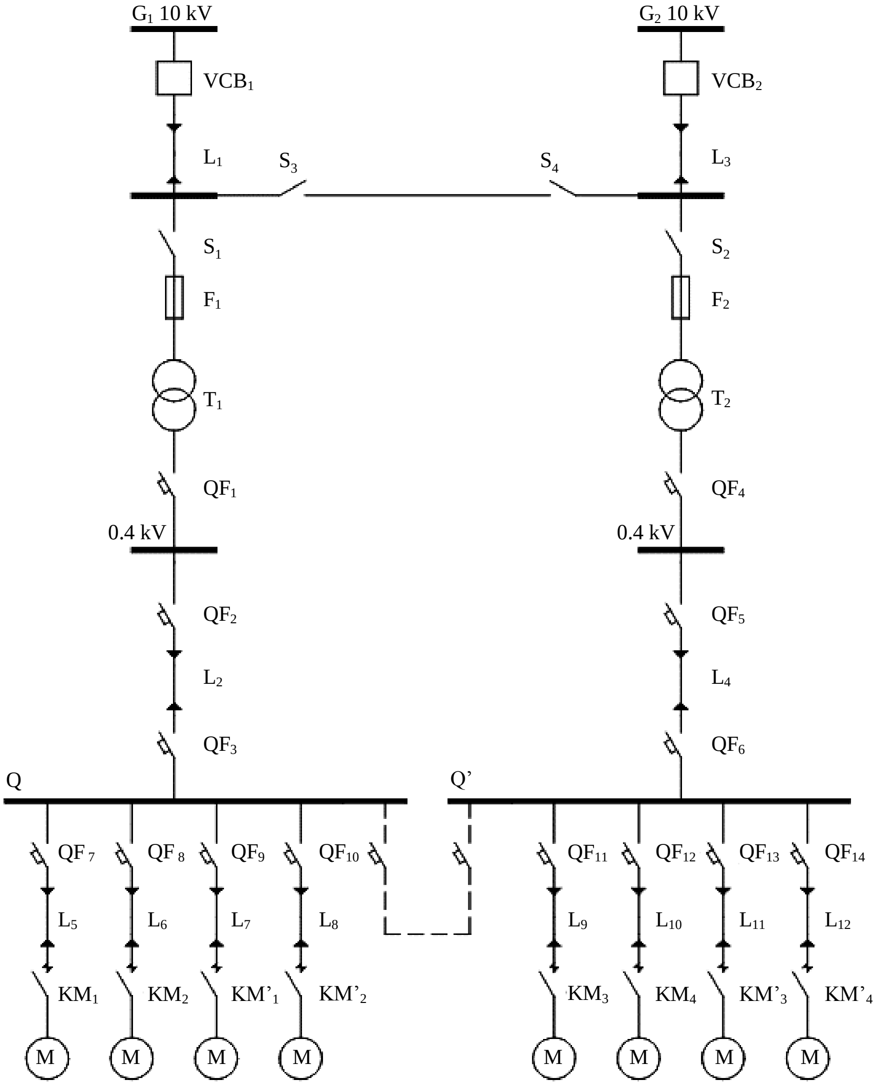

Fig.6. Diagram of a network section with dual redundancy at MV and LV

then the probability of failure is:

$$Q_{\text{G}_1\text{-L}_1} = 1 - e^{-\omega_{\text{G}_1\text{-L}_1}};$$

$$Q_{\text{G}_2\text{-redund}} = 1 - e^{-\omega_{\text{G}_2\text{-redund}}}.$$

The probability of simultaneous failure of the parallel elements G_1-L_1 and G_2-redund (Fig.7, *d*) is determined as the product of the probabilities of failure of these elements

$$Q^* = Q_{\text{G}_1\text{-L}_1} Q_{\text{G}_2\text{-redund}}.$$

The probability of failure-free operation of the parallel elements G_1-L_1 и G_2-redund is:

$$P^* = 1 - Q_{\text{G}_1\text{-L}_1} Q_{\text{G}_2\text{-redund}},$$

then the failure flow rate is:

$$\omega^* = -\ln(P^*).$$

Similar estimations are performed for the parallel branch S_1-Q and S_2-b/jump.

After transforming the series elements of the circuit (Fig.7, *e*, *f*), the failure flow rate is:

$$\omega_{\text{circuit}} = 0.2794.$$

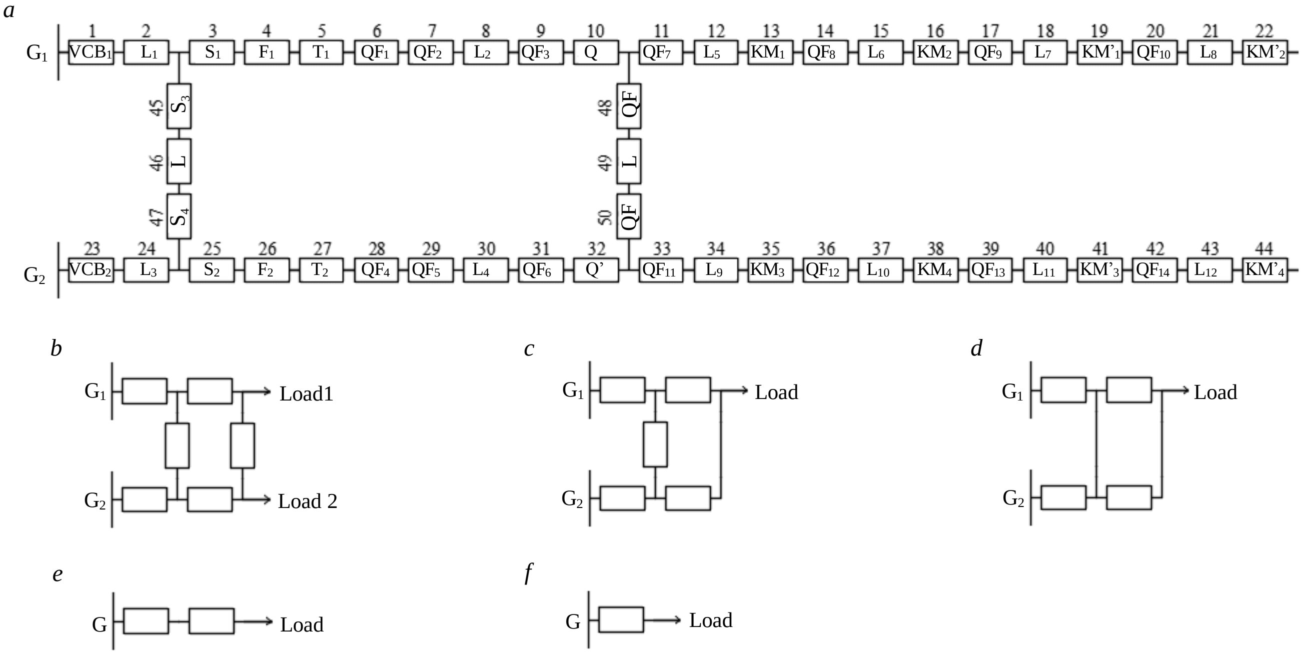

Fig.7. Reliability logic diagram of a network section with dual redundancy (*a*), transformation stages: first (*b*), second (*c*), third (*d*), fourth (*e*), fifth (*f*)

Time between failures is:

$$T_{\text{TBF}} = 1/0.2794 = 3.5791.$$

Table 2 presents the data for determining the failure flow rate and time between failures (see Fig.1, *a*, 2, 4, 6).

Table 2

Data for determining the failure rate parameter and time between failures

Type of circuit redundancy	ω_{circuit}, failures/year	T_{TBF}, year
Without redundancy	0.78280	1.27750
With 0.4 kV b/jump connection	0.38420	2.60280
With 10 kV b/jump connection, without 0.4 kV b/jump	0.37110	2.69470
With both 10 and 0.4 kV b/jump	0.27940	3.57910

The data in Table 2 show that the ω_{circuit} rate of the nonredundant circuit is 0.78280. It decreases by a factor of 2.04 when a 0.4 kV bypass jumper is connected, reaching a value of 0.3842. When the MV circuit is redundant, $\omega_{\text{circuit}} = 0.3711$. With double redundancy, the failure flow rate decreases to $\omega_{\text{circuit}} = 0.2794$, which is nearly three times lower than for the nonredundant circuit. These results demonstrate the high reliability of the double-redundant circuit with the same number of element connections to the line.

The time between failures (T_{TBF}) is inversely proportional to the circuit's failure flow rate (ω_{circuit}). The research results showed:

- the ratio of T_{TBF} for the LV-redundant circuit to T_{TBF} for the nonredundant circuit is 2.6028 : 1.2775 = 2.0374;
- the ratio of T_{TBF} for the MV-redundant circuit to T_{TBF} for the nonredundant circuit is 2.6947 : 1.2775 = 2.1093;
- the ratio of T_{TBF} for the double-redundant circuit to T_{TBF} for the nonredundant circuit is 3.5791 : 1.2775 = 2.8016.

These results are recommended for use in the feasibility study when selecting workshop power supply circuits.

Conclusion

To improve the accuracy of determining reliability parameters for assessing power supply systems at mining industry facilities, it is necessary to consider the causes of potential equipment failures; preventive measures (eliminating known failure causes, optimizing equipment load characteristics); and dependencies between external impacts and reliability indicators.

Redundancy of any electrical equipment elements enhances power supply reliability. However, for the industrial facility under study in Kemerovo, this solution is being proposed for the first time. Similar redundant circuits are used for thermal power plant auxiliary systems, where medium-voltage redundancy is particularly relevant. The estimations proved that redundancy allows increasing the time between failures by a factor of 2.11 with low-voltage or medium-voltage redundancy and by a factor of 2.8 with double redundancy.

The research showed that the failure flow rate for the low-voltage redundant circuit ($\omega_{\text{circuit}} = = 0.3842$) is higher than that for the double-redundant circuit (MV and LV, $\omega_{\text{circuit}} = 0.2794$), with the same number of element connections to the line. We found that the reliability of the redundant circuit is significantly higher than that of the nonredundant circuit ($\omega_{\text{circuit}} = 0.7828$) under the same load.

The time between failures reaches its maximum value with double redundancy ($T_{\text{TBF}} = 3.5791$) and its minimum value for the nonredundant circuit ($T_{\text{TBF}} = 1.2775$). The estimation data show that the TBF of the nonredundant circuit is 2.04 and 2.11 times less than for circuits with redundancy on the low voltage and medium voltage, respectively, and 2.8 times less than for a circuit with double redundancy.

The obtained results can be applied in the design and reconstruction of power supply systems; for feasibility study when selecting optimal circuit variants, including comparative analysis of circuit variants considering capital and operating costs; for estimation of the economic benefit from implementing redundant systems; assessment of the equipment's life cycle cost, considering reliability indicators; in developing measures to improve the quality and efficiency of electrical equipment operation at mining enterprises.

REFERENCES

1. Bagautdinov I.Z. Reliability estimation. *Teoriya i praktika sovremennoj nauki*. 2017. N 4 (22), p. 96-99 (in Russian).

2. Ivanova S.P., Pestryaev D.A., Myasnikova T.V., Sveklova O.V. Reliability assessment of switching process control equipment. 2022 4th International Youth Conference on Radio Electronics, Electrical and Power Engineering (REEPE), 17-19 March 2022, Moscow, Russia. IEEE, 2022, p. 6. DOI: 10.1109/REEPE53907.2022.9731393

3. Skamyin A.N., Dobush V.S., Shklyarskiy Y.E., Vasilkov O.S. Power system parameters in electric facilities with nonlinear loads. *Mining Informational and Analytical Bulletin*. 2024. N 6, p. 88-104 (in Russian). DOI: 10.25018/0236_1493_2024_6_0_88

4. Sadykov R.R. Evaluation of reliability of low voltage commercial networks of industrial power supply. *Power engineering: research, equipment, technology*. 2017. Vol. 19. N 5-6, p. 98-108 (in Russian). DOI: 10.30724/1998-9903-2017-19-5-6-98-108

5. Petrova R.M., Abdullazyanov E.Yu., Gracheva E.I. et al. Study of probability characteristics of reliability of electrical equipment in internal power supply systems. *Kazan state power engineering university bulletin*. 2023. Vol. 15. N 1 (57), p. 93-105 (in Russian).

6. Kirpichnikova I.M., Shipilov S.S. Ensuring uninterrupted power supply to high-tech power enterprises. *Bulletin of South Ural State University. Series "Power Engineering"*. 2022. Vol. 22. N 1, p. 55-61 (in Russian). DOI: 10.14529/power220106

7. Belsky A.A., Glukhanich D.Yu., Ivanchenko D.I. Power supply of controlled telemechanics points of the linear part of the oil pipeline. *News of the Tula state university. Technical sciences*. 2021. Iss. 4, p. 183-191 (in Russian). DOI: 10.24412/2071-6168-2021-4-183-191

8. Zatsepina V.I., Astanin S.S. The Analysis of the Power Supply System Reliability with Relay Protection Fail-Safe Features. *Transactions of the TSTU*. 2020. Vol. 26. N 4, p. 564-570. DOI: 10.17277/vestnik.2020.04.pp.564-570

9. Shpiganovich A., Shpiganovich A., Boychevskiy A. Assessment of Reliability of Individual Units Electrical Equipment by Characteristics Power Supply Systems. 2021 3rd International Conference on Control Systems, Mathematical Modeling, Automation and Energy Efficiency (SUMMA), 10-12 November 2021, Lipetsk, Russia. IEEE, 2021, p. 1088-1090. DOI: 10.1109/SUMMA53307.2021.9632126

10. Abdullazyanov E.Yu., Gracheva E.I., Ibatullin E.E. et al. Analysis of the main indicators of industrial production of facilities of average capacity. *Kazan state power engineering university bulletin*. 2023. Vol. 15. N 2 (58), p. 93-108 (in Russian).

11. Tokarev I.S. Development of parameters for an industry-specific methodology for calculating the electric energy storage system for gas industry facilities. *Journal of Mining Institute*. 2025. Vol. 272, p. 171-180.

12. Shpiganovich A.N., Zatsepin E.P. Assessment of the failure resistance of electrical power supply systems of industrial enterprises. *News of the Tula state university. Technical sciences*. 2018. Iss. 12, p. 29-35 (in Russian).

13. Changchao Gu, Yihai He, Yi Wei, Xu Ming. Reliability modeling of manufacturing systems based on the task network evolved by key quality characteristics. 2015 First International Conference on Reliability Systems Engineering (ICRSE), 21-23 October 2015, Beijing, China. IEEE, 2015, p. 5. DOI: 10.1109/ICRSE.2015.7366468

14. Ying Gao, Qiang Dong, Mo Tao et al. Sensitivity-Analysis-Based Reliability Enhancement for Networked Control Systems. 2021 3rd International Conference on System Reliability and Safety Engineering (SRSE), 26-28 November 2021, Harbin, China. IEEE, 2021, p. 113-117. DOI: 10.1109/SRSE54209.2021.00027

15. Konyukhova Y.A. Research and analysis of the reliability of schemes in the comparison variants of industrial power supply from twotransformer substations. *Kazan state power engineering university bulletin*. 2018. N 4 (40), p. 66-76 (in Russian).

16. Konyukhova E.A. Evaluation of reliability of schemes in the performance of a feasibility study of the option of power supply facilities. *Kazan state power engineering university bulletin*. 2018. N 3 (39), p. 34-44 (in Russian).

17. Shpiganovich A.N., Shpiganovich A.A., Petrova R.M., Gracheva E.I. Study of fault tolerance of power supply systems of industrial enterprises. *Kazan state power engineering university bulletin*. 2024. Vol. 16. N 2 (62), p. 94-105 (in Russian).

18. Yao Cheng, Haitao Liao, Elsayed E.A. From Reliability to Resilience: More Than Just Taking One Step Further. *IEEE Transactions on Reliability*. 2024. Vol. 73. Iss. 1, p. 42-46. DOI: 10.1109/TR.2023.3330960

19. Gasparyan A.A., Komarova G.V. Reliability assessment of a technical equipment complex of a monitoring system of parameters for electrical equipment taking into account reserve elements. 2018 IEEE Conference of Russian Young Researchers in Electrical and Electronic Engineering (EIConRus), 29 January 2018 – 01 February 2018, Moscow and St. Petersburg, Russia. IEEE, 2018, p. 632-635. DOI: 10.1109/EIConRus.2018.8317176

20. Vinogradov A.V., Perkov R.A. Analysis of the failure of electrical network equipment and justification of actions for improvement of power supply reliability for the Orel city consumers. *Vestnik NGIEI*. 2015. N 12 (55), p. 12-21 (in Russian).

21. Akimov V.A., Mishurny A.V. Accidents on Power Supply Systems: Determination of the Priority Index for Restoring Power Supply. *Civil Security Technology*. 2022. Vol. 19. N 4 (74), p. 44-47 (in Russian). DOI: 10.54234/CST.19968493.2022.19.4.74

22. Shenggang X., Jin L., Jiale L., Rushan C. Research on Reliability and Working Life Assessment Method of Mechanical and Electrical Products in Weapon Equipment. 2019 4th International Conference on System Reliability and Safety (ICSRS), 20-22 November 2019, Rome, Italy. IEEE, 2019, p. 364-368. DOI: 10.1109/ICSRS48664.2019.8987718

23. Xueyong Tang, Ning Luo, Xin He et al. Energy Production Element Planning of Integrated Gas and Power systems Considering the Coordination between Economic and Reliability. 2021 6th Asia Conference on Power and Electrical Engineering (ACPEE), 08-11 April 2021, Chongqing, China. IEEE, 2021, p. 1740-1745. DOI: 10.1109/ACPEE51499.2021.9436885

24. Zhang Ruifeng, Hao Shuqing, Deng Donglin et al. Low Voltage Power Supply Reliability Evaluation of Distribution Network Based on Data Quality Governance. 2020 4th International Conference on Power and Energy Engineering (ICPEE), 19-21 November 2020, Xiamen, China. IEEE, 2020, p. 75-78. DOI: 10.1109/ICPEE51316.2020.9311017

25. Zehua Li, Dingkang Liang, Jiahao Wang et al. A Data-driven Technique Based on Power System Reliability Assessment. 2023 3rd Power System and Green Energy Conference (PSGEC), 24-26 August 2023, Shanghai, China. IEEE, 2023, p. 576-581. DOI: 10.1109/PSGEC58411.2023.10255984

26. Bo He, Yong Liang, Jinlong Xie. Research on Power Supply Reliability of Intelligent Distribution Network with Automatic Blocking Evaluation. 2024 IEEE 3rd International Conference on Electrical Engineering, Big Data and Algorithms (EEBDA), 27-29 February 2024, Changchun, China. IEEE, 2024, p. 207-210. DOI: 10.1109/EEBDA60612.2024.10485856

27. Congcong Pan, Bo Hu, Changzheng Shao et al. Reliability-Constrained Economic Dispatch With Analytical Formulation of Operational Risk Evaluation. *IEEE Transactions on Power Systems*. 2024. Vol. 39. Iss. 2, p. 4422-4436. DOI: 10.1109/TPWRS.2023.3317973

28. Zhang Zixuan, Kurnosov R.A., Yu Zhi Zheng. Analysis of the reliability of the power supply systems of mines in China. *News of the Tula state university. Technical sciences*. 2024. Iss. 3, p. 389-396 (in Russian). DOI: 10.24412/2071-6168-2024-3-389-390

29. Chen Ying, Ma Qichao, Wang Ze, Li Yingyi. Reliability analysis of k-out-of-n system with load-sharing and failure propagation effect. *Journal of Systems Engineering and Electronics*. 2021. Vol. 32. Iss. 5, p. 1221-1231. DOI: 10.23919/JSEE.2021.000104

30. Yingying Wang, Vittal V., Khorsand M., Singh C. Composite System Reliability Evaluation With Essential Reliability Services Assessment of Wind Power Integrated Power Systems. *IEEE Open Access Journal of Power and Energy*. 2020. Vol. 7, p. 403-413. DOI: 10.1109/OAJPE.2020.3029119

31. Voltkovskaya N.S., Semenov A.S., Fedorov O.V. Energy efficiency and energy conservation in power supply systems of mining enterprises. *Vestnik GGTU im. P.O.Sukhogo*. 2019. N 3, p. 52-62 (in Russian).

32. Ugolnikov A.V., Makarov N.V. Application of Automation Systems for Monitoring and Energy Efficiency Accounting Indicators of Mining Enterprises Compressor Facility Operation. *Journal of Mining Institute*. 2019. Vol. 236, p. 245-248. DOI: 10.31897/PMI.2019.2.245

33. Ganzulenko O.Yu., Petkova A.P. Energy efficiency of the linear rack drive for sucker rod pumping units. *Journal of Mining Institute*. 2023. Vol. 261, p. 325-338.

34. Bazhin V.Yu., Ustinova Ya.V., Fedorov S.N., Shalabi M.E.Kh. Improvement of energy efficiency of ore-thermal furnaces in smelting of alumosilicic raw materials. *Journal of Mining Institute*. 2023. Vol. 261, p. 384-391.

35. Vystrchil M.G., Gusev V.N., Sukhov A.K. A method of determining the errors of segmented GRID models of open-pit mines constructed with the results of unmanned aerial photogrammetric survey. *Journal of Mining Institute.* 2023. Vol. 262, p. 562-570.

36. Tokarev I.S., Shklyarsky Y.E., Andreeva Y.E., Lavrik A.Y. Analysis of the effectiveness of the algorithm for planning the operation of an electrical complex with an energy storage system. *News of the Tula state university. Technical sciences.* 2024. Iss. 3, p. 334-342 (in Russian). DOI: 10.24412/2071-6168-2024-3-334-335

37. Shklyarsky J.E., Zamyatina E.N., Zamyatin E.O. Evaluation of the energy efficiency of the electrotechnical complex. *News of the Tula state university. Technical sciences.* 2020. Iss. 12, p. 400-404 (in Russian).

38. Skamyin A., Shklyarskiy Y., Gurevich I. Influence of Background Voltage Distortion on Operation of Passive Harmonic Compensation Devices. *Energies*. 2024. Vol. 17. Iss. 6. N 1342. DOI: 10.3390/en17061342

39. Singh P., Singh L.K. Reliability and Safety Engineering for Safety Critical Systems: An Interview Study With Industry Practitioners. *IEEE Transactions on Reliability*. 2021. Vol. 70. Iss. 2, p. 643-653. DOI: 10.1109/TR.2021.3051635

40. Ying Chen, Yanfang Wang, Song Yang, Rui Kang. System Reliability Evaluation Method Considering Physical Dependency with FMT and BDD Analytical Algorithm. *Journal of Systems Engineering and Electronics*. 2022. Vol. 33. Iss. 1, p. 222-232. DOI: 10.23919/JSEE.2022.000022

***Authors*: Renata M. Petrova,** *Postgraduate Student* (*Kazan State Power Engineering University*, *Kazan*, *Republic of Tatarstan*, *Russia*), *1998renata@mail.ru*, *https://orcid.org/0009-0004-2508-8771*, **Elena I. Gracheva,** *Doctor of Engineering Sciences, Professor* (*Kazan State Power Engineering University*, *Kazan*, *Republic of Tatarstan*, *Russia*), *https://orcid.org/0000-0002-5379-847X*.

The authors declare no conflict of interests.

ISSN 2411-3336; e-ISSN 2541-9404

JOURNAL OF MINING INSTITUTE

Zapiski Gornogo instituta

Journal homepage: pmi.spmi.ru

Research article *Geotechnical Engineering and Engineering Geology*

Influence of daily fluctuations in thermodynamic parameters of atmospheric air on its temperature distribution in downcast shafts of potash mines

Mikhail A. Semin, Evgenii V. Kolesov✉, Ruslan R. Gazizullin, Stanislav V. Maltsev
Mining Institute of the Ural Branch of the RAS, Perm, Russia

How to cite this article: Semin M.A., Kolesov E.V., Gazizullin R.R., Maltsev S.V. Influence of daily fluctuations in thermodynamic parameters of atmospheric air on its temperature distribution in downcast shafts of potash mines. Journal of Mining Institute. 2026. Vol. 277, p. 94-106.

Abstract

The amplitude of diurnal variations in atmospheric air temperature may exceed 25 °C depending on the climatic zone and season. This gives rise to unsteady heat-transfer processes in downcast mine shafts and in the subsequent underground workings along the airflow path. The present study focuses on investigating the damping effect of the amplitude of diurnal fluctuations in the thermodynamic parameters of atmospheric air in downcast shafts of potash mines. The thermal damping effect consists in the attenuation of air temperature fluctuation amplitude as the airflow moves down the shaft due to heat exchange with the shaft lining and mass-transfer processes. A combined theoretical and experimental approach is proposed to predict air microclimate parameters at the junction of a downcast shaft with an underground level using a conjugate convective-diffusive heat and mass transfer model that accounts for processes in the shaft air, the lining, and the surrounding rock mass. A methodology for conducting *in situ* measurements at the study sites is described, the necessary experimental and calculation parameters are provided, and field measurement data obtained for two downcast shafts of potash mines with different depths are presented. The experimental data were used to validate the proposed model. The agreement between measured and calculated results confirms the suitability of the selected model for predicting air temperature at the shaft-underground level junction. Effective heat-transfer coefficients between the airflow and the shaft wall were determined for both downcast shafts, along with effective thermal diffusivities of the surrounding rock mass. An empirical relationship was established for the air temperature in the shaft bottom chamber of the underground level as a function of the daily mean temperature, the amplitude of surface temperature fluctuations, and the shaft depth.

Keywords

mine ventilation; daily temperature fluctuations; thermal regime of mine workings; downcast shaft; modeling; thermal damping effect; coupled heat and mass transfer; heat-transfer coefficient; rock thermal diffusivity

Funding

The study was carried out with financial support from the Ministry of Science and Higher Education of the Russian Federation within the framework of the State assignment “Monitoring, modeling, and control of aerological and thermophysical processes in complex mining and technical systems”.

Received: 12.08.2024 ***Accepted: 09.12.2025*** ***Online: 11.02.2026*** ***Published: 27.02.2026***

Introduction

Atmospheric air entering a mine shaft is subject to both diurnal and seasonal temperature variations. Seasonal temperature fluctuations have been actively studied since the mid-20th century, particularly in relation to mines in northern regions operating under natural thermal regimes [1]. Seasonal temperature variations exert a substantial influence on the thermal conditions of underground workings, extending even to remote working areas [2-4]. Diurnal temperature variations, by contrast, affect the thermal regime of mine workings to a lesser extent [5]. Interest in this phenomenon has intensified only in recent decades, as advances in microclimate control technologies and in mathematical methods for evaluating their efficiency have reached a level at which accurate design of ventilation and air-conditioning systems [6-8] requires accounting for additional thermal factors of an unsteady nature [9-11].

The amplitude of diurnal atmospheric air temperature fluctuations depends on the climatic zone and the season of the year and may exceed 25 °C [12]. This leads to the development of unsteady heat-transfer processes in downcast shafts and in the subsequent mine workings along the airflow path [13]. A large portion of the temperature fluctuation amplitude is damped by the downcast shafts themselves [14]. According to some studies [15], the amplitude of temperature oscillations at the junction of a downcast shaft with underground levels is relatively small. However, other investigations [12, 16] indicate that this amplitude can be significant and, in some cases, exceed 10 °C. As correctly noted in [17], the intensity of this phenomenon depends on shaft parameters. That study also identifies the main parameters influencing air-temperature variation at the junction of downcast shafts with the shaft bottom workings (Table 1). In our view, this classification is incomplete, since the listed factors are in many cases interrelated or mutually dependent.

Table 1

Main factors determining the influence of daily temperature variation at the underground level [17]

Atmospheric factors	Physical factors	Dynamic factors
Atmospheric air temperature Atmospheric relative humidity Barometric pressure Presence of water inflows in the shaft Air density	Shaft diameter Shaft shape Shaft wall roughness Shaft wall moisture Shaft equipment	Airflow rate Air travel time Contact time with surfaces

It should be emphasized that, with increasing production capacities, mines require progressively larger volumes of fresh air [18]. This challenge becomes even more pronounced when developing deep-lying levels [19-21]. As a result, both the characteristic dimensions of designed shafts and the ratio of shaft cross-sectional area to its perimeter increase, which reduces the influence of heat exchange with the shaft walls [22, 23] and enhances the thermal damping effect [24, 25]. For this reason, the phenomenon in question requires further investigation.

From a practical standpoint, the study of thermal damping is important for several reasons. First, accurate prediction of dry- and wet-bulb temperatures at the junction of a downcast shaft with an underground level is critical for assessing microclimatic conditions in mine ventilation networks and for deciding whether air-cooling systems are required to ensure acceptable working conditions in mines [26-28]. Second, it is essential for calculating natural ventilation pressure under both normal and reversed ventilation modes, since diurnal temperature variations can produce daily fluctuations in natural draft exceeding 500 Pa for shafts with depths of about 1 km. Third, it is necessary to improve the accuracy of emergency ventilation calculations in mines [29]. As is well known, air distribution in reversed ventilation modes changes, among other reasons, due to variations in natural draft. When the direction of airflow reverses, air temperature in the shafts changes, leading to the development of unsteady heat-transfer processes [11].

The first *in situ* measurements confirming the smoothing of temperature fluctuation amplitudes in downcast shafts were reported in [16]. The concept of the thermal damping effect was introduced, and it was hypothesized that its influence on the thermal regime of shaft bottom workings would differ for different shafts [26]. Analytical solutions accounting for the effect of thermal damping based on unsteady heat and mass transfer processes were subsequently developed and have been implemented in mine ventilation simulators. Experimental observations of the thermal damping effect in polymetallic mines in Canada were also reported, demonstrating that the phase of periodic air-temperature variations changes between summer and winter. In study [30], continuous temperature monitoring data collected over one week at various locations of a gold-copper mine were obtained and analyzed to identify and quantitatively assess the behavior of the thermal flywheel effect. That study showed that this phenomenon cannot be adequately described using steady-state thermal models.

In studies [12, 17], the theoretical interpretation of measurements of diurnal temperature variation in downcast shafts was carried out using neural-network approaches. In particular, a NARX neural-network algorithm was employed in [12, 17] to predict air temperature in shaft bottom workings. In [31, 32], a model based on multiple logistic regression was proposed to predict the direction of heat flow. Despite the effectiveness of these neural-network methods, they suffer from a fundamental drawback, namely the lack of physical transparency of the calculations.

In the present study, a different approach is proposed. It is based on predicting air microclimate parameters at the junctions of downcast shafts with underground levels using a convective-diffusive heat and mass transfer model that accounts for processes occurring in the shaft atmosphere, the shaft lining, and the surrounding rock mass. Through physical analysis, the main dimensionless complexes of the problem are identified, and the parameters governing the attenuation of the amplitude of diurnal temperature fluctuations along the airflow path are determined.

Methodology. Experimental Measurements

To investigate the thermal damping effect, a series of *in situ* experiments was carried out under the conditions of potash mines. The objects of study were a downcast shaft of a mine developing the Verkhnekamskoye potash-magnesium salt deposit (shaft N 1) and a downcast shaft of a mine developing the Gremyachinskoye potash salt deposit (shaft N 2). Both mines employ a central ventilation scheme, in which fresh air is supplied to the mine through downcast shafts and exhausted through upcast ventilation shafts under the action of a pressure depression created by the main surface-mounted ventilation fans. During the cold season, air-handling systems have a significant influence on the formation and maintenance of the required air temperature in downcast shafts, as they largely determine the thermal operating regime of mine shafts [33]. During the warm season, the air-handling systems are switched off.

During the *in situ* investigations conducted in the warm season, diurnal variations in the temperature and humidity of the air supplied to the mine through the downcast shafts were measured. For this purpose, portable meteorological data loggers Kestrel Drop D3 were installed at the summer air intake of the downcast shaft and in the underground section at the junction of the downcast shaft with the haulage level. These devices recorded temperature and relative humidity of the incoming airflow. The data loggers are capable of long-term data storage with a user-defined sampling interval. During the measurements, temperature and relative humidity were recorded at 5-min intervals. The measurement accuracy of the data loggers is ±0.9 °C for temperature and ±2 % for relative humidity. The installation layout of the data loggers in the downcast shaft is shown in Fig.1.

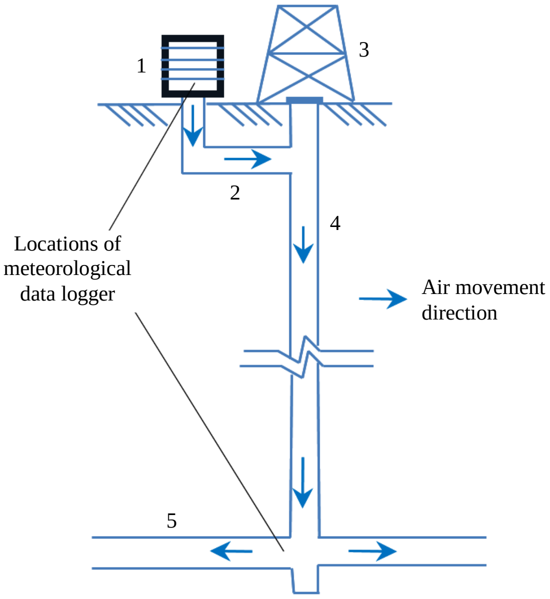

Fig.1. Layout of meteorological data logger installation in the downcast shaft

1 – the summer air intake unit of the heater installation; 2 – air supply duct; 3 – pithead building; 4 – air supply shaft; 5 – haulage level

The air flow rate was determined based on direct measurements of airflow velocity and the cross-sectional area of the excavation in the ventilation workings of the shaft bottom chamber. Airflow velocity was measured using an APR-2 anemometer with an accuracy of ± 0.10 + 0.05V m/s, where V is the measured velocity. The cross-sectional area of the excavation was determined by direct measurements of individual cross-sectional segments followed by calculation of the total area based on the measured parameters, using a Leica Disto X3 laser distance meter with an accuracy of $\pm 2\,(1.0 + 0.1\cdot 10^{-3}X)$ mm, where X is the measured distance.

Downcast shaft N 1 has a clear diameter of 7 m and is equipped with a combined skip-cage hoisting system. The distance from the air intake to the junction with the haulage level is 381 m. The volumetric airflow rate through the shaft reaches 9500 m^3/min, with an average airflow velocity of 4.1 m/s.

Downcast shaft N 2 has a clear diameter of 8 m and is equipped with a skip hoisting system. The depth of the junction with the haulage level is 1094 m. The volumetric airflow rate through the shaft is 19,000 m^3/min, and the average airflow velocity in the shaft is 6.3 m/s.

Both shafts are supported by cast-iron tubbing lining with tubbing back thicknesses ranging from 30 to 70 mm and a behind-tubbing concrete layer with a thickness of 600-750 mm.

Mathematical model

The process of unsteady coupled heat exchange between the airflow, shaft lining, and surrounding rock mass, including moisture transfer, is described by a system of differential equations for convective heat transfer in the shaft airspace

$$\rho_a c_v \frac{dT}{dx} = \frac{P}{\rho_a}\frac{d\rho_a}{dx} - \rho_a L \frac{dm}{dx} + \frac{4}{D}\frac{\alpha}{V}\left(T_m\left(t, D/2, x\right) - T\right) \tag{1}$$

and heat conduction in the lining and surrounding rock mass

$$\frac{\partial T_m\left(t,r,x\right)}{\partial t} = a_m \frac{1}{r}\frac{\partial}{\partial r}\left(r\frac{\partial T_m\left(t,r,x\right)}{\partial r}\right). \tag{2}$$

The model (1) incorporates state equations for moist air:

$$\rho_a = \frac{29P - 0.11\varphi\left[479 + \left(11.52 + 1.62T\right)^2\right]}{8.314\left(T + 273\right)}; \tag{3}$$

$$\varphi = \frac{Pm}{611\left(0.622 + m\right)\exp\left(\dfrac{17.5T}{T + 241.5}\right)}; \tag{4}$$

$$P = P_0 + \rho_0 g x. \tag{5}$$

The boundary condition for the air temperature at the shaft inlet is specified based on experimental measurements:

$$T\left(t,0\right) = T_0\left(t\right). \tag{6}$$

At the initial time, the temperature of the surrounding rock mass at depth x is assumed to be uniform along the radial coordinate r:

$$T_m\left(0,r,x\right) = T_{m0}\left(x\right). \tag{7}$$

The boundary conditions for equation (2) far from the shaft contour correspond to the temperature of the undisturbed rock mass at the given depth:

$$T_m\left(t, R_{out}, x\right) = T_{m0}\left(x\right). \tag{8}$$

The outer radius of the thermal influence zone of the excavation can be estimated from equation (8) according to [34]:

$$R_{out} = \sqrt{4a_m \tau Ln\left(\frac{s\Delta T_0}{4\pi a_m \tau\delta}\right)}. \tag{9}$$

At the shaft contour, the boundary condition for equation (2) is specified in accordance with the Newton – Richman law:

$$\lambda \frac{\partial T_m}{\partial r}\bigg|_{r\to D/2} = \alpha\left(T - T_m\right)\big|_{r\to D/2}. \tag{10}$$

The effective heat-transfer coefficient between the airflow and the shaft lining is determined as follows [11]:

$$\alpha = k \cdot 3.6\frac{V^{0.8}}{D^{0.2}}. \tag{11}$$

In the system of equations (1)-(11), the following notations are used: ρ_a is the air density in the shaft, kg/m^3; c_v is the specific isochoric heat capacity of air, J/(kg·°C); T is the air temperature in the shaft, °C; P is the barometric air pressure at depth x, Pa; L is the latent heat of water condensation, J/kg; m is the air moisture content, specified in the model based on experimental measurements, kg/kg; D is the shaft diameter, m; V is the airflow velocity in the shaft, m/s; s is the heat-exchange surface area, m^2; τ is the total duration of the heat-exchange process, s; ΔT_0 is the initial temperature mismatch between the airflow and the shaft lining, °C; δ is the temperature perturbation at the boundary of the thermal equalization layer, taken as 0.1 °C; α is the effective heat-transfer coefficient, W/(m^2·°C); k is the dimensionless empirical coefficient accounting for wall roughness and moisture content; $T_m(t, r, x)$ is the shaft wall temperature, °C; a_m is the effective thermal diffusivity of the "shaft lining – rock mass" system, m^2/s [35].

Let us introduce the dimensionless variables in the following form:

$$\hat{x} = \frac{x}{H};\quad \hat{T} = \frac{T}{\Delta T_\mathrm{A}};\quad \hat{P} = \frac{P}{P_0};\quad \hat{T}_m = \frac{T_m}{\Delta T_\mathrm{A}};\quad \hat{t} = \frac{t}{\Delta t_\mathrm{day}};\quad \hat{\rho} = \frac{\rho}{\rho_0};\quad \hat{r} = \frac{r}{D},$$

where H is the shaft depth, m; ΔT_A is the surface atmospheric air temperature difference, °C; Δt_day = = 24 h = 86400 s is the period of atmospheric air temperature variation.

Equations (1) and (2) are reduced to the dimensionless form:

$$\hat{\rho}\frac{\partial \hat{T}}{\partial \hat{x}} = \mathrm{K_c}\frac{\hat{\mathrm{P}}}{\hat{\rho}}\frac{\partial \hat{\rho}}{\partial \hat{x}} - \frac{1}{\mathrm{Ste}}\hat{\rho}\frac{\partial m}{\partial \hat{x}} + \mathrm{K_h}\left(\hat{T}_m - \hat{T}\right);$$

$$\frac{\partial \hat{T}_m}{\partial \hat{t}} = \mathrm{Fo}\frac{1}{\hat{r}}\frac{\partial}{\partial \hat{r}}\left(\hat{r}\frac{\partial \hat{T}_m}{\partial \hat{r}}\right);$$

the boundary condition (10) in dimensionless form takes the following form:

$$\frac{\partial \hat{T}_m}{\partial \hat{t}}\bigg| = \mathrm{Bi}\left(\hat{T} - \hat{T}_m\right)\big|_{\hat{r}\to 1/2};$$

$$\mathrm{Bi} = \frac{\alpha D}{\lambda},\quad \mathrm{Fo} = \frac{a_m \Delta t_\mathrm{day}}{D^2};\quad \mathrm{Ste} = \frac{c_v\,\Delta T_\mathrm{A}}{L};\quad \mathrm{K_c} = \frac{P_0}{\rho_0 c_v \Delta T_\mathrm{A}};\quad \mathrm{K_h} = \frac{4\alpha H}{\rho_0 c_v D V},$$

where Bi, Fo, and Ste are dimensionless complexes representing the Biot, Fourier, and Stefan similarity numbers, respectively; $\mathrm{K_c}$ and $\mathrm{K_h}$ are additional dimensionless complexes.

When the surrounding rock mass is modeled as a multilayer structure “tubbing – concrete lining – rock mass”, additional dimensionless complexes appear in the model, representing the ratios of thermal diffusivities of the individual layers.

The Biot number characterizes the ratio of heat transfer within the rock mass to heat transfer at the air-wall boundary. The Fourier number describes the relationship between the rate of change of thermal conditions in the surrounding air and the rate of temperature field adjustment within the “lining – rock mass” system. The Stefan number is defined as the ratio of the characteristic change in the sensible heat of the airflow to the change in latent heat due to moisture phase transitions in the airflow. The dimensionless numbers K_c and K_h characterize, respectively, the intensity of air heating due to its downward movement along the shaft and due to its interaction with the shaft walls.

Results and discussion

As a result of the experimental campaign, time histories of air temperature and relative humidity were obtained at the mine surface, as well as at the junctions of downcast shafts with the haulage levels. The measurement results for shaft N 1 are shown in Fig.2; the monitoring duration was 78 h. From Fig.2, *a* it can be seen that, at the depth of the haulage level, a phase shift of the diurnal temperature oscillations occurs (daily lag) relative to the temperature variations observed at the mine surface. The phase lag ranges from 20 to 65 min. During the investigated period, the average amplitude of diurnal temperature variations at the surface was 5.8 °C, whereas at the underground level it decreased to 2.6 °C. This indicates a pronounced manifestation of the thermal damping effect. The air humidity also exhibits diurnal fluctuations (Fig.2, *b*). The average variation of relative humidity of atmospheric air during the observation period reached 23 % at the surface, while at the haulage level the average variation was 17 %. This confirms that, as the airflow moves down the downcast shaft, not only temperature oscillations but also relative humidity oscillations are substantially attenuated.

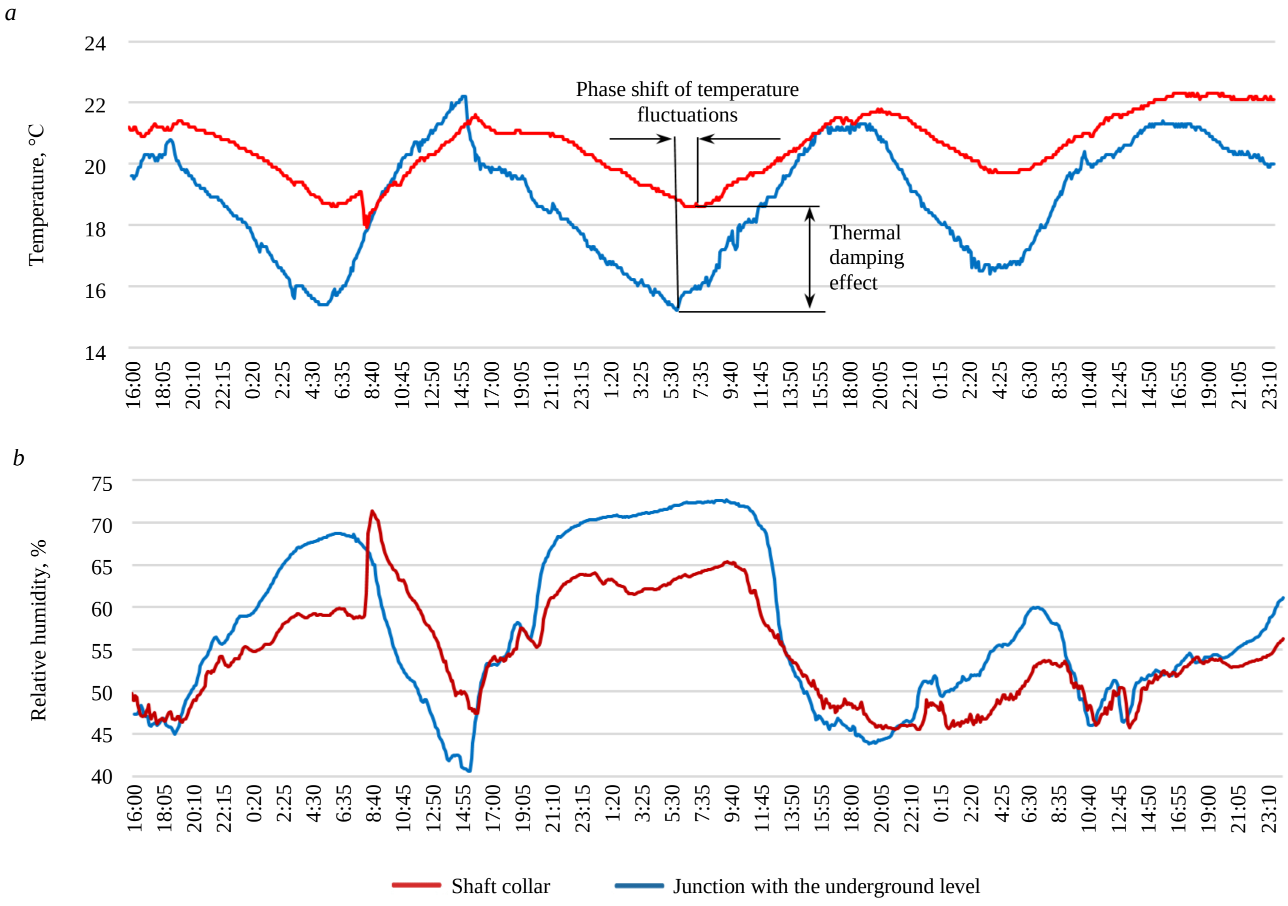

Fig.2. Diurnal variations in air temperature (*a*) and relative humidity (*b*) in shaft N1

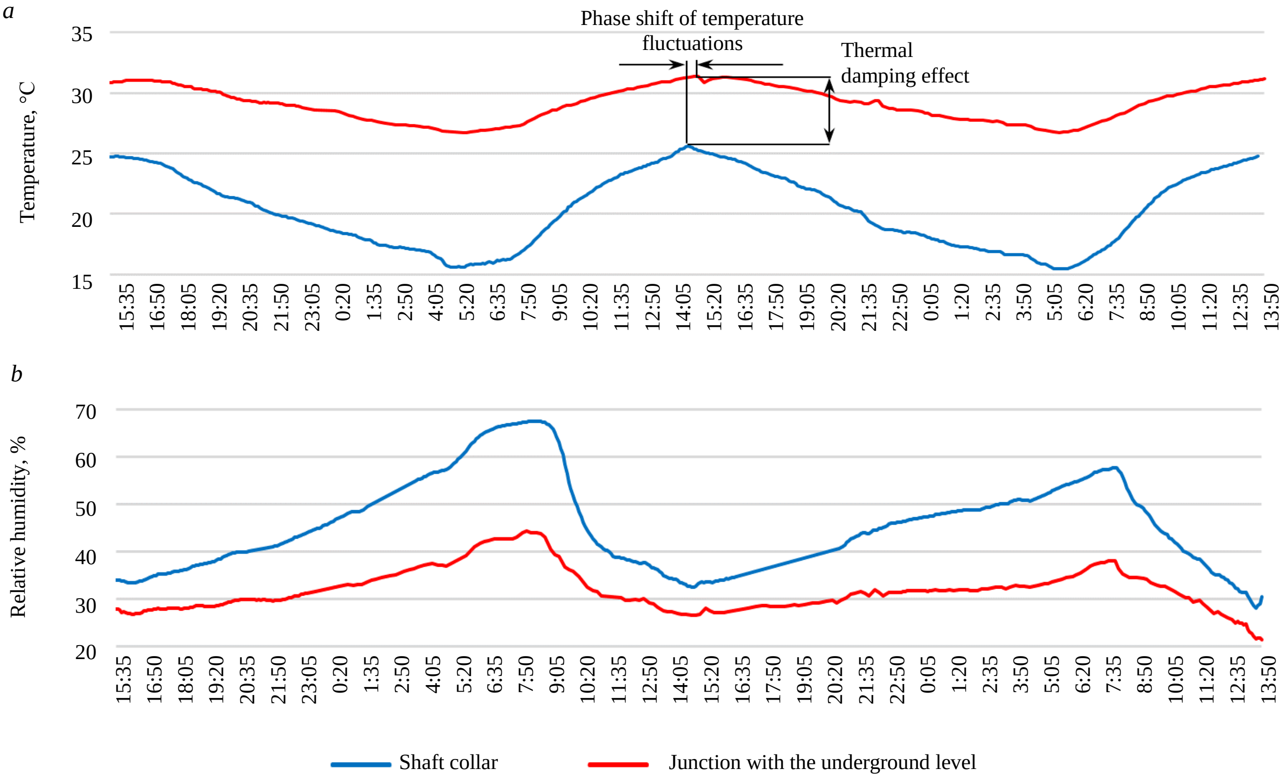

Fig.3. Diurnal variations in air temperature (*a*) and relative humidity (*b*) in shaft N 2

For shaft N 2, measurements were carried out over a period of 46 h. Figure 3, *a* shows a phase shift of diurnal temperature oscillations at the depth of the haulage level of 10-15 min relative to the surface temperature variations. Over this time interval, the air mass passing through the shaft cooled from 31.3 to 25.6 °C during daytime conditions. During nighttime (cold) periods, over the same time interval, the air temperature decreased from 26.7 to 15.6 °C while flowing down the shaft. The average amplitude of diurnal atmospheric air temperature variations was 9.7 °C, whereas the corresponding value at the junction with the underground level was 4.5 °C, which again reflects the effect of thermal damping.

The average variation of relative humidity during the investigated period reached 32 % at the mine surface and 17 % at the haulage level, further confirming the smoothing of relative humidity oscillations of the airflow as it travels along the downcast shaft.

Substituting characteristic values typical for the investigated mine shafts yields the following orders of magnitude for the similarity numbers: Bi $\sim 10^1$-10^2; Fo $\sim 10^{-3}$-10^{-2}; Ste $\sim 10^{-3}$; $K_c \sim 10^1$; $K_h \sim 10^0$. The obtained values of the Biot and Fourier numbers indicate that the main temperature variations occur in the vicinity of the shaft surface, while temperature changes inside the rock mass are relatively small, since heat transfer into the concrete lining proceeds slowly. The small values of the Stefan number imply that significantly more heat is required for phase transitions (condensation or evaporation of moisture in the airflow) than for changing the air temperature. The orders of magnitude of K_c and K_h indicate a substantial contribution to air heating from both air compression during downward movement along the shaft and heat exchange with the shaft walls.

To preliminarily assess the contribution of each heat and mass transfer processes included in equation (1) to the increase in air temperature at the junction with the underground level, characteristic parameter values were substituted (Table 2). The average barometric pressure, average temperature, and average air density in the shafts were taken as the arithmetic mean of the corresponding parameters measured at the shaft collar and at the junction with the underground level.

Table 2

Air properties and shaft parameters

Parameter	Shaft N 1	Shaft N 2
Average air density in the shaft, kg/m^3	1.235	1.26
Average barometric air pressure in the shaft, Pa	103,570	107,593
Average increase in air temperature in the shaft, °C	1.6	9.0
Average increase in moisture content in the shaft, kg/kg	0.83	0.41
Average lining temperature, °C	20.1	27.3
Shaft depth, m	381	1094
Shaft diameter, m	7	8
Air velocity in the shaft, m/s	4.1	6.3
Specific heat capacity of air, J/(kg·°C)	1005	1005
Latent heat of water condensation, kJ/kg	2260	2260
Heat-transfer coefficient between airflow and shaft wall, W/(m^2·°C)	16.6	13.5

Table 3 presents the relative contributions of various heat and mass transfer processes I_i occurring in the investigated shafts to the formation of the final air temperature at the junction with the underground level. The contribution was calculated as the ratio of the heat added to or removed from the airflow by a given factor to the change in internal energy of the airflow:

$$I_i = \frac{W_i}{\rho_a c_a \Delta T} \cdot 100\ \%,$$

where W_i is the heat associated with the *i*-th thermal factor.

The total contribution of all heat and mass transfer processes for each shaft equals 100 %, meaning that the entire change in air temperature within the shaft is explained by these processes.

Table 3

Relative contribution of heat and mass transfer processes to air temperature at the shaft-underground level junction, %

Factor	Shaft N 1	Shaft N 2
Hydrostatic air heating due to compression	+196.9	+84.8
Moisture evaporation from the shaft surface	–116.6	–10.2
Heat exchange with the shaft lining	+19.7	+25.4

Note. A positive sign indicates that the factor contributes to an increase in air temperature with depth, while a negative sign indicates cooling.

Table 3 shows that, for shaft N 1, the dominant factor contributing to air temperature increase is hydrostatic heating due to adiabatic compression, which is approximately ten times greater than the contribution from heat exchange with the shaft lining. At the same time, a significant portion of the airflow energy is expended on moisture evaporation from the lining surface. For shaft N 2, hydrostatic heating due to adiabatic compression also dominates over heat exchange with the lining (by a factor of 3.3); however, owing to the lower moisture content, energy losses due to evaporation are relatively small.

The system of equations (1)-(11) was solved using the finite difference method, employing a first-order explicit time scheme and a second-order central spatial scheme. As a result, time-dependent air temperature profiles at the shaft bottom near the underground level were obtained. The parameters a_m and k were treated as adjustable and were determined by successive approximations so that the results of the modeled air temperature $\tilde{T}(t_i)$ matched the experimental measurements as closely as possible, i.e., satisfying condition

$$\sqrt{\frac{\sum_{i=1}^{n}\left(\tilde{T}(t_i)-T(t_i)\right)^2}{n}} \to \text{min.} \tag{12}$$

Figure 4 shows contour lines of the root mean square error (12) in the phase plane “coefficient k – thermal diffusivity of the rock mass” for the conditions of shaft N 2. The minimum of functional (12) is achieved at $k = 1.3$ and an effective rock-mass thermal diffusivity $a_m = 2.2\cdot10^{-7}$ m^2/s. Figure 5 presents the time evolution of air temperature at the surface and at the junction with the underground level. Curve 3 in Fig.5 corresponds to the solution of equations (1)-(11) obtained with $k = 1.3$ and $a_m = 2.2\cdot10^{-7}$ m^2/s.

Figure 6 shows contour lines of the root mean square error (12) in the “coefficient k – thermal diffusivity of the rock mass” phase plane for shaft N 1. The minimum of functional (12) is reached at $k = 2.2$ and an effective thermal diffusivity $a_m = 150\cdot10^{-7}$ m^2/s. Figure 7 presents the time evolution of air temperature at the surface and at the junction with the underground level. Curve 3 in Fig.7 was obtained by solving equations (1)-(11) with $k = 2.2$ and $a_m = 150\cdot10^{-7}$ m^2/s.

Thus, the mathematical model of unsteady conjugate heat transfer between the airflow, shaft lining, and surrounding rock mass, including moisture transport and calibrated using experimental data, can be applied to predict the temporal evolution of air temperature at the underground level with accuracy sufficient for engineering calculations. The minor deviations between modeled curves and experimental data are mainly attributable to instrumental measurement errors.

The calibrated models for both shafts were subsequently used to determine the functional dependence of the underground level air temperature $T_{\text{lev}}(t)$ on the surface air temperature $T_{\text{A}}(t)$ and shaft depth H. For this purpose, a harmonic variation of surface temperature was specified as boundary condition (6):

$$T_{\text{A}}(t) = \bar{T}_{\text{A}} + \frac{\Delta T_{\text{A}}}{2}\cos\left(\frac{2\pi t}{1440}\right),$$

where $\bar{T}_{\text{A}}$ is the daily mean surface temperature, °C; ΔT_{A} is the amplitude of diurnal atmospheric air temperature variations, °C; t is time, min. The parameters $\bar{T}_{\text{A}}$, ΔT_{A}, and H were varied.

The results of multiparametric modeling made it possible to establish the dependence of underground air temperature on the varied parameters. The dependencies were approximated as a superposition of a time-averaged air temperature and an unsteady component representing harmonic oscillations about this mean value, with certain phase shifts caused by the inertia of the heat conduction process. As a result of the multiparametric simulations, the following expressions were obtained for predicting air temperature at the underground level for the investigated shafts:

$$T_{\text{lev}}(t)_2 = \bar{T}_{\text{A}} + 0.0073H + \frac{18.3\Delta T_{\text{A}}}{H^{0.6}}\cos\left(0.048 + \frac{2\pi t}{1440}\right);$$

$$T_{\text{lev}}(t)_1 = \bar{T}_{\text{A}} + 0.0056H + \frac{9.3\Delta T_{\text{A}}}{H^{0.6}}\cos\left(0.109 + \frac{2\pi t}{1440}\right).$$

The second terms in these expressions characterize the effect of the temperature gradient resulting from the combined influence of hydrostatic compression and the time-averaged heat exchange with the surrounding rock mass.

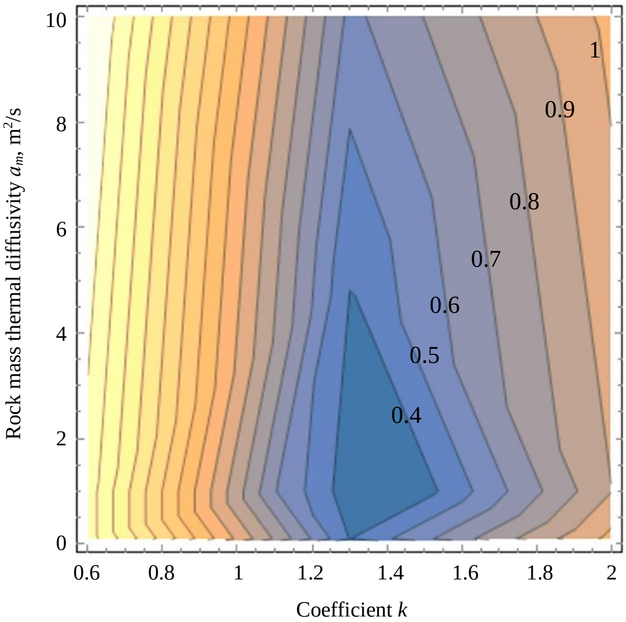

Fig.4. Contour lines of the root mean square error (12) in the phase plane "coefficient k – rock mass thermal diffusivity a_m" for shaft N 2

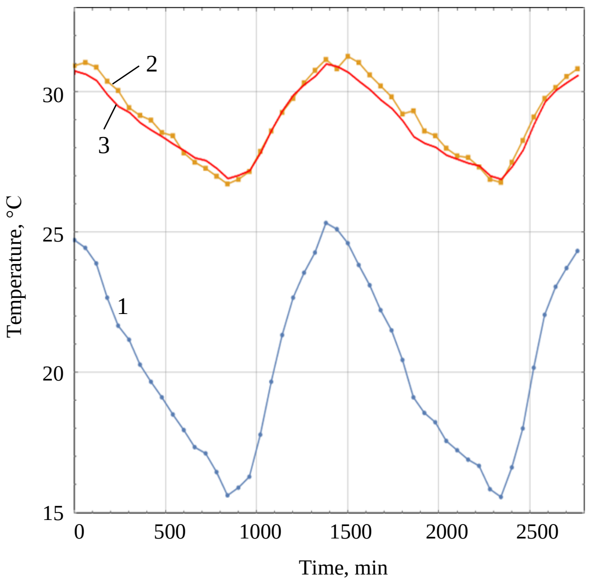

Fig.5. Temporal dynamics of air temperature in shaft N 2
1 – *in situ* measurements at the shaft collar;
2 – *in situ* measurements at the junction of the shaft with the underground level; 3 – calculated temperature dynamics at the junction of the shaft with the underground level

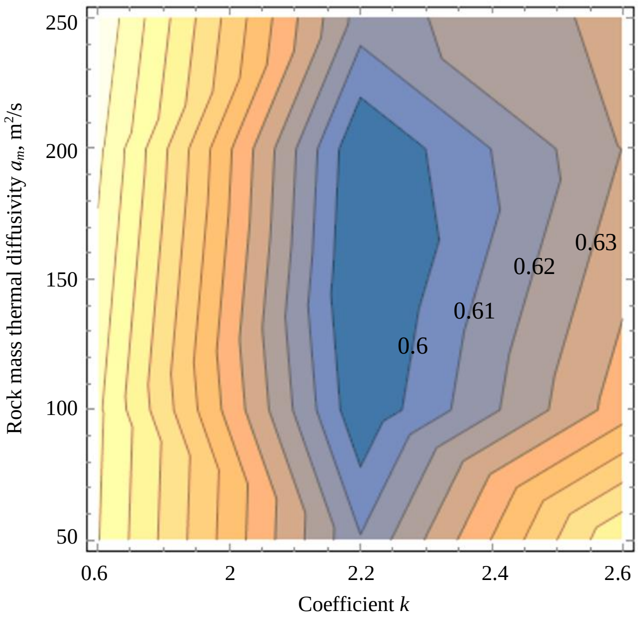

Fig.6. Contour lines of the root mean square error (12) in the phase plane "coefficient k – rock mass thermal diffusivity a_m" for shaft N 1

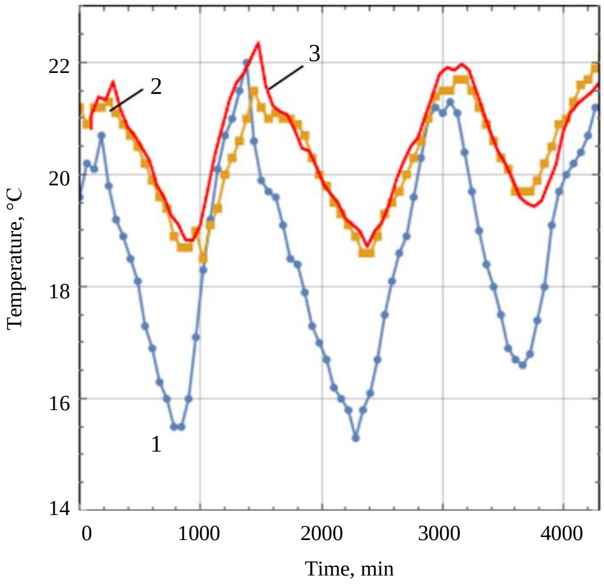

Fig.7. Temporal dynamics of air temperature in shaft N 1
1 – *in situ* measurements at the shaft collar;
2 – *in situ* measurements at the junction of the shaft with the underground level; 3 – modelled temperature dynamics at the junction of the shaft with the underground level

The general form of the calculation formulas for determining the mean air temperature in the shaft bottom chamber of a downcast shaft $\bar{T}_{\text{lev}}$, the diurnal temperature variation ΔT_{lev} and the phase shift of temperature oscillations φ is given by:

$$\bar{T}_{\text{lev}} = \bar{T}_{\text{A}} + aH;$$

$$\Delta T_{\text{lev}} = b\frac{\Delta T_{\text{A}}}{H^{0.6}};$$

$$\varphi = 2\pi\frac{\Delta t}{1440},$$

where Δt is the daily lag of temperature oscillations at the junction with the underground level relative to surface temperature oscillations, min; a and b are empirical coefficients that, in the general case, depend on the similarity numbers Bi, Fo, Ste, as well as on K_c and K_h.

Conclusion

The results of a study on the damping effect of the amplitude of diurnal variations in atmospheric air temperature and humidity in downcast shafts of potash mines are presented. The study is based on a combined theoretical and experimental approach, which includes *in situ* measurements of air microclimate parameters under underground mining conditions, as well as the application of a mathematical model of conjugate convective-diffusive heat and mass transfer within the shaft, its lining, and the surrounding rock mass, to predict air temperature at the junction of the shaft with the underground level.

A methodology for conducting in situ measurements under mine conditions is described, and the obtained data for two downcast shafts of potash mines with different depths are presented. These data were subsequently used for the parameterization and validation of the proposed model of unsteady conjugate heat transfer between the airflow, the shaft lining, and the surrounding rock mass.

Effective heat-transfer coefficients α between the airflow and the shaft wall were determined for the investigated shafts, along with the effective thermal diffusivities of the surrounding rock masses a_m. For shaft N 2, the following values were obtained $\alpha = 4.68(V^{0.8}/D^{0.2})$ W/(m^2·°C), $a_m = 2.2\cdot10^{-7}$ m^2/s; for shaft N 1: $\alpha = 7.92(V^{0.8}/D^{0.2})$ W/(m^2·°C), $a_m = 150\cdot10^{-7}$ m^2/s.

The calibrated models for both shafts were further employed in multiparametric simulations aimed at determining an empirical relationship for the air temperature in the shaft bottom chamber of the underground level as a function of the daily mean surface temperature, the amplitude of surface temperature oscillations, and the shaft depth. As a result, calculation formulas were derived for estimating the mean air temperature in the shaft bottom chamber of a downcast shaft, the diurnal temperature variation, and the phase shift of temperature oscillations. It is shown that the amplitude of air temperature oscillations in the shaft bottom chamber depends on its depth according to a power-law relationship with an exponent of −0.6.

The results of this study can be used for the quantitative assessment of microclimatic conditions in mine ventilation networks and for making decisions on the necessity of air-cooling systems to ensure acceptable working conditions in mines. The proposed approach to evaluating the diurnal variation of air temperature at the underground level also enables refinement of the calculation of the temporal dynamics of natural ventilation pressure, both under normal and reversed ventilation modes, which, in turn, improves the accuracy of predicting emergency ventilation scenarios in mines.

REFERENCES

1. Galkin A.F. The thermal condition of the mines in cryolite zone. *Journal of Mining Institute*. 2016. Vol. 219, p. 377-381 (in Russian). DOI: 10.18454/PMI.2016.3.377

2. Zaitsev A.V., Semin M.A., Parshakov O.S. Features of the thermal regime formation in the downcast shafts in the cold period of the year. *Journal of Mining Institute*. 2021. Vol. 250, p. 562-568. DOI: 10.31897/PMI.2021.4.9

3. Habibi A., Kramer R.B., Gillies A.D.S. Investigating the effects of heat changes in an underground mine. *Applied Thermal Engineering*. 2015. Vol. 90, p. 1164-1171. DOI: 10.1016/j.applthermaleng.2014.12.066

4. Hongbin Zhao, Shihao Tu, Xun Liu et al. Study of energy-efficient heat resistance and cooling technology for high temperature working face with multiple heat sources in deep mine. *International Journal of Coal Science & Technology*. 2023. Vol. 10. N 35. DOI: 10.1007/s40789-023-00590-9

5. Fair R., van Laar J.H., Nell K. et al. Simulating the sensitivity of underground ventilation networks to fluctuating ambient conditions. *South African Journal of Industrial Engineering*. 2021. Vol. 32. N 3, p. 42-51. DOI: 10.7166/32-3-2616

6. Zaitsev A.V., Levin L.Yu., Parshakov O.S. Features of ventilation and air conditioning design in deep mines. *Gornyi zhurnal*. 2023. N 11, p. 57-63 (in Russian). DOI: 10.17580/gzh.2023.11.09

7. Levin L.Yu., Zaitsev A.V. Simulation, Design, and Control of the Thermal Regime of Deep Mines. *Doklady Earth Sciences*. 2022. Vol. 507. Part 2, p. 1160-1168. DOI: 10.1134/S1028334X22600888

8. Alabyev V.R., Novikov V.V., Pashinyan L.A., Bazhina T.P. Normalization of thermal mode of extended blind workings operating at high temperatures based on mobile mine air conditioners. *Journal of Mining Institute*. 2019. Vol. 237, p. 251-258. DOI: 10.31897/PMI.2019.3.251

9. Maurya T., Karena K., Vardhan H. et al. Potential Sources of Heat in Underground Mines – A Review. *Procedia Earth and Planetary Science*. 2015. Vol. 11, p. 463-468. DOI: 10.1016/j.proeps.2015.06.046

10. Zaitsev A., Shalimov A., Borodavkin D. Unsteady Coupled Heat Transfer in the Air and Surrounding Rock Mass for Mine Excavations with Distributed Heat Sources. *Fluids*. 2023. Vol. 8. Iss. 2. N 67. DOI: 10.3390/fluids8020067

11. Kolesov E.V., Semin M.A., Kazakov B.P., Knjazev N.A. Improvement of calculation method for heat transfer coefficient in air shaft based on experimental measurements in reversal ventilation mode. *Mining Informational and Analytical Bulletin*. 2023. N 3, p. 57-71 (in Russian). DOI: 10.25018/0236_1493_2023_3_0_57

12. Scalise K.A., Teixeira M.B., Kocsis K.C. Managing Heat in Underground Mines: the Importance of Incorporating the Thermal Flywheel Effect into Climatic Modeling. *Mining, Metallurgy & Exploration*. 2021. Vol. 38. Iss. 1, p. 575-579. DOI: 10.1007/s42461-020-00323-5

13. Tu Q., Yu C., Li Z. et al. Computer simulation study on heat transfer of surrounding rock in mine roadway of coal mine enterprises. *Thermal Science*. 2020. Vol. 24. Iss. 5. Part B, p. 3049-3058. DOI: 10.2298/TSCI191020079T

14. Pandey A., Sridharan S.J., Sastry B.S. A transient model for predicting psychrometric properties of air at an intake shaft bottom of shallow depth working. *Arabian Journal of Geosciences*. 2022. Vol. 15. Iss. 16. N 1396. DOI: 10.1007/s12517-022-10679-1

15. Duganov G.V., Baratov E.I. Thermal regime of mines. Moscow: Gosgortekhizdat, 1963, p. 144 (in Russian).

16. Stroh R.M. A Note on the Downcast Shaft as a Thermal Flywheel. *Journal of the Mine Ventilation Society of South Africa*. 1979. Vol. 32, p. 77-80.

17. Roghanchi P., Kocsis K.C. Quantifying the thermal damping effect in underground vertical shafts using the nonlinear autoregressive with external input (NARX) algorithm. *International Journal of Mining Science and Technology*. 2019. Vol. 29. Iss. 2. P. 255-262. DOI: 10.1016/j.ijmst.2018.06.002

18. Kobylkin S.S. Systems designing of ventilation of mine. *Mining Informational and Analytical Bulletin*. 2015. N S1, p. 150-156 (in Russian).

19. Tingting Sun, Zhiwen Luo, Tim Chay. An analytical model to predict the temperature in subway-tunnels by coupling thermal mass and ventilation. *Journal of Building Engineering*. 2021. Vol. 44. N 102564. DOI: 10.1016/j.jobe.2021.102564

20. Liskova M.Yu., Vishnevskaya N.L., Plakhova L.V. Effect of microclimate on personnel in deep-level excavations of potash mines. *Mining Informational and Analytical Bulletin*. 2019. N 9, p. 219-230 (in Russian). DOI: 10.25018/0236-1493-2019-09-0-219-230

21. Vishnevskaya N.L., Liskova M.Yu., Plakhova L.V. Personnel physiology and hygiene, and occupational health and safety maintenance in deep mines: Problems and solutions. *Mining Informational and Analytical Bulletin*. 2020. N 10, p. 163-176 (in Russian). DOI: 10.25018/0236-1493-2020-10-0-163-176

22. Shuai Zhu, Jianwei Cheng, Zui Wang, Borowski M. Physical simulation experiment of factors affecting temperature field of heat adjustment circle in rock surrounding mine roadway. *Energy Sources, Part A: Recovery, Utilization, and Environmental Effects*. 2023. Vol. 45. Iss. 4, p. 11278-11295. DOI: 10.1080/15567036.2020.1760969

23. Menglong Bian, Wencai Wang. Prediction model of vertical shaft air temperature and its application. *IOP Conference Series: Earth and Environmental Science*. 2019. Vol. 384. N 012016. DOI: 10.1088/1755-1315/384/1/012016

24. Verbeke S., Audenaert A. Thermal inertia in buildings: A review of impacts across climate and building use. *Renewable and Sustainable Energy Reviews*. 2018. Vol. 82. Part 3, p. 2300-2318. DOI: 10.1016/j.rser.2017.08.083

25. Heier J., Bales C., Martin V. Combining thermal energy storage with buildings – a review. *Renewable and Sustainable Energy Reviews*. 2015. Vol. 42, p. 1305-1325. DOI: 10.1016/j.rser.2014.11.031

26. Borodavkin D.A. Calculation and Management of the Unsteady Thermal Regime in Working Areas of Long Extraction Faces (Case Study: Starobinskoye Potash Deposit): Avtoref. dis. … kand. tekhn. nauk. Perm: Mining Institute of the Ural Branch of the Russian Academy of Sciences, 2024, p. 23 (in Russian).

27. Rudakov M.L., Stepanov I.S. Assessment of professional risk caused by heating microclimate in the process of underground mining. *Journal of Mining Institute*. 2017. Vol. 225, p. 364-368. DOI: 10.18454/PMI.2017.3.364

28. Parshakov O.S. Results of the Study of the Mine Ventilation Network of the Norilsk Industrial District. *Gornoe ekho*. 2021. N 4 (85), p. 119-128. DOI: 10.7242/echo.2021.4.23

29. Semin M., Levin L. Mathematical Modeling of Air Distribution in Mines Considering Different Ventilation Modes. *Mathematics*. 2023. Vol. 11. Iss. 4. N 989. DOI: 10.3390/math11040989

30. Stewart C., Aminossadati S.M., Kizil M.S., Andreatidis T. Diurnal Thermal Flywheel Influence on Ventilation Temperatures in Large Underground Mines. Proceedings of the 16th North American Mine Ventilation Symposium, 17-22 June 2017, Golden, CO, USA. Colorado School of Mines, 2017, p. 9-1 – 9-8.

31. Pandey A., Mondal C., Sastry B.S. Multiple logistic regression based prediction of heat flow direction in an intake incline of shallow depth by integrating thermal flywheel effect: A case study. *Applied Thermal Engineering*. 2022. Vol. 213. N 118765. DOI: 10.1016/j.applthermaleng.2022.118765

32. Scalise K.A., Kocsis K. Utilizing Nonlinear Autoregressive with Exogenous Input Neural Networks to Evaluate the Thermal Flywheel Effect Along Intake Shafts at Nevada Mines. *Mining, Metallurgy & Exploration*. 2021. Vol. 38. Iss. 3, p. 1395-1410. DOI: 10.1007/s42461-021-00411-0

33. Anderson R., De Souza E. Heat stress management in underground mines. *International Journal of Mining Science and Technology*. 2017. Vol. 27. Iss. 4, p. 651-655. DOI: 10.1016/j.ijmst.2017.05.020

34. Zaitsev A.V. Development of Methods for Normalizing Microclimatic Conditions in Underground Workings of Deep Mines: Avtoref. dis. … kand. tekhn. nauk. Perm: Mining Institute of the Ural Branch of the Russian Academy of Sciences, 2013, p. 20 (in Russian).

35. Kolesov E.V. Development of Methods for Controlling Drip Moisture in Mine Ventilation Shafts: Avtoref. dis. … kand. tekhn. nauk. Perm: Mining Institute of the Ural Branch of the RAS, 2023, p. 24 (in Russian).

***Authors*: Mikhail A. Semin,** *Doctor of Engineering Sciences, Head of Laboratory* (*Mining Institute of the Ural Branch of the RAS, Perm, Russia*), *https://orcid.org/0000-0001-5200-7931*, **Evgenii V. Kolesov,** *Candidate of Engineering Sciences, Researcher* (*Mining Institute of the Ural Branch of the RAS, Perm, Russia*), *kolesovev@gmail.com*, *https://orcid.org/0000-0002-0755-7405*, **Ruslan R. Gazizullin,** *Leading Engineer (Mining Institute of the Ural Branch of the RAS, Perm, Russia)*, *https://orcid.org/0009-0004-3122-1647*, **Stanislav V. Maltsev,** *Candidate of Engineering Sciences, Head of Sector* (*Mining Institute of the Ural Branch of the RAS, Perm, Russia*), *https://orcid.org/0009-0002-9887-1455*.

The authors declare no conflict of interests.

ISSN 2411-3336; e-ISSN 2541-9404

JOURNAL OF MINING INSTITUTE

Zapiski Gornogo instituta

Journal homepage: pmi.spmi.ru

Research article

Geotechnical Engineering and Engineering Geology

Physical-geological models of coastal areas based on petrophysical and electric resistivity tomographic modelling

Vladimir V. Glazunov[1], **Ren Yiqiang**[1], **Danil I. Zelikman**[1]✉, **Vladimir A. Shevnin**[2]

[1] *Empress Catherine II Saint Petersburg Mining University, Saint Petersburg, Russia*

[2] *Lomonosov Moscow State University, Moscow, Russia*

How to cite this article: Glazunov V.V., Ren Yiqiang, Zelikman D.I., Shevnin V.A. Physical-geological models of coastal areas based on petrophysical and electric resistivity tomographic modelling. Journal of Mining Institute. 2026. Vol. 277, p. 107-118.

Abstract

The potential of hydroacoustic methods widely used in coastal engineering geophysical survey is limited in the presence of gas-saturated bottom sediments. Under unfavourable conditions it is advisable to use electric prospecting methods. This article analyses the efficiency of modern electric resistivity tomographic (ERT) technologies of the surface and seabed observation systems for studying the geological sections in coastal water areas. Basic geoelectric and electric resistivity tomographic models are synthesized to assess the influence of water salinity and lithological composition of sediments on the results of marine electric prospecting. Petrophysical modelling data showed that, along with the influence of pore water mineralization on the ratio of specific electric resistivity values of dispersed soils, the mineral composition of clay minerals has a significant effect. This effect is manifested as a shift in the position of the inversion point of specific electric resistivity values of sandy-clayey soils with increasing cation exchange capacity typical of different mineralogical types of clays. Results of numerical modelling of electric resistivity tomography sections using surface and seabed observation systems demonstrated that the seabed measurement system provides reliable information on geoelectric structure of sandy-clayey sediment sections, while the sections obtained from the ERT survey on water surface exhibit distortions in the geoelectric section structure and false anomalies. The advantage of seabed ERT for studying the geological structure of coastal marine areas was ascertained. Experimental work in the Luga Bay water area in the Gulf of Finland confirmed the efficiency of the seabed ERT for increasing the reliability of cross-well geological interpolation when constructing composite geological and geophysical sections. The use of seabed ERT ensured a continuous tracking of geoelectric boundaries corresponding to different lithological species in seabed sandy-clayey sediments.

Keywords

bottom sediments; seabed electric resistivity tomography; surface electric resistivity tomography; geoelectric models; pore water mineralization; ion-exchange capacity of clays; geological electric resistivity tomography sections; cross-well geological interpolation

Received: 20.03.2025 ***Accepted: 09.12.2025*** ***Online: 16.02.2026*** ***Published: 27.02.2026***

Introduction

Modern geophysics is successfully developing at the Saint Petersburg Mining University. Research based on observation of geophysical fields covers a wide range of tasks, from the study of deep structure of the Earth [1, 2] to engineering and archaeological research [3, 4]. Active research is conducted to improve the processing of geophysical data [5-7] and solve the urgent problem of oil and gas potential prediction [8, 9].

This article examines the synthetic physical-geological models of coastal sandy-clayey sediments in freshwater and marine environments. Based on modelling results, the potential of aquatorial electric resistivity tomography systems, both surface and seabed, for studying the geological structure of these sediments is assessed.

Designing of port infrastructure construction involves engineering geological survey and geoenvironmental studies within shallow coastal water areas[1]. Primary objectives of research are lithological subdivision of the geological section, determination of the roof of supporting soils, and identification of geological bodies that interfere with dredging operations. To address these challenges, marine geophysical technologies are widely used to improve the detail of engineering geological survey and to substantiate the cross-well interpolation of geological data obtained by drilling.

Currently, the leading role belongs to hydroacoustic methods, including seabed scanning with side-scan sonars and multibeam echo sounders as well as continuous seismic profiling for probing bottom sediments [10, 11]. The main disadvantage limiting the ability of hydroacoustics to fully study the structure of bottom sediments in coastal water area is the presence of the unfavourable factors complicating the investigation of the geological section of marine sediments to the required depth. These include, first of all, the generation of intense multiple reflections which complicate the identification of wanted waves, and the presence of a screening layer of bottom gas-containing silts [10].

Electric prospecting methods are recommended for use as auxiliary procedures in case of low efficiency of hydroacoustic methods for the study of geological structure and engineering geological processes including those occurring in zones of continuous gas-saturated and frozen soils. Electric prospecting is particularly widely used in combination with hydroacoustics for studying the subaquatic cryolithic zone and freshwater areas [12-14].

The above limitations of seismoacoustics determine the demand for the method of aquatorial electric resistivity tomography (ERT) in its above-water (AWERT) and seabed (SERT) modifications [12]. The application of these modifications is promising for increasing the information content of marine geophysics in the study of the geological structure of coastal areas and shallow waters [15-17].

Geophysical research including the aquatorial ERT is widely and quite successfully applied in the framework of biological research and mapping of underwater landscapes to study the geological structure of bottom sediments and flooded areas [18, 19].

A potential area of marine electric prospecting is identification of subaquatic zones of intrusion of underground fresh, mineralized water and contamination zones in coastal areas [18-22]. Important tasks include localization of gas-saturated bottom sediments and near-bottom deposits [23-25]. Monitoring of the evolution of gas shows in coastal sediments using the ERT is relevant [25]. Electric prospecting for engineering and geological surveys in marine conditions is complicated by a high mineralization of pore water in marine sediments, which significantly alters the geoelectric structure of bottom sediments [23, 26, 27]. Seabed electric resistivity tomography was recently actively and successfully applied in underwater archaeology [28-30]. Thus, the assessment of the potential and adaptation of electric prospecting technologies to marine conditions in the course of engineering geological and environmental surveys in the coastal area are urgent tasks [31-33].

This article presents the results of petrophysical studies of water salinity influence on the efficiency of using ERT in the studies of geological structure of bottom sediments by surface and seabed observation systems. Basic geoelectric models of water-saturated sandy-clayey sediments in shallow waters are synthesized. The influence of ion-exchange capacity of clay minerals (IEC) on specific electric resistivity (SER) of dispersed soils with changes in water mineralization is identified and defined. Conditions for the successful application of electric resistivity tomography in studying the geological structure of bottom sediments in coastal waters are formulated.

---

[1] SP 504.1325800.2021 Engineering Surveys for Construction on the Continental Shelf. General Requirements. Moscow: Ministry of Construction of Russia, 2021, p. 176.

Synthesis of geoelectric models of sediments forming the geological structure in coastal water areas

Rocks composing bottom sediments are fully water-saturated and exhibit low SER values. Along with mineral composition and hydrophysical properties, the dominant factor influencing the SER of sediments is mineralization of water that fills the pore space and also penetrates into massive rock formations along cracks and weakened zones [17, 24, 33].

Geoelectric models were synthesized using A.A.Ryzhov's algorithm ("Petrophysics") implemented in Petro software.

In Petro software, pore water resistivity, taking into account the type of cations and anions, as well as salt concentration in water are calculated from the formula

$$\sigma = \left|z_+ z_-\right| CF\left(V_c + V_a\right) e^{\left[\frac{-C}{\left|z_+ z_-\right| n \cdot 1000}\right]},$$

where σ is the electric conductivity of solution, cm/m; C is the salt concentration, mol/m^3; F is the Faraday constant, C/mol; V_c, V_a are mobility of cations and anions of solute, m^2/(s·V); n is the hydration number indicating how many moles of solvent surround the i-th ion in solution, mol/m^3; z_+, z_- are valence of cation and anion.

Soil grain size distribution is noted for particles of different size. For each fraction, the model specifies the porosity and moisture content, capillary radii, the m-Archie value, and IEC (g/l). The IEC in grams per litre differs from the widely used IEC parameter of mg-eq/100 g. Between these parameters, the conversion factor of IEC (g/l) ≈ 0.3IEC (mg-eq/100 g) is adopted.

For coarse-grained soil component, the IEC is considered to be zero. Soil conductivity is calculated from the formula:

$$\sigma_n = \frac{2zFK_n}{r_2^2}\int_0^{r_2} r\left[U_c\left(C_c + C_{c0}\right)\exp\left(\frac{C_c + C_{c0}}{1000zN}\right) + U_a\left(C_c + C_{c0}\right)\exp\left(\frac{C_a + C_{a0}}{1000zN}\right)\right]dr, \qquad (1)$$

where C_{c0}, C_{a0} are ion (cations and anions) concentrations in the cation exchange capacity, g/l; K_n is the rock porosity; r_2 is the capillary radius, mm; $C_c = C_c\left(r\right)$, $C_a = C_a\left(r\right)$ is the concentration of cations and anions in the capillary depending on r, g/l.

Formula (1) contains two salinities, one of which is associated with pore water, and the second one is caused by salinity effect in the IEC [26, 33]. The presence of two salinities allows taking into account the IEC of soil separately and find this value during interpretation. Pore water salinity is usually known.

In the master curve calculation mode, pore water salinity (mineralization) varies from the assigned minimum value (0.01 or 0.1 g/l) in increments sufficiently fine to produce smooth master curves. The fine-grained component content in the mixture ranges from 0 to 100 % to produce 10 curves.

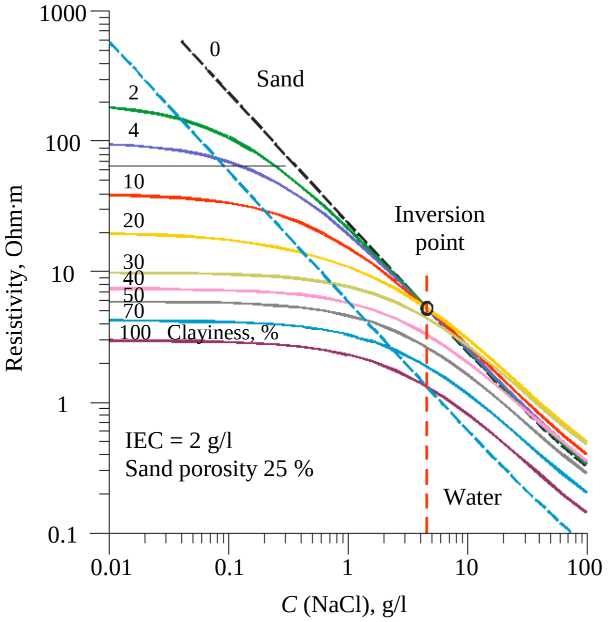

Fig.1. Dependence of a change in SER ratio of sandy-clayey rocks and inversion point position on water mineralization C

In Fig.1, in addition to the graphs of soil resistivity versus water mineralization, the water SER line is shown by blue dots. At high mineralization, soil resistivity graphs extend above the water line, and the difference in vertical deviations, according to Archie's formula, depends on soil porosity. As mineralization decreases, the SER curves bend and intersect the water line. This is due to the effect of a double electric layer forming in clays. The deviation of curves from the sand line increases with a higher clay particle content in soil. Sand and clay lines for clay content of 20 % at mineralization of approximately 1.4 g/l intersect at the so-called SER inversion point of sandy-clayey rocks (Fig.1). At this point, SER values of sandy-clayey rocks are equal.

In the inversion point, the SER of sediments is independent of the composition of dispersed sediments. At lower and higher mineralization relative to the inversion point, the SER ratio of sandy-clayey sediments changes. In areas of lower water mineralization, sands exhibit the highest and clays the lowest SER. At mineralization exceeding the value in the inversion point, clays exhibit the highest resistivity, while sands display the lowest one. On approaching the inversion point, the SER contrast of sandy-clayey sediments decreases markedly, and away from the inversion point, it remains virtually unchanged. With increasing mineralization, the SER values of sandy loam and sand are virtually equal, and SER difference of clays and sandy loams is more pronounced.

The inversion point position is most strongly influenced by the cation exchange capacity (Fig.2). The shift of this point on the log-log diagram of SER dependence on water mineralization occurs linearly. As the IEC increases from 1 to 200 g/l, the coordinates of the inversion point change by several orders.

The IEC value is known to depend on mineral composition of dispersed rocks. Among the rock-forming minerals, clay minerals of kaolinite, illite, and montmorillonite groups have the greatest influence on the IEC [34]. Kaolinite has the lowest physicochemical activity, while montmorillonite has the highest one.

Kaolinite has a rigid crystal lattice in which the exchange reactions occur only along the lateral cleavages. Its IEC ranges between 3-15 mg-eq/100 g.

Illite (hydromicas) also has a rigid crystal lattice. Due to its high negative charge, the exchange reactions occur on basal surfaces. IEC ranges within 10-40 mg-eq/100 g.

Smectite (montmorillonite) is characterized by a mobile crystal lattice. Exchange reactions occur on outer and inner surfaces of structural layers. IEC ranges within 80-150 mg-eq/100 g. Cation exchange occurs on kaolinite and hydromica particles, while intramicellar exchange occurs on montmorillonite particles [34].

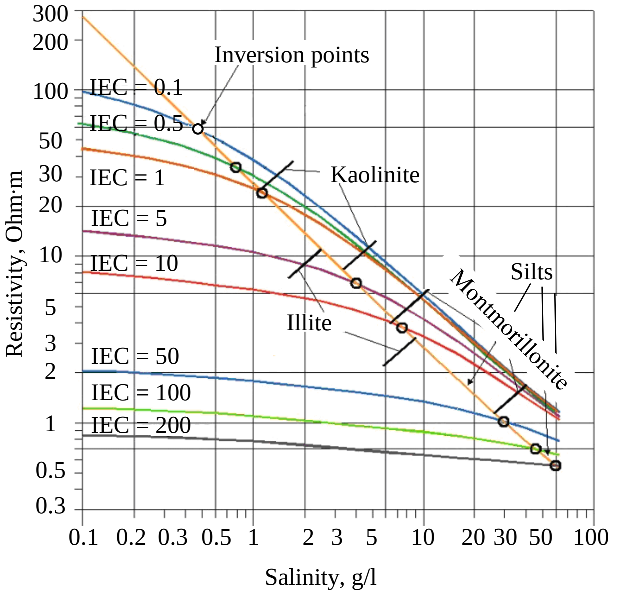

Fig.2. Dependence diagram of inversion point position on IEC values characteristic of different mineralogical clay types

The influence of clay mineral composition on the inversion point position is reflected in the diagram which shows the ranges of IEC values characteristic of different mineralogical types of clays along the inversion point displacement line (Fig.2).

This pattern of dependence is accounted for by the fact that the electric conductivity of dispersed rocks is affected not only by water mineralization, but also by a simple double electric layer (EDL) forming at the clay particle – electrolyte interface. Moreover, the IEC significantly contributes to electric conductivity of dispersed rocks. At IEC 200 g/l, the SER value of water-saturated clay is virtually independent of pore water mineralization (Fig.2).

Comparison of coordinates of inversion points at temperature changes showed that this factor does not affect the position of points with changing water mineralization *C*. The inversion point shifts only along the SER axis.

When designing dredging operations in coastal water area, determination of the roof of hard or semi-hard rocks is of great importance [35]. Petrophysical modelling was performed for semi-hard rocks which are particularly susceptible to the influence of pore water mineralization. Limestone varieties with clayey material inclusions were selected, such as marly limestone with clay content to 10 % and marl with clay inclusions to 50 %. The obtained dependences of limestone SER on pore water mineralization showed that with increasing mineralization the SER of limestones decreases, but this does not lead to formation of an inversion point (Fig.3).

Limestone porosity varies from 1 to 20 %. Black line in Fig.3 corresponds to the boundary between pure and clayey limestones. The curves below this line characterize limestones with different clayiness values. The IEC of clay contained in limestones is 1.5 g/l. Rock temperature is assumed equal to 10 °C.

It should be noted that SER of rocks is also influenced by physical and mechanical properties of rocks depending on porosity and permeability as well as by rock contamination with petroleum products [32].

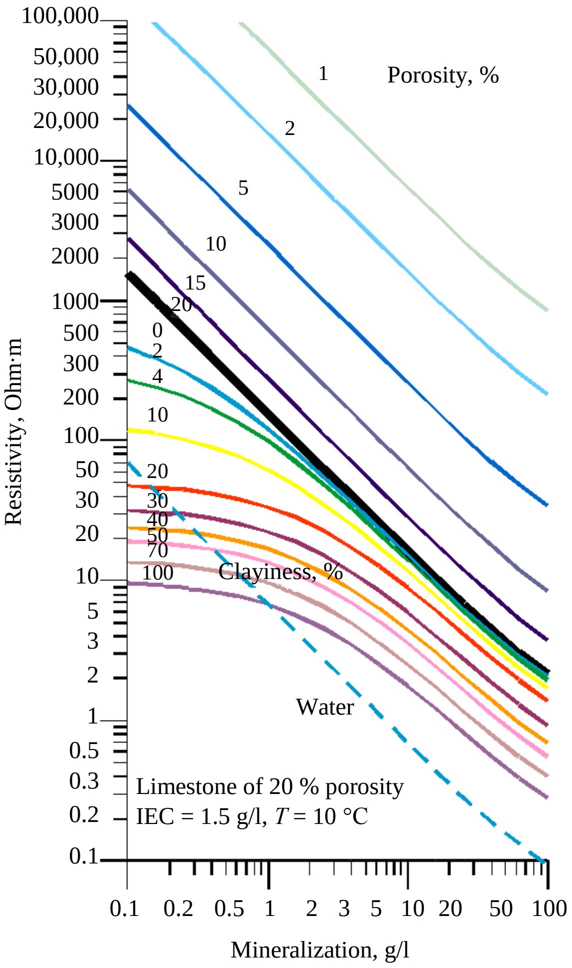

Fig.3. A master curve showing dependence of SER of water-saturated limestones on porosity, clayiness, and pore water mineralization

The resulting multifactorial petrophysical models of bottom sediments should be considered as the basis for a correct interpretation of aquatorial electric prospecting data. They allow assessing and identifying the influence of different hydrophysical conditions on the efficiency of aquatorial electric tomographic surveys, optimizing their methodology, and improving the reliability of geological interpretation of results.

ERT models of bottom sediments in marine and freshwater areas

Currently, hydroelectric prospecting survey is conducted in two modes. The most common method of surface survey involves positioning the electrical survey rig on water surface. The second method is based on surveying with an electric survey streamer mounted on the seabed. The first method is widely used when working in open water, where continuous linear movement of the electric survey streamer along the line is possible. Near the coastline and in the presence of port infrastructure facilities, a seabed-based method is advisable ensuring a stationary position of the electric survey streamer during surveying.

Surface observations are most widely conducted applying the continuous aquatorial sounding technology, which corresponds to vertical electric sounding measurements in motion processed by the electric resistivity tomographic inversion software. Bottom cable surveying offers a distinct advantage, as it allows to perform a full cycle of ERT measurements at a minimal distance from the investigated geological section.

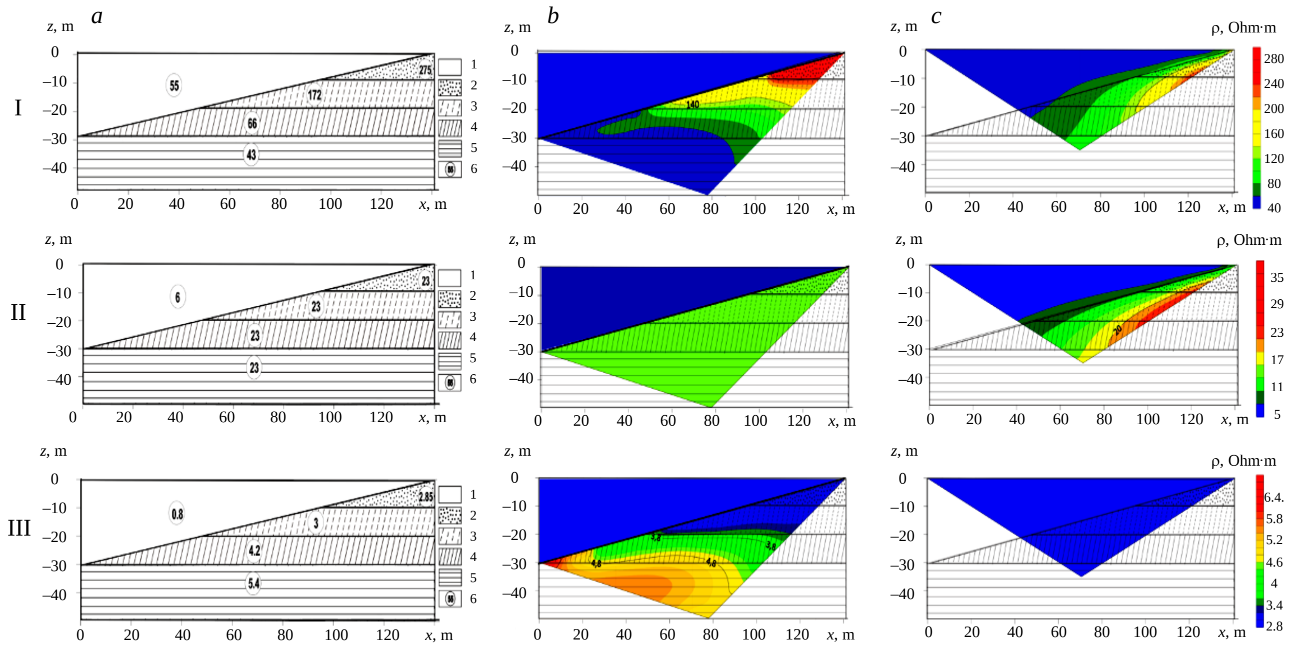

Fig.4. Geoelectric (*a*) and electric resistivity tomography (*b*, *c*) sections of Model 1 synthesized for different water mineralization values during observations with the Schlumberger seabed (*b*) and aquatorial (*c*) arrays

1 – water; 2 – sand; 3 – sandy loam; 4 – loam; 5 – clay; 6 – soil SER value

To evaluate the efficiency of aquatorial electric resistivity tomographic observations when studying the structure of geological sections of bottom sediments under conditions of different water salinity, typical models for SERT and aquatorial measuring unit (AERT) were synthesized.

Geoelectric Model 1 includes sandy-clayey sediments which form horizontal layers of sand, sandy loam, loam, and clay in coastal area (Fig.4). Three versions of Model 1 were developed differing in water mineralization values: 0.1 (version I); 1.29 (version II); and 10 (version III) g/l (Fig.4, *a*).

Mineralization values were selected in such a way that the SER values of sandy-clayey rocks corresponded to the inversion point as well as to the intervals lying left and right of this singular point (see Fig.1, *a*).

Calculations of electric resistivity tomography sections were performed using ZondRes2D (GeoTomo Ltd.) software for the Schlumberger electric survey array. The sections were synthesized for both seabed (Fig.4, *b*) and surface (Fig.4, *c*) measuring arrays which have identical geometric parameters.

Analysis of synthesized ERT models allows to conclude that observation data from the seabed-based measuring system provide a more accurate representation of geoelectric structure of the section. The degree and nature of discrepancy between the electric resistivity tomography section and the geoelectric one from the surface observation system depends more strongly on salinity and thickness of the water layer as well as seabed topography.

In case of freshwater at C = 0.1 g/l (I), the electric resistivity tomography section obtained for the AERT exhibits a distortion of position of geoelectric boundaries. Horizontal boundaries of the original model (Fig.4, *a*) correspond to curvilinear and inclined iso-ohm lines in electric resistivity tomography sections (Fig.4, *c*). The structure of the SERT section is not distorted and generally agrees well with horizontally layered structure of Model 1 (Fig.4, *b*).

At water mineralization C = 1.29 g/l (II) corresponding to the inversion point in which the resistivity of sandy-clayey layers is identical (Fig.4, *a*), the AERT section exhibits false, relatively high-resistivity anomalies (Fig.4, *c*). SERT section is characterized by a homogeneous geoelectric structure of sandy-clayey sediments with identical SER values (Fig.4, *b*), which is fully consistent with the initial model (Fig.4, *a*).

At water salinity corresponding to C = 10 g/l (III) the use of a seabed seismic array does not allow separating sands and sandy loams (Fig.4, *b*). Due to a minor SER contrast, a combined geoelectric layer represented by these sediments forms in the section. Loam and clay layers are clearly visible in the SERT section and are controlled by an increase in SER with depth (Fig.4, *b*), which is consistent with the geoelectric model (Fig.4, *a*).

An important conclusion is that the surface electrode spread does not provide an electric resistivity tomography section adequate to the geoelectric one under high salinity conditions. The influence of the low-resistivity water layer virtually screens the weak anomalous effects from the underlying sediments (Fig.4, *c*).

Modelling results for the varieties of Model 1 show that SERT offers clear advantages over surface observations and allows acquisition of the required geophysical information taking into account petrophysical limitations.

Geoelectric Model 2 includes a horizontally layered sequence of sand, sandy loam, and loam occurring in the coastal zone on a limestone massif (Fig.5, *a*).

Three versions of Model 2 were generated for water mineralization values similar to those adopted for Model 1: 0.1 (I), 1.29 (II), and 10 (III) g/l (Fig.5, *a*).

Electric resistivity tomography sections of Model 2 were synthesized using ZondRes2D software for both the seabed (Fig.5, *b*) and surface Schlumberger measuring arrays (Fig.5, *c*) with identical geometric parameters.

The results of electric resistivity tomographic modelling demonstrated a clear advantage of the seabed-mounted array for obtaining correct information on geoelectric structure of the section at different water mineralization values.

For freshwater (I), the electric resistivity tomography section obtained for the AERT shows distortions in the position of geoelectric boundaries similar to those found for Model 1 (Fig.5, *c*). SERT sections are in good agreement with horizontally layered structure of Model 2 (Fig.5, *b*).

At water mineralization corresponding to the inversion point (II) (Fig. 5, *a*), false anomalies with elevated values are recorded in the AERT section (Fig.5, *c*). The SERT section is characterized by a homogeneous structure of sandy-clayey sediments (Fig.5, *b*) which is in full agreement with the original

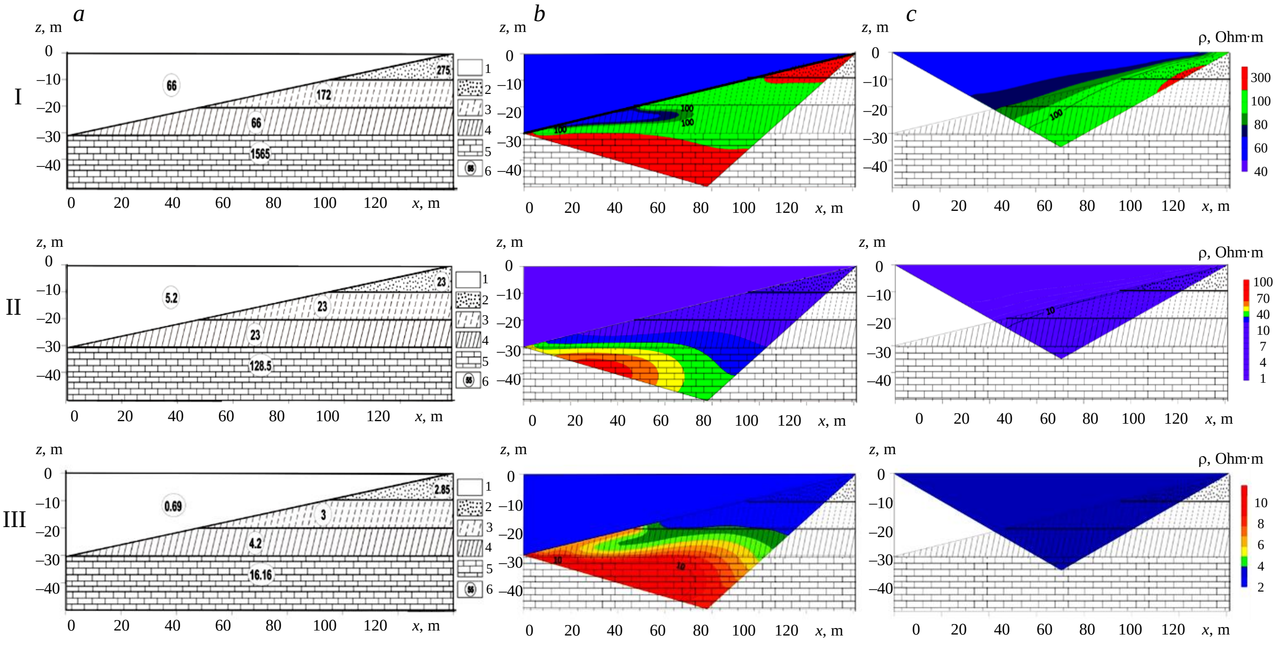

Fig.5. Geoelectric (*a*) and electric resistivity tomography (*b*, *c*) sections of Model 2 synthesized for different water mineralization during observations with seabed (*b*) and aquatorial (*c*) Schlumberger arrays

1 – water; 2 – sand; 3 – sandy loam; 4 – loam; 5 – clay; 6 – soil SER value

model (Fig.5, *a*). Sand, sandy loam, and loam layers have identical SER values and, thus, form a combined geoelectric layer. Limestones are clearly visible in the electric resistivity tomography section as a marked increase in SER.

At water salinity corresponding to $C = 10$ g/l (III), sand and sandy loam layers in SERT section form a combined geoelectric layer represented by these rocks. Loam and limestone layers are clearly visible and are characterized by increasing SER with depth (Fig.5, *b*). The AWERT modification does not allow studying the sediment section to the required depth (Fig.5, *c*).

The results of Model 2 confirm the data obtained for Model 1, according to which SERT modification is more efficient for studying the structure of geological sections of sediments at different water mineralization.

Experimental studies of SERT in coastal water of the Luga Bay in the Gulf of Finland

To evaluate the potential of SERT for studying bottom sandy-clayey sediments, experimental work was conducted in coastal waters of the Luga Bay in the Gulf of Finland, where geological and geophysical investigations are currently conducted. Geophysical survey also included the identification of paleovalleys, a network of which is developed within Saint Petersburg and the Leningrad Region [36].

Seabed topography in the study area is abrasive and accumulative, with a coastal marine terrace traced along the coast. The seabed is predominantly sandy, less frequently silty-loamy.

Engineering and geological characteristic of the study area. According to drilling data, the following features are found in the geological section within the study area (Fig.6):

- Marine sediments comprising medium-grained sands with inclusions of gravel and pebbles (EGE (Engineering Geological Element) 2.1), and heavy silty, fluid loams with silt interlayers (EGE 2.2).
- Fluvioglacial deposits – supra-morainic light to heavy, silty, hard loam (EGE 3.2) and heavy silty, semi-hard to hard loam (EGE 5.2).
- Marine sediments of Mikulino interglacial horizon – light, silty, semi-hard clays (EGE 7.2) and inequigranular sands (EGE 7.1).

Fluvioglacial intermorainic silty semi-hard loams (EGE 3.2; EGE 5.2) are recommended for use as a reliable load-bearing foundation by analogy with Kotlin clays [31].

Hydrogeological structure of the study area is determined by the development of a single aquifer complex comprising hydraulically connected aquifers. Based on the occurrence conditions and the nature of circulation, groundwater in the complex is classified as pore, unconfined. The aquifer complex is recharged by surface water.

According to results of chemical analysis of water, the water area is salty (mineralization 3.47-4.11 g/l), neutral to slightly alkaline (pH 7.47-8.02), moderately hard to very hard (total hardness 4.8-15.30 mg-eq/l), of chloride type as regards the predominant anions and of potassium-sodium type as regards the predominant cations.

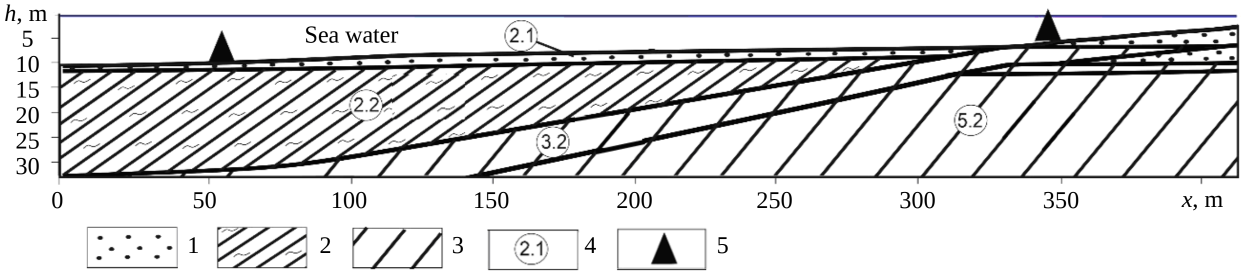

Fig.6. Engineering geological section of the work site based on drilling data from wells 1 and 2
1 – sand; 2 – loam with silt interlayers; 3 – heavy, silty, hard and semi-hard loams; 4 – EGE number; 5 – wells

Gas emission was recorded in some areas of the fluvioglacial intermorainic and marine Mikulino deposits. Gas generation is associated with marine deposits of the Mikulino horizon. Gas shows were discovered during penetration of this horizon in isolated sand lenses and interlayers of fluvioglacial intermorainic deposits. Natural gas was recorded when drilling well 2. During drilling of the layer, an intense gas emission with a characteristic hydrogen sulphide odour occurred. Visible height of the gas cloud reached 4 m above the deck.

Methodology for conducting SERT

The main objective of experimental electric prospecting is to evaluate the potential of SERT for studying the structure of bottom sediments and performing correct cross-well geological interpolation of the sections penetrated by wells 1 and 2. Of particular importance for designing the port infrastructure construction is identification and tracking of boundaries of EGE 5.2 and 7.2 loams.

Different geophysical observation systems are currently used. SERT survey methodology was based on standard observation technology adopted for land-based electric resistivity tomography. Measurements were performed using a Skala 48K12 multi-electrode electrical prospecting instrument (Design Bureau Electrometry LLC). A single-segment 48-electrode streamer with a Kevlar-reinforced cable sheath and enhanced contact waterproofing was applied for the electric resistivity tomographic survey. The quality of electrode waterproofing permitted operation at depths to 20 m. Metal tubes with diameter 17 mm were spaced at 3 m along the streamer as electrodes. Ion-selective electrodes were not applied. Streamer connectors were at 50 m from the first electrode, and the end of the streamer submerged to the seabed was carefully waterproofed. The streamer buffer allowed to accommodate the equipment on board a boat. To conduct underwater observations, a 141 m long working section of the streamer was laid along the observation line and anchored to the seabed with weights. The streamer layout was moved along the line by towing it submerged by a boat. Positions of the streamer initial and final electrodes on the seabed were secured by buoys in the water area, the coordinates of which were determined using a GPS navigator.

Measurements were taken using a Schlumberger electrode array (AMNB) with N-factor not exceeding 5 to reduce the influence of induction on galvanic observation results. Current values during measurements ranged from 1.5 to 1.8 A, and potential differences varied between 1 and 7 mV, i.e. they were standard ones for calculating the apparent resistivity (ASER).

As is known, the induction effect should manifest itself as an increase in measured ASER values at large spacings, in the form of an induction asymptote (Karinsky, Shevnin, 2001). This effect was not recorded in the obtained geoelectric sections, as the selected characteristics of measurement modes ensured the minimal contribution of the induction field component.

Standard computational procedures implemented in the certified Xeris software which is attached to the Skala 48K12 electric prospecting equipment were used to process the data and determine the ASER.

Office processing was performed by inverting the underwater observation data using Res2Dinv software (GeoTomo Ltd.). Inversion of SERT data was performed taking into account the water SER values and seafloor topography.

Results of experimental studies

SERT results are presented as a geoelectric section in which geoelectric boundaries are drawn taking into account the lithological columns of wells 1 and 2 (Fig.7).

The boundaries separate rocks classified by lithological composition and physical and mechanical properties into different EGE, the indices of which are shown in the engineering geological section (see Fig.6).

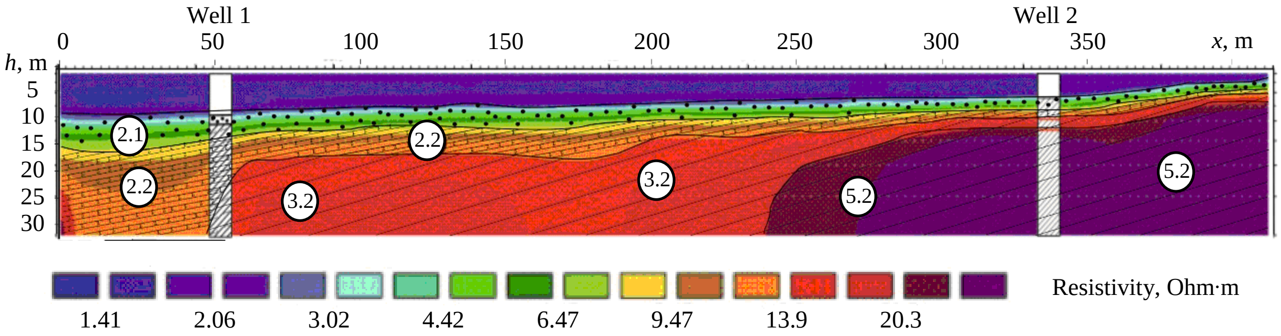

Fig.7. Geoelectric section showing lithologic columns for wells 1 and 2
2.1 – sand; 2.2 – loam with silt interlayers; 3.2 – heavy, silty, hard loam; 5.2 – semi-hard loam

SER values of sandy-clayey sediments in water area correspond to pore water mineralization interval which is right of the inversion point in the diagram (see Fig.1, *a*). For this reason, the lowest SER values in the electric resistivity tomography section are characteristic of sand (EGE 2.1) and loam with silt interlayers (EGE 2.2).

SER of heavy, silty, semi-hard loams (EGE 5.2) is higher than that of hard loams (EGE 3.2). This can be accounted for by two geological factors. Firstly, EGE 5.2 loams have a higher porosity coefficient (equal to 0.63) than EGE 3.2 loams for which this value is close to 0.47. The second probable reason is that EGE 5.2 loams lie directly on gas-generating Mikulino clays and are overlain by denser EGE 3.2 loams (see Fig.6).

The combination of these factors creates the geological preconditions for the formation of elevated gas saturation in EGE 5.2 loam layer. The increase in SER of these deposits can be due to gas coming from the Mikulino deposits.

Topography of the roof of dense supra-morainic soil sequence revealed from the SERT data points to the presence of an ancient valley channel of fluvioglacial origin.

Thus, the obtained SERT results significantly complement and refine the interpretation of the engineering geological section in the cross-well interval and allow localization of the paleochannel, information on the location of which is necessary to substantiate the design solutions for the construction of the port berthing facilities.

Conclusion

The results of petrophysical modelling revealed the influence of ion-exchange capacity of dispersed rocks on the position of the SER inversion point. This influence manifests itself as a shift in the SER inversion point of sandy-clayey soils with increasing water salinity caused by a change in mineral composition of clays. This circumstance should be taken into account when interpreting data and designing marine electric prospecting. Furthermore, this feature can be regarded as indicating the mineral composition of clayey rocks.

Analysis of electric resistivity tomography sections synthesized for different water salinity showed that the efficiency of using ERT in aquatorial and seabed areas for investigating the geological structure of coastal areas differs significantly. Seabed ERT provides reliable information on geoelectric structure of sandy-clayey sediment section, while electric resistivity tomography sections obtained from the above-water ERT survey exhibit distortions in the structure of geoelectric sections, and false anomalies appear. Numerical modelling results demonstrate the advantage of seabed ERT for studying marine coastal areas.

Experimental work demonstrated the efficiency of using SERT for cross-well geological interpolation in the course of marine engineering and geological survey. The influence of gas saturation of sediments on the results of ERT studies was revealed.

Electrotomographic studies using seabed observations are particularly relevant in the presence of gas-saturated silts which screen the propagation of seismoacoustic pulses. Such conditions are, as a rule, recorded in coastal areas of the Gulf of Finland, where engineering geological surveys are usually conducted for the construction of port facilities and dredging operations.

The authors express their gratitude to GT MorGeo Ltd. for providing the materials and assistance in conducting the seabed electric tomography experiments as well as to GM-Service Ltd. for providing the ZondRes2D software.

REFERENCES

1. Gorelik G.D., Egorov A.S., Shuklin I.A., Ushakov D.E. Substantiation of optimal range of geophysical surveys to study deep structure of the Lake Vostok area. *Gornyi zhurnal*. 2024. N 9, p. 56-61 (in Russian). DOI: 10.17580/gzh.2024.09.09

2. Egorov A., Antonchik V., Senchina N. et al. Impact of the Regional Pai-Khoi-Altai Strike-Slip Zone on the Localization of Hydrocarbon Fields in Pre-Jurassic Units of West Siberia. *Minerals*. 2023. Vol. 13. Iss. 12. N 1511. DOI: 10.3390/min13121511

3. Vasilyev S.A., Grigoreva N.V., Medvedev N.O. et al. Plakun Burial Ground: a new discovery of the well-known site based on the results of the aerial lidar and ground penetrating radar research. *Ufa Archaeological Herald*. 2024. Vol. 24. N 3, p. 573-586 (in Russian). DOI: 10.31833/uav/2024.24.3.038

4. Daniliev S., Danilieva N., Mulev S., Frid V. Integration of Seismic Refraction and Fracture-Induced Electromagnetic Radiation Methods to Assess the Stability of the Roof in Mine-Workings. *Minerals*. 2022. Vol. 12. Iss. 5. N 609. DOI: 10.3390/min12050609

5. Sysoev A.P., Zaitsev S.A. Separate issues of amplitude inversion of wave field. *Geology and mineral resources of Siberia*. 2023. N 3 (55), p. 52-58 (in Russian). DOI: 10.20403/2078-0575-2023-3-52-58

6. Yakovleva A.A., Movchan I.B., Medinskaia D.K., Sadykova Z.I. Quantitative interpretations of potential fields: from parametric to geostructural recalculations. *Bulletin of the Tomsk Polytechnic University. Geo Assets Engineering*. 2023. Vol. 334. N 11, p. 198-215 (in Russian). DOI: 10.18799/24131830/2023/11/4152

7. Daniliev S.M., Mulev S.N., Shnyukova O.M. Correlation and regression analysis of natural electromagnetic and acoustic emission activity in rock samples of the Oktyabrsky deposit. *Gornyi zhurnal*. 2024. N 9, p. 51-55 (in Russian). DOI: 10.17580/gzh.2024.09.08

8. Sysoev A.P. Analytical solutions to the problems of compensation of near-surface heterogeneity in seismic exploration using seismic reflection method. *Geology and mineral resources of Siberia*. 2023. N 1 (53), p. 36-43 (in Russian). DOI: 10.20403/2078-0575-2023-1-36-43

9. Kalinin D.F., Egorov A.S., Bolshakova N.V., Sekerina D.D. Information and statistical forecast of oil and gas potential in the marginal part of the Koryak-Kamchatka folded region. *Bulletin of Kamchatka Regional Association Educational-Scientific Center. Earth Sciences*. 2023. N 1. Vol. 57, p. 63-88 (in Russian). DOI: 10.31431/1816-5524-2023-1-57-63-88

10. Budanov L.M., Sergeev A.Yu., Chekulaev A.V. High-frequency sub-bottom profiling on desalinated shallow-water in case of the Neva bay. Inzhenernaya i rudnaya geofizika 2023: Sbornik materialov 19-i nauchno-prakticheskoi konfe-rentsii i vystavki “Inzhenernaya i rudnaya geofizika 2023”, “Inzhenernaya i rudnaya geologiya 2023”, “Morskie tekhnologii 2023”, 15-19 maya 2023, Saint Petersburg, Russia. Moscow: Geomodel, 2023, p. 124-133 (in Russian).

11. Mirinets A.K., Rybalko A.E., Aleshin M.I., Subetto D.A. The structure if the Quaternary sheet in the Petrozavodsk Bay of Lake Onega according to seismoacoustics. *Moscow University Bulletin. Series 4. Geology*. 2024. N 1, p. 123-129 (in Russian). DOI: 10.55959/MSU0579-9406-4-2024-63-1-123-129

12. Mirinets A.K., Bobachev A.A., Mironyuk S.G. The detection of frozen and gas-saturated soils in the gulf of Ob of the Kara Sea according to the data of the underwater electrical resistivity tomography with acoustic profiling and drilling. *Geophysics*. 2022. N 6, p. 35-42 (in Russian). DOI: 10.34926/geo.2022.11.15.005

13. Mirinets A.K., Bobachev A.A., Rybalko A.E. Bottom sediments investigations of lake Onega applying underwater seismic and electromagnetic surveys. *Science and Technological Developments*. 2022. Vol. 101. N 2, p. 5-22 (in Russian). DOI: 10.21455/std2022.2-2

14. Budanov L.M., Glazunov V.V., Sergeev A.Yu., Efimova N.N. Use of hydroelectric prospecting methods for mapping paleorelief forms in Sestroretsky Razliv water area. Estestvennye i tekhnicheskie nauki. 2017. N 3 (105), p. 52-57 (in Russian).

15. Zi-Yin Ren, Xiu-Jun Guo, Jing-Xin Wu. Simulation and Analysis of Detection Results of Shallow Gas Under Shallow Water with a Navigated DC Marine Resistivity Method. *Periodical of Ocean University of China*. 2019. Vol. 49. Iss. 7, p. 56-63. DOI: 10.16441/j.cnki.hdxb.20180231

16. Chang Gao, Xiujun Guo, Shuai Shao, Jingxin Wu. Using MODFLOW/MT3DMS and electrical resistivity tomography to characterize organic pollutant migration in clay soil layer with a shallow water table. *Environmental Technology*. 2021. Vol. 42. Iss. 28, p. 4490-4499. DOI: 10.1080/09593330.2020.1767699

17. Tassis G.A., Tsourlos P.I., Rønning J.S. Detection and characterization of fracture zones in bedrock in marine environment: possibilities and limitations. *Near Surface Geophysics*. 2020. Vol. 18. Iss. 1, p. 91-103. DOI: 10.1002/nsg.12086

18. Neevin I.A., Budanov L.M., Sergeev A.Yu. et al. Marine geological and geophysical methods as a source of basic information for biological research and marine landscape mapping. *Regional ecology*. 2015. N 4 (39), p. 5-24 (in Russian).

19. Shkiria M.S., Lankin Yu.K., Tereshkin S.A. et al. Applying ground geophysical prospecting using the method of electrical resistivity tomography as part of engineering and geological surveys of a flooded area in one of the residential areas of Irkutsk. *Bulletin of the Tomsk Polytechnic University. Geo Assets Engineering.* 2022. Vol. 333. N 11, p. 160-170. DOI: 10.18799/24131830/2022/11/3766

20. Niculescu B.M., Andrei G. Application of electrical resistivity tomography for imaging seawater intrusion in a coastal aquifer. *Acta Geophysica*. 2021. Vol. 69. Iss. 2, p. 613-630. DOI: 10.1007/s11600-020-00529-7

21. Mironyuk S.G., Khlebnikova O.A. Signs and Geological Prerequisites of Seawater Intrusion into Coastal Aquifers (the Example of the Black Sea). *Doklady Earth Sciences*. 2022. Vol. 507. Suppl. 1, p. S163-S172. DOI: 10.1134/S1028334X22601572

22. Ekwok S.E., Ben U.C., Eldosouky A.M. et al. Towards understanding the extent of saltwater incursion into the coastal aquifers of Akwa Ibom State, Southern Nigeria using 2D ERT. *Journal of King Saud University – Science*. 2022. Vol. 34. Iss. 8. N 102371. DOI: 10.1016/j.jksus.2022.102371

23. Cheng Xing, YuPing Luo, XiuJun Guo et al. Simulation analysis of monitoring effect of electrical resistivity tomography in seawater-groundwater exchange process. *Progress in Geophysics*. 2022. Vol. 37. Iss. 6, p. 2622-2629. DOI: 10.6038/pg2022FF0603

24. Guangxiang Zhu, Xiujun Guo, Le Yu et al. Analysis on Resistivity Characteristics and Resistivity Model Building of Marine Soil with High Clay Content. *Journal of Jilin University* (*Earth Science Edition*). 2019. Vol. 49. N 5, p. 1457-1465. DOI: 10.13278/j.cnki.jjuese.20180226

25. Hao Sun, JiTong Sun, JingXin Wu et al. Simulation analysis of monitoring effect of marine resistivity method in shallow gas evolution process. *Progress in Geophysics*. 2022. Vol. 37. Iss. 3, p. 1311-1320. DOI: 10.6038/pg2022FF0199

26. Xiaoteng Xiao, Yufeng Zhang, Tengfei Fu et al. The two salinity peaks mode of marine salt supply to coastal underground brine during a single tidal cycle. *Frontiers in Marine Science*. 2024. Vol. 10. N 1324163. DOI: 10.3389/fmars.2023.1324163

27. Tao Zhang, Songyu Liu, Guojun Cai. Correlations between electrical resistivity and basic engineering property parameters for marine clays in Jiangsu, China. *Journal of Applied Geophysics*. 2018. Vol. 159, p. 640-648. DOI: 10.1016/j.jappgeo.2018.10.012

28. Capozzoli L., Giampaolo V., De Martino G. et al. ERT and GPR Prospecting Applied to Unsaturated and Subwater Analogue Archaeological Site in a Full Scale Laboratory. *Applied Science*. 2022. Vol. 12. Iss. 3. N 1126. DOI: 10.3390/app12031126

29. Simyrdanis K., Papadopoulos N., Kim J.-H. et al. Archaeological investigations in the shallow seawater environment with electrical resistivity tomography. *Near Surface Geophysics*. 2015. Vol. 13, p. 601-611. DOI: 10.3997/1873-0604.2015045

30. Papadopoulos N., Oikonomou D., Simyrdanis K., Loke Meng Heng. Practical considerations for shallow submerged archaeological prospection with 3-D electrical resistivity tomography. *Archaeological Prospection*. 2022. Vol. 29. Iss. 1, p. 1003-123. DOI: 10.1002/arp.1841

31. García-Menéndez O., Ballesteros B.J., Renau-Pruñonosa A. et al. Using electrical resistivity tomography to assess the effectiveness of managed aquifer recharge in a salinized coastal aquifer. *Environmental Monitoring and Assessment*. 2018. Vol. 190. Iss. 2. N 100. DOI: 10.1007/s10661-017-6446-9

32. Dusart J., Tarits P., Fabre M. et al. Characterization of gas-bearing sediments in the coastal environment using geophysical and geotechnical data. *Near Surface Geophysics*. 2022. Vol. 20. Iss. 5, p. 478-493. DOI: 10.1002/nsg.12230

33. Moulds M., Gould I., Wright I. et al. Use of electrical resistivity tomography to reveal the shallow freshwater–saline interface in The Fens coastal groundwater, eastern England (UK). *Hydrogeology Journal*. 2023. Vol. 31. Iss. 2, p. 335-349. DOI: 10.1007/s10040-022-02586-2

34. Korolev V.A. Theory of electric surface phenomena in soils and their use. Moscow: Sam poligrafist, 2015, p. 486 (in Russian).

35. Dashko R.E., Karpenko A.G. Scientific-Practical Enhancement Principles for the Long-Term Stability of Cultural Heritage Objects through a Multi-Component Underground Space Analysis. *Heritage*. 2024. Vol. 7. Iss. 8, p. 4455-4471. DOI: 10.3390/heritage7080210

36. Dashko R.E., Lokhmatikov G.A. The Upper Kotlin clays of the Saint Petersburg region as a foundation and medium for unique facilities: an engineering-geological and geotechnical analysis. *Journal of Mining Institute*. 2022. Vol. 254, p. 180-190. DOI: 10.31897/PMI.2022.13

***Authors*: Vladimir V. Glazunov,** *Doctor of Engineering Sciences, Professor* (*Empress Catherine II Saint Petersburg Mining University, Saint Petersburg, Russia*), *https://orcid.org/0000-0001-5816-0507*, **Ren Yiqiang,** *Postgraduate Student* (*Empress Catherine II Saint Petersburg Mining University, Saint Petersburg, Russia*), *https://orcid.org/0009-0006-6172-4514*, **Danil I. Zelikman,** *Postgraduate Student* (*Empress Catherine II Saint Petersburg Mining University, Saint Petersburg, Russia*), *Zelikman26danil07@gmail.com*, *https://orcid.org/0009-0003-0044-2298*, **Vladimir A. Shevnin,** *Doctor of Physics and Mathematics, Professor* (*Lomonosov Moscow State University, Moscow, Russia*), *https://orcid.org/0000-0001-9517-6188*.

The authors declare no conflict of interests.

ISSN 2411-3336; e-ISSN 2541-9404

JOURNAL OF MINING INSTITUTE
Zapiski Gornogo instituta
Journal homepage: pmi.spmi.ru

Research article

Economic Geology

Sino-Russian cooperation in the Arctic: options for joint development of rare earth metals

Aleksei E. Cherepovitsyn[1], **Irina P. Dorozhkina**[1]✉, **Kou Jingna**[2]
[1] *Empress Catherine II Saint Petersburg Mining University, Saint Petersburg, Russia*
[2] *Taiyuan University of Technology, Taiyuan, China*

***How to cite this article*:** Cherepovitsyn A.E., Dorozhkina I.P., Kou Jingna. Sino-Russian cooperation in the Arctic: options for joint development of rare earth metals. Journal of Mining Institute. 2026. Vol. 277, p. 119-135.

Abstract

The rare earth metals (REM) industry plays an important role in the modern global economy due to the extensive use of these elements in high-technology sectors. Russia possesses substantial REM reserves, giving the country a major competitive advantage: a strong mineral resource base capable of meeting growing demand in both domestic and global markets, where China remains the dominant player. China accounts for more than 70 % of global REM production, while Russia's share does not exceed 1 %. In recent years, countries worldwide have paid increasing attention to the REM supply chain, intensifying international competition in this sector. In this context, the development of Sino-Russian cooperation represents a key factor in strengthening the two countries' positions in the global market and should be based on collaboration in strategically significant areas for both sides. The purpose of this study is to explore options for implementing a Sino-Russian partnership in strategic sectors, using the REM industry as a case study. The Russian Arctic, where REM deposits unique in terms of reserves and concentrations of valuable components are concentrated, is considered a potential site for the implementation of technological cooperation. The study is based on a critical analysis of Russia's key REM deposits, with particular attention to Arctic sites, as well as a comparative analysis of the Russian and Chinese consumer markets and forecasts of their development. These analyses form the basis for proposed options for technological cooperation between the two countries. The findings indicate that the most promising form of Sino-Russian partnership is a consortium model, similar to joint projects such as Yamal LNG and Power of Siberia. This format enables Russia to attract investment and technologies, while allowing China to secure access to new sources of raw materials and strengthen its presence in the Arctic.

Keywords

rare earth metals; Sino-Russian cooperation; technological partnership; consortium; joint venture; mineral resource development; global market; Arctic; Tomtor deposit

Received: 16.09.2025 ***Accepted: 24.12.2025*** ***Online: 20.02.2026*** ***Published: 27.02.2026***

Introduction

Today, rare earth metals (REM) are regarded as critically important materials and strategic resources for modern industry. They are widely used in electronics and mechanical engineering, energy, metallurgy, the production of advanced transport technologies, catalysts, the defense industry, and other sectors [1-3]. Globally, demand for these elements has been growing rapidly, driven by the development of new technologies, artificial intelligence, autonomous robotics, and related fields. In Russia, annual REM consumption amounts to approximately 1.1-1.2 thousand t [1]. The key consumers include petrochemicals and oil refining, metallurgy, and the nuclear industry [4]. At the same time, more than 40 % of global REM consumption is concentrated in the production of magnetic materials, which are subsequently used, for example, in wind turbines. As a result, the expansion of green energy in the context of decarbonization and the global energy transition, alongside the growth of other high-technology sectors, has led to an almost twofold increase in global REM demand over the past decade [5].

---

[1] State Report on the Status and Use of Russian Mineral Resources in 2023. Moscow: Rosnedra, 2024, p. 710 (in Russian).

Currently, China alone consumes more than 170,000 t of REM annually. As for the growth potential of the Russian REM market, the key medium-term driver is the development of new high-technology industries, including renewable energy, electric vehicle manufacturing, aircraft production, etc. [6]. In China, in addition to green energy and advanced transport technologies, the most promi-sing areas for REM demand growth include robotics, electronics, the production of inverter air conditioners, energy-efficient elevators, and other applications[2].

Russia possesses one of the strongest competitive advantages in the global REM market, namely substantial reserves estimated at approximately 10 million t in categories A, B, and C1, and more than 30 million t in category C2. More than two-thirds of these reserves are concentrated in deposits located in the Russian Arctic, primarily in the Murmansk Region and the Sakha Republic (Yakutia). In terms of total reserves, Russia ranks after China, the current leader with approximately 44 million t, as well as Vietnam (22 million t) and Brazil (21 million t), where industrial processing facilities are absent[3]; however, favorable geological assessments show that it may overtake the aforementioned countries in the future. Overall, about 60 % of global REM reserves outside China account for only 30 % of global production, indicating a low level of resource development[4]. At present, a full value chain for high-technology products based on REM exists only in China. The country leads not only in reserves, but also in extraction, processing, separation, the production of metals and alloys, and the manufacture of final products. By contrast, the United States, Australia, Myanmar, Vietnam, and other countries have production capacities and commercial development at only certain stages of the value chain. However, China's leadership comes with a number of inherent challenges related to resource base development. Scientific research in recent years has focused on addressing issues such as resource depletion and intensified production, which requires the development of new, more technologically complex deposits. The imbalance in the distribution of heavy and light rare earth elements, the structural deficit of heavy elements accompanied by an excess of light elements, and the environmental consequences necessitate the development of environmentally friendly mining operations, land reclamation practices, and waste recycling methods [7-9].

In Russia, the rare earth supply chain is limited to ore extraction and the production of rare earth metal concentrates, which are subsequently exported. REM consumed domestically are, in turn, largely imported from China[5]. This contradiction, combined with Russia's substantial resource endowment, raises concerns regarding the country's technological sovereignty, considering that governments worldwide have paid increased attention to REM supply chains since 2023. Amid intensifying international competition, REM have gained growing recognition as critical materials for the aerospace, defense, electric vehicles, and other sectors. Western countries, particularly the United States, have significantly intensified their focus on REM production cycles by introducing policy measures and legislation aimed at securing domestic supply, while simultaneously expanding their global influence. In this context, the strengthening of Sino-Russian relations plays a crucial role in enhancing the competitive positions of both countries on the global stage, with the Arctic serving as a connecting platform, partly due to the increasing interest in the region from other nations [10, 11].

Ongoing geopolitical shifts are reshaping traditional trade routes and necessitating the search for new avenues of cooperation. Accordingly, a strategic partnership between Russia and China may represent a response to the challenges associated with diversifying supply chains and identifying new markets [12]. For Russia, the tightening of Western sanctions underscores the need to strengthen ties

---

[2] Zhiyan Consulting: Analytical Report on the Current Performance and Development Trends in the Chinese Rare Earth Industry in 2023 (in Chinese). URL: https://www.chyxx.com/industry/1137248.html (accessed 28.04.2025).

[3] Mineral Commodity Summaries 2024. U.S. Geological Survey, 2024, p. 212. DOI: 10.3133/mcs2024

[4] Huibo Smart Investment Research: In-Depth Analysis of the Rare Earth Industry: Supply-Demand Balance and Market Landscape (in Chinese). URL: https://www.hibor.com.cn/data/ec51894e6abe55ca5187ab4bf54bd162.html (accessed 28.04.2025).

[5] State Report on the Status and Use of Russian Mineral Resources in 2023. Moscow: Rosnedra, 2024, p. 710 (in Russian).

with new partners, while for China, the introduction of new tariffs by the U.S. presidential administration amid the trade war has imposed additional economic conditions. Cooperation between the two countries should therefore focus on strategically important sectors of the economy and be based on mutually beneficial terms. By strengthening their positions through joint initiatives and projects, Russia and China can create a stable foundation for long-term economic development.

The purpose of this study is to substantiate optimal forms for implementing Sino-Russian technological partnerships in strategically important economic sectors, using the rare earth industry as a case study. The research objectives are as follows:

- to analyze the state of Russia's rare earth mineral resource base and assess the structure of key Arctic deposits;
- to identify potential sites for international cooperation;
- to compare the consumer markets of Russia and China, as well as development forecasts, in order to identify common features and fundamental differences;
- to develop and compare options for long-term technological cooperation between the two countries in the rare earth industry;
- to determine the most effective forms of cooperation based on the principle of maximum benefits with minimum risks for both parties.

Literature review

Issues related to the development of the mineral resource base, particularly in the Russian Arctic, remain highly relevant in contemporary scientific literature [13-15]. General challenges associated with supplying Russian industry with critical minerals, including REM, are discussed in [16]. It is noted that, in recent years, the mineral resource base of critical metals in Russia has exhibited positive growth, although many complex ore deposits remain undeveloped. According to [17-19], the main obstacles hindering the development of the rare earth industry in Russia include the lack of technologies for separating rare earth oxides and producing metals and alloys, the negative environmental impact of mining and processing, the generally low quality of raw materials, logistical inaccessibility of deposits, especially in the Arctic, high barriers to entering global markets, heavy reliance on imports, limited domestic demand for rare earth metals, insufficient regulatory and industry support mechanisms, the capital-intensive nature of projects, and geopolitical tensions. Nevertheless, several studies [1, 2] indicate promising prospects for the development of the Russian rare earth industry in response to growing domestic and global demand.

The works [20, 21] examine the geological characteristics of specific rare earth deposits in the Murmansk Region, estimate reserve values, provide data on elemental composition, and consider processing technologies, as well as the potential for further development of the rare earth industry in the region. Other studies [22, 23] focus on the development and processing of complex ores at the Tomtor deposit in the Sakha Republic, including data on the granulometric, mineral, and chemical composition of the ores. However, Russian scientific literature still lacks comprehensive approaches for assessing the reserve structure of Arctic rare earth deposits, identifying the most and least abundant elements, and comparing resource availability with market potential, including in the context of increasing exports.

Certain aspects of the development of Chinese rare earth metal deposits are addressed in [7, 24, 25], highlighting issues such as resource depletion and the uneven distribution of heavy and light elements within deposit reserves. Studies examining the development of Russia's mineral resources sector as a whole [26, 27] note that it currently faces significant global geopolitical and climatic challenges, requiring alternative strategies for industry development.

The issues surrounding the implementation of a Sino-Russian partnership in the rare earth industry have been insufficiently addressed in the scientific literature. Existing studies examine technological cooperation between the two countries in related sectors, such as fuel and energy. For example, the joint Yamal LNG project has provided China with a new trade route and strengthened its role in Arctic infrastructure development, while allowing Russia to attract investment for accelerated regional development and to acquire critical technologies amid tightening European sanctions and the withdrawal of several companies from the Russian market [10]. Another example of successful energy cooperation is the Power of Siberia project, which opens new prospects for ensuring energy security and economic development for both countries [12], while also reinforcing their positions on the global stage and maintaining strategic balance [28]. However, these studies focus mainly on the mutual benefits of cooperation and generally identify risks only for Russia. Moreover, they do not analyze forms of Sino-Russian partnership in strategic sectors from the perspective of optimality for both parties.

The experience of previously implemented initiatives can serve as a basis for refining the forms of Sino-Russian technological partnership in new areas. The scientific hypothesis of this study is as follows: the implementation of a Sino-Russian partnership in the Arctic rare earth industry, based on a comprehensive assessment of reserve structure and market potential, will be optimal and mutually beneficial if it considers the complementarity of resources and technologies and provides specific benefits while minimizing risks for both partners. The scientific novelty of the study lies in its comprehensive assessment of Arctic rare earth metal deposits, review of possible forms of Sino-Russian partnership in the rare earth industry, and the development of optimal partnership models that account for both benefits and risks for the involved parties.

Methods

The study employs an empirical-theoretical approach (Fig.1). The research methodology primarily relies on qualitative methods, supplemented by quantitative data. The theoretical framework incorporates the following methods: analysis of relevant scientific literature, general scientific techniques such as analysis, synthesis, comparison, analogy, and conceptual modeling. Comparative analysis serves as a core method throughout the study. It is applied to examine and contrast the structure and volume of rare earth metal reserves at Russian deposits, the production cycles in Russia and China, the composition of consumer demand for rare earth metals in both countries, and various forms and examples of international partnerships. The analogy method is used to draw insights from successful Sino-Russian projects in the fuel and energy sector, such as the Yamal LNG project, the Power of Siberia project, and the joint venture Razrezugol LLC, all of which are implemented in the Russian Arctic. These projects are analyzed and compared based on criteria including process segmentation (investment activities, resource extraction, infrastructure development, provision of equipment and technology, etc.) and the resulting benefits and risks for both parties. Conceptual modeling involves designing a descriptive organizational and economic framework for international partnerships, identifying potential targets for implementation, and developing optimal partnership models based on the principle of maximum benefits and minimum risks.

The primary empirical method employed is statistical analysis, which involves the collection and examination of secondary empirical data from a wide range of sources, including official reserve statistics, industry reports and analytical reviews, regulatory documents, and prior research conducted by the authors.

The object of the study is the rare earth industry, while the subject is the economic and managerial relationships arising from the implementation of a Sino-Russian partnership in the industry, exemplified by the development of Arctic rare earth deposits.

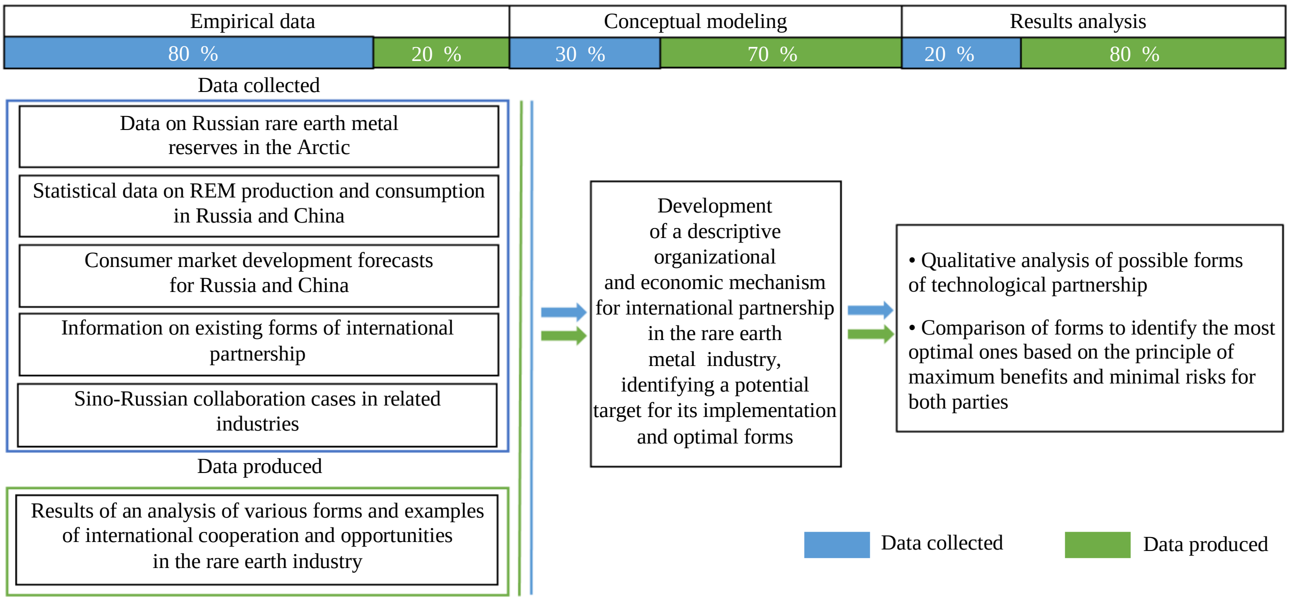

Fig.1. Research methodology

Results and discussion

An analysis of Russian rare earth metal reserves

Currently, Russia has approximately ten rare earth metal deposits[6], with total reserves of around 30 million t in categories A, B, C1, and C2 (Fig.2). Reserves in categories A, B, and C1 alone amount to roughly 10 million t, positioning Russia as one of the world leaders in rare earth metal reserves (fourth after China, Vietnam, and Brazil)[7]. Approximately two-thirds of these reserves are concentrated in deposits located in the Russian Arctic, including the Murmansk Region and the Sakha Republic.

Fig.2. Key Russian REM deposits and their reserves

---

[6] State Report on the Status and Use of Russian Mineral Resources in 2023. Moscow: Rosnedra, 2024, p. 710. (in Russian).

[7] U.S. Geological Survey: Mineral Commodity Summaries 2024. URL: https://pubs.usgs.gov/publication/mcs2024 (accessed 01.03.2025).

The largest REM reserves are found in deposits within Murmansk Region, such as the Lovozerskoye deposit and the Khibiny group (Kukisvumchorr, Yukspor, Apatitovy Tsirk, Rasvumchorr Plateau, Koashva, Nyorkpahk, and others). Currently, rare earth production in Russia is limited to the Lovozerskoye deposit, which produces approximately 2700 t of metals annually, over 90 % of which are exported as carbonates[8]. Promising deposits such as Tomtor, Zashikhinskoye, and Yaregskoye are being prepared for development. It is important to note that these deposits are polymetallic and contain other valuable components. For example, the Khibiny deposits primarily produce apatite-nepheline ores and also contains aluminum and titanium reserves. The Yaregskoye deposit is notable as the world’s only source of ultra-high-viscosity oil produced by underground mining and is currently being prepared for the extraction of titanium and other metals, including rare earth elements. The Tomtor and Zashikhinskoye deposits also contain niobium, zirconium, and uranium [18, 19, 22].

Rare earth metals comprise 17 elements from both light and heavy groups. The light group includes lanthanum, cerium, praseodymium, neodymium, promethium, samarium, and europium, while the heavy group includes gadolinium, terbium, dysprosium, holmium, erbium, thulium, ytterbium, lutetium, and yttrium [5]. Scandium is the seventeenth element, which does not belong to either of the two groups.

Global REM reserves are commonly calculated by converting them into the sum of their trioxides ($\sum TR_2O_3$), which can vary significantly in content. For example, the TR_2O_3 content in the ore of the Tomtor deposit can reach 12 %, one of the highest levels globally, whereas the average content in deposits on the Kola Peninsula does not exceed 1 %[8]. By comparison, at the world’s largest deposit, Bayan Obo in Inner Mongolia, China (with reserves exceeding 36 million t, more than 80 % of China’s total), the average TR_2O_3 content is 3-5 %[8]. In Russia, REM oxides are not produced. The production cycle ends at the production of carbonates obtained from loparite concentrate at Solikamsk Magnesium Plant, which are subsequently exported. The full REM production cycle is illustrated in Fig.3.

In Russia, stages from oxide separation to the production of end products are absent. These stages generate the highest added value. Consequently, Russia exports more REM than it imports in bulk, but imports exceed exports in monetary terms. The main importers of Russian REM are China and EU countries, where metallurgical processing separates REM oxides and produces metals and alloys for high-tech products with significant added value.

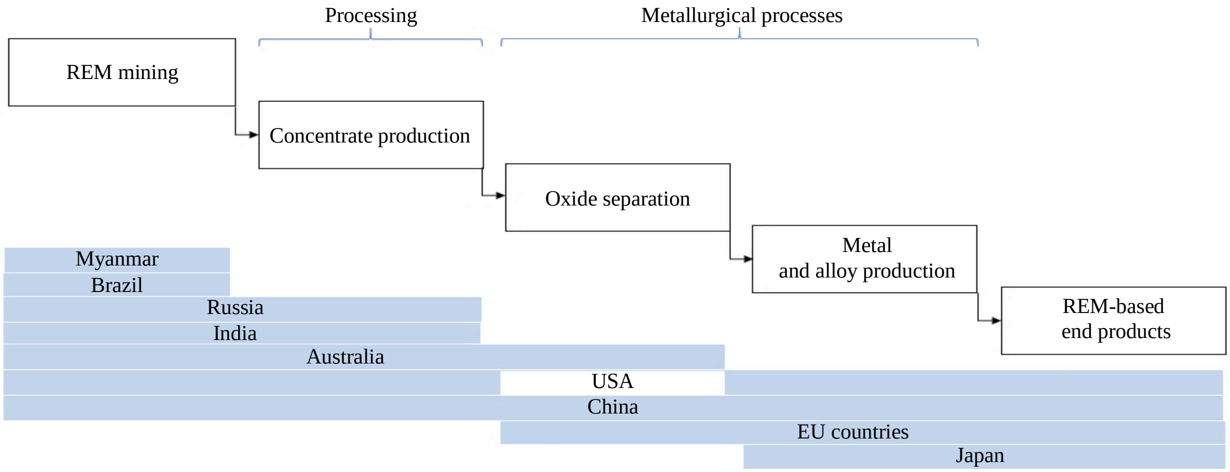

Fig.3. Full REM production cycle [20]

---

[8] State Report on the Status and Use of Russian Mineral Resources in 2023. Moscow: Rosnedra, 2024, p. 710 (in Russian).

The global REM market faces a so-called "balance problem" [5, 17]: an oversupply of light metals and a corresponding shortage of heavy metals, due to the complexity and heterogeneous composition of the ores. Isolating individual elements requires specific separation technologies for each REM. Furthermore, while some metals, such as lanthanum and cerium, are abundant, high-tech industries generate significant demand for heavy elements such as dysprosium and yttrium, and other heavy elements, which are essential for advanced technologies in defense, aviation and aerospace engineering, and other sectors. Consequently, the oversupply of certain REM leads to a decrease in their prices, while scarcity of others drives price increases.

Russian deposits contain reserves of both light and scarce heavy REM, although their composition can vary considerably. Table 1 presents the results of an analysis of the reserve structure of key Arctic deposits: Lovozerskoye (loparite and eudialyte), the Khibiny group, and Tomtor.

Table 1

Light and heavy REM content, thousand t [20, 21, 29, 30]

Deposit	Light REM						Heavy REM					
	La	Ce	Nd	Pr	Sm	Eu	Y	Tb	Gd	Dy	Er	Yb
Lovozerskoye (loparite)	+ 9.6	+ 15.7	+ 2.9	+ 0.9	–	–	–	–	–	–	–	–
REM total	29						–					
Lovozerskoye (eudialyte)	+ 283.1	+ 684.1	+ 330.3	+ 94.4	+ 99.1	+ 22.2	+ 542.6	+ 21.2	+ 59	+ 80.2	+ 47.2	+ 44.8
REM total	1 513						795					
Khibiny group	+ 3058.2	+ 5213.7	+ 1704	+ 462.7	+ 259.6	+ 79	+ 22.6	+ 33.9	+ 214.4	+ 101.6	+ 45.1	+ 45.1
REM total	10777.2						462.7					
Tomtor	+ 754	+ 1380	+ 541	+ 134	+ 80	+ 26	+ 206	+ 8	+ 54	+ 27	+ 18	–
REM total	2915						313					
Total by element	4104.9	7293.5	2578.2	692.2	438.7	127.2	771.2	63.1	327.4	208.8	110.3	89.9
REM total	15234.7						1570.7					

As can be seen from Table 1, the only currently developed deposit, Lovozerskoye (loparite), contains reserves of light REM, such as cerium, lanthanum, neodymium, and praseodymium. These elements are also abundant in the Khibiny group and the Tomtor deposit, which, in addition, contain heavy metals that account for the largest share of their reserves (approximately 10 % of the total). Among the deposits considered, the Khibiny group holds the largest total REM reserves. Total reserves of light metals exceed 10 million t, while heavy metals amount to approximately 460 thousand t; by comparison, the Tomtor deposit, with reserves three times smaller, contains about 310 thousand t of heavy elements. The Tomtor deposit stands out with the highest REM content among the deposits examined, reaching up to 12 %. This represents a significant competitive advantage, as low concentrations of useful components in ore reduce extraction profitability and can render the development of certain reserves economically unfeasible. Figure 4 illustrates the distribution of REM reserves across the examined deposits, ranked from most to least abundant.

Analysis of the reserve structure of the three Arctic deposits indicates that light REM are more abundant than heavy REM. Cerium is the most prevalent element, comprising over 40 % of total reserves. Among heavy elements, gadolinium is the most abundant and terbium the scarcest. The Tomtor deposit in the Sakha Republic stands out due to its significant reserves. The presence of scarce

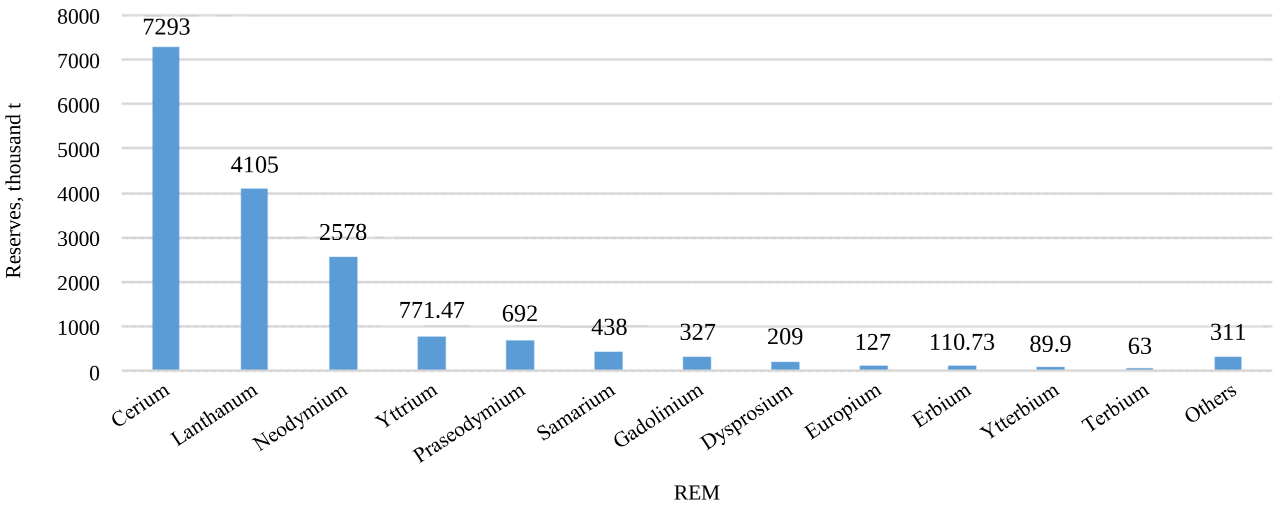

Fig.4. Russian REM reserves by metal

heavy elements, along with unique concentrations of useful components, is expected to boost extraction profitability and improve the KPIs of potential projects. These factors justify selecting this deposit as a potential candidate for certain forms of Sino-Russian technological partnership.

Assessment of rare earth metal applications in industry: comparison of Russian and Chinese consumer markets

The creation of a full production cycle for rare earth metals and their derived products must be supported by corresponding industrial demand. REM are used across a wide range of high-tech sectors, with each element having specific applications. Table 2 summarizes the primary uses of REM.

Table 2

REM applications [31-34]

REM	Application
Lanthanum	Automotive catalysts, cracking catalysts, metallurgy, hybrid engines, glass industry, polishing powders, batteries, luminophores, optics, lasers, nuclear technology
Cerium	Automotive catalysts, cracking catalysts, metallurgy, glass industry, polishing powders, batteries, luminophores, textile industry
Praseodymium	Magnets, automotive catalysts, metallurgy, glass industry, polishing powders, batteries
Neodymium	Magnets, catalysts, metallurgy, glass industry, batteries, electronics, lasers, hybrid engines
Yttrium	Luminophores, glass industry, optics, lasers, ceramics, metallurgy, aerospace, nuclear technology
Gadolinium	Magnets, luminophores, optics, lasers, X-ray technology
Terbium	Magnets, luminophores, X-ray technology
Dysprosium	Magnets, catalysts, nuclear power, hybrid engines
Samarium	Batteries, computers, measuring instruments, magnets
Europium	Luminophores, nuclear power
Promethium	Nuclear power, measuring instruments
Holmium	Glass industry, lasers
Erbium	Luminophores
Thulium	X-ray technology
Ytterbium	Lasers, metallurgy
Lutetium	Cracking catalysts
Scandium	Metallurgy, aviation, aerospace engineering, automotive engines

According to Table 2, lanthanum, cerium, praseodymium, neodymium, and yttrium are in highest demand. Praseodymium and neodymium are particularly important for permanent magnets, which are widely used in wind turbines. Globally, magnet production accounts for roughly 42 % of REM demand[9]. In China, which is the global leader in wind energy, REM consumption is strongly correlated with the growth of wind power capacity [6]. Several REM are also used in solar photovoltaic devices due to their fluorescent properties[10]. Accordingly, the green energy sector is expected to drive the most significant growth in REM demand worldwide in the near future.

Lanthanum and cerium are primarily used in catalysts and in battery production, which in turn supports electric vehicles and other forms of transport. Electric vehicle production in China has increased 20-fold over the past decade, driving substantial growth in demand for these metals[11]. Consequently, global and Chinese demand for REM is closely tied to the expansion of high-tech sectors.

Yttrium, a scarce rare earth element of the heavy group, is used in metallurgy as an alloy additive, for example in high-strength steel and cast iron. While its applications are less widespread than for permanent magnets, the inclusion of yttrium can improve the quality and durability of finished products, particularly in metallurgical applications.

REM consumption in Russia remains limited, with the petrochemical and oil refining sector accounting for roughly 70 %, metallurgy about 10 %, the nuclear industry, and others making up the remainder. Annual consumption is approximately 1.2 thousand t, and this figure has remained largely unchanged[12]. Previous studies by the authors [6, 31] indicate that medium-term growth in domestic demand will primarily be driven by emerging sectors, such as electric vehicles and green energy, alongside increased usage in traditional industries such as metallurgy and petrochemicals. Forecasts suggest that by 2030, Russian REM consumption could reach 2.3 thousand t, nearly double the current level, with neodymium being the most widely consumed element (Fig.5).

In the medium term, light REM are expected to be the most sought-after in the Russian consumer market. Among these, neodymium, which is used in magnets, batteries, and other high-tech applications, will likely experience the highest demand, followed by lanthanum, which is widely

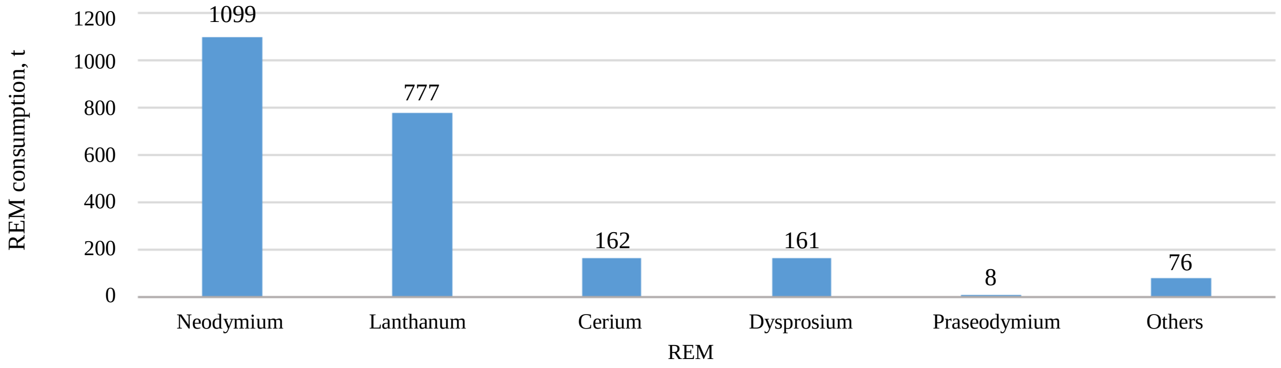

Fig.5. REM consumption in Russia: forecast for 2030 based on [6]

---

[9] Demand for rare earth oxides worldwide in 2019 and 2025 by end use. URL: https://www.statista.com/statistics/449722/rare-earth-estimated-demand-globally-by-application (accessed 16.09.2025).

[10] Zhiyan Consulting: Analytical Report on the Current Performance and Development Trends in the Chinese Rare Earth Industry in 2023 (in Chinese). URL: https://www.chyxx.com/research/yejin/list_6.html (accessed 28.04.2025).

[11] Electric vehicles – China. URL: https://www.statista.com/outlook/mmo/electric-vehicles/china#unit-sales (accessed 16.09.2025).

[12] State Report on the Status and Use of Russian Mineral Resources in 2023. Moscow: Rosnedra, 2024, p. 710 (in Russian).

employed in metallurgy, petrochemicals, and oil refining. The projected consumption of heavy REM, including dysprosium, is expected to remain significantly lower than that of light REM. However, heavy metals are used in nuclear power, X-ray imaging, and the military sector. Should growth in these sectors accelerate, total demand for REM in Russia could increase further. Given current and potential future demand, self-sufficiency in domestic reserves would allow Russia to satisfy internal needs over many years while exporting a portion of production with a focus on the Chinese market. In this context, global supply must also continue to meet worldwide demand.

China currently consumes over 170 thousand t of REM annually[13], with the largest share (over 40 %) used in the production of magnetic materials. The structure of Chinese REM demand closely mirrors global trends, encompassing metallurgy and instrument manufacturing, petrochemicals and oil refining, ceramics, hydrogen storage materials, luminophores, polishing powders, catalysts, and other sectors. Future growth in Chinese demand will be driven by several key factors[14]:

- Continuing growth in demand for electric vehicles and other types of transport and their improvement. China's market for new vehicles is experiencing rapid growth, supported by government policies that sustain high consumer demand. REM are essential in electric vehicles for motors, power steering, and other key components. Lithium batteries and automotive exhaust catalysts also contain REM [35]. Their compact size, light weight, and high performance provide significant advantages, and ongoing technological improvements in both vehicle production and REM materials drive industry growth.
- Advancements in robotics and digital technologies. Robots are used across sectors including automotive, electronics, and household appliances. China has established a full production cycle, from key components to industrial robots and integrated robotic systems. Advances in core technologies, research and development, and mass production capacity continue to expand. In this context, REM are primarily used in robotic server systems and greatly enhance their operational speed.
- Growth in wind energy capacity. China's carbon neutrality and energy transition policies promote the expansion of wind power [36]. Consequently, demand for REM-based magnets is expected to increase. Recent improvements in semi-direct drive permanent magnet generators, which use less magnetic material than direct-drive systems, may result in lower growth rates of REE magnet demand compared to previous projections.
- Increased production of inverter air conditioners, energy-efficient elevators, and household electronics. New energy efficiency standards have boosted the adoption of high-performance inverter air conditioners, which rely on efficient permanent REM-magnets. REM are also used in energy-saving elevator traction systems, which benefit from their small size, high efficiency, and wear resistance. Neodymium magnets are further applied in speakers, smartphones, wireless headphones, tablets, PC, wearable devices, and wireless chargers. Combined with growth in artificial intelligence and related technologies, this trend is expected to sustain gradual increases in REM demand, particularly for permanent magnet applications.

---

[13] Zhiyan Consulting: Analytical Report on the Current Performance and Development Trends in the Chinese Rare Earth Industry in 2023 (in Chinese). URL: https://www.chyxx.com/research/yejin/list_6.html (accessed 28.04.2025).

[14] Huibo Smart Investment Research: In-Depth Analysis of the Rare Earth Industry: Supply–Demand Balance and Market Landscape (in Chinese). URL: https://www.hibor.com.cn/data/ec51894e6abe55ca5187ab4bf54bd162.html (accessed 28.04.2025).

Overall, REM demand is projected to rise in both Russia and China in the medium term. China seeks to secure additional resources to satisfy growing domestic and global demand, while Russia requires technology and investment to establish closed-loop production cycles. In this context, it is essential to identify strategic sectors where Sino-Russian technological partnerships could be mutually beneficial, including in new, promising regions such as the Arctic. The benefits and risks for each country must be evaluated, and the most optimal forms of collaboration determined, using rare earth production as a case study.

Forms of cooperation between Russia and China in the context of the rare earth industry

To identify potential forms of international cooperation, it is necessary to consider the legal framework. Table 3 presents the types of partnerships regulated by relevant legislation, including the Civil Code of the Russian Federation.

Among these, consortia and joint ventures are the most promising forms for the REM industry, as they can facilitate joint deposit development and the creation of processing facilities. Cross-border clusters, which focus on supply chain integration, may become relevant in later stages of cooperation, provided that relevant companies exist in the bordering regions. Other forms, such as research consortia and special investment contracts, primarily support technological development and infrastructure construction, which have already been applied in Russia. One of the key conditions for cooperation in the REM sector, however, is that it must be optimal for and bring benefits to both parties.

Table 3

Forms of international cooperation[15]

Cooperation form	Participants	Validity period	Features	Application potential in the REM industry
Consortium	Temporary merger of companies without forming a legal entity	Project deadline	Flexible structure, contractual liability, no need to create a legal entity	Establishment of processing industries, joint development of deposits
Joint venture	Russian and international legal entities and individuals	Indefinitely (according to the charter)	Restrictions regarding strategic industries, the possibility of government control; the need to create a legal entity	Establishment of processing industries, joint development of deposits
Concession agreement with international participation	The government and international investors	Established by agreement	The investor receives the right to operate the facility (usually infrastructure), whereas the government retains ownership	Infrastructure development
Special investment contract (SPIC)	The government and Russian/international investors	Up to 15-20 years (validity period may be extended)	Mandatory localization: preferential terms are provided to investors in exchange for localization of production	Establishment of high-tech REM-based production, development of new technologies
Research consortium	Research organizations, universities, corporations	3-10 years on average	Joint research and development activities, the possibility of receiving government support, joint use of results	Development of technologies for the extraction and processing of rare earth metals, creation of new materials
Cross-border clusters	Businesses operating in bordering regions	Long term	Association of businesses operating in bordering regions, production cycles coordination, special economic regimes	Establishment of logistics chains for rare earth metals

---

[15] Civil Code of the Russian Federation (Part One) N 51-FZ of November 30, 1994 (as amended on July 29, 2017); Federal Law N 115-FZ "On Concession Agreements" of July 21, 2005 (as amended on November 30, 2024); Federal Law N 160-FZ "On Foreign Investments in the Russian Federation" of July 9, 1999.

As for concession agreements, they are typically used in infrastructure projects. A notable example of this type of cooperation between Russia and China is the Amur River bridge project[16].

Currently, there are no examples of Sino-Russian cooperation in REM extraction and processing. Unlike other strategic sectors, such as energy, the REM industry remains largely untapped in terms of Sino-Russian partnership potential (Table 4).

One of the most well-known examples of successful cooperation is the Yamal LNG project. Implemented in the Yamalo-Nenets Autonomous Region, the project's investors include Novatek (Russia), CNPC (China), and the Silk Road Fund. Its significance for Russia lies not only in gaining access to technologies adapted to harsh Arctic conditions but also in providing a route to Asian markets amid restricted access to Western resources [10]. Within the project, China contributed financing (both direct and credit investments), technology, and equipment, including LNG tankers, gas liquefaction modules. For China, the project provided increased energy supplies, a new trade route, and a stronger position in Arctic infrastructure development.

Another example is the Power of Siberia gas pipeline project, which serves as a channel for Russian gas supplies to China and other Asian countries while linking Russia's domestic gas transportation systems. The project was designed to reduce Russia's dependence on European gas markets amid geopolitical tensions and to access rapidly growing Asian markets. For China, it represents a new energy source that complements domestic production and is cheaper than LNG delivered by tankers. The benefits are mutual: for China, the project expands influence in Russian energy markets, mitigates energy risks from the United States and allies, supports internationalization of the yuan, and reduces legal risks via investment in Russia [12]. For Russia, the pipeline guarantees sales, generates revenue, and creates jobs. However, reliance solely on raw materials cooperation poses a risk to Russia's manufacturing industry. Moreover, China maintains long-term contracts for pipeline gas from Kazakhstan, Uzbekistan, and Turkmenistan (the latter alone accounted for 50 % of China's natural gas imports in 2023[17]) and is pursuing new agreements with Qatar, Australia, and other suppliers, which may limit Russia's market share despite potential increases in supply.

These examples illustrate the consortium model, which is the most common form of international partnership. A joint venture represents a more complex mechanism. Examples of such cooperation between Russia and China include Razrezugol LLC, a joint venture established by Russia's energy company En+ and China's CHN Energy. The project involves the construction of infrastructure for a coal deposit in Zabaikalsky Krai, which is currently underway. The deposit is expected to reach its full design capacity by the end of 2027[18]; however, the project is already facing financing difficulties related to sanction-induced restrictions on international payments. Another example of a joint venture is Sakhalin Energy LLC, which, although not a Sino-Russian partnership, previously served as the operator of the Sakhalin-2 oil and gas development project. At the time of its establishment, three international companies (Shell, Mitsui, and Mitsubishi) were shareholders, and operations were conducted under a Production Sharing Agreement with the Russian Federation. In 2007, Gazprom became a shareholder. In 2022, however, international partners withdrew from the project due to geopolitical factors. As a result, the original company was r eplaced by the Russian entity

---

[16] Construction of the first cross-border road bridge across the Amur River between the Russian Federation and China (Blagoveshchensk – Heihe) (in Russian). URL: https://www.btsmost.ru/object/blagoveshensk (accessed 16.09.2025).

[17] Energy Institute: Statistical Review of World Energy 2024. URL: https://www.connaissancedesenergies.org/sites/connaissancedesenergies.org/files/pdf-actualites/Statistical%20Review%20of%20World%20Energy%202024.pdf (accessed 18.06.2025).

[18] En+ is investing approximately 50 billion rubles in the largest coal project in Transbaikalia. URL: https://enplusgroup.com/ru/media/news/press/en-investiruet-poryadka-50-mlrd-rubley-v-krupneyshiy-ugolnyy-proekt-za-baykalya/ (accessed 16.09.2025).

Table 4

Examples of technological partnerships between Russia and China

Cooperation form	Implementation	Process segmentation	Benefits		Risks	
			For Russia	For China	For Russia	For China
Consortium	Yamal LNG	Capital investment (direct and credit financing): Russia, China, France (early stages). Infrastructure development: Russia, China. Technology provision: China, Russia. Resource extraction: Russia. Processing: Russia, China	• Attracting investment and resources for the development of the Arctic. • Supply of imported technologies and equipment. • Creation of new jobs in the region	• New sources of energy supplies. • New trade routes for the export of energy resources and other goods. • Expanding influence in the Arctic Region	• Environmental risks associated with the need to comply with more stringent environmental requirements in the region. • Risks associated with the unstable LNG pricing system. • Technological risks, such as the risk of restrictions on project modernization and digitalization due to sanctions, and increased dependence on Chinese technology and equipment	• In addition to environmental risks, there is additional reputational liability, as well as the necessity to comply with Russian legislation. • Currency risks due to high ruble volatility. • Dependence on Russian infrastructure, including nuclear icebreakers. • Political and sanctions risks. • Changes in Russian tax legislation. • Dependence on long-term contracts; limited flexibility in the face of market fluctuations
	Power of Siberia	Capital investment: Russia (China signed a 30-year sales agreement worth 400 USD billion). Infrastructure development: Russia (partially China). Technology provision: Russia. Resource extraction: Russia. Processing: China, Russia	• Access to fast-growing Asian energy markets. • New reliable distribution channels. • Creation of new jobs in the underdeveloped Far East Region. • Expansion of Russia's gas transportation system	• New sources of relatively inexpensive energy supplies and the associated reduction in energy dependence risks. • Long-term (30-year) contracts for resource supplies. • Supplier diversification. • Obtaining preferential pricing conditions among buyers of Russian gas. • Reduction in logistics costs. • Creation of infrastructure for future projects (Power of Siberia-2)	• The stagnation of processing technology development and the lack of high-value-added production in Russia create technological risks. • The raw material supply sector is sensitive to geopolitical fluctuations. • Limited opportunities for expanding cooperation as a result of China's diversification of raw material supply sources. • Risks to fragile ecosystems associated with infrastructure development (pipelines, roads)	• Geopolitical tensions introduce uncertainty into new contracts. • Dependence on Russian infrastructure. • Sanctions pressure due to cooperation with Gazprom. • Risk of supply disruptions due to pipeline accidents

End of Table 4

Cooperation form	Implementation	Process segmentation	Benefits		Risks	
			For Russia	For China	For Russia	For China
Joint venture	Razrezugol LLC	Capital investment: Russia, China. Infrastructure development: Russia, China. Technology provision: Russia, China. Resource extraction: Russia, China	• Receiving financial investment from CHN Energy in resource development and infrastructure. • Infrastructure development, improving transport and energy logistics in the region through the construction of roads, a railway station, and energy sector facilities. • Creation of jobs. • Increased export potential; diversification of coal markets. • Use of Chinese technologies in coal mining and logistics	• Guaranteed coal supplies and long-term access to Russian energy resources. • Reduced dependence on other suppliers. • Logistics savings due to the deposit's proximity to the Chinese border. • Strengthening CHN Energy's position in the Russian coal industry, opening up opportunities for new projects	• Funding issues due to sanctions. • There is a risk of foreign partners leaving, which will require a company reorganization (similar to Sakhalin Energy). • Potential limitations in equipment maintenance or spare parts supplies. • Growth in coal mining may lead to environmental pollution, protests by local residents, and stricter regulations. • High influence of global market conditions on coal sales	• Tighter regulation or nationalization of assets may impact investment returns. • Sanctions against Russia may complicate coal transportation (e.g., restrictions on maritime shipping). • Tighter regulation in the coal industry may require additional investment in environmental measures. • In the long term, tightening climate policies both in China and globally may lead to a decrease in coal demand

Sakhalin Energy LLC[19]. The reviewed forms of Sino-Russian partnership, along with their associated benefits and risks, are summarized in Table 4.

Among the forms of technological cooperation considered, a consortium-based joint project appears to be the most optimal option for both Russia and China. This format allows Russia to attract investment, advanced technologies, and equipment required for Arctic development, while providing China with access to new sources of raw materials. Such cooperation is expected to yield long-term benefits for both parties: upon completion of the project, Russia will retain the technologies necessary to establish full production cycles in the rare earth industry, while China will secure new strategic trade routes, particularly via the Northern Sea Route, and strengthen its presence in the Arctic Region. Compared with other forms of cooperation, such as joint ventures, a consortium is a more flexible arrangement implemented within a defined timeframe, which helps mitigate pricing, market, and long-term geopolitical risks. Moreover, joint ventures require the establishment of a legal entity, creating additional risks for Russia: in the event of a partner's withdrawal, the company must undergo rapid restructuring. For China, participation in a joint venture must be justified not only by current demand but also by long-term strategic needs, which are inherently difficult to forecast. Overall, the risks associated with consortium-based cooperation are significantly lower than those of joint ventures, which, as past experience demonstrates, are more vulnerable to shifts in market conditions, geopolitical dynamics, and other conditions due to their organizational and economic features.

Conclusion

Russia currently lags behind China, which has established full production cycles for rare-earth metal products used in electronics, robotics, electric vehicle, renewable energy, and other industries. In Russia, these sectors are either underdeveloped or at an early stage of formation. However, the development of the mineral resource base represents a key area where the strategic interests of Russia and China converge. The Arctic Region possesses substantial potential for the development of its mineral resources and the expansion of new trade routes, making it an area of growing interest for multiple nations. The unique reserves of the Tomtor deposit could serve as a foundation for the advancement of Sino-Russian cooperation in the Arctic. Russia's resource potential enables it to meet both domestic and international demand, which is of particular interest to China amid sustained growth in global REM consumption.

This study of Sino-Russian partnership in the Arctic, using the REM industry as a case study, has yielded results with both scientific and practical relevance for strategic economic sectors. Among the cooperation models examined, a consortium-based partnership, similar to the Yamal LNG and Power of Siberia projects, emerges as the most promising. This format allows Russia to attract investment and technology, while enabling China to secure access to new sources of raw materials and enhance its strategic position in the Arctic. Alternative formats, such as joint ventures, are less advantageous for Russia and entail additional risks for China. Other forms of cooperation, including research consortia, cross-border clusters, and concession agreements, are not optimal at the current stage for either of the two parties but may be applied at later phases of technological partnership.

The findings of this research may be used at the national level to inform strategies for the development of the REM industry and other strategic segments of the mineral resources sector, strengthen international cooperation between Russia and China, and support businesses planning investment projects in the Arctic, including mineral resource development and the establishment of full production cycles. Future research may focus on strengthening the economic and geopolitical dimensions of the analysis, particularly by examining the impact of international sanctions and trade restrictions on

---

[19] Sakhalin Energy. Company Profile. Overview. URL: https://www.sakhalinenergy.ru/ru/company/overview/ (accessed 16.09.2025).

Sino-Russian cooperation, as well as exploring opportunities to diversify REM export markets, including countries in Asia and the Middle East. Additional research may also assess Arctic infrastructure projects, identifying opportunities for logistics optimization and cost reduction in order to generate both qualitative and quantitative insights.

Overall, Sino-Russian partnership in the Arctic has significant potential to strengthen the global positions of both countries in the REM market. The successful implementation of joint projects, including the development of Arctic deposits, could become a key driver of technological and economic growth. However, achieving maximum impact requires careful consideration not only of economic benefits, but also of environmental, social, and geopolitical risks. Continued research in this area will contribute to a deeper understanding of the opportunities and challenges associated with Arctic resource development.

REFERENCES

1. Kryukov V.A., Yatsenko V.A., Kryukov Ya.V. The REM-Energy Transition Interrelation in the Context of Full-Cycle Projects. *Geology of Ore Deposits.* 2023. Vol. 65. N 5, p. 416-427. DOI: 10.1134/S1075701523050057

2. Yatsenko V.A., Lebedeva M.E. Demand Forecasting in World Rare Earth Metals Market. *World of Economics and Management.* 2021. Vol. 21. N 4, p. 124-145 (in Russian). DOI: 10.25205/2542-0429-2021-21-4-124-145

3. Mikhailov A.V., Bouguebrine C., Shibanov D.A., Bessonov A.E. Impact Evaluation of Excavator Positioning on Open Pit Slope Stability. *International Journal of Engineering, Transactions A: Basics*. 2025. Vol. 38. Iss. 1, p. 99-107. DOI: 10.5829/ije.2025.38.01a.10

4. Petrov I.M., Belousova E.V., Petrova A.I. The development of renewable energy and environmentally friendly transport – the main directions of growth in global demand for high-tech rare metals. *Prospect and protection of mineral resources.* 2020. N 3, p. 53-56 (in Russian).

5. Kryukov V.A., Yatsenko V.A., Kryukov Ya.V. Rare Earth Industry – How to Take Advantage of Opportunities. *Russian Mining Industry.* 2020. N 5, p. 68-84. DOI: 10.30686/1609-9192-2020-5-68-84

6. Cherepovitsyn A.E., Dorozhkina I.P., Soloveva V.M. Forecasts of Rare-earth Elements Consumption in Russia: Basic and Emerging Industries. *Studies on Russian Economic Development.* 2024. Vol. 35. N 5, p. 688-696. DOI: 10.1134/S1075700724700229

7. Xingli Jia, Bo Zhang, Zhongshuai Jia et al. Recovery of niobium, titanium and rare earths from Bayan Obo tailings via silicothermic reduction and targeted crystallization. *Minerals Engineering*. 2025. Vol. 234. N 109718. DOI: 10.1016/j.mineng.2025.109718

8. Jihye Kim, Junhyun Choi, Sugyeong Lee. A Review of Rare Earth Elements Recovery from Bastnaesite Ore: From Beneficiation to Metallurgical Processing. *Journal of Sustainable Metallurgy*. 2025. Vol. 11, p. 773-798. DOI: 10.1007/s40831-025-01019-0

9. Niam A.C., Ya-Fen Wang, Shyh-Wei Chen, Sheng-Jie You. Recovery of rare earth elements from waste permanent magnet (WPMs) via selective leaching using the Taguchi method. *Journal of the Taiwan Institute of Chemical Engineers*. 2019. Vol. 97, p. 137-145. DOI: 10.1016/j.jtice.2019.01.006

10. Afanasev S.N., Fadeev A.M. Sino-Russian technological partnership in the Arctic on the example of Yamal LNG project. *Arctic and Innovations.* 2025. Vol. 3. N 1, p. 33-41 (in Russian). DOI: 10.21443/3034-1434-2025-3-1-33-41

11. Iakhiaev D., Grigorishchin A., Zaikov K. et al. Methodological approach to assessing the digital infrastructure of the northern regions of the Russian Federation. *Journal of Infrastructure, Policy and Development*. 2024. Vol. 8. Iss. 12. N 8747. DOI: 10.24294/jipd.v8i12.8747

12. Zemtsov A.S. Benefits and risks for Russia and China from the interconnection of energy infrastructure. *Bulletin of Moscow Witte University. Series 1: Economics and Management.* 2024. N 2 (49), p. 80-88 (in Russian). DOI: 10.21777/2587-554X-2024-2-80-88

13. Nevskaya M., Shabalova A., Nikolaichuk L., Kirsanova N. Development of a Quantitative Assessment Algorithm for Operational Risks in Mining Engineering. *Resources*. 2025. Vol. 14. Iss. 4. N 53. DOI: 10.3390/resources14040053

14. Semenova T., Sokolov I. Theoretical Substantiation of Risk Assessment Directions in the Development of Fields with Hard-to-Recover Hydrocarbon Reserves. *Resources*. 2025. Vol. 14. Iss. 4. N 64. DOI: 10.3390/resources14040064

15. Dmitrieva D., Solovyova V. Russian Arctic Mineral Resources Sustainable Development in the Context of Energy Transition, ESG Agenda and Geopolitical Tensions. *Energies*. 2023. Vol. 16. Iss. 13. N 5145. DOI: 10.3390/en16135145

16. Bortnikov N.S., Volkov A.V., Galyamov A.L. et al. Fundamental Problems of Development of the Mineral-Resource Base of High-Tech Industry and Energy of Russia. *Geology of Ore Deposits.* 2022. Vol. 64. N 6, p. 313-328. DOI: 10.1134/S1075701522060022

17. Bryantseva O.S. The state and development opportunities of the Russian rare earth industry in the context of the fourth industrial revolution. *Russian Economic Bulletin.* 2022. Vol. 5. N 6, p. 264-271 (in Russian).

18. Maksimova V.V., Krasavtseva E.A., Savchenko Ye.E. et al. Study of the composition and properties of the beneficiation tailings of currently produced loparite ores. *Journal of Mining Institute.* 2022. Vol. 256, p. 642-650. DOI: 10.31897/PMI.2022.88

19. Ponomareva M.A., Cheremisina O.V., Mashukova Yu.A., Lukyantseva E.S. Increasing the efficiency of rare earth metal recovery from technological solutions during processing of apatite raw materials. *Journal of Mining Institute*. 2021. Vol. 252, p. 918-927. DOI: 10.31897/PMI.2021.6.13

20. Kalashnikov A.O., Konopleva N.G., Danilin K.P. Rare earths of the Murmansk Region, NW Russia: Minerals, extraction technologies and value. *Applied Earth Science: Transactions of the Institutions of Mining and Metallurgy*. 2023. Vol. 132. Iss. 1, p. 52-61. DOI: 10.1080/25726838.2022.2153000

21. Kalashnikov A.O., Konopleva N.G., Pakhomovsky Ya.A., Ivanyuk G.Yu. Rare Earth Deposits of the Murmansk Region, Russia – A Review. *Economic Geology*. 2016. Vol. 111. N 7, p. 1529-1559. DOI: 10.2113/econgeo.111.7.1529

22. Malkova M.Yu., Zadiranov A.N., Zaya Kyaw, Dkhar P. Ore of the Tomtor rare-earth deposit for its industrial processing. *Journal of Physics: Conference Series*. 2020. Vol. 1687. N 012038. DOI: 10.1088/1742-6596/1687/1/012038

23. Matveev A.I., Tolstov A.V., Petrov I.M. The proposal for developing a rare metal cluster in the Republic of Sakha (Yakutia). *Arctic and Subarctic Natural Resources*. 2025. Vol. 30. N 1, p. 7-27 (in Russian). DOI: 10.31242/2618-9712-2025-30-1-7-27

24. Houjian Li, Yanjiao Li, Fangyuan Luo, Lili Guo. Navigating extreme risk spillovers: Building a synergistic network of rare earths, green bonds, and clean energy markets in China. *Energy Economics*. 2025. Vol. 147. N 108562. DOI: 10.1016/j.eneco.2025.108562

25. Tian-Yu Zhao, Wei-Lun Li, Kelebek S. et al. A comprehensive review on rare earth elements: resources, technologies, applications, and prospects. *Rare Metals*. 2025. Vol. 44. Iss. 10, p. 7011-7040. DOI: 10.1007/s12598-025-03459-9

26. Jingna Kou, Fengjun Sun, Wei Li, Jie Jin. Could China Declare a “Coal Phase-Out”? An Evolutionary Game and Empirical Analysis Involving the Government, Enterprises, and the Public. *Energies*. 2022. Vol. 15. Iss. 2. N 531. DOI: 10.3390/en15020531

27. Galevskiy S., Haidong Qian. Developing and validating comprehensive indicators to evaluate the economic efficiency of hydrogen energy investments. *Operational Research in Engineering Sciences: Theory and Applications*. 2024. Vol. 7. Iss. 3, p. 188-207. DOI: 10.5281/zenodo.15093154

28. Savostova T.L., Biryukov A.L. Institutional mechanisms for the strategic partnership between Russia and China: the innovative integration. *Russian Journal of Industrial Economics*. 2016. N 2, p. 108-115 (in Russian). DOI: 10.1707/2072-1663-2016-2-108-115

29. Lalomov A.V., Grigoreva A.V. Mineralogy of rare-metal pacer deposits of the Lovozero massif. *Trudy Fersmanovskoi nauchnoi sessii GI KNTs RAN*. 2022. N 19, p. 190-194 (in Russian). DOI: 10.31241/FNS.2022.19.035

30. Kalashnikov A.O., Konopleva N.G., Ivanyuk G.Yu. Valuation of rare earth elements in ore deposits in the Murmansk Region. *Gornyi zhurnal*. 2020. N 9, p. 42-46 (in Russian). DOI: 10.17580/gzh.2020.09.05

31. Cherepovitsyn A.E., Dorozhkina I.P., Guseva T.V., Burvikova Yu.N. Problems and institutional framework for the development of the rare earth metals industry in Russia. *Tsvetnye metally*. 2024. N 8, p. 58-69 (in Russian). DOI: 10.17580/tsm.2024.08.09

32. Marinina O.A., Ilyushin Y.V., Kildiushov E.V. Comprehensive Analysis and Forecasting of Indicators of Sustainable Development of Nuclear Industry Enterprises. *International Journal of Engineering, Transactions B: Applications*. 2025. Vol. 38. Iss. 11, p. 2527-2536. DOI: 10.5829/ije.2025.38.11b.05

33. Cheremisina O.V., Balandinsky D.A., Gorbacheva A.A. et al. Physicochemical features of action of ethoxylated esters of phosphoric acid with different degree of ethoxylation in conditions of froth flotation of apatite. *Colloids and Surfaces A: Physicochemical and Engineering Aspects*. 2025. Vol. 708. N 135974. DOI: 10.1016/j.colsurfa.2024.135974

34. Yujra Rivas E., Vyacheslavov A., Gogolinskiy K.V. et al. Deformation Monitoring Systems for Hydroturbine Head-Cover Fastening Bolts in Hydroelectric Power Plants. *Sensors*. 2025. Vol. 25. Iss. 8. N 2548. DOI: 10.3390/s25082548

35. Shiyue Zheng, Xiaoyong Zhu, Zixuan Xiang et al. Technology trends, challenges, and opportunities of reduced-rare-earth PM motor for modern electric vehicles. *Green Energy and Intelligent Transportation*. 2022. Vol. 1. Iss. 1. N 100012. DOI: 10.1016/j.geits.2022.100012

36. Lisha Tang, Pervukhin D.A. Enhancing operational efficiency in coal enterprises through capacity layout optimisation: A cost-effectiveness analysis. *Operational Research in Engineering Sciences: Theory and Applications*. 2024. Vol. 7. Iss. 3, p. 144-167. DOI: 10.5281/zenodo.15093139

***Authors*: Aleksei E. Cherepovitsyn,** *Doctor of Economics, Professor, Head of Department (Empress Catherine II Saint Petersburg Mining University, Saint Petersburg, Russia), https://orcid.org/0000-0003-0472-026X*, **Irina P. Dorozhkina,** *Postgraduate Student (Empress Catherine II Saint Petersburg Mining University, Saint Petersburg, Russia), irinadorozhkina.99@gmail.com, https://orcid.org/0009-0009-9292-2064*, **Kou Jingna,** *PhD in Economics, Associate Professor (Taiyuan University of Technology, Taiyuan, China), https://orcid.org/0000-0003-2240-2505.*

The authors declare no conflict of interests.

ISSN 2411-3336; e-ISSN 2541-9404

JOURNAL OF MINING INSTITUTE

Zapiski Gornogo instituta

Journal homepage: pmi.spmi.ru

Research article

Geotechnical Engineering and Engineering Geology

Mechanism of microcrack zone formation in rock samples of various lithological types under triaxial stress state fracture conditions

Vladimir L. Trushko✉, **Mikhail D. Ilinov, Aleksandr O. Rozanov, Malik M. Saitgaleev, Dmitrii N. Petrov, Daniil A. Karmanskii, Aleksandr A. Selikhov**
Empress Catherine II Saint Petersburg Mining University, Saint Petersburg, Russia

***How to cite this article*:** Trushko V.L., Ilinov M.D., Rozanov A.O., Saitgaleev M.M., Petrov D.N., Karmanskii D.A., Selikhov A.A. Mechanism of microcrack zone formation in rock samples of various lithological types under triaxial stress state fracture conditions. Journal of Mining Institute. 2026. Vol. 277, p. 136-145.

Abstract
Study of fracture mechanics in heterogeneous rocks, including crack initiation and propagation, has practical applications for geocontrol and identification of fracture zones in hydrocarbon well extraction. The features of microcrack zone formation depending on the type of rock heterogeneity under triaxial stress state conditions are considered. The research was conducted using an MTS 815 servo-hydraulic testing frame integrated with a Milne DAQ acoustic emission system (Itasca International Company, UK). The paper presents the fracture results of samples of various lithological types manufactured from cores of post-magmatic rocks. Fine-grained samples with gneissic and banded textures, as well as a coarse-grained sample with massive texture, were tested. During the tests, acoustic emission (AE) was recorded using 12 piezoceramic sensors. To describe the geometry of the fracture zone, the coordinates of AE event hypocenters were calculated, then the configuration of hypocenters distribution was analyzed using a tomography procedure (layer-by-layer construction of AE event density maps), and the angles β between the direction of the macrocrack and the axial stress σ_1 were determined. To interpret the failure evolution, trends of the *b*-factor and AE activity were calculated, the intervals of critical behavior of which were correlated with the localization and tomography data. After testing the samples, the types of their deformation and the mechanism of destruction with the phenomenon of dilatation were revealed. It is established that for the considered types of sample inhomogeneities, various microcrack structures are formed under the same volumetric loading conditions. In fine-grained rock of gneissic texture, a linear distribution of AE hypocenters is formed, indicating the formation of microcracks along the direction of layering. For the fine-grained rock with banded texture, the hypocenter distribution is characterized by the formation of distinct clusters, reflecting areas of the most intensive fracturing. In the coarse-grained massive texture sample, a volumetric distribution of hypocenters is observed, manifesting dilatancy properties and the formation of an extensive microcrack network.

Keywords
triaxial compression; dilatancy; microcrack; acoustic emission; fracture mechanism; *b*-factor

Funding
The work was carried out within the framework of the State assignment FSRW-2024-0008.

Received: 15.09.2025 ***Accepted: 24.12.2025*** ***Online: 11.02.2026*** ***Published: 27.02.2026***

Introduction

The advancement of fracture mechanics and the identification of open fracturing in rocks of varying lithological types and structures, based on laboratory methods for determining fracture system parameters that affect the productivity of oil and gas as well as geothermal reservoirs, is a relevant research direction with practical significance for enhancing the efficiency of well-based hydrocarbon production [1, 2]. Alongside the determination of the physical and mechanical properties of rocks, it is necessary to investigate the structural and textural features of rock masses and their influence on fluid saturation in well placement areas. To increase the efficiency of oil and gas wells in the hydrocarbon production, a comprehensive assessment of the properties of the formation is carried out, including the determination of natural fracturing of the formation, tectonic disturbances, and core studies are also carried out [3, 4]. It is noted in [5, 6] that the main indicators of reservoir fluid saturation are karst formation, zones of cracks and fault zones. The permeability of fractured reservoirs depends most on the orientation of the fracture systems and disturbances relative to the main stresses [7]. To clarify the reservoir properties of the deposit, the structure of the distribution of lithotypes by reservoir volume is analyzed [8].

During deep drilling [9, 10], it is necessary to take into account not only the effect of increasing the strength of rocks by increasing the all-round pressure, but also the orientation of the inhomogeneities with respect to the maximum main stress. It was shown in [11-13] that the heterogeneous structure of arock mass has a significant effect on its mechanical characteristics, in particular, on strength limit. Process modeling has established that during virtual compression, the maximum deviation of strength values from the average reaches 60 % when the angle of inclination of the system of inhomogeneities in the form of cracks changes relative to the horizontal plane from 0 to 75°.

The experimental study of the physical and mechanical properties of rocks and their degree of fracturing is carried out using laboratory testing methods involving extensometers and servo-controlled testing machines [14-16]. To investigate the influence of the heterogeneous rock structure on strength characteristics, numerical modeling methods based on discrete grain-based elements (GBM) are being developed [17, 18]. Among laboratory methods, the acoustic emission (AE) technique [19-21] is gaining increasing relevance, used for real-time study of the formation and evolution of defect structures, as well as the influence of heterogeneities on strain localization under mechanical loading.

The fracture of solids is accompanied by the formation of an acoustic field caused by the emission of elastic waves during crack formation [22-24]. The informational content of the acoustic field in studying the fracture process implies the existence of unambiguous relationships between the characteristics of the radiation source (a propagating crack), the properties of the object under study (rock), and the parameters of the AE [25-27]. Since acoustic emission arises from the rupture of bonds at the crack tip, accompanied by the instantaneous release of strain potential energy when the local material strength limit is exceeded, the radiated energy depends on the crack size and the magnitude of local stress [28]. From the onset of crack initiation to the formation of a macroscopic fracture, the scale of the process varies from the destruction of mineral grains in the rock to the coalescence of microcracks into a main rupture. The formation of a microcrack zone during brittle fracture triggers the dilatancy process [29-31].

Research methods

The study of rock sample behavior under a triaxial stress state was conducted using an MTS 815 servo-hydraulic testing system integrated with a Milne DAQ acoustic emission system (Itasca International Company, UK). The technical specifications of the MTS 815 system allow for the application of a confining pressure of up to 80 MPa and an axial load on the sample of up to 4600 kN. The MTS 815 system comprises a load frame, a triaxial compression chamber, confining and pore pressure intensifiers, controllers, and a software package for automatic loading control, as well as for data acquisition and processing from the load cell and deformation sensors. The samples were tested under a confining pressure of 40 MPa.

Examples of the fracture of three samples of different lithological types, manufactured from post-magmatic rock cores, are considered. Figure 1 shows photographs of the samples before testing: two fine-grained samples with gneissic (A) and banded (B) textures, and one coarse-grained sample with massive texture (C). The gneissose texture of sample A is oriented at an angle of 50-60° to the core axis. The banded texture of sample B is defined by heterogeneities aligned with the maximum principal stress (at an angle of 0-5° to the sample axis).

AE signal acquisition was performed by the Milne DAQ data acquisition system in triggered mode. The main triggering and recording parameters were controlled via the Milne Leach software module: signal sampling frequency – 10 MHz; number of samples per signal – 2048 samples; band-pass filter for signal processing – 100-1200 kHz; dynamic range – 5 V; trigger threshold per channel – 80-100 mV.

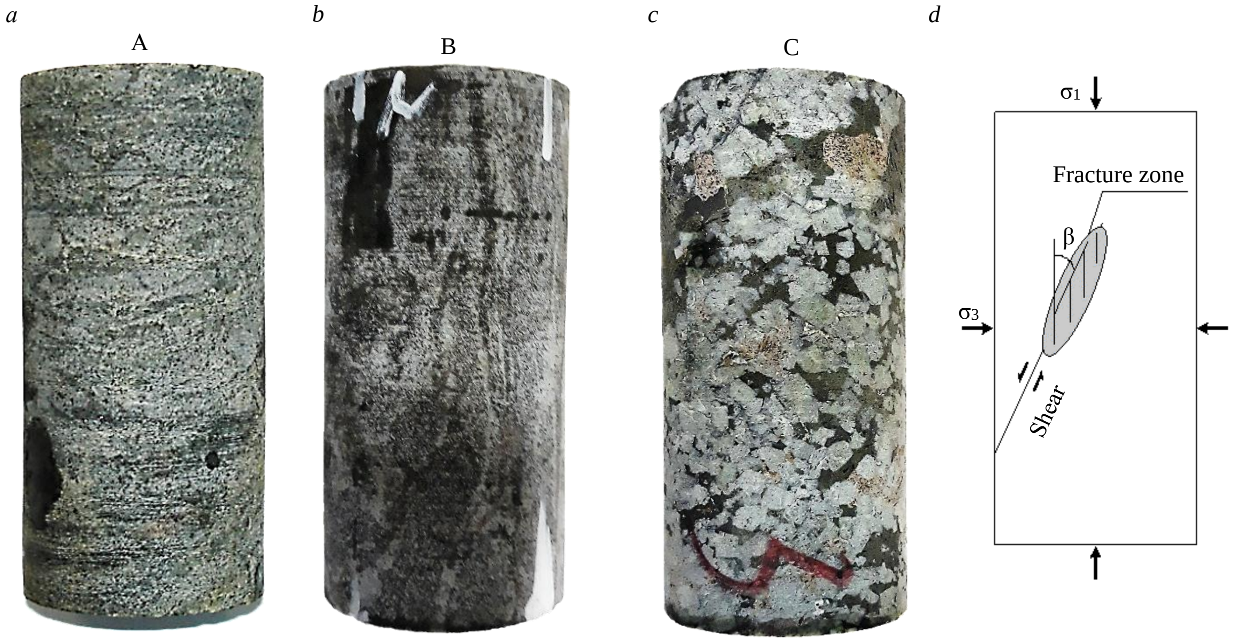

Fig.1. Samples before testing: *a* – fine-grained gneissic texture A; *b* – fine-grained banded texture B; *c* – coarse-grained massive texture C; *d* – schematic of rock sample loading and fracture

The samples were made in the form of cylinders 125 mm high and 50 mm in diameter. The side and end surfaces of the sample were sealed using a rubber shell. 12 acoustic emission sensors were installed on the side surface of the sample. The sample was then placed in a three-axis compression chamber, in which a lateral pressure of σ_3 equal to 40 MPa was created with mineral oil. After that, the sample was loaded with an axial load σ_1 at a speed of 0.01 mm/min.

The coordinates of the AE hypocenters and the construction of event density maps were calculated using the ASC InSite Seismic Processor software (Itasca International Company. 2019, v 3.15, UK). The wave velocities used in calculating the coordinates were measured by ultrasound before testing each sample. As a result, for samples A and B, the wave velocities were set in the calculation as V_p = 3517 m/s and V_s = 1691 m/s, and for sample C – V_p = 4767 m/s and V_s = 3150 m/s. To determine the arrival times of the *P*-wave for each channel of the AE event, the function of automatically determining the time of the first entry of the signal, built into the InSite Seismic Processor, was used.

Figure 1, *d* shows a general scheme illustrating the process of consolidated rocks destruction under conditions of all-round pressure [32]. This model was developed by the authors based on the analysis of AE event location data in samples of Westerly granite and analytically described stress fields of expanding microcracks [33]. According to the model, the origin of a macrofracture begins with the formation of a fracture preparation zone as a result of the unstable interaction of separation microcracks in the area of their critical concentration. Stress fields related to shear along the fracture enhance the opening of microcracks in the fracture preparation area, thereby transferring the process of formation of new microcracks to unstable and making the transition to macrofracture. In this case, the rupture spreads in a plane forming an angle β = 20-30° to the axis of maximum compression stress σ_1.

To determine the geometry of the fracture zone, the configuration of the distribution of AE event hypocenters was analyzed. The AE event density maps were calculated, the shape of which described the fracture structure and estimated the angle β between the direction of the macrofracture and the axial stress σ_1 (Fig.1, *d*). To clarify the nature of the fracture, the results of the location were compared with the fracture geometry, which was visually revealed by the predominant direction of macroscopic cracks on the surface of the tested samples.

To illustrate the energy of AE events, the magnitude M_L values corresponding to the color diagrams were displayed on the distributions of their hypocenters. The magnitude was determined using a function built into the InSite Seismic Processor program for each location event as the logarithm of the average of the number of sensors, the product of the standard deviation of each event signal by the distance between the corresponding sensor and the event source:

$$M_L = \log\left(\frac{\sum_{m=1}^{n}\left(W_m^{RMS} d_m\right)}{n}\right),$$

where n – the number of AE sensors; d_m – the distance between the sensor m and the source; W_m^{RMS} – the standard deviation of the signal along the channel m.

The b-factor and AE activity were used to interpret the fracture evolution. In accordance with the Guttenberg – Richter law [34], the b-factor was determined as follows:

$$b = \lg\frac{N_{AE}^1}{N_{AE}^2}\Big/\lg\frac{A_2}{A_1},$$

where N_{AE}^1 – the number of AE events with an amplitude greater than A_1; N_{AE}^2 – the number of AE events with an amplitude greater than $A_2\left(A_2 > A_1\right)$.

The signal values, the maximum of all recorded signals for each AE event, were compared with the amplitudes A_1 and A_2. The b-factor changes in such a way that an increase in the number of high-amplitude events causes a decrease in the b values for the specified time intervals of a certain test. Thus, the b-factor acquires the meaning of the probability of a critical condition of the rock – the lower the b value, the more likely the condition is close to brittle fracture.

When constructing trends of the b-factor and AE activity, the method of a sliding time window of variable duration was used, which sequentially moved along the time axis of each test. The window duration was chosen in such a way as to ensure sufficient trend resolution, and at the same time statistically significant estimates of the b-factor and AE activity. The calculation of the b-factor and AE activity was performed using a computer application developed by the authors.

Results

In order to analyze the structure of the zone of microcracks formed during loading, tomography was performed for all samples, which consists in layer-by-layer construction of event density maps. The resolution of the density maps, thickness, and orientation of the layers were set in such a way as to identify the most characteristic features of the microcrack structure for each sample.

The event density of sample A was calculated for 2.5 mm thick layers with a resolution of 33×83. Figure 2 shows the locations of AE event hypocenters, an event density map, and a photo after testing for this sample. It can be seen that the main cluster of events has a linear shape located at an angle $\beta = 51°$ to the axis of the sample (Fig.2, *a*, upper part of the sample). When comparing the distribution of hypocenters of events (Fig.2, *a*) with the photo of the sample after testing (Fig.2, *c*), it can be concluded that this direction corresponds to the main fracture formed in the form of a macrofracture (a light trace on the sample).

The event density of sample B was calculated for 5 mm thick layers with a resolution of 20×50. Figure 3 shows the locations of AE event hypocenters, event density maps, and a sample after testing [35]. It can be seen from Fig.3, *a* that the crack formation structure differs significantly from Sample A of the gneissic texture. It is characterized by a volumetric distribution with a tendency to localize hypocenters. Using the tomography procedure, two distinct spherical clusters were identified at levels differing in height (Fig.3, *b*, *c*). At the same time, the macrofracture, as can be seen in Fig.3, *d*,

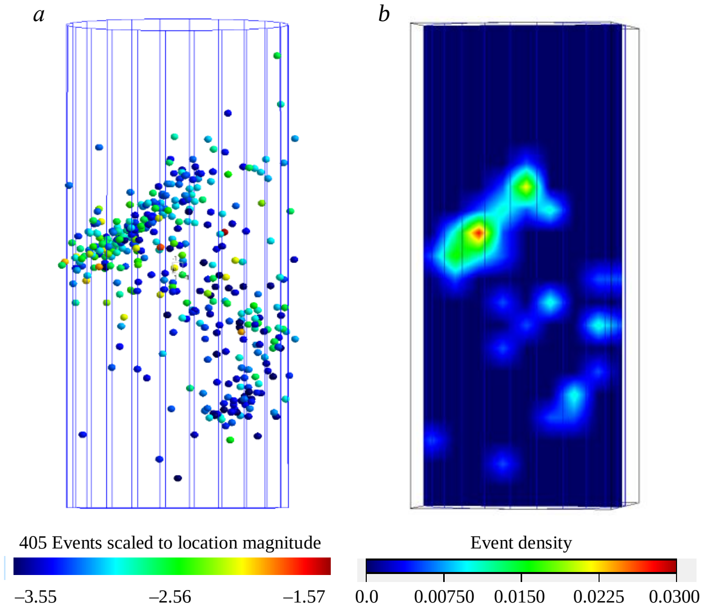

Fig.2. Analysis of the microcrack zone for a fine-grained sample A of gneissic texture (strength limit 467 MPa): *a* – distribution of AE event hypocenters for the entire test time; *b* – event density map; *c* – sample after testing

formed as a rectilinear rupture with an angle β of approximately 21°. This angle lies in the range of values predicted in [32] for brittle fracture.

The event density of sample C was calculated for 2.5 mm thick layers with a resolution of 22×55. Figure 4 shows the locations of AE event hypocenters, event density maps, and a sample after testing. The distribution of hypocenters is most scattered here (Fig.4, *a*) compared to the previous samples. At the same time, the detailed location results reveal two characteristic clusters with the highest event density compared to previous samples (Fig.4, *b*, *c*). It can be seen from Fig.4, *d* that the macro-fracture was formed in the form of a smooth curved line. An analysis of the evolution of the fracture process over time, the parameters of which are the activity and the AE *b*-factor, showed that this macrofracture

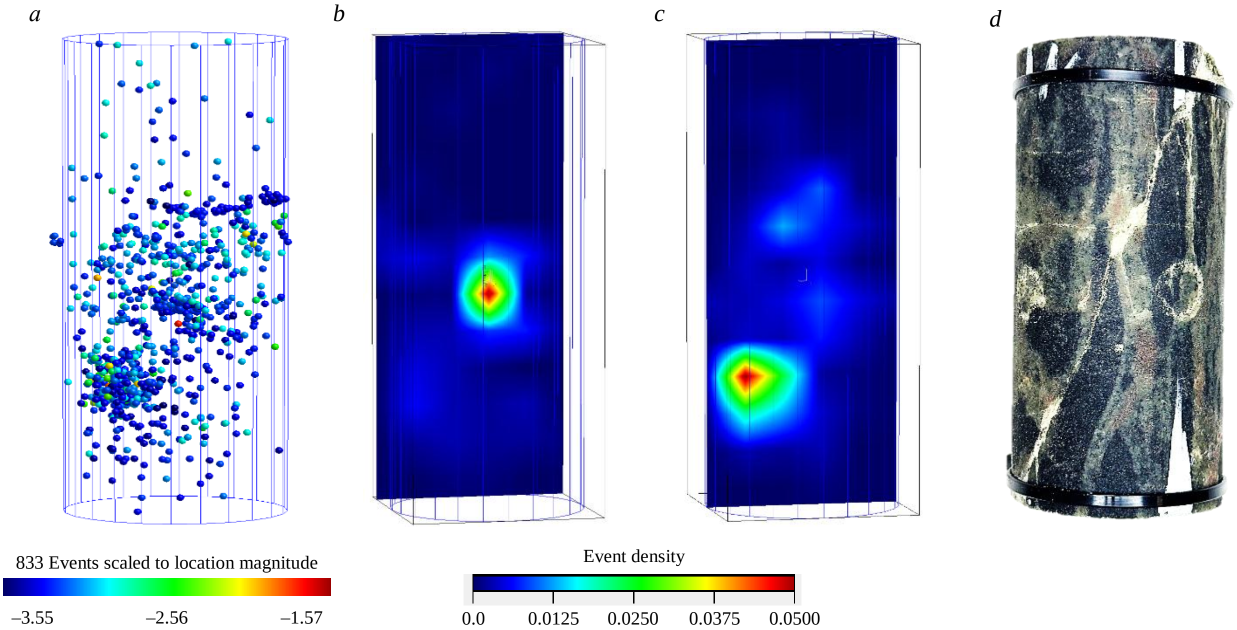

Fig.3. Analysis of the microcrack zone for a fine-grained sample B of a banded texture (strength limit 520 MPa): *a* – distribution of AE event hypocenters over the entire test period; *b* – event density map revealing the first cluster; *c* – event density map revealing the second cluster; *d* – sample after testing

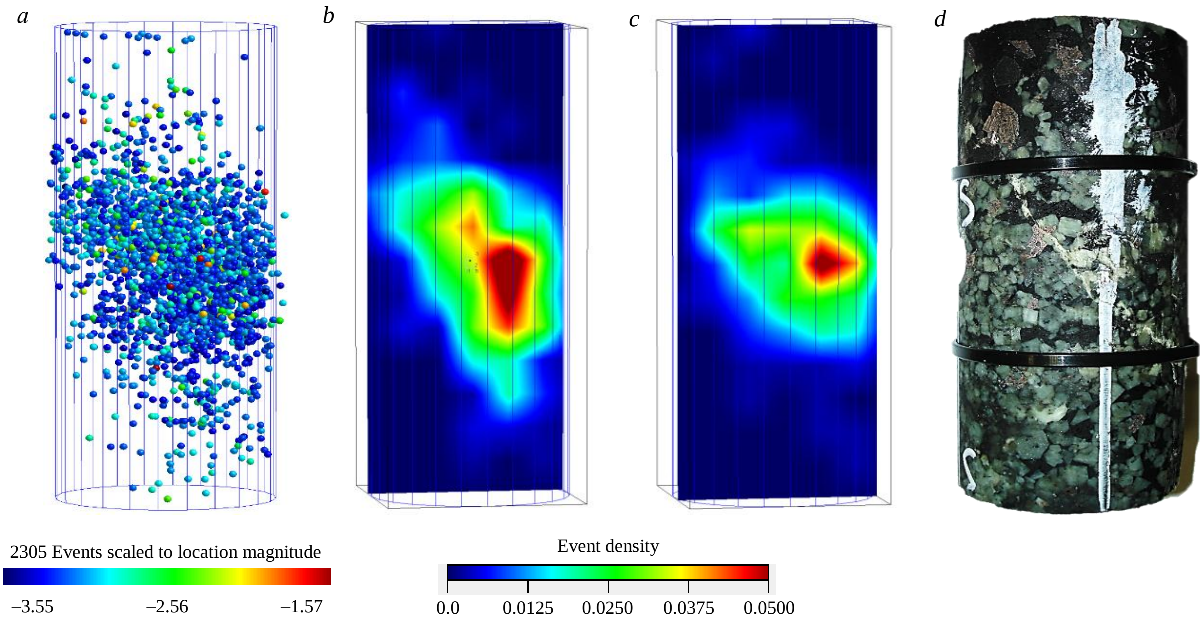

Fig.4. Analysis of the microcrack zone for coarse-grained sample C of massive texture (strength limit 341 MPa):
a – distribution of AE event hypocenters for the entire test time; *b* – event density map, first cluster;
c – event density map, second cluster; *d* – sample after testing

curve can be roughly decomposed into two straight lines (Fig.5). These lines are identified sequentially if the hypocenter distributions are plotted separately for the events of the first peak of activity corresponding to the interval 4100-5100 s in Fig.6, and for the events of the main peak of activity for the interval 9800-10,600 s.

Thus, according to the distributions of AE hypocenters, a visual assessment was made of the prevailing direction of source placement for the stage of the intermediate surge of AE activity and for the main peak associated with destruction. The angle of inclination β for the line corresponding to the stage of the first peak is 34.6° (see Fig.5, *a*), and for the line of the second peak – 44.5° (see Fig.5, *b*). One can imagine the development of fracture in such a way that the fracture zone seems to unfold counterclockwise over time, this leads to a smooth curvature of the resulting fault line. This kind of turn can also be noted on the density maps (see Fig.4, *b*, *c*) of the distributions of the total number of events over the entire test period. Density maps correspond to two layers that display the distribution in different areas of the sample.

To analyze the process of crack formation over time, the activity trends and the AE *b*-factor were calculated. Figure 6 shows the results of calculating the activity and *b*-factor for sample C in a massive texture. Moreover, the activity is plotted for all location events recorded during the test, and the *b*-factor is only for the intervals in the area of the first and second peaks of activity. Next, the average value of the *b*-factor was calculated for these intervals, indicated as a level by the green line in Fig.6. This representation of information most clearly reveals the signs of uncritical and critical crack formation processes. The uncritical process of macrofracture formation corresponds to the stable state of the sample and does not lead to catastrophic destruction. In Fig.6, such a formation

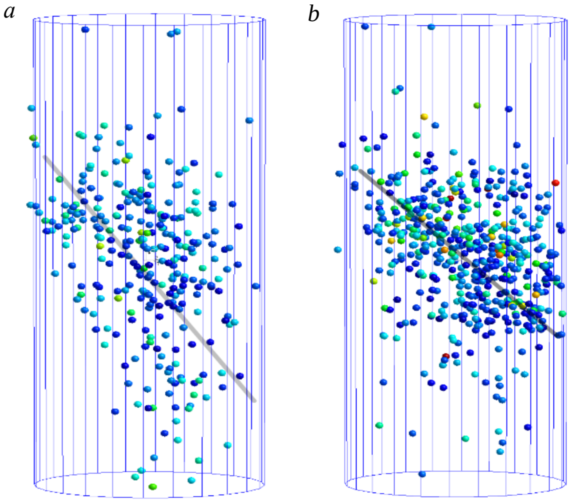

Fig.5. Decomposition of the resulting fault
for sample B into two predominant directions:
a – according to the distribution of hypocenters of events
corresponding to the sample 4463-4767 s on the time axis,
the area of the first peak of AE activity;
b – according to the distribution of hypocenters of events
corresponding to the sample 10,334-10,619 s on the time axis,
the area of the second peak of AE activity

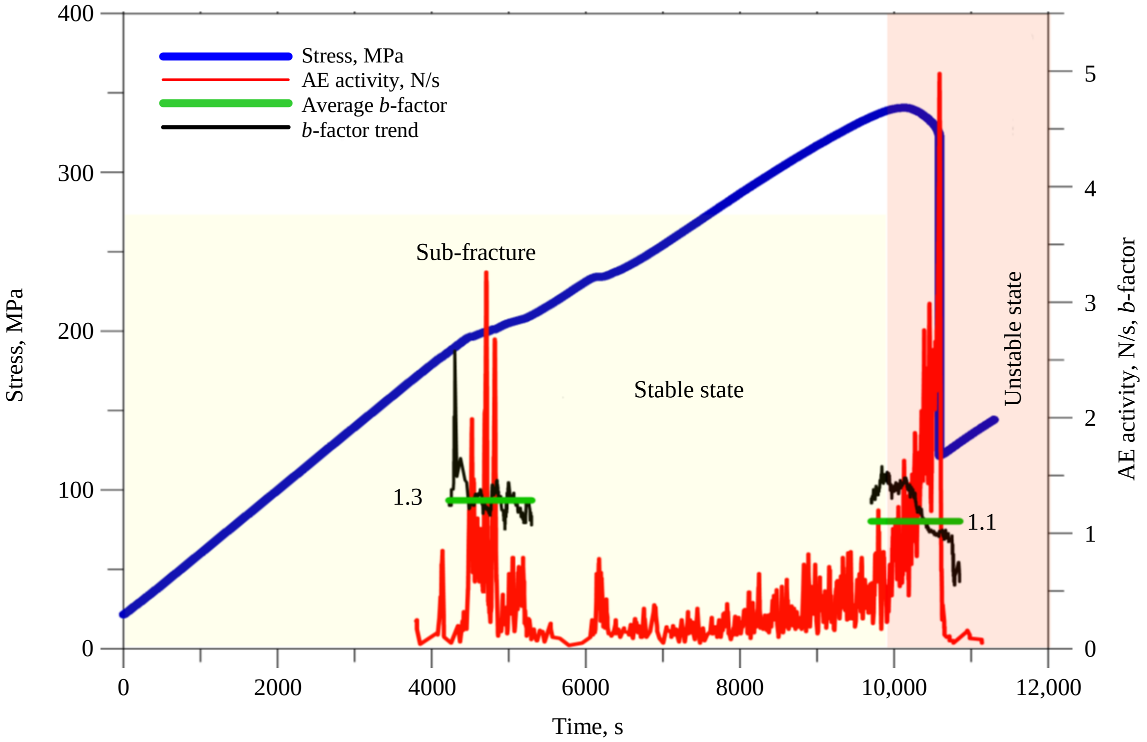

Fig.6. Trends of AE activity and *b*-factor for sample C in comparison with the loading curve

is designated as a sub-fracture. It is characterized by a peak of activity equal to 3.26 N/s and an average value of the *b*-factor in the range of 1.3. The critical process of macrofracture formation corresponds to the unstable state of the sample and leads to catastrophic destruction, characterized by a maximum value of activity and a sharp stress drop. Here, the peak of activity is 4.98 N/s, and the average value of the *b*-factor in this interval corresponds to 1.1. Thus, criteria of stable and unstable state in the process of cracking are identified for this sample. The stable state is characterized by a lower peak of activity and a higher average value of the *b*-factor. At the same time, the crack formation proceeds intensively already at a load of 59 % of the strength limit. In this interval, a sub-fracture forms at an angle β equal to 34.6° (see Fig.5, *a*). The unstable state leading to brittle fracture is characterized by a large peak of activity and a lower average value of the *b*-factor. At the same time, the fracture angle β increases to 44.5° (see Fig.5, *b*).

Discussion of results

The paper considers the features of microcrack zone formation depending on the type of rock heterogeneity. Samples A and B are characterized by textural heterogeneity: sample A has a reticulated structure (gneissic texture oriented at 50-60° to the maximum principal stress), while sample B has a banded structure (with banded heterogeneities aligned parallel to the maximum principal stress). Sample C is characterized by compositional heterogeneity, related to the uneven distribution of grains of different minerals. Using the acoustic emission source location method, it was established that these types of heterogeneity form different microcrack structures under identical loading conditions.

The destruction of sample A occurs due to the formation of a macrofracture at an angle of 51° to the axis of the sample (see Fig.2), close to the orientation of the gneissic texture. The location procedure clearly reveals the linear structure of the hypocenter distribution associated with the macrofracture (see Fig.2, *a*). Tomography revealed two more characteristic linear clusters of hypocenters of lower density in the lower part of the sample, located parallel to the main one (see Fig.2, *b*). It is obvious that they also belong to the slip sites formed by layering. Thus, it can be concluded that in sample A, the fracture is determined by the layered texture of the rock, which, under given orientation and loading conditions, causes a plastic deformation mechanism.

The fracture zone in sample B is formed in a completely different way (see Fig.3). Hypocenters have a volumetric distribution (see Fig.3, *a*), but with pronounced clusters (see Fig.3, *b*, *c*). Clusters are approximately described by a spherical shape. Presumably, the nature of their formation is associated with an intensive process of destruction in places of banded inclusions. The fault has the form of a strictly diagonal crack forming an angle β equal to 21°. According to the model [32], macrofracture is characterized as brittle.

Based on the activity trend (Fig.6) and the complex loading curve for sample C, the process of forming the resulting macrofracture can be divided into two stages. Given the correspondence between the events of the first activity peak stage (Fig.6) and the predominant orientation of the first line (see Fig.5, *a*), we assume that a sub-fracture developed during this loading interval. This sub-fracture did not lead to macroscopic failure or loss of sample stability. The angle β for this sub-fracture is estimated at 34.6°. During the interval corresponding to the second activity peak, the formation of a catastrophic fracture occurs, characterized by crack formation at an angle of 44.5° (see Fig.5, *b*). This counterclockwise rotation of the macrofracture during the fracture process can be physically interpreted as a decrease in the internal friction angle and deformation modulus, which can be observed on the loading curve (Fig.6) after the first activity peak. The rock becomes fractured, and its strength properties change. Studies of the strength properties of various rocks have been conducted, for example, in works [36, 37]. The distribution of events accumulated over the entire test duration has the form of a highly dispersed cloud, from which the direction of the resulting fracture cannot be discerned (see Fig.4, *a*). This indicates a distinct manifestation of the dilatancy property with the formation of an extensive microcrack network.

Conclusion

Laboratory investigations of the deformation and fracture processes of rock samples with various lithological types under a triaxial stress state, conducted using an MTS 815 servo-hydraulic testing system integrated with a Milne DAQ acoustic emission system, enabled the study of crack initiation and propagation over time, as well as trends in acoustic emission activity and the *b*-factor.

As a result, it is established:

- Under identical triaxial loading conditions, samples of different lithological types (gneissic, banded, and massive textures) form distinct microcrack structures and fracture mechanisms.
- In fine-grained samples with gneissic texture, fracture occurs through the formation of a macrofracture at an angle of 51° to the sample axis, closely aligned with the gneissic foliation. This is accompanied by the development of a plastic deformation process.
- In fine-grained samples with banded texture, fracture proceeds via the formation of a diagonal fracture, accompanied by the development of two distinct clusters. The macrofracture angle here is 21° relative to the sample axis, and the process is characterized as brittle.
- In coarse-grained samples with massive texture, fracture develops in two stages of acoustic emission activity. During the first activity peak, a sub-fracture forms at an angle β = 34.6°, which does not lead to complete failure. During the second peak, a fault forms at an angle β = 44.5°, accompanied by an extensive microcrack network. Dilatancy properties are manifested in this process.

Further experimental studies are planned under thermobaric conditions simulating great depths (up to 10 km) using a series of samples to improve the reliability of the tests and identify patterns of their destruction.

REFERENCES

1. Tananykhin D., Korolev M., Stecyuk I., Grigorev M. An Investigation into Current Sand Control Methodologies Taking into Account Geomechanical, Field and Laboratory Data Analysis. *Resources*. 2021. Vol. 10. Iss. 12. N 125. DOI: 10.3390/resources10120125
2. Zhukov V.S., Kuzmin Yu.O. Experimental evaluation of compressibility coefficients for fractures and intergranular pores of an oil and gas reservoir. *Journal of Mining Institute*. 2021. Vol. 251, p. 658-666. DOI: 10.31897/PMI.2021.5.5
3. Bosikov I.I., Klyuev R.V., Gavrina O.A. Analysis of geological-geophysical materials and qualitative assessment of the oil and gas perspectives of the Yuzhno-Kharbizhinsky area (Northern Caucasus). *Geology and Geophysics of Russian South*. 2021. Vol. 11. N 1, p. 6-21 (in Russian). DOI: 10.46698/VNC.2021.36.47.001

4. Petrakov D.G., Kupavykh K.S., Kupavykh A.S. Experimental study of elastic-plastic properties of oil reservoir rocks with account of saturation. *Construction of oil and gas wells on land and sea*. 2020. N 3 (327), p. 33-38 (in Russian). DOI: 10.33285/0130-3872-2020-3(327)-33-38

5. Glassley W.E. Geothermal Energy. Renewable Energy and the Environment. CRC Press, 2010, p. 320. DOI: 10.1201/EBK1420075700

6. Krumbholz J.F., Krumbholz M., Wadas S.H., Tanner D.C. Characterisation of the fracture- and karst-controlled geothermal reservoir below Munich from geophysical wireline and well information. *Geothermal Energy*. 2024. Vol. 12. N 9. DOI: 10.1186/s40517-024-00286-6

7. Kashnikov Yu.A., Shustov D.V., Yakimov S.Yu. Consideration of the geomechanical state of a fractured porous reservoir in reservoir simulation modelling. *Journal of Mining Institute*. 2025. Vol. 271, p. 42-52.

8. Putilov I.S., Vinokurova E.E., Guliaeva A.A. et al. Conceptual Geological Modelling based on Lithological and Petrographic Studies (The Case of the Permo-Carboniferous Deposit of the Usinskoye Field). *Perm Journal of Petroleum and Mining Engineering*. 2020. Vol. 20. N 3, p. 214-222 (in Russian). DOI: 10.15593/2712-8008/2020.3.2

9. Dvoynikov M.V., Sidorkin D.I., Kunshin A.A., Kovalev D.A. Development of Hydraulic Turbodrills for Deep Well Drilling. *Applied Sciences*. 2021. Vol. 11. Iss. 16. N 7517. DOI: 10.3390/app11167517

10. Kucherov V.G., Bessel V.V. Challenges and risks of deep and super deep drilling. *Burenie i neft*. 2020. N 3, p. 12-16 (in Russian).

11. Protosenya A.G., Verbilo P.E., Karasev M.A. Research of the mechanical characteristics’ anisotropy of apatite-nepheline ores block rock mass. *International Journal of Mechanical Engineering and Technology*. 2018. Vol. 9. Iss. 11, p. 1962-1972.

12. Trushko V.L., Protosenya A.G., Verbilo P.E. Predicting strength of pillars in fractured rock mass during development of apatite-nephelinic ores. *ARPN Journal of Engineering and Applied Sciences*. 2018. Vol. 13. N 8, p. 2864-2872.

13. Verbilo P.E., Iovlev G.A., Belyakov N.A. Parameter selection for the Hoek-Brown model with softening of rock mass based on laboratory experiments on rock samples and discrete numerical simulations of jointed rock mass. *Mining Informational and Analytical Bulletin*. 2025. N 2, p. 57-77 (in Russian). DOI: 10.25018/0236_1493_2025_2_0_57

14. Ilyinov M.D., Petrov D.N., Karmanskiy D.A., Selikhov A.A. Physical simulation aspects of structural changes in rock samples under thermobaric conditions at great depths. *Mining Science and Technology*. 2023. Vol. 8. N 4, p. 290-302. DOI: 10.17073/2500-0632-2023-09-150

15. Tongwen Jiang, Wei Yao, Xiongwei Sun et al. Evolution of anisotropic permeability of fractured sandstones subjected to true-triaxial stresses during reservoir depletion. *Journal of Petroleum Science and Engineering*. 2021. Vol. 200. N 108251. DOI: 10.1016/j.petrol.2020.108251

16. Kozyrev A.A., Kuznetcov N.N., Shokov A.N. Rockburst hazard assessment of hard rocks in the Zhdanovskoe deposit (Kola Peninsula). *Russian Mining Industry*. 2022. N 6, p. 75-82 (in Russian). DOI: 10.30686/1609-9192-2022-6-75-82

17. Hofmann H., Babadagli T., Jeoung Seok Yoon et al. A grain based modeling study of mineralogical factors affecting strength, elastic behavior and micro fracture development during compression tests in granites. *Engineering Fracture Mechanics*. 2015. Vol. 147, p. 261-275. DOI: 10.1016/j.engfracmech.2015.09.008

18. Karasev M.A., Petrushin V.V., Rysin A.I. The hybrid finite/discrete element method in description of macrostructural behavior of salt rocks. *Mining Informational and Analytical Bulletin*. 2023. N 4, p. 48-66 (in Russian). DOI: 10.25018/0236_1493_2023_4_0_48

19. Dresen G., Kwiatek G., Goebel T., Ben-Zion Y. Seismic and Aseismic Preparatory Processes Before Large Stick–Slip Failure. *Pure and Applied Geophysics*. 2020. Vol. 177. Iss. 12, p. 5741-5760. DOI: 10.1007/s00024-020-02605-x

20. Damaskinskaya E.E., Hilarov V.L., Nosov Yu.G. et al. Defect structure formation in quartz single crystal at the early stages of deformation. *Physics of the Solid State*. 2022. Vol. 64. Iss. 4, p. 451-457. DOI: 10.21883/PSS.2022.04.53500.262

21. Hilarov V.L., Damaskinskaya E.E. Modeling of fracture and acoustic emission in pol-ycrystalline solids with the discrete elements method. *Physics of the Solid State*. 2022. Vol. 64. Iss. 6, p. 664-669. DOI: 10.21883/PSS.2022.06.54369.295

22. Davidsen J., Goebel T., Kwiatek G. et al. What Controls the Presence and Characteristics of Aftershocks in Rock Fracture in the Lab? *Journal of Geophysical Research: Solid Earth*. 2021. Vol. 126. Iss. 10. N e2021JB022539. DOI: 10.1029/2021JB022539

23. Sheng-Qi Yang, Jing Yang, Zong-Long Mu et al. Experimental Study on Mechanical Behavior, Fracture Characteristics, and Acoustic Emission Damage Characteristics of Sandstone Under Triaxial Multistage Stress Disturbance. *Rock Mechanics and Rock Engineering*. 2024. Vol. 57. Iss. 10, p. 8633-8655. DOI: 10.1007/s00603-024-03994-4

24. Jianfeng Liu, Yang Wu, Junjie Liu et al. Acoustic emission evolution and fracture mechanism of rock for direct tensile failure. *International Journal of Rock Mechanics and Mining Science*. 2025. Vol. 185. N 105974. DOI: 10.1016/j.ijrmms.2024.105974

25. Boese C.M., Kwiatek G., Plenkers K. et al. Performance Evaluation of AE Sensors Installed Like Hydrophones in Adaptive Monitoring Networks During a Decametre-Scale Hydraulic Stimulation Experiment. *Rock Mechanics and Rock Engineering*. 2023. Vol. 56. Iss. 10, p. 6983-7001. DOI: 10.1007/s00603-023-03418-9

26. Rasskazov M.I., Tereshkin A.A., Tsoi D. I. et al. Assessment of geomechanical behavior of rock mass by the data of seismic monitoring with acoustic sensing at rockburst-hazardous deposits. *Mining Informational and Analytical Bulletin*. 2021. N 12-1, p. 167-182 (in Russian). DOI: 10.25018/0236_1493_2021_121_0_167

27. Loseva E., Lozovsky I., Zhostkov R. Refining Low Strain Pile Integrity Testing for Minor Flaw Detection with Complex Wavelet Transform. *Civil Engineering Journal*. 2024. Vol. 10. N 10, p. 3194-3207. DOI: 10.28991/CEJ-2024-010-10-05

28. Shuting Miao, Peng-Zhi Pan, Arno Zang et al. Laboratory Shear Behavior of Tensile- and Shear-Induced Fractures in Sandstone: Insights from Acoustic Emission. *Rock Mechanics and Rock Engineering*. 2024. Vol. 57. Iss. 8, p. 5397-5413. DOI: 10.1007/s00603-024-03780-2

29. Davis R.O., Selvadurai A.P.S. Plasticity and Geomechanics. Cambridge University Press, 2002. 287 p. DOI: 10.1017/CBO9780511614958

30. Jie Li, Mingyang Wang, Kaiwen Xia et al. Time-dependent dilatancy for brittle rocks. *Journal of Rock Mechanics and Geotechnical Engineering*. 2017. Vol. 9. Iss. 6, p. 1054-1070. DOI: 10.1016/j.jrmge.2017.08.002

31. Stanchits S., Yarushina V., Sabitova A. et al. Dilatancy in Shale During a Creep Monitored by Volumetric Deformation, Acoustic Emission, and Ultrasonic Transmission Techniques. *85th EAGE Annual Conference & Exhibition*. 2024. Vol. 2024, p. 5. DOI: 10.3997/2214-4609.202410540

32. Reches Z., Lockner D.A. Nucleation and growth of faults in brittle rocks. *Journal of Geophysical Research: Solid Earth*. 1994. Vol. 99. Iss. B9, p. 18159-18173. DOI: 10.1029/94JB00115

33. Pollard D.D., Segall P. Theoretical displacements and stresses near fractures in rock: with applications to faults, joints, veins, dikes, and solution surfaces. Fracture Mechanics of Rock. Academic Press, 1987, p. 277-349. DOI: 10.1016/B978-0-12-066266-1.50013-2

34. Gutenberg B., Richter C.F. Frequency of earthquakes in California. *Bulletin of the Seismological Society of America*. 1944. Vol. 34. N 4, p. 185-188. DOI: 10.1785/BSSA0340040185

35. Trushko V.L., Rozanov A.O., Saitgaleev M.M. et al. Acoustic emission criteria for analyzing the process of rock destruction and evaluating the formation of fractured reservoirs at great depths. *Journal of Mining Institute*. 2024. Vol. 269, p. 848-858.

36. Stavrogin A.N., Protosenya A.G. Rock Deformation and Fracture Mechanics. Moscow: Nedra, 1992, p. 224.

37. Kozyrev A.A., Kasparyan E.V., Kuznetcov N.N., Shokov A.N. Analysis of the hard rock failure conditions in dynamic form under triaxial compression. *Naukosfera*. 2020. N 11 (2), p. 77-85 (in Russian). DOI: 10.5281/zenodo.4309363

Authors**: Vladimir L. Trushko,** *Doctor of Engineering Sciences, Director of Research Institute "Deep Metageology"* (*Empress Catherine II Saint Petersburg Mining University, Saint Petersburg, Russia*), *Trushko_VL@pers.spmi.ru*, *https://orcid.org/0000-0002-9742-1076*, **Mikhail D. Ilinov,** *Candidate of Engineering Sciences, Head of Laboratory* (*Empress Catherine II Saint Petersburg Mining University, Saint Petersburg, Russia*), *https://orcid.org/0009-0007-2185-8638*, **Aleksandr O. Rozanov,** *Senior Researcher* (*Empress Catherine II Saint Petersburg Mining University, Saint Petersburg, Russia*), *https://orcid.org/0009-0006-4615-0401*, **Malik M. Saitgaleev,** *Leading Engineer* (*Empress Catherine II Saint Petersburg Mining University, Saint Petersburg, Russia*), *https://orcid.org/0000-0002-9859-5799*, **Dmitrii N. Petrov,** *Candidate of Engineering Sciences, Associate Professor* (*Empress Catherine II Saint Petersburg Mining University, Saint Petersburg, Russia*), *https://orcid.org/0000-0002-5513-1871*, **Daniil A. Karmanskii,** *Leading Engineer* (*Empress Catherine II Saint Petersburg Mining University, Saint Petersburg, Russia*), *https://orcid.org/0000-0002-3214-5322*, **Aleksandr A. Selikhov,** *Postgraduate Student* (*Empress Catherine II Saint Petersburg Mining University, Saint Petersburg, Russia*), *https://orcid.org/0009-0005-8163-2249*.

The authors declare no conflict of interests.

ISSN 2411-3336; e-ISSN 2541-9404

JOURNAL OF MINING INSTITUTE
Zapiski Gornogo instituta
Journal homepage: pmi.spmi.ru

Research article *Geology*

Accumulation of impurity elements under hydrothermal crystallization of pyrite: selectivity of surface phases

Sergei V. Lipko✉, Aleksandr V. Nikolaev, Dmitrii N. Babkin, Vladimir L. Tauson
Vinogradov Institute of Geochemistry, SB RAS, Irkutsk, Russia

***How to cite this article*:** Lipko S.V., Nikolaev A.V., Babkin D.N., Tauson V.L. Accumulation of impurity elements under hydrothermal crystallization of pyrite: selectivity of surface phases. Journal of Mining Institute. 2026. Vol. 277, p. 146-156.

Abstract
Limited data on the behavior of impurity elements during the formation of ore minerals in hydrothermal systems reduce their potential as indicators of the physicochemical conditions of ore formation. One of the most common sulfides capable of concentrating precious metals and other valuable components is pyrite. The distribution of a number of typomorphic impurity elements in pyrite under its crystallization in hydrothermal conditions at a temperature of 450 °C and a pressure of 1 kbar was studied. Using X-ray spectral microanalysis, scanning electron microscopy, and inductively coupled plasma and laser ablation mass spectrometry, data were obtained on the forms of occurrence, content ratios, and correlation relationships of impurity elements in the volume and surface layer of pyrite crystals. For the first time, the parameter S of surface phase selectivity with respect to main (Co, Cu, Ni) and minor impurities (noble metals, As, Zn, Mn) was determined, which averaged 1.9 (Co), 2.1 (Cu), 1.3 (Ni), 4.2 (Pd), 18.5 (Au), 6 (As), 10.2 (Zn), and 9.1 (Mn). The correlations between elements are significantly different for the surface and volume, which is explained by the influence of surface phase selectivity. The dual nature of the correlation between Au and As allows their relationship to be considered a surface phenomenon. Palladium, a critically important metal widely used in chemical catalysis and other areas of technology, exhibits unusual behavior in pyrite, concentrating mainly on its surface, which suggests the possibility of its concurrent extraction from pyrite ores at gold extraction enterprises. The observed correlations are considered from the perspective of the incorporation of impurity elements into the bulk structure of pyrite and into the compositions of surface phase-like formations (non-autonomous phases) that evolve during crystal growth and are enriched with incompatible elements.

Keywords
hydrothermal synthesis; pyrite; impurity elements; distribution; surface; selectivity; LA-ICP-MS

Funding
The research was supported by Russian Science Foundation grant N 24-27-00140, https://rscf.ru/project/24-27-00140/.

Received: 16.06.2025 ***Accepted: 09.12.2025*** ***Online: 16.02.2026*** ***Published: 27.02.2026***

Introduction

The discovery of phase-like formations (so-called non-autonomous phases, NAP) on mineral surfaces, capable of absorbing concentrations of impurity elements that are excessive in relation to the volume of the crystal [1, 2], poses a number of new problems for geochemists. On the one hand, this circumstance creates additional difficulties in interpreting the results, especially in multisystems where micro- and nano-phases may appear that are difficult to diagnose and have different origins. On the other hand, this mechanism of trace elements (TE) absorption is important for understanding the primary concentration of valuable impurities, including noble metals, REE, and other rare elements, in crystals formed from hydrothermal solutions [1]. A similar effect of TE accumulation exists for intracrystalline surfaces of pyrite, represented by dislocation boundaries of one type or another [3-5].

Interest in pyrite in this regard is not accidental – it is one of the most common sulfides formed in various geochemical environments, in particular, in ore deposits of various types, genesis, and specialization [6-8]. Although modern literature contains a large number of analyses of the chemical composition of pyrite using various methods [9-11], the characteristics of the distribution of elements in hydrothermal systems with pyrite have been little studied and do not allow the typomorphic capabilities of this mineral to be used correctly. For example, cobalt, a critically important metal used in lithium-ion batteries, is a common component of pyrite in volcanogenic sulfide deposits, but the conditions and reasons for its enrichment in pyrite remain unclear [12]. The potential of such a geochemical tool for solving ore genesis problems as the Co/Ni ratio in pyrite does not seem sufficiently justified [13]. It should also be taken into account that pyrite is the main mineral matrix for Au in many gold deposits, and the technological schemes for its extraction significantly depend on its phase and chemical state in sulfide ores [14-16]. It is currently believed that so-called invisible Au in refractory ores is mainly present in the form of nanoparticles (NP) and in a structurally bound form, and that NP can be extracted from pyrite without destroying its structure [17]. This applies even more to the surface-bound form of Au found in NAP.

The purpose of this work is to study the distribution of a number of typomorphic impurity elements in pyrite under its crystallization in hydrothermal conditions. For the first time, data on both the «volumetric» and surface contents of impurity elements will be presented, and the correlation between them will be considered.

Experimental and analytical methods

The scheme of thermogradient hydrothermal synthesis coupled with fluid sampling is presented and discussed in detail in [1]. Experimental parameters: temperature in the growth zone 450 °C, temperature drop along the outer wall of the autoclave 15 °C, duration 25-30 days, of which the first 4 days were maintained at an isothermal regime for the purpose of homogenizing the system. The pressure of 100 MPa (1 kbar) was set by the filling coefficient of the inner working vessel (passivated titanium liner, VT-8 alloy, volume ~50 cm^3). The liners were placed in stainless steel autoclaves with screw seals designed by the SKTB Institute of Crystallography of the USSR Academy of Sciences. Internal sampling was carried out using a trap – a titanium cylinder fixed to the upper part of the liner. Ammonium chloride-based solutions (reagent grade) served as mineralizers. The charge varied in terms of the S/Fe atomic ratio (1.9-2.5) and the addition of impurity elements in the form of sulfides (ZnS and MnS), oxides (NiO, CoO, and CuO), and simple substances (As, Se, Au, Pd, Pt). The purity grades of the reagents used were as follows: Fe, S, Se – “especially pure”; ZnS – “chemically pure”; MnS and As – “pure”; CuO – “pure for analysis”; NiO and CoO – “pure”; Au 99.99, Pt and Pd 99.95. According to optical emission spectral analysis, reagents of the “pure” grade contained elevated concentrations (up to 0.01 wt.%) of elements that were already present in the charge as components of individual reagents. The main foreign impurity was Pb, which, however, was not detected in the solid synthesis products. The experiments were terminated by quenching the autoclaves in cold running water at a rate of ~5 deg/s. This paper presents the results of 10 successful experiments in which no depressurization of the liner was observed, a sufficient amount of pyrite crystals was formed for study, and a representative volume of fluid was captured.

Analysis of the fluids trapped in the collectors was carried out using Perkin-Elmer Model 403, 503, and Analyst 800 atomic absorption spectrometers (USA) at the Institute of Geochemistry, SB RAS. The accuracy of determining the elements Fe and Mn ±2; Co, Ni, Cu, Zn ±5; As, Au, Pt, Pd ±10 rel.%, the detection limits for elements with low concentrations (precious metals) were 0.3; 5, and 50 μg/L for Au, Pd, and Pt, respectively; palladium and platinum were determined by tristirylphosphine extraction [1].

The crystalline products of the experiments were analyzed using powder X-ray diffraction (XRD), electron probe microanalysis (EPMA), scanning electron microscopy with energy-dispersive spectroscopy (SEM-EDS), and laser ablation inductively coupled plasma mass spectrometry (LA-ICP-MS).

The phase composition of the products and the features of the real structure of pyrite crystals were determined at the Institute of Geochemistry, SB RAS, using a Bruker D8 ADVANCE diffractometer (Germany) equipped with a scintillation detector and a Göbel mirror, operated in step-scan mode over a 2θ diffraction angle range from 8 to 70° using CuKα radiation. The experiments were performed at room temperature under the following conditions: 40 kV accelerating voltage, 40 mA tube current, exposure time of 2 s, and a step size of 0.02° 2θ. The obtained data were processed using the DIFFRAC^{plus} software package. The samples were identified using the PDF-2 powder diffraction database (ICDD, 2007) and indexed using EVA software (Bruker, 2007). The error in determining the parameter of the unit cell is in the fifth digit (nm), and the size of crystallites in pyrite (coherent scattering regions, CSR) is ±2 nm.

EPMA was used for the quantitative determination of major elements in the bulk of crystals mounted in epoxy resin. The analysis was carried out at the Institute of Geochemistry, SB RAS, using a Superprobe JXA-8200 microanalyzer (JEOL Ltd., Japan). Quantitative elemental analysis was performed using wavelength-dispersive spectrometers at an accelerating voltage of 20 kV, a probe current of 20 nA, and a probe diameter of 1 μm. Matrix-effect correction factors and elemental concentrations were calculated using the ZAF correction method implemented in the quantitative analysis software of the microanalyzer. Well-characterized reference materials were used as standards, including minerals of known composition – sphalerite (ZnS), pyrite (FeS_2), chalcopyrite ($CuFeS_2$), and arsenopyrite (FeAsS) – certified as standard samples of the enterprise (ESS) at the Institute of Geology and Mineralogy, SB RAS (Novosibirsk), as well as pure metals (Mn, Pd, Pt, Au), elemental Se, and an Fe-Ni-Co alloy certified as reference materials by the Institute of Geochemistry, SB RAS, and Irgiredmet JSC (Irkutsk). The minimum detection limit (MDL) for the analyzed elements was 0.1 wt.%. Superpositions of the analytical lines of the determined elements are taken into account in the concentration calculations using overlap coefficients.

The distribution of elements in the surface layer of synthesized pyrite crystals was studied using a TESCAN TIMA 3 X LMH FEG scanning electron microscope (Czech Republic) with EDAX Element Pulse Tor 30 energy dispersive spectrometers (USA) at Irgiredmet JSC. The pyrite crystal samples were glued with carbon tape to a special sample table. TIMA software was used to calculate the elemental contents. The spectral resolution of the EDS detectors was 129 eV on the MnKα line. The range of recorded elements was from Be to Am. Surface photographs were accumulated from two detectors, secondary electrons (SE) and backscattered electrons (BSE), to understand the topographic and compositional contrast, respectively. The accelerating voltage of the electron beam during EDS analysis and image accumulation was 25 kV.

The main objective was to identify areas on the crystal surface suitable for local studies using LA-ICP-MS. At the same time, information was obtained on the microphases of impurity components present on the surface. The detection limit for the elements determined in these measurements was 0.5 wt.%.

The LA-ICP-MS analysis was performed at the Limnological Institute, SB RAS, using an Agilent 7500ce instrument with a New Wave Research UP-213 laser ablation platform (USA). The method was applied in two variants. In the first, crystals placed in an epoxy pellet and polished were analyzed. The results were related to the volume content of the element. In the second variant, natural crystal faces were analyzed to determine the content of elements in their surface layers. The scanning parameters were as follows: plasma power 1400 W, carrier gas flow rate 1.16 L/min, laser power 90 %, laser beam projected onto a fixed point, beam projection diameter 55 μm, scanning time 17 s. The crater depth, determined by optical and electron microscopy [2], was 20±3 μm.

The following element isotopes were analyzed: ^{55}Mn, ^{59}Co, ^{60}Ni, ^{63}Cu, ^{64}Zn, ^{75}As, ^{77}Se, ^{106}Pd, ^{194}Pt, ^{197}Au. Calibration and processing of point LA-ICP-MS analysis data was performed using the NIST 612 standard sample and our own reference sulfide material [2], and to calculate the concentrations of the main metal impurities (Co, Ni, Cu), pyrite from one of the experiments was used, analyzed by EPMA and showing the most uniform distribution of elements and their best sum.

The analysis was performed at 20 points of each sample, in 3-4 grains. The calculated detection limits were, µg/g: Mn – 6.1, Co – 0.5, Ni – 0.8, Cu – 0.6, Zn – 1.0, As – 2.1, Se – 28.2, Pd – 0.1, Pt – 0.9, Au – 0.5.

Analytical data processing was carried out using an approach that involves forming criterion-based statistical sampling (CBSS) corresponding to a specific form of an element occurrence. In article [18] based on experimental and analytical studies, it was assumed that the structural form of a microelement and its surface form (including NAP) are in a relationship of mutual masking. When analyzing a data set for surface forms, it is logical to impose the same conditions on the dispersion of TE content as for structural impurities. This will allow us to cut off forms corresponding to autonomous phase impurities and random surface contamination. However, given that the accuracy of LA-ICP-MS analysis is usually around ±30 % [1], the deviation limit from the average for a sample related to a given form should be increased to 50 % (20 % due to natural heterogeneity plus 30 % analytical error). Unfortunately, in this work, it was not possible to apply the technology of analytical data selections for single crystals (ADSSC) to separate the surface and volume components of the impurity content [1, 18] due to the insufficient number of idiomorphic crystals in the experiments. The correlation coefficients *r* between the elements in the crystal volume and in the surface layer were calculated in Python 3.9.7 using the Pandas library (https://pandas.pydata.org/). The reliability of the correlation was assessed using Pearson's criterion.

Experimental results

Pyrite crystals up to 2 mm in size were obtained in various associations with enargite, sphalerite, and covellite (Table 1, Fig.1). Pyrite has characteristic habit forms, predominantly {100}, usually complicated {111}, less often {110} and {hk0}, but mainly crystals were subhedral with fragmentary faceting.

Table 1

Hydrothermal synthesis of pyrite with impurities at 450 °C and a pressure of 1 kbar

Experiment number	Composition of the initial charge, wt.%*												Composition of the solution, wt.%	Synthesized phases**
	Main components		Impurity components											
	$(S/Fe)_{at}$	Fe + S	ZnS	MnS	NiO	CoO	CuO	As	Se	Au	Pt	Pd		
1	1.9	70	10	3.33	3.33	3.33	3.33	3.33	–	1.12	1.12	1.11	9 NH_4Cl + 1 Na_2S	Py + Sph + En
2	2.3	80	10	1.67	1.67	1.67	1.67	1.67	–	0.55	0.55	0.55	10 NH_4Cl	Py + En + Sph
3	2.3	85.8	1.67	1.67	3.34	3.34	1.67	0.83	–	0.56	0.56	0.56	10 NH_4Cl	Py + En
4	2.3	80	10	1.67	1.67	1.67	1.67	–	1.67	0.55	0.55	0.55	10 NH_4Cl	Py + Cv + Sph
5	2.3	78.3	1.67	3.33	5	5	3.33	1.67	–	0.56	0.56	0.56	10 NH_4Cl	Py + En
6	1.9	85.8	1.67	1.67	3.34	3.34	1.67	0.83	–	0.56	0.56	0.56	9 NH_4Cl + 1 Na_2S	Py + Sph + En
7	1.9	78.3	1.67	3.33	5	5	3.33	1.67	–	0.56	0.56	0.56	9 NH_4Cl + 1 Na_2S	Py + En
8	2.3	85.8	1.67	1.67	3.34	3.34	1.67	–	0.83	0.56	0.56	0.56	10 NH_4Cl	Py
9	2.5	70	10	3.33	3.33	3.33	3.33	–	3.33	1.12	1.12	1.12	10 NH_4Cl	Py + Cv + Sph
10	2.3	78.3	1.67	3.34	5	5	3.34	–	1.67	0.56	0.56	0.56	10 NH_4Cl	Py

---

* Charge weight 6 g. ** Py – pyrite, Sph – sphalerite, En – enargite, Cu_3AsS_4, Cv – Fe, Se-containing covellite.

According to the XRD, pyrite crystals have a slightly increased unit cell parameter (0.5422-0.5427 nm) compared to the standard value for pure pyrite of 0.5418 nm, the sizes of the crystallites indicate a relatively perfect submicroscopic structure – the sizes of the CSR are 92-156 nm. No crystalline phases other than pyrite were detected in the crystals at the XRD sensitivity level (1 wt.%).

Study of the surface of pyrite and its accompanying phases using SEM-EDS and EPMA methods showed that sphalerite is present in the form of polycrystalline aggregates, which greatly complicates its analysis. According to quantitative EPMA, enargite is characterized by a slight copper deficiency

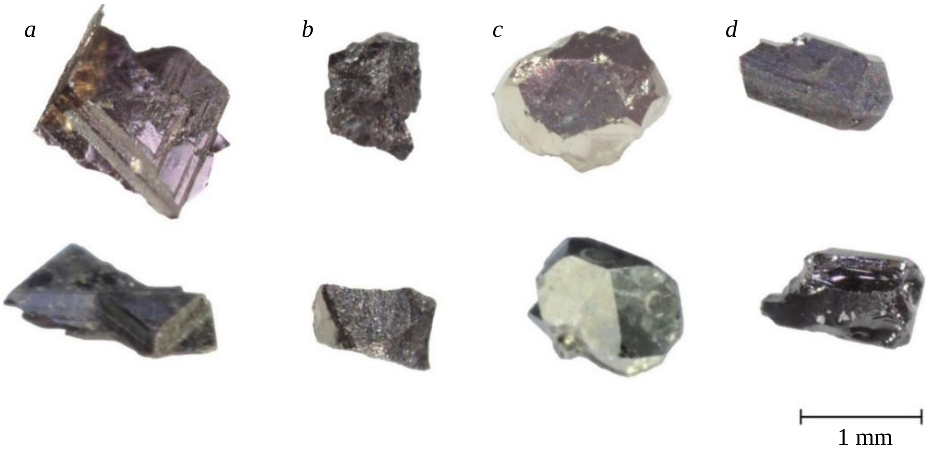

Fig.1. Synthesised crystals of pyrite and associated minerals:
a – covellite; *b* – sphalerite; *c* – pyrite; *d* – enargite

(calculated formula $Cu_{2.95}AsS_4$, exp. 2, Table 1). It contains a fairly large amount of Au (400 μg/g) compared to pyrite. Covellite contains Fe and Se, as well as Au (780-980 μg/g). Its chemical formulas, based on the analysis of crystals from exp. 4 and 9 (Table 1), indicate a slight excess of anions: $(Cu_{0.9}Fe_{0.17})_{1.07}(SSe_{0.12})_{1.12}$ and $(Cu_{0.93}\,Fe_{0.18})_{1.11}(SSe_{0.21})_{1.21}$ respectively.

In Figure 2, on a clean surface selected for LA-ICP-MS analysis, near the laser crater, analysis at points S10 and S11 shows a surface composition close to pyrite, but with a slight sulfur deficiency: $FeS_{1.87}$ and $FeS_{1.74}$ respectively.

Fine phases and their clusters on the surface (S12, S13) are close in stoichiometry to sphalerite (Zn, Fe, Mn, Cu)S. They are characterized by Cu contents of 1.5-2 at.% and unusually high Mn contents of 7.5-11 at.%. Some larger particles contain As and Cu (about 1 and 2 at.%, respectively, S14); no other impurity elements were detected by SEM-EDS analysis. It should be borne in mind that the data obtained for microparticles on the surface are purely estimates. However, their comparison with the results for the flat surface on clean areas of the crystal face shows that the capture of the pyrite matrix during analysis is minimal (judging by the Fe and S contents).

The results of determining the pH and element content in the fluids captured by the traps are presented in Table 2.

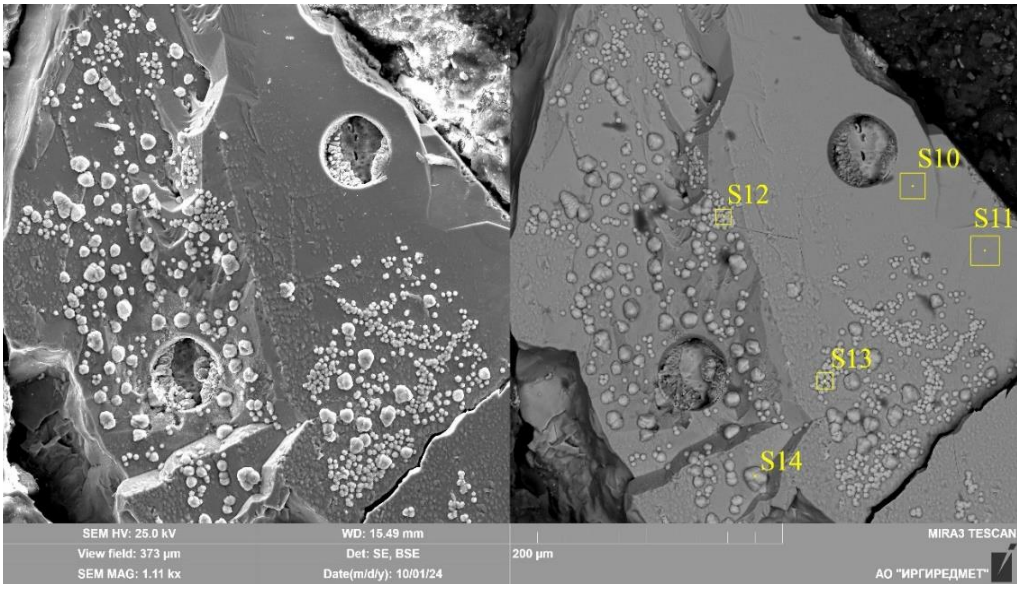

Fig.2. Surface of a pyrite crystal facet in secondary (SE) and backscattered
electrons (BSE). Two LA-ICP-MS analysis craters are visible, SEM-EDS analysis points are shown

Table 2

Elemental content in fluids based on atomic absorption spectrometry of solutions from traps

Experiment number	Element content, μg/g										pH of the solution in the trap
	Fe	Co	Ni	Mn	Cu	Zn	As	Au	Pt	Pd	
1	56	0.47	0.08	720	39	770	300	1.2	0.11	0.03	7.4
2	92	2.8	0.48	165	14	1850	235	0.74	0.19	0.06	2.2
3	330	1.6	0.42	270	65	600	26	0.75	0.12	0.01	5.2
4	43	0.26	0.1	22	84	2650	–	1.6	0.09	0.02	1.6
5	70	2.8	0.16	280	28	575	40	0.53	0.25	0.02	2.6
6	90	2.7	0.58	195	62	650	18	1.9	0.22	0.02	7.0
7	95	4.5	0.66	400	48	250	16	0.59	0.26	0.04	6.8
8	140	4.1	1.0	115	100	525	–	1.6	0.29	0.02	6.2
9	69	2.1	1.1	210	71	3200	–	0.83	0.18	0.02	1.7
10	230	14.8	2.6	65	215	1320	–	1.1	0.25	0.02	5.8

Of the impurity elements studied in this work, only selenium was not determined in the fluid due to the lack of an appropriate certified method. The contents of platinoids (Pt, Pd) exceed the minimum detection limit (MDL) by at least 2 times. Table 3 presents the data of LA-ICP-MS analysis of impurity elements in the volume and surface layer of pyrite crystals with a thickness of ~20 μm, obtained by the CBSS procedure described above.

Table 3

Chemical compositions of the volume (vol) and surface layer (sur) of pyrite crystals and the selectivity parameter *S* = C^{sur}/C^{vol} according to LA-ICP-MS data

Sample number	Main impurities, wt.%				Microimpurities, μg/g					
	Co	Ni	Cu	Se	Mn	Zn	As	Pd	Pt	Au
1vol	0.32±0.04	0.032±0.006	0.24±0.04	–	3±3	1.4±0.2	55±4	0.14±0.03	0.2±0.1	1.5±0.9
1sur	1.01±0.09	0.046±0.004	1.3±0.1	–	50±10	70±30	220±60	0.58±0.09	n/d	12±4
S	**3.2**	**1.4**	**5.4**	**–**	**16.7**	**50**	**4**	**4.1**	**n/a**	**8**
2vol	0.29±0.03	0.04±0.005	0.41±0.05	–	n/d	2.1±0.4	8±3	0.1±0.03	n/d	1.8±0.4
2sur	0.6±0.1	0.03±0.01	0.79±0.02	–	15±10	10±4	25±10	0.34±0.08	n/d	6±3
S	**2.1**	**0.8**	**1.9**	**–**	**n/a**	**4.8**	**3.1**	**3.4**	**n/a**	**3.3**
3vol	0.41±0.09	0.041±0.008	1.03±0.03	–	n/d	1.8±0.6	25±4	0.27±0.05	n/d	2±1
3sur	0.7±0.2	0.03±0.01	4.1±0.9	–	8±4	26±7	50±30	3.4±0.9	n/d	18±6
S	**1.7**	**0.7**	**4**	**–**	**n/a**	**14.4**	**2**	**12.6**	**n/a**	**9**
4vol	0.2±0.03	0.035±0.005	0.46±0.06	0.88±0.05	4±2	1.7±0.4	–	36±6	n/d	1±0.5
4sur	0.18±0.03	0.012±0.002	0.5±0.1	0.91±0.07	13±10	5.4±0.5	–	200±40	n/d	90±10
S	**0.9**	**0.3**	**1.1**	**1**	**3.2**	**3.2**	**–**	**5.6**	**n/a**	**90**
5vol	0.55±0.08	0.037±0.006	1.05±0.07	–	0.6±0.3	1.9±0.3	19±1	3.4±0.9	2±2	3±2
5sur	0.6±0.3	0.03±0.01	1.4±0.2	–	14±3	32±6	250±60	4±1	0.4±0.1	31±8
S	**1.1**	**0.8**	**1.3**	**–**	**23.3**	**16.8**	**13.2**	**1.2**	**0.2**	**10.3**
6vol	0.28±0.06	0.04±0.008	0.8±0.1	–	n/d	1.8±0.2	22±1	70±20	n/d	n/d
6sur	0.54±0.04	0.12±0.01	1.3±0.1	–	4±1	4±2	31±7	310±30	n/d	1.2±0.7
S	**1.9**	**3**	**1.6**	**–**	**n/a**	**2.2**	**1.4**	**4.4**	**n/a**	**n/a**
7vol	0.23±0.04	0.025±0.004	0.51±0.05	–	1.3±0.2	2.1±0.2	19.0±0.8	170±50	0.4±0.1	n/d
7sur	0.5±0.04	0.055±0.005	0.8±0.1	–	6±5	5±1	18±2	670±90	n/d	2±1
S	**2.2**	**2.2**	**1.6**	**–**	**4.6**	**2.4**	**0.9**	**3.9**	**n/a**	**n/a**
8vol	0.18±0.07	0.014±0.003	0.9±0.2	0.038±0.003	1.5±0.2	2.3±0.3	–	24±4	n/d	n/d
8sur	0.5±0.2	0.023±0.005	1.6±0.1	0.026±0.002	5±1	5.4±0.6	–	90±20	0.3±0.1	0.8±0.1
S	**2.8**	**1.6**	**1.8**	**0.7**	**3.3**	**2.3**	**–**	**3.8**	**n/a**	**n/a**
9vol	0.23±0.09	0.013±0.002	0.41±0.07	1.7±0.1	3±1	2±1	–	0.14±0.05	n/d	2±1
9sur	0.26±0.05	0.012±0.003	0.51±0.06	1.1±0.1	10±6	6±1	–	0.2±0.2	0.6±0.3	13±6
S	**1.1**	**0.9**	**1.2**	**0.6**	**3.3**	**3**	**–**	**1.4**	**n/a**	**6.5**
10vol	0.45±0.09	0.018±0.005	1.42±0.09	0.19±0.02	2.2±0.2	1.5±0.2	–	8±2	0.4±0.1	3±3
10sur	0.8±0.2	0.022±0.007	1.5±0.2	0.12±0.02	n/d	4.2±0.7	–	13±3	4±3	7±2
S	**1.8**	**1.2**	**1.1**	**0.6**	**n/a**	**2.8**	**–**	**1.6**	**10**	**2.3**

Note. Dash – no element added to the system; n/d – not detected (below MDL or only a small number of points above MDL); n/a – not available.

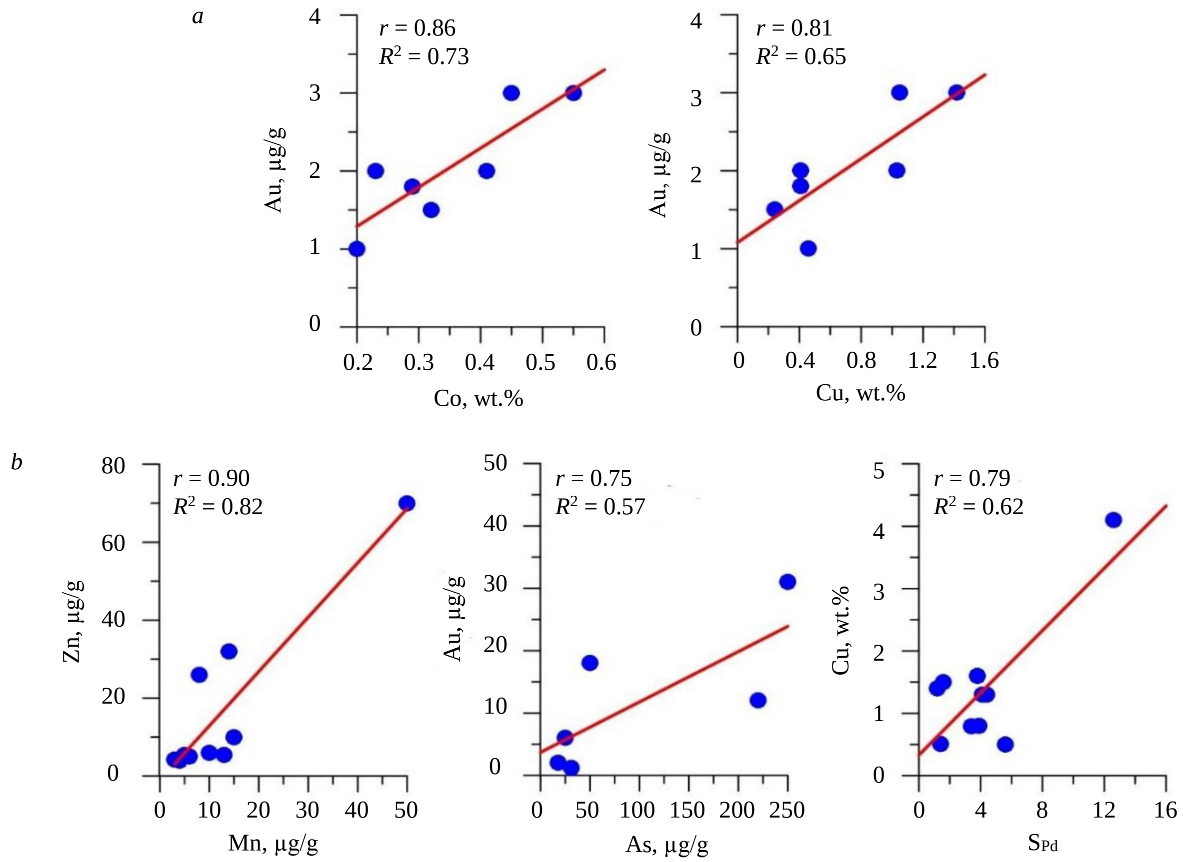

Fig.3. Correlations of impurity elements in the bulk (*a*) and on the surface (*b*) of the synthesized pyrite crystals.
The *P* values are 0.014 (Au-Co), 0.028 (Au-Cu), 0.001 (Zn-Mn), 0.084 (Au-As), 0.0065 (Cu-S_{Pd}).
The correlations are statistically significant as $P < 0.1$ at a significance level corresponding to a confidence probability of 0.9

The selectivity parameter *S* of the surface NAP is also given, expressed as a simple ratio of the concentrations of the element in the surface and in the volume [2]. The error is given for $\alpha = 0.9$. In most cases, the Pt content is below the MDL, and it is difficult to make any judgments about its behavior. It should be borne in mind that the obtained *S* values are minimal, since, as measurements have shown, the average crater depth is 20 µm, i.e., significantly exceeds the thickness of the NAP layer on pyrite (~500 nm). Despite this, LA-ICP-MS shows good agreement with other (independent) methods [2]. The reason is that for incompatible TE, super-enrichment is associated only with the first layer with a thickness of 1-1.5 µm, while deeper layers practically do not differ in composition from the volume. In this work, we are interested not so much in the absolute values of pyrite surface enrichment with impurities, as in the relationships between these impurities in the volume and surface layer of crystals. The most statistically reliable correlations between elements are illustrated in Fig.3. The remaining correlations (Table 4) are discussed at the level of trends; their reliability cannot be confirmed statistically, mainly due to insufficient sample sizes.

Discussion of results

***Contents and correlations of elements in volume* (*Table 3, vol, Table 4, Fig.3, a*).** When discussing the results obtained, we will take into account the previously established fact of the presence of a non-autonomous phase in the surface layer of pyrite crystals [19]. The sulfur deficiency detected by SEM-EDS analysis may be related to this circumstance, namely, the incorporation into the analysis of a surficial NAP of pyrrhotite stoichiometry, with a layer thickness of ~300-500 nm, according to atomic force microscopy, X-ray photoelectron spectroscopy, and Auger electron spectroscopy data [19]. It should also be noted that due to the limited experimental data, the interpretation of the results was carried out mainly within the framework of descriptive statistics – primary data analysis and visualization.

Table 4

Sampling correlations with unconfirmed statistical significance

Elements or parameters *	Belonging to the volume *v*, surfaces *s*, fluid *f*	Correlation coefficient *r*	Elements or parameters *	Belonging to the volume *v*, surfaces *s*, fluid *f*	Correlation coefficient *r*
Au-As	*v-v*	–0.46	Zn-As	*s-s*	0.8
Co-Ni	*v-v*	0.33	Mn-As	*s-s*	0.65
Co-Ni	*f-f*	0.93	Zn-Se	*s-s*	0.68
Zn-Mn	*v-v*	–0.49	Mn-Se	*s-s*	0.85
Pd-pH	*v-f*	0.4	Pd-S_{Au}	*v-s/v*	0.96
Au-Co	*s-s*	–0.49	Pd-S_{Au}	*s-s/v*	0.99
Au-Cu	*s-s*	–0.18	As-S_{Au}	*s-s/v*	0.66
Pd-Ni	*s-s*	0.48	S_{As}-S_{Au}	*s/v-s/v*	0.54
Ni-pH	*s-f*	0.59	S_{Pd}-S_{Cu}	*s/v-s/v*	0.52

---

* Selectivity *S* is expressed as the ratio of the contents in the surface layer *s* and in the volume of the crystal *v*.

Gold shows agreement with the limit of its incorporation into hydrothermal pyrite known from the literature – 3±1 µg/g [20]. Data on the strong influence of As on this value [21-23] for volume contents under the conditions of our experiments are not confirmed: Au and As show a negative correlation ($r = –0.46$, Table 4). A discrepancy between Au and As is noted for conditions of rapid pyrite crystallization [24], and no connection with As is noted for the "invisible" form of Au at high concentrations [22]. The question of whether the Au-As connection is of a crystal-chemical nature or caused by structural defects [25], has not been definitively resolved. At the same time, there is a clear correlation between Au and Co and Cu (r = 0.86 and 0.81, respectively, Fig.3, *a*) – the main cationic impurities in the synthesized pyrite, distributed fairly uniformly. The scheme of joint entry of gold and copper into pyrite assumes a neutral vacancy in the metal sublattice: $\mathrm{Au^+ + Cu^+ = Fe^{2+} + V_{Fe}}$. The nature of the correlation between Au and Co is not entirely clear; perhaps cluster isomorphism is at work here, which has recently been given increasing importance [26]. In particular, in [27] high-resolution atomic probe tomography was used to identify Co nanoclusters in cobalt-enriched pyrite (up to 1.4 wt.%).

The methods used to determine the conditions of formation and diagnose the genetic type of pyrite, based on the contents of impurity elements and their ratios (Co/Ni, etc.), are still empirical in nature and do not have a reliable theoretical and experimental basis. The Co/Ni ratio is a priority in this regard. Cobalt and nickel in the volume of pyrite crystals are positively correlated, but weakly ($r = 0.33$, Table 4), which is quite unexpected given their high correlation in the fluid ($r = 0.93$, Table 4) and natural data showing, as a rule, stable correlation characteristics of these elements in pyrites of various genesis. The contents of Co and Ni and their ratios in pyrite are widely used as empirical indicators of the conditions of its formation. It is believed that a Co/Ni ratio < 1 characterizes sedimentary or diagenetic pyrite, while a ratio > 1 is associated with a magmatic-hydrothermal source [28-30]. Formally, this corresponds to our results: according to Table 3, pyrite in a hydrothermal system at 450 °C and 1 kbar has an average Co/Ni ratio in the crystal volume of 12±6, which can be taken as a characteristic of relatively high-temperature hydrothermal pyrite.

The average As content in pyrite crystals is 25±13 µg/g (average of 6 values with the smallest errors), with pyrite coexisting with its own As phase, enargite (Cu_3AsS_4) and, thus, it is close to arsenic saturation at a temperature of 450 °C. The zinc and manganese contents are close to each other and to the MDL of these elements and are 1.9±0.2 and 2.2±0.9, respectively. The correlation between them is negative (Table 4), but insignificant for this statistical sample size. Obviously, the isomorphism of these elements in the pyrite structure is extremely limited. Of considerable interest is the situation with palladium, which shows wide variations in experiments – from the first tenths of µg/g to several tens of µg/g. It has recently been shown that pyrite obtained by the salt solution-melting method can contain up to 0.7 wt.% Pd at 580 °C and sulfur fugacity lg $fS_2 = –0.4$ [31]. X-ray absorption spectroscopy has shown that Pd replaces Fe in a divalent form. In our experiments, Pd in pyrite does not correlate significantly with other elements or correlates negatively; there is only a weak positive correlation with the pH of the solution (r = 0.4, Table 4), which may indicate that its behavior depends on the chemical environment in the fluid (in particular, on fS_2). Experiments with sulfur activity control should provide a more accurate answer to this question. Our data only show (see Table 3) that the presence of impurities such as As and Se is not in itself the cause of high Pd, Au, and Pt contents in pyrite.

***Contents and correlations of elements in the surface* (*Table 3, sur, Table 4, Fig.3, b*).** Surface concentrations usually exceed bulk concentrations, especially in the case of microelements, and correlation relationships often reverse. Thus, the strong positive correlation between Au and Co and Cu becomes negative at the surface (r = –0.49 and –0.18, Table 4). The Co/Ni ratio increases at the surface relative to the volume and averages 19±9. Co is absorbed more strongly by the surface than Ni, which further reduces their correlation compared to the volume. Work [32] shows that high concentrations of Co in FeS_2 may be associated with a phase size effect, i.e., a phenomenon dependent on surface energy. Co lowers this value, which is why it concentrates on the surface of pyrite. The correlation between Zn and Mn on the surface becomes positive and significant (r = 0.9, Fig.3, *b*). This is apparently due to the appearance on the surface of microphases with stoichiometry close to sphalerite and high Zn and Mn contents. In contrast to the situation in the volume, Au correlates with As (r = 0.75, Fig.3, *b*). It has been suggested that the relationship between Au and As may be surface-related [33, 34], and this is confirmed by our experiments. It is believed [34], that the presence of As causes distortion and surface modification of the structure, facilitating the entry of large cations (Au^+, etc.). Pd in the surface correlates positively with Ni (r = 0.48, Table 4), while its correlation with other elements (Cu, Co, Zn, As) is negative. Ni, like Pd, correlates with the pH of the fluid (r = 0.59, Table 4). Palladium, a critically important metal widely used in catalysis, electronics, and hydrogen energy, exhibits unusual behavior in pyrite, concentrating mainly on its surface, which suggests the possibility of its concurrent extraction from pyrite ores at gold mining enterprises. Several palladium sulfides are known, and some of them (PdS, and at higher sulfur activity, possibly PdS_2) can be precipitated from solution in the form of nanoparticles on the surface of iron sulfides – pyrite and pyrrhotite [35]. The positive correlation of Zn and Mn with As (r = 0.8 and 0.65, Table 4) may be associated with the incorporation of As in the surface microphases of sphalerite stoichiometry (see Fig.2). Perhaps for the same reason, Zn and Mn correlate with Se (r = 0.68 and 0.85, Table 4), which replaces sulfur in such phases, but the number of experiments with selenium is too small to draw reliable conclusions.

Selectivity of element accumulation. Comparison of the obtained data (see Table 3) with previously published data is possible for Mn and Pd [2]. The selectivity parameters for pyrite synthesized at 400 °C and 1 kbar in 10 % NH_4Cl in association with pyrrhotite, according to the ADSSC and LA-ICP-MS methods, averaged 1.2 and 15.6, respectively. According to Table 3, S for Mn averaged 9, and S for Pd – 4.2. Two circumstances should be taken into account here: in work [2] the Mn content in the volume of pyrite crystals and their surface was significantly higher, which naturally reduced the relative magnitude of the surface concentration effect; the second circumstance is the significantly more complex composition of the system in the present work, which could affect the compositions of the surface phases. Thus, it can be concluded that the numerical value of selectivity strongly depends on the experimental conditions and the composition of the system, although its qualitative nature remains unchanged ($S > 1$).

Some of the most interesting correlations involving selectivity are presented in Table 4 and Fig.3, *b*. It can be assumed that the factors responsible for the selectivity of Au are also responsible for the content of Pd, both in the volume and in the surface layer. Formally high r values (Table 4) should not be overestimated due to the small number of points and their clustering. The same can be said about As, whose correlation coefficient with S Au in the surface is 0.66, and the selectivity of S As correlates with S Au (r = 0.54) (Table 4). The correlation of S Pd with the Cu content in the surface and S Cu (r = 0.79 and 0.52, respectively, Fig.3, *b*, Table 4) may indicate the participation of surface phases based on copper sulfides – chalcopyrite and covellite. The latter was recorded in the form of crystals in systems with Se (see Table 1, Fig.1).

If the phase composition of the surface is formed by a mechanism involving the participation of NAPs in the growth process, then the conditions under which certain components enter into the composition of NAP according to the principle of continuity of phase formation on mineral surfaces become important [36]. At the same time, the precursors of bulk phases that appear on the surface-nanoscale NAP – gradually change their composition, forming surface nuclei of a stable or metastable autonomous phase, which we can observe on the surface in the form of nano- and microparticles [1].

Conclusion

- The first experimental data on the ratios of impurity element contents and their correlation relationships in the volume and surface layer of pyrite crystals synthesized under hydrothermal conditions at 450 °C and a pressure of 1 kbar have been obtained.
- Surface element contents generally exceed bulk contents, especially for microelements, and correlation relationships are found to be unstable. The surface phases responsible for this behavior exhibit selectivity primarily with respect to incompatible elements in pyrite (Mn, Zn, As, Pd, Au), for which the selectivity parameter *S* averages 9.1; 10.2; 6, 4.2, and 18.5, respectively. The main impurities (Co, Cu, Ni) fractionate more weakly into the surface ($S = 1.9$; 2.1, and 1.3, respectively); nevertheless, this should be taken into account when analyzing the edge areas of even flat-polished crystals when determining the typomorphic relationships of elements (Co/Ni, etc.).
- The presence of As and Se in the system is not in itself a cause of high Pd, Au, and Pt contents in pyrite. The Au content in the crystal volume, identified as a structural impurity [1, 20], does not exceed 3 μg/g and correlates negatively with As; at the surface, it increases by about an order of magnitude and shows a positive correlation with As, confirming the surface nature of the relationship between these elements. Pd shows wide variations in content and no correlations with other elements (except for Ni in the surface); its behavior appears to be determined by the sulfur regime in the experiments. In the volume of pyrite crystals, there is a strong positive correlation between Au and the main cationic impurities Co and Cu, which is presumably associated with cluster and vacancy mechanisms of Au entry into pyrite, which are not manifested at the surface.

The authors are grateful O.Yu.Belozerova, I.Yu.Voronova, and E.V.Kaneva (Vinogradov Institute of Geochemistry SB RAS) for their assistance in the analytical studies. The cooperation with the scientists at the shared research centers "Isotope-geochemical Studies" of the Vinogradov Institute of Geochemistry SB RAS and "Ultra-microanalysis" of the Limnological Institute SB RAS are greatly appreciated.

REFERENCES

1. Tauson V.L., Lipko S.V., Smagunov N.V., Kravtsova R.G. Trace Element Partitioning Dualism under Mineral–Fluid Interaction: Origin and Geochemical Significance. *Minerals*. 2018. Vol. 8. Iss. 7. N 282. DOI: 10.3390/min8070282

2. Lipko S., Tauson V., Smagunov N., Babkin D., Parkhomenko I. Distribution of Trace Elements (Ag, Pd, Cd, and Mn) between Pyrite and Pyrrhotite and Selectivity of Surficial Nonautonomous Phases in a Hydrothermal System. *Minerals*. 2022. Vol. 12. Iss. 9. N 1165. DOI: 10.3390/min12091165

3. Vukmanovic Z., Reddy S.M., Godel B. et al. Relationship between microstructures and grain-scale trace element distribution in komatiite-hosted magmatic sulphide ores. *Lithos*. 2014. Vol. 184-187, p. 42-61. DOI: 10.1016/j.lithos.2013.10.037

4. Fougerouse D., Reddy S.M., Sumail et al. Dislocation-mediated interfacial re-equilibration of pyrite: An alternative model to interface-coupled dissolution-reprecipitation and gold remobilisation. *Geochimica et Cosmochimica Acta*. 2024. Vol. 374, p. 136-145. DOI: 10.1016/j.gca.2024.04.027

5. King S.A., Cook N.J., Ciobanu C.L. et al. Coupled Microstructural EBSD and LA-ICP-MS Trace Element Mapping of Pyrite Constrains the Deformation History of Breccia-Hosted IOCG Ore Systems. *Minerals*. 2024. Vol. 14. Iss. 2. N 198. DOI: 10.3390/min14020198

6. Vikentyev I.V. Invisible and Microscopic Gold in Pyrite: Methods and New Data for Massive Sulfide Ores of the Urals. *Geology of Ore Deposits*. 2015. Vol. 57. N 4, p. 237-265. DOI: 10.1134/S1075701515040054

7. Gopon P., Douglas J.O., Auger M.A. et al. A Nanoscale Investigation of Carlin-Type Gold Deposits: An Atom-Scale Elemental and Isotopic Perspective. *Economic Geology*. 2019. Vol. 114. N 6, p. 1123-1133. DOI: 10.5382/econgeo.4676

8. Tolstykh N., Bortnikov N., Zhukova I. et al. Trace elements in pyrite from Ausingle bond Ag epithermal deposits of Kamchatka, Russia: Comparison with geochemical features of mineral systems. *Journal of Geochemical Exploration*. 2025. Vol. 275. N 107774. DOI: 10.1016/j.gexplo.2025.107774

9. Guotao Sun, Qingdong Zeng, Lingli Zhou et al. Mechanisms for invisible gold enrichment in the Liaodong Peninsula, NE China: *In situ* evidence from the Xiaotongjiapuzi deposit. *Gondwana Research*. 2022. Vol. 103, p. 276-296. DOI: 10.1016/j.gr.2021.10.008

10. Kexin Wang, Degao Zhai, Jiajun Liu, Han Wu. LA-ICP-MS trace element analysis of pyrite from the Dafang gold deposit, South China: Implications for ore genesis. *Ore Geology Reviews*. 2021. Vol. 139. Part A. N 104507. DOI: 10.1016/j.oregeorev.2021.104507

11. Yumiao Meng, Xiaowen Huang, Chunxia Xu, Songning Meng. Trace element and sulfur isotope compositions of pyrite from the Tianqiao Zn–Pb–Ag deposit in Guizhou province, SW China: implication for the origin of ore-forming fluids. *Acta Geochimica*. 2022. Vol. 41. Iss. 2, p. 226-243. DOI: 10.1007/s11631-021-00511-0

12. Lei Yan, Xianzheng Guo, Yu Fan et al. The occurrence of cobaltite nanoparticles in pyrite from the De'erni deposit, NW China. *Ore Geology Reviews*. 2024. Vol. 173. N 106268. DOI: 10.1016/j.oregeorev.2024.106268

13. Bralia A., Sabatini G., Troja F. A revaluation of the Co/Ni ratio in pyrite as geochemical tool in ore genesis problems. *Mineralium Deposita*. 1979. Vol. 14. Iss. 3, p. 353-374. DOI: 10.1007/BF00206365

14. Volkov A.V., Sidorov A.A. Invisible gold. *Herald of the Russian Academy of Sciences.* 2017. Vol. 87. N 1, p. 40-48. DOI: 10.1134/S1019331617010051

15. Palyanova G.A. Gold and Silver Minerals in Sulfide Ore. *Geology of Ore Deposits.* 2020. Vol. 62. N 5, p. 383-406. DOI: 10.1134/S1075701520050050

16. Molchanov V.P. Development of approaches to the creation of technology for extracting "invisible" gold from the ores of the Sukhoe deposit (Primorye). *Proceedings of the Voronezh State University of Engineering Technologies.* 2022. Vol. 84. N 3, p. 177-182 (in Russian). DOI: 10.20914/2310-1202-2022-3-177-182

17. Hongping He, Haiyang Xian, Jianxi Zhu et al. Evaluating the physicochemical conditions for gold occurrences in pyrite. *American Mineralogist*. 2023. Vol. 108. N 1, p. 211-216. DOI: 10.2138/am-2022-8207

18. Tauson V.L., Lustenberg E.K. Quantitative determination of modes of gold occurrence in minerals by the statistical analysis of analytical data samplings. *Geochemistry International.* 2008. Vol. 46. N 4, p. 423-428. DOI: 10.1134/S0016702908040101

19. Tauson V.L., Babkin D.N., Lustenberg E.E. et al. Surface typochemistry of hydrothermal pyrite: Electron spectroscopic and scanning probe microscopic data. I. Synthetic pyrite. *Geochemistry International.* 2008. Vol. 46. N 6, p. 565-577. DOI: 10.1134/S0016702908060037

20. Tauson V.L. Gold solubility in the common gold-bearing minerals: Experimental evaluation and application to pyrite. *European Journal of Mineralogy*. 1999. Vol. 11. N 6, p. 937-947. DOI: 10.1127/ejm/11/6/0937

21. Deditius A.P., Reich M., Kesler S.E. et al. The coupled geochemistry of Au and As in pyrite from hydrothermal ore deposits. *Geochimica et Cosmochimica Acta*. 2014. Vol. 140, p. 644-670. DOI: 10.1016/j.gca.2014.05.045

22. Filimonova O.N., Tagirov B.R., Trigub A.L. et al. The state of Au and As in pyrite studied by X-ray absorption spectroscopy of natural minerals and synthetic phases. *Ore Geology Reviews*. 2020. Vol. 121. N 103475. DOI: 10.1016/j.oregeorev.2020.103475

23. Kusebauch C., Gleeson S.A., Oelze M. Coupled partitioning of Au and As into pyrite controls formation of giant Au deposits. *Science Advances*. 2019. Vol. 5. Iss. 5. N eaav5891. DOI: 10.1126/sciadv.aav5891

24. Ya-Fei Wu, Evans K., Si-Yu Hu et al. Decoupling of Au and As during rapid pyrite crystallization. *Geology*. 2021. Vol. 49. N 7, p. 827-831. DOI: 10.1130/G48443.1

25. Merkulova M., Mathon O., Glatzel P. et al. Revealing the Chemical Form of "Invisible" Gold in Natural Arsenian Pyrite and Arsenopyrite with High Energy-Resolution X-ray Absorption Spectroscopy. *ACS Earth and Space Chemistry*. 2019. Vol. 3. Iss. 9, p. 1905-1914. DOI: 10.1021/acsearthspacechem.9b00099

26. Kovalchuk E.V., Tagirov B.R., Borisovsky S.E. et al. Gold and Arsenic in Pyrite and Marcasite: Hydrothermal Experiment and Implications to Natural Ore-Stage Sulfides. *Minerals*. 2024. Vol. 14. Iss. 2. N 170. DOI: 10.3390/min14020170

27. Xiao-Wen Huang, Yu-Miao Meng, Tao Long, Liang Qi. Cobalt mineralization in an evolving skarn system: Insights from co-bearing minerals in the Cihai Fe-Co deposit, NW China. *Journal of Asian Earth Sciences*. 2025. Vol. 290. N 106674. DOI: 10.1016/j.jseaes.2025.106674

28. Román N., Reich M., Leisen M. et al. Geochemical and micro-textural fingerprints of boiling in pyrite. *Geochimica et Cosmochimica Acta*. 2019. Vol. 246, p. 60-85. DOI: 10.1016/j.gca.2018.11.034

29. Baisong Du, Zuoman Wang, Santosh M. et al. Role of metasomatized mantle lithosphere in the formation of giant lode gold deposits: Insights from sulfur isotope and geochemistry of sulfides. *Geoscience Frontiers*. 2023. Vol. 14. Iss. 5. N 101587. DOI: 10.1016/j.gsf.2023.101587

30. Hanwen Yang, Baisong Du, Santosh M. et al. Role of As in the formation of giant Au deposits: Insights from sulfur isotope and geochemistry of pyrite from the Shuangwang Au deposit, West Qinling, central China. *Ore Geology Reviews*. 2024. Vol. 175. N 106363. DOI: 10.1016/j.oregeorev.2024.106363

31. Filimonova O.N., Snigireva I.I., Thompson P., Wermeille D. Incorporation of palladium into pyrite: Insights from X-ray absorption spectroscopy analysis and modelling. *Science of the Total Environment*. 2024. Vol. 920. N 170927. DOI: 10.1016/j.scitotenv.2024.170927

32. ShiWen Xie, FuLai Liu, HuiNing Wang et al. Micro- to nanoscale cobalt occurrence in Co-enriched pyrite: A case study from Dahenglu Cu-Co deposit. *Acta Petrologica Sinica*. 2024. Vol. 40. Iss. 10, p. 3028-3036. DOI: 10.18654/1000-0569/2024.10.05

33. Fleet M.E., Mumin A.H. Gold-bearing arsenian pyrite and marcasite and arsenopyrite from Carlin Trend gold deposits and laboratory synthesis. *American Mineralogist*. 1997. Vol. 82. N 1-2, p. 182-193. DOI: 10.2138/am-1997-1-220

34. Deditius A.P., Reich M. Constraints on the solid solubility of Hg, Tl, and Cd in arsenian pyrite. *American Mineralogist.* 2016. Vol. 101. N 6, p. 1451-1459. DOI: 10.2138/am-2016-5603

35. Romanchenko A.S., Mikhlin Yu.L. An XPS study of products formed on pyrite and pyrrhotine by reacting with palladium(II) chloride solutions. *Journal of Structural Chemistry.* 2015. Vol. 56. N 3, p. 531-537. DOI: 10.1134/S002247661503021X

36. Tauson V.L. The Principle of Continuity of Phase Formation at Mineral Surfaces. *Doklady Earth Sciences.* 2009. Vol. 425A. N 3, p. 471-475. DOI: 10.1134/S1028334X09030283

***Authors*: Sergei V. Lipko,** *Candidate of Chemical Sciences, Senior Researcher (Vinogradov Institute of Geochemistry, SB RAS, Irkutsk, Russia), slipko@yandex.ru, https://orcid.org/0000-0001-8335-5656*, **Aleksandr V. Nikolaev,** *Leading Engineer (Vinogradov Institute of Geochemistry, SB RAS, Irkutsk, Russia), https://orcid.org/0009-0007-6444-3678*, **Dmitrii N. Babkin,** *Leading Engineer (Vinogradov Institute of Geochemistry, SB RAS, Irkutsk, Russia), https://orcid.org/0009-0001-5150-9021*, **Vladimir L. Tauson,** *Doctor of Chemical Sciences, Chief Researcher (Vinogradov Institute of Geochemistry, SB RAS, Irkutsk, Russia), https://orcid.org/0000-0001-8704-6105*.

The authors declare no conflict of interests.

ISSN 2411-3336; e-ISSN 2541-9404

JOURNAL OF MINING INSTITUTE

Zapiski Gornogo instituta

Journal homepage: pmi.spmi.ru

Research article *Economic Geology*

Substantiation of the optimal performance parameters for a quarry during the stage-wise development of steeply dipping ore deposits

Sergey I. Fomin, Maxim P. Ovsyannikov✉

Empress Catherine II Saint Petersburg Mining University, Saint Petersburg, Russia

How to cite this article: Fomin S.I., Ovsyannikov M.P. Substantiation of the optimal performance parameters for a quarry during the stage-wise development of steeply dipping ore deposits. Journal of Mining Institute. 2026. Vol. 277, p. 157-166. DOI: 10.31897/PMI.2022.73

Abstract

The use of stage-wise schemes in the development of deep quarries is one of the ways to increase the economic efficiency of mining a deposit and determining the optimal stage parameters remains an urgent task. Such parameters are stage depth, bench height, block length, etc. However, there is a wide range of values for these parameters. Therefore, to select the optimal values and evaluate the effectiveness of design solutions, it is advisable to use the net present value, which is an international notion. As a result of the analysis of data on deposits, a large number of variable indicators can be identified that presumably affect the efficiency of mining. The article proposes to divide all parameters of the quarry mining into two types: mine engineering and economic. The importance of each of them is determined by the measure of influence on the net present value. Thus, to assess the measure of influence of mining indicators, the average values of each of them are taken, and as a result of the alternating change of one parameter under study, the measure of its influence on the discounted income received is estimated. The results of the analysis of relevant factors, their evaluation and comparative analysis are important indicators that significantly affect the design decisions made and the effectiveness of the investment project.

Keywords

steeply dipping ore deposits; stage-wise method; temporarily non-working wall; NPV; net present value; analysis of significant factors

Received: 02.06.2022 ***Accepted: 21.07.2022*** ***Online: 05.10.2022*** ***Published: 27.02.2026***

Introduction

In a volatile and dynamically changing market for mineral raw materials, mining enterprises that develop deep, steeply dipping deposits with constant productivity are forced to adapt to increasing requirements. One of the ways to increase the efficiency of mining is stage-wise mining schemes with a temporarily non-working wall [1].

An immense potential in the field of improving existing open pit mining technologies and increasing their economic efficiency lies in the stand-by mode of a part of overburden rocks and creating a temporarily non-working zone within the quarry field, which will reduce the volume of capital mining and the number of overburden operations at initial stages of the quarry.

The design of quarries in stages, each with an intermediate contour, is advisable to minimize economic costs [2]. An important task is to determine the stage parameters [3, 4]. Efficiency of the stage-wise mining method depends on the implementing the mining operation mode, which will ensure the required volume and quality of products while minimizing the level of mining costs [5]. This is primarily due to the fact that the design and process parameters of the quarry and, as a result, the performance indicators of mining as a whole depend on the mining operation mode.

The development of a quarry in stages is characterized by the procedure for conducting mining operations, in which a pillar is formed in the working area, a temporarily non-working wall (TNW), which contributes to a stage-by-stage increase in the volume of stripping operations over time. The formed pillar can be used not only in stage-wise mining schemes, but also within the same operational time period. In this case, during the formation of a temporarily non-working wall, when the working area length is reduced, work is carried out to eliminate the pillar in the upper horizons of the non-working wall [6].

Formulation of the problem

When choosing options for the location of the stage contours in the deposit, one should consider many economic, mining, geological, and mine engineering factors. The use of stage-wise schemes is successfully implemented at large steeply dipping ore deposits: Maly Kuibas, Olenegorsky, Sarbaisky quarries, etc.

The proposed mining method can be used in groups of quarries that develop isolated steeply dipping ore deposits, or in quarries elongated along strike with the division of the working area into two sections.

At each of the allocated sections, in turn mining is proposed. During mining operations at one section, a temporarily non-working wall is removed at the other and the transition to the next stage of mining is implemented. The scheme of the working order is shown in Fig.1.

Mining operations at the deposit begin in the southern section, marked with I. During the first period of operation, all reserves in the T_1 contour are mined. In the next time period T_2, mining operations are started in the northern area (II). At the same time, the temporarily non-working wall is removed in the southern section. After the end of period T_2, mining resumes in section I, and in section II, work begins to eliminate the pillar, etc. The entire deposit is mined in a similar way.

While the stage mining is underway at one of the sections, at the second section the rock wall moves from the boundaries of the previously mined area to the boundaries of the next stage. During the advancement of the TNW from the current position to the boundaries of the new stage, a section

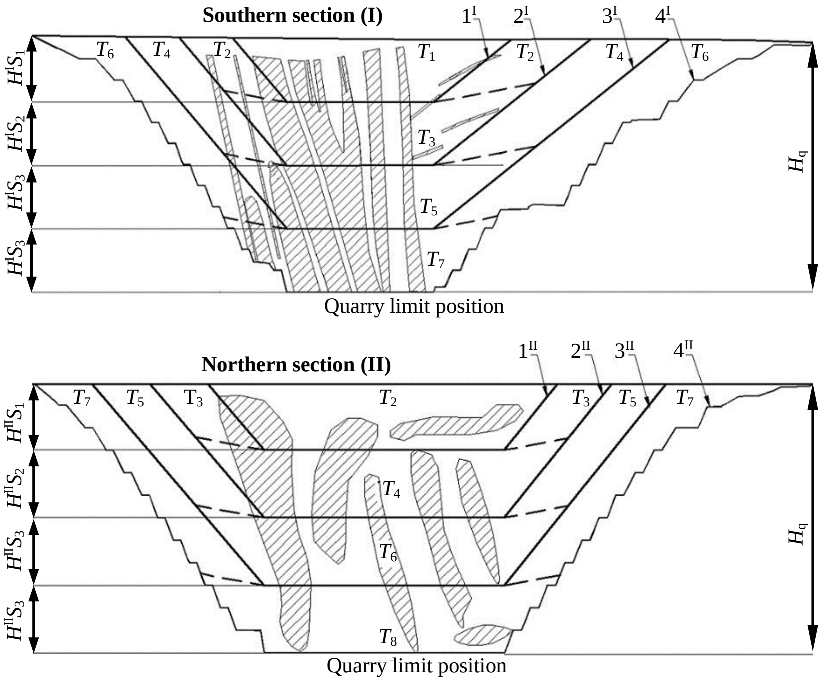

Fig.1. The mining order by stages of a quarry divided into two sections

T_n – deposit development period; $H^{I}S_n$, $H^{II}S_n$ – stage depth in the first and second sections, respectively; 1^{I}-4^{I} – section boundaries; H_q – quarry depth at the end of mining of the working wall with working ramps on each horizon is created in the mining zone. This enables to provide free access to the development of mineral reserves at the next stage [1, 7, 8]. The non-working wall of the quarry at the mining stage should be removed after all reserves in the stage contour are developed. Thus, the TNW slope angle can reach the design slope angle of the quarry wall at the end of its development.

Each new mined stage should have a greater depth than the previous (worked out) one. The fulfilment of this condition will make it possible to ensure uninterrupted mining at the deposit at the same vertical rate of the TNW removal and the speed of deepening in both selected sections of the deposit.

Since, according to the proposed mining scheme, within the stage limits, the slope angle of the working wall of the quarry can increase significantly, it becomes possible to preserve large volumes of overburden. The postponement of overburden excavation for future stages makes it possible to increase the deposit productivity in terms of minerals, which enables to increase the mining efficiency in market conditions of price volatility and variable demand for raw materials [2, 9].

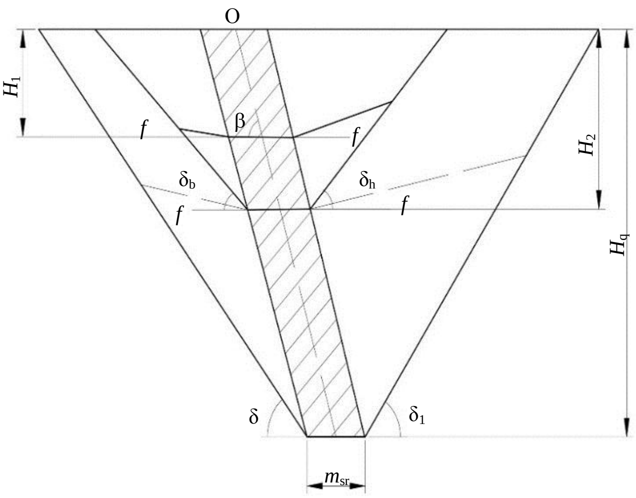

Fig.2. Scheme of the working area development in a quarry during mining a steeply dipping ore deposit in stages

H_1, H_2 – depth of the first and second stages, m; β – ore body dipping angle, deg; δ_b, δ_h – slope angle of the temporarily non-working wall from the side of the bottom and hanging walls of the deposit, deg; δ, δ_1 – slope angle of the quarry wall in the final position, deg; *f* – slope angle of the working wall with working ramps of normal width, deg; m_{sr} – ore body thickness, m; O – ore body dipping axis

The calendar plan for the development of overburden and mining operations in a deposit mined without distinguishing stages, as a rule, contains one main period of normal operation, which is characterized by stable annual volumes of minerals and overburden. If the deposit is developed in stages or with the use of temporarily non-working walls, then the graphic representation of the calendar plan is stepped (the number of steps corresponds to the number of spatial stages in quarry development).

The growth in demand for mineral raw materials determines (with or without stages) mining operations with maximum intensity. Therefore, an increase in the quarry productivity is possible only if the area of the ore body involved in mining increases [4].

It is advisable to take the duration of the development stage as long as possible if the stripping ratio in this period is less than the stripping ratio in the subsequent period. Therefore, mining with the maximum duration of the first calendar stage is the most effective.

While creating an analytical model for the development of a quarry space during mining in two stages, it is advisable to consider the quarry contour and the ore body as simplified regular geometric figures (Fig.2). A mineral deposit with simple occurrence conditions is normalized to a regular shape with a sufficient degree of accuracy by constructing a steeply dipping ore body by the average values of the true thickness and dipping angle of the ore body [5, 10-12].

The stage-wise development of a quarry field within the final quarry limits suggests a wide range of possible values for the first stage depth.

For the economic evaluation of the investment project, the net present value from the deposit development project should be used [13, 14]

$$\mathrm{NPV}=\sum_{t=0}^{T}(R_t-\mathrm{Ex}_t)\frac{1}{(1+E)^t}-\sum_{t=1}^{T_\mathrm{i}}\mathrm{K}(1+E).$$

Let us write out the difference in cash flows

$$R_t - \mathrm{Ex}_t = \mathrm{P}A_\mathrm{p} - \mathrm{C}A_\mathrm{p}, \tag{1}$$

where R_t is the results achieved at the t-th stage of the project implementation, rub.; Ex_t – expenses at the t-th stage of the project implementation, rub.; P – ore price, rub./m^3; C – cost of ore, rub./m^3; A_p – quarry mineral productivity, m^3/year.

Ore mining cost is determined by the formula:

$$\mathrm{C} = \mathrm{C}_\mathrm{m} + K_\mathrm{o}\mathrm{C}_\mathrm{o},$$

where C_m – specific operating costs for mining of 1 ton of ore (without overburden operations), rub./t; C_o – specific operating costs per 1 m^3 (1 t) of overburden, rub./m^3 (rub./t); K_o – current overburden ratio, m^3/t (m^3/m^3, t/t).

NPV formula with values substituted from equation (1):

$$\mathrm{NPV} = \sum_{t=0}^{T}\left(\mathrm{P}A_\mathrm{p} - \mathrm{C}A_\mathrm{p}\right)\frac{1}{\left(1+E\right)^t} - \mathrm{K},$$

where K – capital costs for the project implementation, rub.; E – discount rate; T – working time; t – year.

The quarry mineral productivity is determined by the following formula [15]:

$$A_\mathrm{p} = h_0 h L_\mathrm{bl}\left(\mathrm{ctg}\varphi + \mathrm{ctg}\beta\right)\frac{1-\eta}{1-\rho}, \tag{2}$$

where φ – slope angle of the quarry working wall, deg.; h – bench height, m; h_0 – deepening rate, m/year; L_bl – length of the work front per excavator, m; β – deepening angle, deg; η – ore loss index; ρ – ore impoverishment index.

Deepening angle [16]

$$\beta = \mathrm{arctg}\frac{B + h\mathrm{ctg}\alpha}{h},$$

where B – standard width of working ramps, m; α – bench slope angle, deg.

Substituting all the dependencies obtained into the original formula, we get the net present value of the field development:

$$\mathrm{NPV} = \sum_{t=0}^{T}(\mathrm{P}-\mathrm{C})\left(h_0 h L_\mathrm{bl}\mathrm{ctg}\varphi + \left(\mathrm{arctg}\frac{B + h\mathrm{ctg}\alpha}{h}\right)\right)\frac{1-\eta}{1-\rho} - \sum_{t=1}^{T_\mathrm{i}}\mathrm{K}(1+E).$$

As a rule, deep ore quarries are mined over a very long period of time. Thus, reinvestment of capital takes place during its operation [17-19]. Investment is the capital flow in the mine construction and the income stream from operation, discounted at an assumed interest rate (i).

The net present value can be understood as the net present value of the project, the total discounted profit, or the net profit of the investment project.

In world practice, net present value (NPV) is used as the main tool for assessing the economic efficiency of design decisions. NPV calculation methods consider all items of expenses and income of the enterprise, which is confirmed by reference sources [20, 21]. Thus, in further calculations, the generally accepted international symbol NPV was used. For a correct assessment of the project using the net present value criterion, it is necessary to choose the discount rate, time period of the assessment, as well as the formulas for determining NPV. Calculation methods may differ in the presence or absence of the residual project value in the formula, which is normalized to the moment of planning by discounting. NPV shows only the quality of the net cash flow from the project implementation at the accepted discount rate.

When comparing different options for the implementation of investment projects, it is necessary to consider the risk of losing money, which is determined by the probability of a change in the interest rate [3, 22, 23]. This risk is characterized by possible capital losses from the expected interest gain and is calculated as the difference between the internal rate of return (IRR_{pi}) and the rate of return calculated from the equality of discounted capital investments to the discounted income stream minus it during the payback period of capital investments [24]

$$\sum_{j=1}^{-T} NC_j \left(1+i_R\right)^{-n} - \sum_{j=1}^{T_{\mathrm{pb}}} NC_j \left(1+i_R\right)^{-n} - \sum_{t=1}^{T_{\mathrm{i}}} I_t \left(1+i_R\right)^{-n} = 0,$$

where T_{pb} – payback period of capital investments at the rate i; I_t – amount of investment in the design, construction, and operation of a quarry in the t-th year; NC_j – net current profit from quarrying in the j-th year; i_R – rate of return; n – ordinal number of the assessment year.

Interest rate of reinvestment [21]

$$R = IRR_{\mathrm{pi}} - i_R.$$

The net present value of the project (including reinvestment) is a dynamic value for assessing the effectiveness of capital investments in the quarry development, considering interest without the risk of losing investments [25, 26].

The net present value of the project, considering the increase in income since its inception at the reinvestment interest rate

$$\mathrm{NPV}_R = \sum_{j=1}^{T} NC_j \frac{\left(1+R\right)^{nT_{\mathrm{per}}}}{\left(1+i\right)^n} - \sum_{t=1}^{T_{\mathrm{per}}} I_t \left(1+i\right)^{-n}, \tag{3}$$

where T_{per} is the quarry construction period, years.

To account for changes in investment values, a discount factor is used, which is necessary to normalize economic values of various times to a single point in time [21, 25],

$$q^{-n} = \left(1+i\right)^{-n}.$$

Each option for dividing a quarry field into the development stages, due to the complex dependence of the parameters and indicators of mining operations on the stage depth H_{st}, is characterized by obtaining different net present values of the project implementation [27].

Research methodology

To assess the sensitivity of NPV to changes in indicators, we consider the period of quarry mining within one stage by transforming formula (3):

$$\mathrm{NPV} = \sum_{j=1}^{T_1} NC_j\, q_j^{-n} - \left(\sum_{\omega=1}^{T_{\mathrm{i}}} K_\omega\, q_\omega^{-n} + \sum_{m=1}^{T_{\mathrm{ir}}} K_m\, q_m^{-n} \right) \to \max. \tag{4}$$

Net current profit is determined using formula (2):

$$NC = A\left(\mathrm{Pr} - \mathrm{C}\right). \tag{5}$$

Let us write formula (5) by substituting the quarry productivity value from formula (2),

$$NC = h_0 h L_{\mathrm{bl}} \left(\mathrm{ctg}\varphi + \mathrm{ctg}\left(\mathrm{arctg}\frac{B + h\,\mathrm{ctg}\alpha}{h} \right) \right) \frac{1-\eta}{1-\rho} \left(\mathrm{Pr} - \mathrm{C}\right).$$

The deepening rate of a stage is defined as the stage depth ratio to the time of its completion

$$h_0 = \frac{H_{\text{st}}}{T_n},$$

where T_n is the stage completion time, year.

Substituting all the dependencies obtained into formula (4), we calculate the criterion indicator for determining NPV for the first stage of mining:

$$\text{NPV} = \sum_{j=1}^{T_1} \frac{H_{\text{st}}}{\text{T}_j} hL_{\text{bl}} \left(\text{ctg}\varphi + \text{ctg}\left(\text{arctg} \frac{B + h\text{ctg}\alpha}{h} \right) \right) \frac{1-\eta}{1-\rho} (\text{Pr} - \text{C}) q_j^{-n} - \left(\sum_{\omega=1}^{T_{\text{i}}} K_\omega q_\omega^{-n} + \sum_{m=1}^{T_{\text{ir}}} K_m q_m^{-n} \right), \quad (6)$$

where Pr – ore concentrate price, rub./t; C – cost of ore mining and ore concentrate production rub./t; $q_j^{-n} = (1+i)^{-n}$ – discount factor for the net current profit at the first stage of quarry mining in the j-th year; $q_\omega^{-n} = (1+i)^{-n}$ – discount factor for investments in the quarry construction in the ω-th year; $q_m^{-n} = (1+i)^{-n}$ – discount factor for investments in reconstruction in order to move to the second stage of mining in the m-th year; K_ω – amount of investment in the quarry construction in the ω-th year; K_m is the amount of investment in reconstruction in order to move to the second stage of mining in the m-th year.

Based on the results of generalization and analysis of data on quarries and analogous deposits, the values of the ranges of changes in the studied mine engineering and economic factors were taken. To determine the measure of significance of the studied factors on the NPV, we estimate the range of change for each of the factors (see Table).

Initial data for the analysis of the sensitivity of performance parameters and indicators-arguments to the NPV

Parameter	Range	Average value	Increment
Bench height h, m	12-19	15	1
Work front length L_{bl}, m	1200-2600	1800	200
Working ramp width B, m	30-65	45	5
Slope angle of the quarry working wall φ, deg	12-19	15	1
Ore loss η	0.02-0.048	0.032	0.004
Ore dilution ρ	0.01-0.15	0.07	0.02
Bench slope angle, deg α	50-85	65	5
Stage depth H_{st}, m	70-210	130	20
Stage time T_j, year	11-18	14	1
Ore concentrate price Pr, rub./t	200,000-270,000	250,000	10,000
Cost of ore mining and ore concentrate production C, rub./t	30,000-65,000	47,500	5000
Discount factor for net operating income at the first stage of quarry mining in the j-th year q_j, monetary unit	0.287-0.13	0.205	–
Discount factor for investments in the quarry construction in the ω-th year q_w, monetary unit	0.893-0.404	0.636	–
Discount factor for investment in reconstruction in order to move to the second stage of mining in the m-th year q_m, monetary unit	0.567-0.257	0.404	–
Amount of investment in the quarry construction K_w, million roubles	10,000-17,000	13,000	1000
Amount of investment in reconstruction in order to move to the second stage of mining K_m, million roubles	300-1000	600	100

When calculating dependence (6), we use the average values of indicators

$$\text{NPV} = \frac{130}{14} \cdot 15 \cdot 1800 \left(\text{ctg}15^\circ + \text{ctg}\left(\text{arctg} \frac{45 + 15\text{ctg}65^\circ}{15} \right) \right) \frac{1 - 0{,}032}{1 - 0{,}07} \times$$

$$\times (250000 - 47500) 0{,}205 - (13000000000 \cdot 0{,}636 + 60000000 \cdot 0{,}404) = 40.$$

Then, in a similar way, we substitute the average values of all the factors under consideration, changing only the values of the argument under study. Thus, by changing the value of one of the parameters, it is possible to assess the measure of influence of each indicator on the NPV [28, 29].

To assess the measure of influence of factors on the change in the NPV, the coefficient of elasticity is used. It shows by what percentage the estimated parameter will change when one of the studied indicators is transformed [28, 30, 31]

$$\varepsilon = \frac{100}{n-1}\sum_{1}^{n-1}\frac{\Delta y_i x_i}{\Delta x_i y_i},$$

where n is the number of points; y_i is the function value at the i-th point; Δy_i is the function increment at the i-th point; x_i is the argument value at the i-th point; Δx_i is the argument increment in the i-th point.

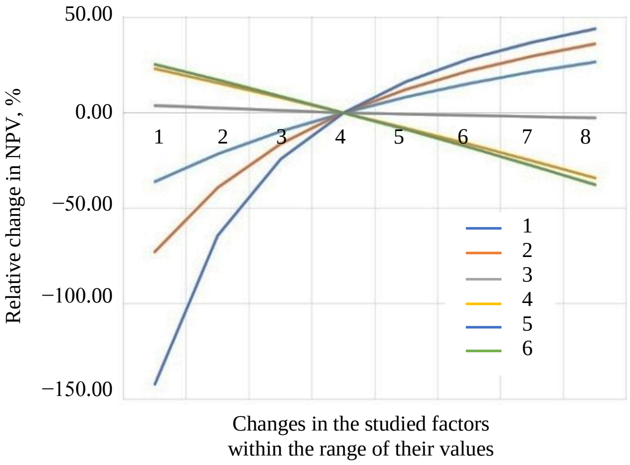

Fig.3. Influence of quarry mine engineering parameters on the relative change in NPV

1 – bench height; 2 – block length; 3 – ramp width; 4 – working wall slope angle; 5 – stage depth; 6 – stage duration

Thus, when analysing the results obtained, a number of significant performance factors can be identified that have the greatest impact on the estimated NPV.

Figures 3, 4 show the dependence graphs of the quarry mine engineering parameters and the economic indicators of mining on the relative change in NPV.

By the measure of influence of the quarry mine engineering parameters on net present value, they are divided into two groups. Values that have a considerable influence belong to the group of values of high importance (stage duration, bench height, working wall slope angle, block length, stage depth), the rest of the values fall into the group of low importance (working ramp width) [20, 28].

By the measure of influence of the quarry economic parameters on the net present value, three groups of values can be distinguished that affect the importance of the parameter under study: high importance – ore price, discount factor during the mining stage; medium importance – production cost, discount factor during the construction period, amount of investment during the construction period; low importance.

Figure 5 shows a graph reflecting the results of determining the coefficient of elasticity for mine engineering and economic parameters and indicators of the deposit. Values exceeding 100 % indicate that when the parameter changes in the accepted range, the NPV changes more than twice.

Economic indicators (profit, capital costs), as well as the duration of the development stages are functionally associated with the operational overburden removal ratio and the stage depth. Let us assume that all the indicated factors that influence the rational depth of the development stage remain unchanged at the level given in the table (average values), with the exception of one, the factor under study. In this case, each value of the studied factor corresponds to a certain value of the rational depth of the stage. When the factor changes, we obtain a

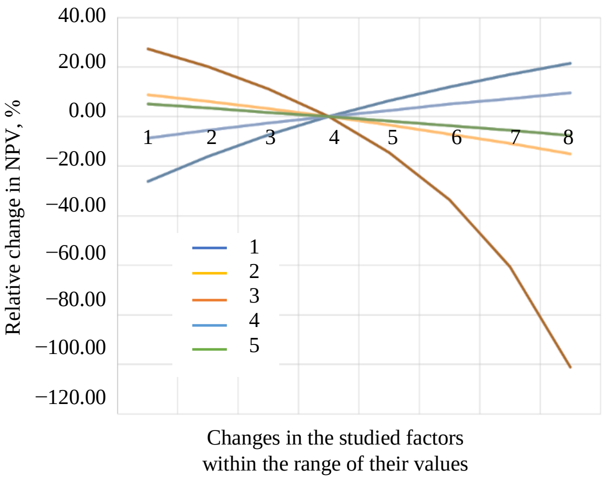

Fig.4. Influence of the quarry economic parameters on the relative change in NPV

1 – ore price; 2 – cost of ore mining;
3 – discount factor during the development of the first stage;
4 – discount factor during the construction period;
5 – amount of investment during the construction period

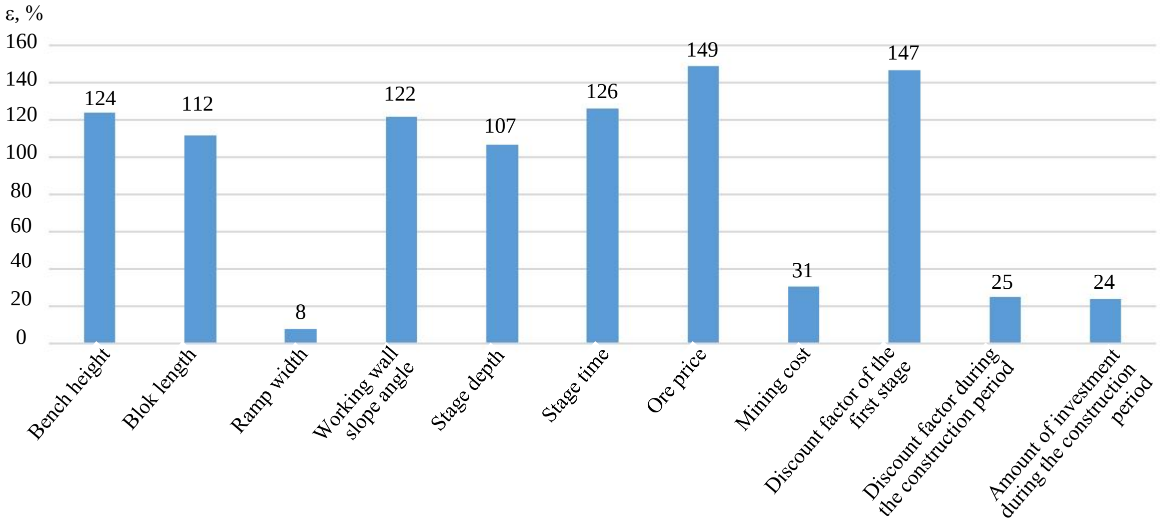

Fig.5. Coefficient of elasticity for various performance parameters and indicators

corresponding change in the rational depth of the stage. The rational depth of the development stage is significantly influenced by factors related to the current volumes of mining operations and time parameters. For the considered limits of determining factors, the ratio of the final depth of the quarry and the rational depth of the development stage is in the range of 44-67 % and has an average value of about 55 %.

Conclusion

The main quarry parameters when designing mining in stages are significantly influenced by the adopted parameters of the stage, which significantly affect the economic efficiency of mining in general. It is customary to conduct a comparative evaluation of investment projects according to the maximum NPV criterion. Using the proposed methodology, it is possible to analyse the measure of influence of the parameters and indicators of the development stage on the change in net present value and determine the optimal values for each stage parameter.

As a result of the analysis of the influence of numerous factors on the NPV, the following conclusions can be drawn:

- The value of the total discounted income is significantly influenced by a number of economic and mine engineering factors during the development of the first stage.
- With the accepted average values, the considered factors, by the measure of their influence on the NPV, are arranged in decreasing order as follows: discount factor during the first stage of mining, ore price, discount factor for the first stage, mining stage duration, bench height, working wall slope angle, working block length, stage depth, ore mining cost, discount factor during the construction period, amount of investment during the construction period, working area width.

It was established that in order to make effective design decisions at the first stage of mining of open-pit reserves, their feasibility study is necessary according to the NPV criterion, considering the measure of influence of mine engineering factors, determined using the proposed methodology and expressed by the coefficient of elasticity.

Economic indicators (profit, capital costs), as well as the duration of the development stages are functionally associated with the operational overburden removal ratio and the stage depth.

The results of the analysis of the influence of numerous factors on the rational depth of the first stage of development allow us to draw the following conclusions:

- The rational depth of the development stage is significantly influenced by factors related to the current mining volumes and time parameters.

- For the considered limits of determining factors, the ratio of the final depth of the quarry and the rational depth of the development stage is in the range of 0.44-0.67, the average value is 0.55.
- For the accepted average values of the initial data, depending on the coefficient of elasticity, the factors influencing the rational depth of the stage are distributed from the most significant to the least significant: final depth of the quarry, slope angle of the TNW, interest rate, progress rate of mining operations during the open cut of the TNW, cost of overburden removal, specific capital investment.
- Comparative economic evaluation of field development options does not depend on the point at which costs are reduced, but this point should be the same for all compared options. All costs should be reduced to the starting point of the field operation. Thus, the entire time of operation is divided into two periods: the period of quarry construction and the period of direct operation. The financial costs of building a quarry are considered as past costs, and operating costs are considered as future costs.

REFERENCES

1. Rakishev B.R., Moldabaev S.K. Order of mining of close steeply falling ores on example of Lomonosov deposit of iron ore. *Mining informational and analytical bulletin*. 2016. N 9, p. 284-295 (in Russian).
2. Yakovlev V.L., Sakantsev G.G., Yakovlev A.V., Perekhod T.M. Regulation of the mining mode on deep quarries of big extension with the use of combined temporarily non-working boards. *Problems of Subsoil Use*. 2020. N 1 (24), p. 18-25 (in Russian). DOI: 10.25635/2313-1586.2020.01.018
3. Kosolapov A.I., Ptashnik A.I., Ptashnik Yu.P. Analysis of possibility productive capacity variation on open-pit mining with sloping ore deposits. *Mining informational and analytical bulletin*. 2013. N 9, p. 55-61 (in Russian).
4. Kosolapov A.I., Ptashnik A.I. The study on the potential possibilities of the intensification of the productive capacity during staging development of the steeply dipping deposits in the modern conditions. *Mining informational and analytical bulletin*. 2011. N 6, p. 50-66 (in Russian).
5. Holodnyakov D.G., Loginov E.V. Mode control of mining operations and the angle of repose of the working pit. *Mining informational and analytical bulletin*. 2015. N 2, p. 71-74 (in Russian).
6. Bekher V.G. Methodological basis for justification of the parameters of open pit mining stages in the conditions of changing prices on the coal market. *Mining informational and analytical bulletin*. 2021. N S8, p. 3-10 (in Russian).
7. Rakishev B.R. Classification of technological complexes of the opencast mining. *Mining informational and analytical bulletin*. 2014. N S1, p. 297-306 (in Russian).
8. Rakishev B.R., Moldabayev S.K. Appropriate technology of open-pit mining with the use of motor vehicles. *Mining informational and analytical bulletin*. 2015. N 1, p. 27-34 (in Russian).
9. Alenichev V.M., Sytenkov V.N., Kornilkov S.V., Yakovlev V.L. Open pit management strategy. *Gornyy zhurnal*. 2020. N 3, p. 34-39. DOI: 10.17580/gzh.2020.03.06
10. Belyakov N.N. Modeling of open pits. *Mining informational and analytical bulletin*. 2014. N 12, p. 45-51 (in Russian).
11. Fedotov G.S., Pastikhin D.V. Influence of access road pattern on mine rock volume within the ultimate pit limit. *Mining informational and analytical bulletin*. 2019. N 6, p. 115-123 (in Russian). DOI: 10.25018/0236-1493-2019-06-0-115-123
12. Nemova N.A., Belsh T.A. Assessment of pit wall and pit bottom reserves working options in the mine “Oleniy ruchey”. *Bulletin of the Tomsk Polytechnic University. Geo Assets Engineering*. 2020. Vol. 331. N 2, p. 45-51 (in Russian). DOI: 10.18799/24131830/2020/2/2480
13. Titova A.V., Golik V.I. On Diversification of Ore Mining Complex as Direction for Development of Depressive Economic System. *Russian Mining Industry*. 2020. N 6, p. 112-117 (in Russian). DOI: 10.30686/1609-9192-2020-6-112-117
14. Tolobekova B.T. Features of the modern mining projects management. *Problemy nauki*. 2018. N 5 (29), p. 117-119.
15. Kholodnyakov G.A., Abdulaev M.D. Dependence of open pit ore productivity on bench height. *Journal of Mining Institute*. 2014. Vol. 207, p. 84-86 (in Russian).
16. Vedrova D.A., Reshetnyak S.P. Methods to improve the waste rock dumping efficiency and reclamation under the north condition. 5th International Conference “Arctic: History and Modernity”, 18-19 March 2020, Saint-Petersburg, Russia. 2020. Vol. 539. DOI: 10.1088/1755-1315/539/1/012037
17. Zaitsev A.Yu. Methodological Approach to Substantiation of Capital Investments of Gold Fields Based on Unit Costs. *Journal of Mining Institute*. 2019. Vol. 238, p. 459-464. DOI: 10.31897/PMI.2019.4.459
18. Katysheva E.G. Industry-specific features of the formation of proper financial resources at mining enterprises. *Novyy vzglyad. Mezhdunarodnyy nauchnyy vestnik*. 2014. N 4, p. 172-185.
19. Cherskih O.I. Procedure to select technical-technological solutions on rational mining mode at open pit coal mine with thick gently dipping seams. *Mining informational and analytical bulletin*. 2015. N S1-1, p. 275-290 (in Russian).

DOI: 10.31897/PMI.2022.73

20. Sokolov I.V., Smirnov A.A., Nikitin I.V. Methods of economic assessment of strategic decisions at the combined mining of ore deposits. *Izvestiya Tula State University. Sciences of Earth*. 2021. N 3, p. 314-325 (in Russian). DOI: 10.46689/2218-5194-2021-3-1-308-319

21. Sinha S.K., Choudhary B.S. Pit Optimization for Improved NPV and Life of Mine in Heterogeneous Iron Ore Deposit. *Journal of The Institution of Engineers (India): Series D*. 2020. Vol. 101, p. 253-264. DOI: 10.1007/s40033-020-00236-z

22. Peshkova M.K., Shulgina O.V. Modern methods of evaluation of investment attractiveness of companies mineral complex. *Mining informational and analytical bulletin*. 2015. N S1, p. 193-208 (in Russian).

23. Kazanin O.I., Sidorenko A.A., Meshkov A.A., Sidorenko S.A. Reproduction of the longwall panels: Modern requirements for the technology and organization of the development operations at coal mines. *Eurasian Mining*. 2020. Vol. 2, p. 19-23. DOI: 10.17580/em.2020.02.05

24. Fomin S.I., Pasynkov D.V., Semenov A.S. Determining the effectiveness of investments in the implementation of ore open-pit projects. *Journal of Mining Institute*. 2009. Vol. 180, p. 12-14 (in Russian).

25. Gilani S.-O., Sattarvand J., Hajihassani M., Abdullah S.S. A stochastic particle swarm based model for long term production planning of open pit mines considering the geological uncertainty. *Resources Policy*. 2020. Vol. 68, N 101738. p. 8-12. DOI: 10.1016/j.resourpol.2020.101738

26. Ligotsky D.N., Mironova K.V. Perspective technology of open-pit mining of limestone and dolomite. *Journal of Engineering and Applied Sciences*. 2018. Vol. 13. Iss. 7, p. 1613-1616. DOI: 10.36478/jeasci.2018.1613.1616

27. Fathollahzadeh K., Ali Asad M.W., Mardaneh E., Cigla M. Review of Solution Methodologies for Open Pit Mine Production Scheduling Problem. *International Journal of Mining, Reclamation and Environment*. 2021. Vol. 35. Iss. 8, p. 564-599. DOI: 10.1080/17480930.2021.1888395

28. Fomin S.I., Bazarova E.I. Sensitivity analysis of ore open pit parameters at the preliminary designing stage. *Journal of Mining Institute*. 2015. Vol. 216, p. 76-81 (in Russian).

29. Loginov E., Ligotsky D., Argimbaev K. Averaging the operating stripping ratio for sinking mining systems based on mathematical simulation. *Journal of Physics: Conference Series*. 2020. Vol. 1614. DOI: 10.1088/1742-6596/1614/1/012050

30. Galiev Zh.K., Galieva N.V. Efficiency of functioning of the large coal-mining enterprises. *Ugol*. 2019. N 6 (1119), p. 59-63 (in Russian). DOI: 10.18796/0041-5790-2019-6-59-63

31. Zuev B.Yu., Zubov V.P., Fedorov A.S. Application prospects for models of equivalent materials in studies of geomechanical processes in underground mining of solid minerals. *Eurasian Mining*. 2019. Vol. 1, p. 8-12. DOI: 10.17580/em.2019.01.02

Authors: **Sergey I. Fomin,** *Doctor of Engineering Sciences*, *Professor* (*Empress Catherine II Saint Petersburg Mining University*, *Saint Petersburg*, *Russia*), *https://orcid.org/0000-0002-0939-1189*, **Maxim P. Ovsyannikov,** *Postgraduate Student* (*Empress Catherine II Saint Petersburg Mining University*, *Saint Petersburg*, *Russia*), *ovsyannikovmp@gmail.com*, *https://orcid.org/0000-0003-0267-5469*.

The authors declare no conflict of interests.

ISSN 2411-3336; e-ISSN 2541-9404

JOURNAL OF MINING INSTITUTE

Zapiski Gornogo instituta

Journal homepage: pmi.spmi.ru

Review article *Geotechnical Engineering and Engineering Geology*

Constructed Floating Wetlands – a phytotechnology for wastewater treatment: application experience and prospects

Lyubov A. Ivanova[1,2], **Evgeniya A. Krasavtseva**[2,3]✉, **Tamara T. Gorbacheva**[2]

[1] *Polar-Alpine Botanical Garden-Institute of N.A.Avrorin, Federal Research Centre, Kola Science Centre of the RAS, Kirovsk, Russia*

[2] *Institute of North Industrial Ecology Problems, Kola Science Centre of the RAS, Apatity, Russia*

[3] *Laboratory of Nature-Inspired Technologies and Technosphere Safety of the Arctic, Nanomaterials Research Centre, Kola Science Centre of the RAS, Apatity, Russia*

How to cite this article: Ivanova L.A., Krasavtseva E.A., Gorbacheva T.T. Constructed Floating Wetlands – a phytotechnology for wastewater treatment: application experience and prospects. Journal of Mining Institute. 2026. Vol. 277, p. 167-180.

Abstract

The article is devoted to the actively developing area of wastewater treatment – Constructed Floating Wetlands (CFW, floating bioplatforms). The paper explores the creation history and operational experience of CFW in Russia and abroad. It describes the designs and preferred compositions of substrates and plants for creating phytomodules, paying special attention to the use of natural minerals and the selection of local macrophyte plant species. The CFW technology is suitable for treating various types of wastewater, including inorganic effluents from mining enterprises. The research examines the results of applying phytotechnology for wastewater treatment for pollutants (total nitrogen and phosphorus, organic matter, suspended particles, heavy metals, sulphates, boron, etc.). The article shows successful practices of using CFW for acidic drainage effluents, which are the most challenging for phytotechnology application. The study identifies key factors affecting pollutant removal efficiency – water depth, flow rate, coverage area, aeration, and temperature. The research presents methods to enhance the depth of water treatment at low temperatures. It also notes the positive impact of floating bioplatforms on the condition of water bodies where they are located. The study provides cost estimates for applying CFW technology for wastewater treatment and gives recommendations based on the experience of implementing the technology at a settling pond of a mining enterprise in the Murmansk Region.

Keywords

Constructed Floating Wetlands; bioplatforms; wastewater treatment; industrial enterprises; phytotechnologies; nitrogen compounds; heavy metals; water bodies

Funding

The study was conducted under the research projects FMEZ-2025-0046, FMEZ-2025-0044, FMEZ-2024-0012.

Received: 04.12.2024 ***Accepted: 16.07.2025*** ***Online: 21.11.2025*** ***Published: 27.02.2026***

Introduction

Mining industry is one of the rapidly developing sectors of the Russian economy, and all enterprises in this field are recognized as facilities that have a negative impact on the environment. Their responsibilities include approving standards for maximum permissible discharge of pollutants into water bodies. Quarry, shaft, drainage waters coming from the mining enterprises are dominated by mineral components and nitrogen compounds (for quarry wastewater using explosives), while domestic wastewater in industrial areas contains organic matter. Water is disposed to treatment facilities (separate or combined), and then, through settling ponds, into natural water bodies or recycled water supply for enterprise needs. The impact of insufficiently treated effluents results in changes in the hydrological and temperature regimes, increased water turbidity, bottom silting, and restructuring of the species composition of microbiota, flora, and fauna[1] [1]. In 2022, the Information and Technical

---

[1] RD 52.24.622-2001. Methodological guidelines. Estimating background concentrations of chemicals in watercourses. St. Petersburg: Gidrometeoizdat, 2001, p. 69.

Reference on Best Available Technologies for Wastewater Treatment (ITS NDT 8-2022[2]) was introduced. It recognizes biosorption, ozonation, ferrate oxidation, aerobic and anaerobic microbiological treatment, coagulation/flocculation, and membrane distillation as the most promising wastewater treatment methods. Phytotechnologies are highlighted as a direction that, as international experience showed, besides their important environmental significance, confirmed their high economic efficiency in water treatment systems. In 2000, the International Water Association issued the main design and operation document for phytotreatment systems [2]. National water treatment standards are developed based on it, considering local features[3] [3, 4].

Phytotechnologies are actively being implemented worldwide, as evidenced by a number of review articles published in international periodicals on water treatment of various types [5, 6], removal of metals and metalloids using bioplatforms [7], and increasing process intensification [8]. The scientific literature extensively covers the experience of operating phytoremediation systems in cold climates (Finland, Canada, Norway, Northern China) [9-11].

In Russia, among the articles in the Scientific Electronic Library over the past five years and related to the industrial-scale implementation of phytotechnologies, only two are devoted to treating quarry waters for nitrogen at a mining enterprise in the Murmansk Region [12] and desalinating drainage waters in irrigation systems in Kalmykia [13]. Although these technologies have not yet gained wide distribution in Russia, the development of methods for their design and operation in various climatic zones of the country and for a wide range of pollutants attracts the attention of the scientific community [14, 15].

History of floating platforms development

A promising direction in phytotechnology is the creation of floating platforms. The scientific literature provides various names for this technology: Floating treatment wetland, Floating island, Ecological floating bed, Artificial floating island, Planted floating system bed, Vegetated floating island, Hydroponic root mat, Natural floating wetland, Constructed Floating Wetlands. In recent years, the most commonly used term is Constructed Floating Wetlands (CFW), which we will use in this text.

The methods of forming such vegetative structures have been known since ancient times, when countries suffering from regular flooding of fertile lands began to develop aquatic agricultural technologies (floating-bed agriculture). This method is still widely used in Bangladesh, India, Vietnam, Indonesia, Thailand, and the Philippines. It involves creating artificial floating islands for hydroponic cultivation of vegetable and cereal crops in long-term flooded areas [16, 17]. A distinctive feature of floating bioplatforms is the development of the root system in the aquatic environment, while the leaf biomass grows above the water surface. Easily decomposable remnants of aquatic plants – *Eichhornia* and *Lémna* – are used as substrate-soil substitutes. These plants are characterized by active accumulation of nitrogen, phosphorus, and potassium, thus simultaneously serving as bio-fertilizers.

The development of CFW technology initially took place within the framework of Constructed Wetlands (CW) technology, which emerged in Germany in the 1950s. However, CFW quickly evolved into an independent scientific field. The first report on the creation of CFW for water treatment came from Germany and was published in [18]. Although floating bioplatforms cannot technically be called “artificial wetlands”, the term remains widely used. This is because CFW combines water treatment mechanisms found in both natural and artificial wetlands (ponds) with freely floating vegetation [19]. The cost of CFW technology is significantly lower than CW, as it does not require

---

[2] Wastewater treatment during production, work, and services at large enterprises. ITS NDT 8-2022. Moscow: NDT Bureau, 2022, p. 93.

[3] Standard DWA-A 262E. Principles for Dimensioning, Construction and Operation of Wastewater Treatment Plants with Planted and Unplanted Filters for Treatment of Domestic and Municipal Wastewater. German Association for Water, Wastewater and Waste, 2018, p. 68.

the construction and maintenance of hydraulic structures. A detailed retrospective analysis of CW technology development, including CFW, was conducted in [20]. Research on hydroponic technologies (floating and non-floating (rooted) wetlands) and their differences from CW and biological treatment ponds was presented in [19].

In the late 1980s, CFW technology began to actively develop in China, the USA, and Japan [21], primarily for treating domestic and stormwater runoff. Further development focused on both improving and expanding the range of removable pollutants and combining with classical and modern water treatment technologies, leading to the development of hybrid systems [22].

Currently, the leading countries in implementing CW technologies are China, the USA, Germany, Japan, and Australia. For CFW technologies, the leaders are China and Pakistan [4].

Floating bioplatform structures

Due to the active implementation of nature-inspired technologies such as CFW for water treatment and landscape design, the USA company Floating Islands International launched industrial production of bioplatform frames made from recycled PET foam. More often, frames are constructed from scrap materials based on proprietary designs [23]. Ensuring the bioplatform frame buoyancy and the ability to combine separate modules into clusters are particularly important. PVC or polyethylene pipes, as well as bamboo stems, are used for this purpose [24]. There is experience in using 1.5-litre PET bottles as floats. The bioplatform base is made of foamed polymer plastics (polyurethane foam, polyethylene foam, polypropylene foam, recycled PETE). The most rational area of individual modules is 2 m^2, but the literature provides options for frames ranging from 0.025 to 50 m^2 [24]. Modules are connected using natural or synthetic fibres [25] or special straps.

Figure 1 shows a patented design of a floating bioplatform phytomodule [26] used for testing quarry water treatment technology at the settling pond of AO Olkon (Olenegorsk, Murmansk Region) [12]. The structure includes a rectangular base frame constructed from plastic pipes 1 and 2 m long, with diametres of 20 or 50 mm, connected at right angles with elbows. A plastic grid with 3×3 cm cell size, covering an area of 2 m^2, is placed on the frame. This serves as a bio-loading platform for pre-grown carpet-like grass turf (Fig.1, *a*) or phytomats [27] (Fig.1, *b*), both planted with marsh plants [28].

The formed rows of phytomodules were attached to the bank of the reservoir using cables with carabiners, while clusters were installed in the centre of the reservoir and held in deep-water areas using an anchor consisting of a bag filled with stones weighing approximately 15 kg. Details of the connection between phytomodules and methods of strengthening the structure are provided in the patent [26]. Fig.2 shows how the phytomodules were installed on the water surface.

In addition to floating bioplatforms, phytoplants [29] were used in open areas of the reservoir with depths to 2 m. The design of these consists of a rigid base made of buoyant material, a mesh bed part, and an anchor (Fig.3).

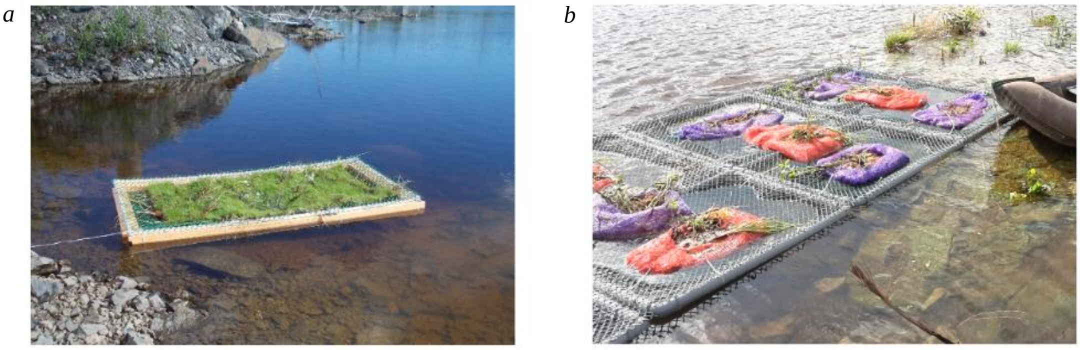

Fig.1. General view of the floating bioplatform phytomodule with marsh plants planted in the turf (*a*) and phytomates (*b*)

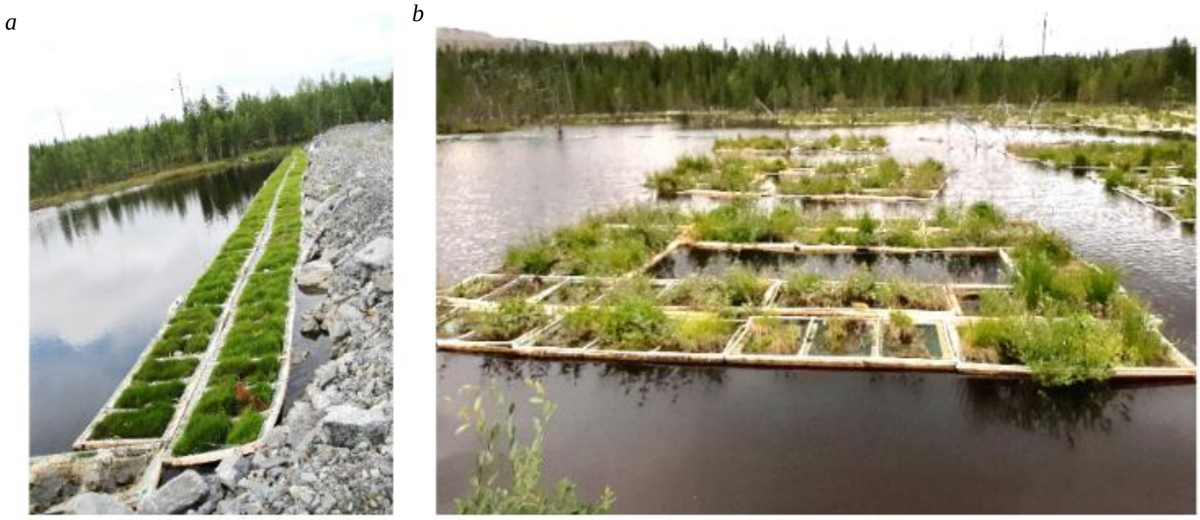

Fig.2. Installation of phytomodules in a row (*a*) and clusters (*b*) in the deep-water part of the reservoir

In CFW technologies, when selecting substrates for plants, the following material parameters are considered: porosity, capillary, and fertilizing value. The most commonly used materials include coconut and bamboo fibre, compost, activated carbon, biochar, vermiculite, perlite, and plastic granules. Recommendations for substrate selection and optimization are outlined in a

Fig.3. Floating plant beds installed in deep-water sections of the reservoir:
a – general view of the phytomodule; *b* – plant bed filled with local aquatic plant species; *c* – plant beds installed in a row configuration

review article [30]. The primary requirement for these materials is minimal impact on water pH and non-toxicity to microbiota and plants. The authors of [28] used Vipon brand thermo-vermiculite of various fractions, widely employed in other hydroponic technologies, as well as fresh and bedding wood sawdust.

The selection of plants in CFW technology is of fundamental importance, as their ability to rapidly grow biomass and accumulate pollutants in it largely determines the degree of water treatment. Equally important is the presence of aerenchyma in the root system – an air-containing tissue composed of cells with large intercellular spaces filled with air [18]. This tissue, commonly found in aquatic and marsh plants, ensures the necessary level of gas exchange under anaerobic conditions.

In favourable climatic conditions, the following plants are most commonly used in water treatment for various pollutants: common bulrush (*Schoenoplectus* (*Scirpus*) *lacustris*), sedge (*Carex* sp.), water lettuce (*Pistia stratiotes*), broad-leaved cattail (*Typha latifolia*), duckweed (*Lémna minor*), soft rush (*Juncus effusus*), common reed (*Phragmites australis*), common water hyacinth (*Eichhornia crassipes*). Pilot studies by M.A.Pashkevich et al. [31] revealed the active transport of Zn, Cu, and Mn in broad-leaved cattail and common arrowhead (*Alisma plantago-aquatica*), indicating hyperaccumulation of heavy metals by macrophyte plants.

In northern conditions, based on existing experience, the following plants can be recommended for use as biological loading for floating bioplatforms: red fescue (*Festuca rubra*), grey foxtail (*Elytrigia intermedia*), perennial ryegrass (*Lolium perenne*), timothy grass (*Phleum pratense*) – for forming carpet-like grass turf [28]; white-winged marsh plant (*Calla palustris*), marsh trefoil (*Menyanthes trifoliata*), goat willow (*Salix caprea*), tea-leaved willow (*S. phylicifolia*), creeping buttercup (*Ranunculus repens*), coltsfoot (*Tussilago farfara*), various sedges, narrow-leaved cotton-grass (*Eriophorum angustifolium*), cotton-grass (*E. vaginatum*), Scheuchzer’s cotton-grass (*E. scheuchzeri*), marsh cinquefoil (*Comarum palustre*), sphagnum mosses (*Sphagnum* spp.), marsh horsetail (*Equisetum palustre*), stream horsetail (*E. fluviatile*) – native bog species for additional planting in the created vegetation cover [27]. In open water areas with shallow depths (to 1 m) in backwaters, it is possible to use goat willow and tea-leaved willow, marsh marigold (*Cáltha palústris*), creeping buttercup (*Ranunculus repens*), floating hook-moss (*Warnstofia fluitans*), floating pondweed (*Potamogeton natans*), duckweed (Fig.4), common water-pepper (*Hippuris vulgaris*), marsh horsetail and stream horsetail.

It should be noted that the selection of plant assortment was based on many years of experience in their application. Preference was given to relatively tolerant to technogenic pollution (including

Fig.4. Using duckweed to swamp a pond’s backwater

biogenic elements) perennial macrophytes (hydro- and hydatophyte plants) growing in the Murmansk Region, excluding interspecific conflicts and intraspecific competition, capable of vegetative reproduction under pollution conditions, accumulating large biomass, and performing filtration (settling of suspended solids), absorption (absorption of biogenic elements and organic substances), accumulation (accumulation of certain metals and organic substances), oxidative (enrichment of water with oxygen), and detoxification (conversion of toxic compounds into non-toxic ones) functions.

A significant role in CFW technology is played by the symbiosis of plants with microorganisms (bacteria, algae, fungi), especially in the rhizosphere (root) zone. To enhance treatment efficiency, measures are taken to create an artificial biofilm – a consortium of bacteria, fungi, algae, and protozoa united by extracellular polymeric compounds on a solid carrier. The main polymeric components are polysaccharides, proteins, nucleic acids, and lipids. The biodiversity in this community is higher than in water, which increases biomass, microbocenosis stability, and the surface area of CFW [18]. The biofilm is particularly effective in removing suspended solids, phosphorus, and nitrogen, mitigating the negative impact of uneven water flow, temperature, and anthropogenic load on the bioplatform plants [32].

As carriers for biofilm, both natural and synthetic materials are used: plant residues, basalt fibre, zeolites, activated carbon, borosilicate glass, vermiculite, perlite, natural fibres, clinoptilolite (natural ion exchanger), polyethylene, polypropylene, polyurethane. Methods for forming artificial biofilm in water treatment technologies are detailed in [33]. In pilot experiments, the surface area of the biofilm increases through the use of bio-ball garlands filled with porous material. The appearance and method of attaching bio-balls to the root zone of plants are presented in [34].

Among the variety of water types successfully treated with CFW technologies, the following are distinguished: domestic wastewater, quarry water, stormwater (surface runoff, street and roadway wash-offs), agricultural wastewater (livestock and poultry farming), food industry plant effluents, oil-contaminated water, wastewater from textile and sugar processing industries, eluates (effluents from solid domestic waste landfills), drainage water, process water.

The development of CFW technology is based on data from laboratory, pilot (microcosm), and field studies. For practical implementation, field experiment results are undoubtedly more valuable, but they are described much less frequently in scientific literature compared to laboratory and pilot research findings. For the first time, a detailed review of comparing water treatment efficiencies obtained through various types of experiments within the framework of CFW technology application was conducted by Chinese experts in [21]. Out of an extensive body of scientific articles published in English and Chinese, only 28 are devoted to field experiment results (*in situ* research), with 11 of them relating to hybrid systems (e.g., those with submerged plants and forced aeration). The highest efficiency of CFW phytotechnology was noted for removing all forms of nitrogen (ammonium, nitrate, nitrite, organic), phosphate phosphorus and organically bound phosphorus, as well as for reducing biochemical oxygen demand (BOD) and chemical oxygen demand (COD) indicators in water. Research on treating faecal-contaminated water have also delivered encouraging results [22].

Efficiency of water treatment by floating bioplatforms

Scientific literature documents the results of water treatment for a wide range of pollutants using CFW.

Total nitrogen and phosphorus. Total nitrogen in water exists in ammonium, nitrate, nitrite, and organic forms. There are three ways to treat water for nitrogen: denitrification, sedimentation, and bioaccumulation by aquatic plants and microorganisms. Denitrification (reduction of nitrates to molecular nitrogen) removes to 80 % of nitrogen, while sedimentation and bioaccumulation account for a combined maximum of 20 % [21]. To enhance denitrification, authors recommend increasing the area of the rhizosphere zone and ensuring optimal water retention time in the treated water body. The degree of phosphorus removal with CFW varies from 5 to 88 % [18], with sorption by biofilm and sedimentation recognized as the main extraction mechanisms.

Organic pollutants. High organic matter content in water, as a labile carbon source, leads to uncontrolled algal growth. When organic matter decomposes under bacterial action, a large amount of oxygen is consumed, which causes the death of fish and other aquatic organisms. Organic matter is removed during water treatment through direct absorption by bacteria, algae, and higher plants, transformation of high-molecular compounds into simpler ones with lower molecular weight under the influence of microorganisms, adsorption of hydrophobic organic compounds on suspended particles or biofilm, followed by sedimentation as bottom deposits.

Suspended matter. Suspended particles increase water turbidity, which reduces the availability of solar radiation for bacteria, macrophytes, and benthic organisms. Suspended particles affect the survival rate of fish fry and the viability of zooplankton. Suspended solids are typically inorganic particles about 2 μm in size but can also have organic origins (algae, bacteria, and their remains). Since suspended particles have no nutritional value, they are not directly absorbed by plants or microorganisms. Instead, they sediment in the water layer between the bioplatform surface and bottom deposits, as well as on plant roots [21].

Heavy metals. Heavy metals (HM) enter water bodies through industrial discharges and runoff from road surfaces. These pollutants primarily appear in suspended form, with only a small portion in dissolved form, which can be directly absorbed by plants through interaction between HM ions and functional groups of the cell wall. High mineralization and multicomponent composition of incoming waters reduce the depth of treatment due to mutual influence of ions. The efficiency of suspended particle absorption depends on water composition, Eh, pH, HM concentration, nutrient availability, and physiological characteristics of plants included in the bioplatform. Examples of applying classical CW technologies for heavy metal removal are presented in [14], where treatment efficiency of up to 99 % is reported. There are few studies evaluating the effectiveness of HM extraction using CFW [35, 36]. Available results show that sedimentation of suspended forms in the rhizosphere zone and on biofilm is more effective than direct plant absorption. Therefore, it is recommended to focus on developing robust root mass and increasing biofilm surface area when implementing this technology.

Sulphates. A three-year experience in sulphate removal from drainage water in a settling pond is described in [37]. The field experiment was conducted in the Sudbury region (Canada), using soil as a substrate to create anaerobic conditions. The phytomodule included cattails, sedges, and rushes. The authors provided evidence of CFW effectiveness in reducing conditions at a low pH (5.0) and during prolonged operation of the bioplatform at low temperatures. The active development of sulphate-reducing bacteria was noted, which contributed to the reduction of sulphates to insoluble sulphides and their precipitation.

Boron. The problem of water ecosystem contamination with boron compounds is relevant in Chile, Turkey, New Zealand, and the USA due to territorial natural features. The boron concentration in drainage waters from boron-containing ore mines in Turkey reaches 2000 mg/l, while the average global surface water boron content is 0.1 mg/l [38]. The study shows that cattails, reeds, and duckweeds can act as boron hyperaccumulators when applied in CW systems. The main processes for boron removal in phytoremediation systems are sorption and plant bioaccumulation. To enhance boron removal efficiency, it is recommended to increase the content of organic matter and clay minerals in the substrate.

Selenium. Selenium is present in water in anionic form as selenates and selenites. A comprehensive assessment of selenium extraction efficiency using swampflower (the main macrophyte in floating wetlands in China) and Se concentration along the food chain was conducted in pilot experiments [39]. The results indicate the need to consider Se accumulation by all living organisms inhabiting the bioplatform.

Petroleum products and phenols. A comprehensive review of CFW technology application for petroleum- and phenol-contaminated water treatment is presented in [40]. The technology is recognized as highly effective both when using plants alone (primarily reeds and cattails) and with additional bacterial cultures. Experiments were mainly conducted in warm climate regions, but there are positive examples from northern regions as well. It is stated that rhizosphere microbiota of bioplatform plants handles petroleum contamination as effectively as introduced bacterial cultures. Therefore, measures to stimulate its growth are recommended.

When discussing the intricacies of implementing CFW technology, it is important to consider the modern direction of biosorption [41]. Both living biomass of plants and microorganisms, as well as detritus (which is often more effective), can serve as sorbents. Sorption is primarily due to the presence of oxygen-containing functional groups in living plant cells or detritus. Biosorption has extracellular, intracellular, and surface characteristics. Passive biosorption of pollutants occurs through interaction with the cell wall, which is a physicochemical process. Bioaccumulation, on the other hand, depends on intracellular metabolism and is therefore considered an active process.

When treating waters contaminated with heavy metals, biosorption plays a leading role. The sorption capacity of detritus is comparable to that of chemical sorbents, reaching hundreds of milligrams per gram. This method is particularly actively developed for extracting rare and dispersed elements, as well as precious metals, from wastewater.

Factors affecting the efficiency of CFW water treatment

Despite the fact that the main mechanisms of accumulation of various pollutants by plants are well known from numerous studies on phytoremediation and restoration of plant cover on technologically disturbed lands, it is quite difficult to predict the success of phytoremediation measures. The main factors affecting the efficiency of water treatment include water chemistry, water depth and flow rate, coverage area, aeration conditions, environmental conditions (water and air temperature, amount of precipitation).

Water chemistry is particularly important when selecting treatment methods, especially for wastewater from mining and industrial enterprises. On the one hand, effluents with extremely high or low pH values and elevated pollutant concentrations can have a phytotoxic effect on planted vegetation, leading to plant death [28, 42]. On the other hand, the joint presence of various pollutants in water can reduce treatment efficiency (compared to laboratory experiments) due to competition [21].

The optimal depth of the reservoir when applying CFW technology is considered to be 0.6-1.1 m, although experiments were conducted at various depths – from 0.25 to 3 m [43]. At shallow depths, plant roots of the bioplatform may touch the bottom sediments of the reservoir and gradually grow into the soil. Additionally, shallow depths reduce aeration efficiency, which decreases microbiological activity. With increasing water levels, plants may detach, potentially leading to their death. When selecting bioplatform plants, it is necessary to consider the maximum length of their root systems. In field trials at a settling pond for quarry waters, the depth reached 2 m during certain seasons due to increased discharge volumes [28]. This affected the efficiency of nitrate removal due to high water flow velocities and weak influence on the bioplatform plants (due to transit water flow). High flow velocities increase dissolved oxygen content in the water, which negatively affects denitrification [44]. Large water inflows contribute to biofilm washout or restructuring of its species composition [43]. Mathematical models were developed to simulate optimal flow rates and water retention times in the reservoir, an example of which is provided in [45].

To enhance treatment efficiency, the water surface coverage area is selected empirically to ensure proper oxygen levels in the water. A coverage exceeding 50 % may cause oxygen deficiency, while insufficient coverage results in low treatment efficiency. A 100 % coverage is only recommended in exceptional cases, such as nitrate removal, where denitrification (which occurs predominantly under anaerobic conditions) is the primary process [24]. At the settling pond of OA Olkon, 50 % of water surface was covered, amounting to 1300 m^2. This was accomplished by creating 25 clusters with 19 floating phytomodules each, along with 150 additional phytomodules arranged in rows in shallow bank areas.

Dissolved oxygen content in water is crucial for root system development and biofilm formation. Aeration of the rhizosphere zone is important for removing organic matter and phosphate phosphorus but has an inhibitory effect on denitrification and sedimentation. Based on the target treatment objective, the oxygen regime in phytomodule-occupied zones is monitored and adjusted accordingly.

Climate conditions in areas where CFW systems are located can significantly impact the efficiency of water treatment. It is commonly believed that CFW technology is effective only during the summer period due to its reliance on microbiological activity, which decreases with lower temperatures. This is particularly relevant for nitrification-denitrification, which almost ceases at temperatures below 10 °C [11]. However, the removal of suspended solids is primarily a physical process driven by sedimentation and is therefore less dependent on temperature. High levels of BOD and COD reduction is observed in CFW systems in cold climate countries like Sweden and Canada. Denitrification is almost completely inhibited at temperatures below 10 °C. A study by H.Postila et al. [46] evaluated the efficiency of total nitrogen removal in open-type phytoremediation systems in Finland, even during the summer period, showing only 12-14 % effectiveness (based on an assessment of 14 facilities).

Wetland treatment in cold regions using CFW (Talkeetna, Alaska) also showed insufficient effectiveness to meet regulatory standards [47]. However, a study conducted in Alberta (Canada) achieved high efficiency in municipal wastewater treatment [48]. The authors suggested that the positive results were due to maturation of the CFW system accompanied by enhanced interaction between plants and microorganisms, increased area of phytomodules, as well as addition of aeration under the CFW.

Relatively low water and air temperatures slow down plant growth and biomass accumulation. All macrophytes, such as reeds, cattails, and sedges, die off under prolonged exposure to low temperatures due to ice crystal formation in their cells and protein denaturation. Decaying biomass becomes a source of secondary water pollution.

To enhance water treatment efficiency during cold periods, the following methods are employed – introduction of biofilm carrier materials into the water body. Addition of labile organic matter sources (e.g., straw). Application of fibrous material suspensions and microbial mass in floating wetlands. The effectiveness of treatment directly correlates with microbial biodiversity within the system – the higher the diversity, the better the treatment even in cold conditions. Biotechnologies for cultivating cold-resistant macrophyte species, including genetic engineering, are actively developing. Particular attention is being paid to the study of benthic organisms, which contribute to the increased efficiency of CFW technology at low temperatures.

When assessing the impact of the environment, it is important to consider the projected consequences of climate change, as detailed in [21]: rising temperatures, changes in precipitation patterns, increased duration of dry periods. It is expected that warming will lead to an extension of the growth and development period for plants and the operational period of bioplatforms. However, increased precipitation intensity will reduce the water retention time in reservoirs with CFW and promote rapid nutrient leaching.

It should be emphasized that the results of field and pilot experiments differ significantly: under natural conditions, treatment efficiency decreases by an average of 20-30 %, and for phosphorus removal by more than 50 % compared to pilot studies. In some cases, secondary water pollution with nitrogen, phosphorus, and suspended solids occurs *in situ*.

Features of the floating bioplatform operation

Floating bioplatforms have a positive impact on the condition of water bodies where they are placed [21]. Since effective treatment requires a water surface coverage of at least 50 % by floating phytomodules, shading of the water surface occurs. This limits the development of phytoplankton and restructures its species composition – the proportion of blue-green algae, which cause water blooming, decreases. Thus, the application of CFW technology is recognized as promising in solving the problem of eutrophication of water bodies. However, an excessively high coverage area of the water surface with plant structures can lead to an extended period of water stratification, which must be monitored and regulated.

In [49], it is provided an example of the formation of an aquatic biocenosis in areas where CFW was applied on the Chicago River (USA), where the activity of zooplankton, insects, amphibians, reptiles, fish, and birds was noted in areas occupied by floating plant structures. Research [28] noted the active colonization of the floating bioplatform area by mosses and higher plants not included in the artificial phytocenosis, as well as the appearance of frogs, ducks, waders, hares, otters, and mice. The condition of the plant phytomodules observed in this study at the quarry water settling pond in 2024 is shown in Fig.5, 6.

The efficiency of water treatment for most pollutants largely depends on the power of root system development of bioplatform plants and the formation of biofilm on it. The example of root development noted in the studies [28] is shown in Fig.6.

Maintenance of floating wetlands involves monitoring the hydrological regime of the reservoir, controlling the physico-chemical composition of water, monitoring the formation of bottom sediments and biofilm on plant roots, periodic inspection of the condition of phytomodules, replacing damaged elements, planting new plant species, and observing their vegetation. To prevent secondary water pollution, it is necessary to periodically remove excess plant biomass of CFW, including plant residues [50]. This procedure is also necessary to maintain the required oxygen level in the aquatic

Fig.5. The state of phytocenoses created using different phytomodules:
a – floating plant beds; *b* – bioplatform + grass turf; *c* – bioplatform + phytomats

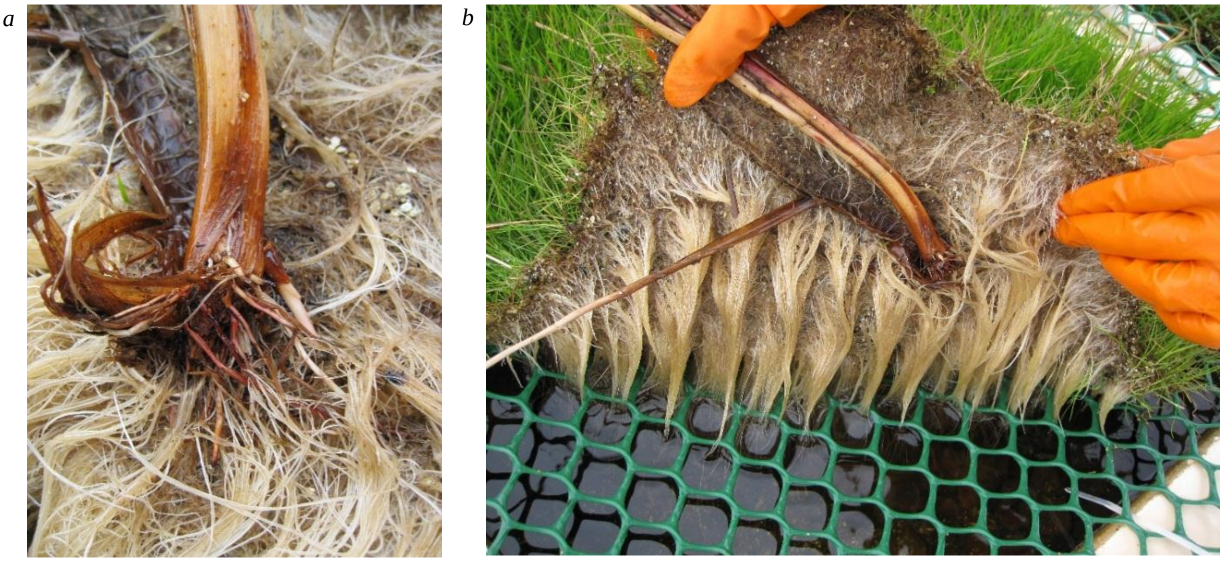

Fig.6. Root system condition of plants on floating phytomodules:
a – Scheuchzer's cotton-grass; *b* – turf

environment. The collected biomass is suitable for use as biofuel, biochar production, biofertilizers, and biosorbents [51]. In the USA, CFW technologies are actively being developed for growing ornamental plants on stormwater runoff. This allows not only to clean the water but also to generate high income from selling flowers and biomaterials for landscape design [52].

The cost of CFW varies widely depending on the complexity of the design, configuration, materials used, coverage area, plant composition, maintenance level, and other parameters. According to [4], the cost range is from \$5 to \$12.5 per 1 m^2. The highest price is noted for treatment facilities for stormwater and domestic wastewater with a total area of 400 m^2, both self-made and industrially manufactured. The lowest cost is observed for combined treatment of municipal (60 %) and industrial wastewater (40 %) over an area of 4000 m^2.

The cost of commercially produced CFW ranges from \$38 (Beemats products) to \$377 (BioHaven products) per 1 m^2 [53]. Other studies estimate costs not per unit area of CFW but per 1000 m^3 of treated water. M.Afzal et al. [25] report a treatment cost of \$0.26 per 1000 m^3 of wastewater in Pakistan. In China, the cost of municipal wastewater treatment at municipal treatment facilities is as follows: conventional treatment facilities \$770 per 1000 m^3; CW technology \$22.3 per 1000 m^3; CFW technology \$0.26 per 1000 m^3 [54]. In the Russian Federation, the cost of treating municipal wastewater at wastewater treatment plants in the Northwestern Federal District ranges from \$7 to \$270 per 1000 m^3, depending on the depth of nitrogen removal (ITS-10-2015[4]). These cost estimates clearly demonstrate the obvious advantages of using floating bioplatform technology, in addition to its important environmental protection significance.

Conclusion

We made a comprehensive review of the experience and prospects of applying the rapidly developing phytotechnology – Constructed Floating Wetlands. The paper describes the history of floating bioplatform creation and examines various design options. We present the results of water treatment from different sources using CFW and identify factors influencing the process efficiency. The study describes operational features of floating bioplatforms and approximate cost estimates for technology implementation in different countries.

The undeniable advantage of implementing floating bioplatforms in practice is the simplicity of manufacturing, placement, and maintenance of their phytomodules, which ensures high economic

---

[4] Wastewater treatment using centralized wastewater disposal systems in settlements and urban districts. ITS NDT 10-2015. Moscow: NDT Bureau, 2015, p. 394.

efficiency. The comparative analysis indicates the need for multifactorial experimental modelling during pilot experiments and mandatory verification of treatment efficiency under field conditions. The application of the technology at an enterprise should be based on the results of laboratory, scaled-up, and pilot-scale tests. After these tests are completed, a final decision on implementation is made.

The introduction of CFW technology holds great promise for treating various types of water for a wide range of pollutants, as well as for landscape design in different climatic conditions of the Russian Federation.

The authors express their gratitude to the initiator of research on the development and application of CFW phytotechnology in the Far North, Honoured Ecologist of the Russian Federation, Doctor of Biological Sciences G.A.Evdokimova, and to the researchers of the Institute of North Industrial Ecology Problems V.A.Myazin, M.V.Korneykova, and N.V.Fokina, who participated in the research on this topic.

REFERENCES

1. Nefedeva E.E., Sivolobova N.O., Kravtsov M.V., Shaikhiev I.G. Wastewater post-treatment using phytoremediation. *Vestnik tekhnologicheskogo universiteta*. 2017. Vol. 20. N 10, p. 145-148.

2. Kadlec R., Knight R., Vymazal J. et al. Constructed Wetlands for Pollution Control: Processes, Performance, Design and Operation. IWA Publishing, 2000, p. 159.

3. Nivala J., van Afferden M., Hasselbach R. et al. The new German standard on constructed wetland systems for treatment of domestic and municipal wastewater. *Water Science and Technology*. 2018. Vol. 78. Iss. 11, p. 2414-2426. DOI: 10.2166/wst.2018.530

4. Arslan M., Iqbal S., Islam E. et al. A protocol to establish low-cost floating treatment wetlands for large-scale wastewater reclamation. *STAR Protocols*. 2023. Vol. 4. Iss. 4, p. 102671. DOI: 10.1016/j.xpro.2023.102671

5. Shuting Shen, Xiang Li, Xiwu Lu. Recent developments and applications of floating treatment wetlands for treating different source waters: a review. *Environmental Science and Pollution Research*. 2021. Vol. 28. Iss. 44, p. 62061-62084. DOI: 10.1007/s11356-021-16663-8

6. Vymazal J., Yaqian Zhao, Mander Ü. Recent research challenges in constructed wetlands for wastewater treatment: A review. *Ecological Engineering*. 2021. Vol. 169. N 106318. DOI: 10.1016/j.ecoleng.2021.106318

7. Guanlong Yu, Guoliang Wang, Tianying Chi et al. Enhanced removal of heavy metals and metalloids by constructed wetlands: A review of approaches and mechanisms. *Science of The Total Environment*. 2022. Vol. 821. N 153516. DOI: 10.1016/j.scitotenv.2022.153516

8. Fuhao Zhang, Jie Wang, Liyuan Li et al. Technologies for performance intensification of floating treatment wetland – An explicit and comprehensive review. *Chemosphere*. 2024. Vol. 348. N 140727. DOI: 10.1016/j.chemosphere.2023.140727

9. Varma M., Gupta A.K., Ghosal P.S., Majumder A. A review on performance of constructed wetlands in tropical and cold climate: Insights of mechanism, role of influencing factors, and system modification in low temperature. *Science of The Total Environment*. 2021. Vol. 755. Part 2. N 142540. DOI: 10.1016/j.scitotenv.2020.142540

10. Heikkinen K., Karppinen A., Karjalainen S.M. et al. Long-term purification efficiency and factors affecting performance in peatland-based treatment wetlands: An analysis of 28 peat extraction sites in Finland. *Ecological Engineering*. 2018. Vol. 117, p. 153-164. DOI: 10.1016/j.ecoleng.2018.04.006

11. Kumwimba M.N., Batool A., Xuyong Li. How to enhance the purification performance of traditional floating treatment wetlands (FTWs) at low temperatures: Strengthening strategies. *Science of The Total Environment*. 2021. Vol. 766. N 142608. DOI: 10.1016/j.scitotenv.2020.142608

12. Korneykova M.V., Myazin V.A., Ivanova L.A. et al. Development and optimization of biological treatment of quarry waters from mineral nitrogen in the Subarctic, *Geography, Environment, Sustainability*. 2019. Vol. 12. N 2, p. 97-105. DOI: 10.24057/2071-9388-2019-5

13. Suprun V.A., Ustinova V.V. Evaluation of the Technical and Economic Efficiency of Using the Developed Bioengineering Facility for Treatment and Decrease in the Mineralization of Drainage and Run-off Water. *Ecology and Industry of Russia*. 2023. Vol. 27. Iss. 8, p. 4-9 (in Russian). DOI: 10.18412/1816-0395-2023-8-4-9

14. Rybka K.Yu., Shchegolkova N.M. The role of constructed wetlands in toxic metal wastewater treatment. *Water: Chemistry and Ecology*. 2018. N 1-3 (114), p. 101-112 (in Russian).

15. Rybka K.Y., Shchegolkova N.M. Principles of constructed wetlands designing. *RUDN Journal of Ecology and Life Safety*. 2019. Vol. 27. N 4, p. 255-263 (in Russian). DOI: 10.22363/2313-2310-2019-27-4-255-263

16. Pyka L.M., Al-Maruf A., Shamsuzzoha M. et al. Floating gardening in coastal Bangladesh: Evidence of sustainable farming for food security under climate change. *Journal of Agriculture, Food and Environment (JAFE)*. 2020. Vol. 1. N 4, p. 161-168. DOI: 10.47440/JAFE.2020.1424

17. Ghosh T.K., Singh A.K., Mitra S., Karmakar S. Gathering insights of the global scenario of floating-bed agriculture through systematic literature review for its promotion in Indian context. *Progress in Disaster Science*. 2024. Vol. 24. N 100367. DOI: 10.1016/j.pdisas.2024.100367

18. Hoeger S. Schwimmkampen: Germany's artificial floating islands. *Journal of Soil and Water Conservation*. 1988. Vol. 43. Iss. 4, p. 304-306. DOI: 10.1080/00224561.1988.12456222

19. Zhongbing Chen, Cuervo D.P., Müller J.A. et al. Hydroponic root mats for wastewater treatment – a review. *Environmental Science and Pollution Research*. 2016. Vol. 23. Iss. 16, p. 15911-15928. DOI: 10.1007/s11356-016-6801-3

20. Vymazal J. The Historical Development of Constructed Wetlands for Wastewater Treatment. *Land*. 2022. Vol. 11. Iss. 2. N 174. DOI: 10.3390/land11020174

21. Ran Bi, Chongyu Zhou, Yongfeng Jia et al. Giving waterbodies the treatment they need: A critical review of the application of constructed floating wetlands. *Journal of Environmental Management*. 2019. Vol. 238, p. 484-498. DOI: 10.1016/j.jenvman.2019.02.064

22. Hamad M.T.M.H. Comparative study on the performance of Typha latifolia and Cyperus Papyrus on the removal of heavy metals and enteric bacteria from wastewater by surface constructed wetlands. *Chemosphere*. 2020. Vol. 260. N 127551. DOI: 10.1016/j.chemosphere.2020.127551

23. Lucke T., Walker C., Beecham S. Experimental designs of field-based constructed floating wetland studies: A review. *Science of The Total Environment*. 2019. Vol. 660, p. 199-208. DOI: 10.1016/j.scitotenv.2019.01.018

24. Samal K., Kar S., Trivedi S. Ecological floating bed (EFB) for decontamination of polluted water bodies: Design, mechanism and performance. *Journal of Environmental Management*. 2019. Vol. 251. N 109550. DOI: 10.1016/j.jenvman.2019.109550

25. Afzal M., Arslan M., Müller J.A. et al. Floating treatment wetlands as a suitable option for large-scale wastewater treatment. *Nature Sustainability*. 2019. Vol. 2. Iss. 9, p. 863-871. DOI: 10.1038/s41893-019-0350-y

26. Evdokimova G.A., Ivanova L.A., Mjazin V.A. Patent N 2560631 RF. Device for biological purification of waste quarry waters. Publ. 20.08.2015. Bul. N 23 (in Russian).

27. Ivanova L.A., Korneikova M.V., Myazin V.A., Fokina N.V., Redkina V.V., Evdokimova G.A. Patent N 189759 RF. Phytosystem module for biological treatment of industrial wastewater from mineral pollutants. Publ. 03.06.2019. Bul. N 16 (in Russian).

28. Ivanova L.A., Myazin V.A., Korneikova M.V. et al. It's time to clean up the Arctic. Development of a phytotreatment system for post-treatment of nitrogen compounds from mining wastewater. Apatity: Izd-vo Kol'skogo nauchnogo tsentra, 2021, p. 88. DOI: 10.37614/978.5.91137.449.5

29. Ivanova L.A., Kornejkova M.V., Myazin V.A., Fokina N.V., Redkina V.V., Evdokimova G.A. Patent N 2773122 RF. Module of a phytosystem for biological purification of industrial waste water from mineral contaminants. Publ. 30.05.2022. Bul. N 16 (in Russian).

30. Chao Yang, Xiangling Zhang, Yuqi Tang et al. Selection and optimization of the substrate in constructed wetland: A review. *Journal of Water Process Engineering*. 2022. Vol. 49. N 103140. DOI: 10.1016/j.jwpe.2022.103140

31. Pashkevich M.A., Korotaeva A.E., Matveeva V.A. Experimental simulation of a system of swamp biogeocenoses to improve the efficiency of quarry water treatment. *Journal of Mining Institute*. 2023. Vol. 263, p. 785-794.

32. Fuchao Zheng, Tiange Zhang, Shenglai Yin et al. Comparison and interpretation of freshwater bacterial structure and interactions with organic to nutrient imbalances in restored wetlands. *Frontiers in Microbiology*. 2022. Vol. 13. N 946537. DOI: 10.3389/fmicb.2022.946537

33. Lago A., Rocha V., Barros O. et al. Bacterial biofilm attachment to sustainable carriers as a clean-up strategy for wastewater treatment: A review. *Journal of Water Process Engineering*. 2024. Vol. 63. N 105368. DOI: 10.1016/j.jwpe.2024.105368

34. Shengjiong Deng, Deshou Cun, Rufeng Lin et al. Enhanced remediation of real agricultural runoff in surface-flow constructed wetlands by coupling composite substrate-packed bio-balls, submerged plants and functional bacteria: Performance and mechanisms. *Environmental Research*. 2024. Vol. 263. Part 2. N 120124. DOI: 10.1016/j.envres.2024.120124

35. Xuehong Zhang, Yue Lin, Hua Lin, Jun Yan. Constructed wetlands and hyperaccumulators for the removal of heavy metal and metalloids: A review. *Journal of Hazardous Materials*. 2024. Vol. 479. N 135643. DOI: 10.1016/j.jhazmat.2024.135643

36. Sharma R., Vymazal J., Malaviya P. Application of floating treatment wetlands for stormwater runoff: A critical review of the recent developments with emphasis on heavy metals and nutrient removal. *Science of The Total Environment*. 2021. Vol. 777. N 146044. DOI: 10.1016/j.scitotenv.2021.146044

37. Gupta V., Courtemanche J., Gunn J., Mykytczuk N. Shallow floating treatment wetland capable of sulfate reduction in acid mine drainage impacted waters in a northern climate. *Journal of Environmental Management*. 2020. Vol. 263. N 110351. DOI: 10.1016/j.jenvman.2020.110351

38. Türker O.C., Vymazal J., Türe C. Constructed wetlands for boron removal: A review. *Ecological Engineering*. 2014. Vol. 64, p. 350-359. DOI: 10.1016/j.ecoleng.2014.01.007

39. Chuanqi Zhou, Jung-Chen Huang, Fang Liu et al. Selenium removal and biotransformation in a floating-leaved macrophyte system. *Environmental Pollution*. 2019. Vol. 245, p. 941-949. DOI: 10.1016/j.envpol.2018.11.096

40. Stanley M., Palace V., Grosshans R., Levin D.B. Floating treatment wetlands for the bioremediation of oil spills: A review. *Journal of Environmental Management*. 2022. Vol. 317. N 115416. DOI: 10.1016/j.jenvman.2022.115416

41. Rai P.K. Novel adsorbents in remediation of hazardous environmental pollutants: Progress, selectivity, and sustainability prospects. *Cleaner Materials*. 2022. Vol. 3. N 100054. DOI: 10.1016/j.clema.2022.100054

42. Zhongbing Chen, Cuervo D.P., Müller J.A. et al. Hydroponic root mats for wastewater treatment – a review. *Environmental Science and Pollution Research*. 2016. Vol. 23. Iss. 16, p. 15911-15928. DOI: 10.1007/s11356-016-6801-3

43. Baoshan Shi, Xiangju Cheng, Junheng Pan et al. Impact of water depth and flow velocity on organic matter removal and nitrogen cycling in floating constructed wetlands. *Science of The Total Environment*. 2024. Vol. 954. N 176731. DOI: 10.1016/j.scitotenv.2024.176731

44. Xiaohan Li, Xing Yan, Haojie Han et al. The trade-off effects of water flow velocity on denitrification rates in open channel waterways. *Journal of Hydrology*. 2024. Vol. 637. N 131374. DOI: 10.1016/j.jhydrol.2024.131374

45. Stephenson R., Sheridan C. Review of experimental procedures and modelling techniques for flow behaviour and their relation to residence time in constructed wetlands. *Journal of Water Process Engineering*. 2021. Vol. 41. N 102044. DOI: 10.1016/j.jwpe.2021.102044

46. Postila H., Ronkanen A.-K., Kløve B. Wintertime purification efficiency of constructed wetlands treating runoff from peat extraction in a cold climate. *Ecological Engineering*. 2015. Vol. 85, p. 13-25. DOI: 10.1016/j.ecoleng.2015.09.066

47. Kadlec R., Johnson K. Treatment wetlands of the far north. *Ecological Engineering*. 2023. Vol. 190. N 106923. DOI: 10.1016/j.ecoleng.2023.106923

48. Arslan M., Wilkinson S., Naeth M.A. et al. Performance of constructed floating wetlands in a cold climate waste stabilization pond. *Science of The Total Environment*. 2023. Vol. 880. N 163115. DOI: 10.1016/j.scitotenv.2023.163115

49. Chih-Yu Wang, Sample D.J., Day S.D., Grizzard T.J. Floating treatment wetland nutrient removal through vegetation harvest and observations from a field study. *Ecological Engineering*. 2015. Vol. 78, p. 15-26. DOI: 10.1016/j.ecoleng.2014.05.018

50. Rehman K., Imran A., Amin I., Afzal M. Inoculation with bacteria in floating treatment wetlands positively modulates the phytoremediation of oil field wastewater. *Journal of Hazardous Materials*. 2018. Vol. 349, p. 242-251. DOI: 10.1016/j.jhazmat.2018.02.013

51. Ladislas S., Gérente C., Chazarenc F. et al. Floating treatment wetlands for heavy metal removal in highway stormwater ponds. *Ecological Engineering*. 2015. Vol. 80, p. 85-91. DOI: 10.1016/j.ecoleng.2014.09.115

52. Locke-Rodriguez J., Troxler T., Sukop M.C. et al. Floating flowers: Screening cut-flower species for production and phytoremediation on floating treatment wetlands in South Florida. *Environmental Advances*. 2023. Vol. 13. N 100405. DOI: 10.1016/j.envadv.2023.100405

53. Lynch J., Fox L.J., Owen Jr. J.S., Sample D.J. Evaluation of commercial floating treatment wetland technologies for nutrient remediation of stormwater. *Ecological Engineering*. 2015. Vol. 75, p. 61-69. DOI: 10.1016/j.ecoleng.2014.11.001

54. Dong Qing Zhang, Jinadasa K.B.S.N., Gersberg R.M. et al. Application of constructed wetlands for wastewater treatment in developing countries – A review of recent developments (2000-2013). *Journal of Environmental Management*. 2014. Vol. 141, p. 116-131. DOI: 10.1016/j.jenvman.2014.03.015

***Authors*: Lyubov A. Ivanova,** *Doctor of Biological Sciences, Chief Researcher* (*Polar-Alpine Botanical Garden-Institute of N.A.Avrorin, Federal Research Centre, Kola Science Centre of the RAS, Kirovsk, Russia*), *Leading Researcher* (*Institute of North Industrial Ecology Problems, Kola Science Centre of the RAS, Apatity, Russia*), *https://orcid.org/0000-0002-7994-5431*, **Evgeniya A. Krasavtseva,** *Candidate of Engineering Sciences, Researcher* (*Institute of North Industrial Ecology Problems, Kola Science Centre of the RAS, Apatity, Russia*), *Researcher* (*Laboratory of Nature-Inspired Technologies and Technosphere Safety of the Arctic, Nanomaterials Research Centre, Kola Science Centre of the RAS, Apatity, Russia*), *vandeleur2012@yandex.ru*, *https://orcid.org/0000-0002-8821-4446*, **Tamara T. Gorbacheva,** *Candidate of Biological Sciences, Leading Researcher* (*Institute of North Industrial Ecology Problems, Kola Science Centre of the RAS, Apatity, Russia*), *https://orcid.org/0000-0001-5014-4385*.

The authors declare no conflict of interests.